IMPERIAL COLLEGE OF SCIENCE, TECHNOLOGY AND MEDICINE

Faculty of Engineering

Department of Chemical Engineering and Chemical Technology

Electrochemical Separation and Purification of Metals from Waste Electrical and Electronic Equipment (WEEE)

By

Umi Fazara Md Ali

Thesis Submitted for the Degree of Doctor of Philosophy and for the

Diploma of Imperial College

June 2011

Abstract

This thesis reports on results of a novel process to recover metals selectively by electrodeposition by pumping aqueous acidic chloride solutions produced by leaching of shredded waste electrical and electronic equipment (WEEE) through the potentiostatically controlled cathode of an electrochemical reactor. The WEEE solutions contained low concentrations of precious metals, including Ag, Au, Pd and high concentrations of Cu. Electrodeposition from low concentrations of such dissolved metals requires electrodes with high mass transport rate coefficients and specific surface areas to increase cross-sectional current densities and optimise capital and operating costs. Hence, to recover gold from solutions with concentrations < 10 mol m^{-3} in the WEEE leachate, a three-dimensional cathode was used consisting of a circulating particulate bed of 0.5-1.0 mm diameter graphite particles, on which ($Au^{III}Cl_4^-$ + $Au^{I}Cl_2^-$) ions were reduced. The temporal decay of the solution absorbance of $AuCl_4^-$ ions at 312 nm was recorded on-line by a quartz flow cell connected to a UV-visible spectrophotometer using fibre optics, enabling its time dependent concentration to be determined in real time. Total dissolved gold concentrations were determined by Inductively-coupled Plasma Optical Emission Spectroscopy (ICP-OES). The results from the reactor experiments were modelled in terms of a mass transport controlled reaction in a plug flow electrochemical reactor operated in batch recycle with a continuous stirred tank reservoir.

As copper is the dominant element in WEEE, and hence in the leach solution, its electrodeposition was investigated using an electrochemical reactor with a Ti/Ta_2O_5-IrO_2 anode, cation-permeable membrane and a Ti mesh cathode in a fluidised bed of 590-840 μm glass beads to enhance mass transfer rates and to improve copper deposit morphologies. As for other metals, the effects were determined of cathode potential and solution flow rate on electrodeposition rates, charge yields, specific electrical energy consumptions, and deposit morphologies, imaged subsequently by scanning electron microscopy, and purities determined by X-ray fluorescence (XRF) and X-ray diffraction spectroscopy (XRD). While depleting Cu^{II} concentrations from 500 to 35 mol m^{-3}, copper purities of > 99.79 %, as required for commercial purity Cu, were achieved with charge yields of 0.90 and specific electrical energy consumptions of 2000 kW h $tonne^{-1}$. In addition, the circulating particulate bed cathode depleted solutions rapidly from 15 mol m^{-3} Cu^{II} ca. 100 ppm.

Experiments with a rotating vitreous carbon cathode confirmed predictions from a kinetic model for a small electrode potential window within which to achieve selective electrodeposition of tin from synthetic Sn^{IV}-Pb^{II} aqueous chloride solutions, from which Pb could be electrodeposited subsequently. Al^{III}, Fe^{II}, Zn^{II} and Ni^{II} remained in solution after the recovery of Au, Cu, Sn and Pb from the WEEE leachate. Unlike Al, it is possible to electrodeposit Fe from aqueous solution, and it was decided to add NaOH (+ air) to increase the pH to ca. 3.25 to precipitate '$Fe(OH)_3$', which was recovered by filtration. This option also enabled subsequent electro-co-deposition of Ni and Zn with high charge yields, as the higher pH decreased the driving force for H_2 evolution. A one- dimensional mathematical model was developed in MAPLE™ to predict the kinetics of Ni-Zn electro-co-deposition, which was validated experimentally. The model also considered the potential and concentration profiles in the cathode | electrolyte boundary layer for conditions in which migration and convective diffusion all contribute to overall transport rates, to predict the behaviour and optimize the process parameters of the electrochemical reactors.

Acknowledgements

I would like to express my sincere appreciation and million thanks to my supervisor, Professor Geoff Kelsall for offering high quality guidance, support, critical review, advice and even counseling from inception to completion of this Ph.D. research project. I feel very fortunate to be able to learn under his supervision and won't ever forget this valuable experience.

I would also like to thank Dr. Chun-Yee Cheng for the excellent advice that she offered throughout my PhD, and for the many helpful discussions that we had relating to all aspects of my work. She always made time to help with research and offer advice, which was greatly appreciated.

I would like to extend my sincere appreciation to Patricia Carry for the provision and help with ICP, Dr. Khoo Ji Yi for the help with XRD and Dr Steve Denisson who has helped me with SEM. Special thanks to Dr. Waheedah and Dr. Tengku Zetty Maztura for spending their precious time to proof-read my thesis. My gratitude is extended to Mr. Richard Wallington for the workshop help, Mr. Keith Walker and Mr. Tawanda Nyabango for supplying materials and consumables. I also appreciate the work done by the technical and administrative staff to keep things running smoothly, especially Susi Underwood for processing my documentation over the course of my Ph.D studies.

I also appreciate the help I have received from present and past members of Prof Kelsall's group including Dr. Doraswami, Dr. Mechelhoff, Dr. Hartley, Dr. Nicholas, Kathryn, Chin, Melanie, Candice, Palang and Anna. Many thanks for the friendship and the pleasant working environment in the lab and outside working hours.

The funding given by Ministry of Higher Education of Malaysia (MOHE), and University Malaysia Perlis (UniMAP) for the duration of my PhD studies are greatly appreciated.

I would like to thank my husband, Dr. Mohd Irfan Hatim for going through this Ph.D. journey with me, through thick and thin, ups and down and the roller coaster ride of good and bad times. I'm very grateful that I have you as my companion. Special tribute and thousand of loves to my two children, Muhammad Wafiq and Wafa Sajeedah, even if we are thousand of miles away, I always feel your presence here with me, I can't wait to meet both of you in Malaysia. To my parents, Md Ali Sujan and Shahidah Shaari, you are always be my first

supporters, my advisors, my mentors and who have been a constant source of encouragement throughout my studies, for that, I would like to say a million thanks.

Last but not least, this is for all my family and friends, ‘Thank You’.

Table of Contents

Abstract……..1

Acknowledgements……2

Table of Contents……...4

List of Figures……...11

List of Tables…….21

Nomenclature……22

1. INTRODUCTION 25

1.1. Background 25
1.2. Project Motivation and Aims 28
1.3. Thesis Organization..... 29
1.4. References 30

2. PRINCIPLES OF ELECTROCHEMICAL SYSTEMS 32

2.1. Chapter Overview 32
2.2. Fundamental Definitions 32
2.3. Electrochemical Thermodynamics 32
2.4. Electrochemical Kinetics..... 34
2.5. Rotating Disc Electrode (RDE)..... 37
2.6. Rotating-Ring Disc Electrode (RRDE) 38
2.7. Non-steady State Systems 39
2.8. Transport Processes in Electrochemical Systems 40
2.9. Phase Formation and Growth..... 42
2.10. Electrochemical Figures of Merit..... 43
2.10.1. Cell Voltage..... 43

2.10.2. Charge Yield 44
2.10.3. Specific Electrical Energy Consumption (SEEC) 45
2.11. Electrochemical Reactors for Metal Recovery 45
2.11.1. Mode of operation and model description of the electrochemical reactor 46
2.11.2. Mass transport properties for a mesh cathode in a fluidised bed of inert particles of an electrochemical reactor 48
2.12. Chapter Summary 49
2.13. References 49

3. LITERATURE REVIEW 51

3.1. Chapter Overview 51
3.2. Electrical and Electronic Equipment (EEE) 51
3.2.1. Definition of EEE 51
3.2.2. Characterisation of WEEE 51
3.3. Overview on Current Situation 54
3.3.1. Legislative Issue for WEEE 56
3.3.2. Review on Industrial Metal Recovery 57
3.4. Economic Perspectives 62
3.5. Research at Imperial College London on hydrometallurgical process 63
3.6. Electrochemical Metal Recovery for PM (Au) and Base Metals (Cu, Sn, Pb, Ni, Zn, Al) 65
3.6.1. Gold Electrodeposition 70
3.6.2. Copper Electrodeposition 72
3.6.3. Selective Recovery of Tin by Electrodeposition from Tin-Lead Solutions 74
3.6.4. Fate of other metals not recovered at pH 0 76
3.6.5. Metal Precipitation 76
3.6.6. Electro-co-deposition 76
3.7. Electrochemical Reactor Design 78
3.7.1. Electrochemical Reactor with 2-D electrodes 80
3.7.2. Electrochemical Reactor with 3-D electrodes 83

3.7.3. Circulating particulate bed electrode 86
3.8. Project Objectives 89
3.9. References 91

4. MATERIALS AND EXPERIMENTAL METHODS 105

4.1. Chapter Overview 105
4.2. Materials 106
4.2.1. Chemicals 106
4.2.2. Electric and Electronic Equipment Waste 108
4.3. Electrochemical Measurement Equipment 110
4.3.1. General remarks 110
4.3.2. pH and Conductivity 111
4.3.3. Rotating Disc Electrode (RDE) 111
4.3.4. Rotating Ring-Disc Electrode 113
4.3.5. Special Precautionary Measures 114
4.3.6. Repeatability & Reproducibility 115
4.4. Reactor Experiments 116
4.4.1. Mesh Electrode in a Fluidised Bed of Inert Particles 116
4.4.2. Circulating Particulate Bed Cathode 118
4.5. Precipitation Experiments 122
4.6. Analytical Techniques 122
4.6.1. UV-Visible Spectrophotometry 122
4.6.2. Inductively Coupled Plasma Spectroscopy Optical Emission Spectroscopy (ICP-OES) 125
4.6.3. X-Ray Fluorescence Spectroscopy (XRF) 126
4.6.4. X-Ray Diffraction (XRD) 126
4.6.5. Scanning Electron Microscopy (SEM) and Energy Dispersive X-ray microanalysis (EDAX) 127
4.7. Software 127
4.8. Chapter Summary 127
4.9. References 128

5. GOLD ELECTRODEPOSITION 129

5.1. Chapter Overview 129
5.2. Thermodynamic Analysis 129
5.3. Transport and Kinetic Analyses 131
5.4. Kinetic Model of $AuCl_n^-$ reduction 137
5.5. Gold Electrodeposition in Circulating Particulate Beds Electrode (CPBE) Reactor 139
5.6. Deposit morphologies 147
5.7. Chapter Summary 150
5.8. References 151

6. COPPER ELECTRODEPOSITION 152

6.1. Chapter Overview 152
6.2. Thermodynamics 152
6.2.1. Copper 152
6.2.2. Silver 154
6.3. Transport and Kinetic Analyses 156
6.3.1. Cu-Cl-H_2O 156
6.3.2. Ag-Cl-H_2O system 160
6.4. Modelling of the Mechanisms Occurring in the System 160
6.4.1. Electrochemical Reduction of Cu^{II} Ions from Aqueous Chloride Electrolytes 161
6.5. Determination of dark coloured intermediate (mixed metal and mixed oxidation state of Cu) 163
6.5.1. Voltammetry Analyses 164
6.6. Electrochemical Reactor Experiments 169
6.6.1. Electrodeposition of $CuCl_n^-$ with Mesh Electrode in a Fluidised Bed of Inert Particles 170
6.6.2. Electrodeposition of low concentration of $CuCl_n^-$ in circulating particulate bed electrode 175
6.7. Deposit Morphologies 181

6.8. Chapter Summary 184
6.9. References 186

7. SELECTIVE ELECTRODEPOSITION OF TIN FROM TIN (Sn^{IV})- LEAD (Pb^{II}) AQUEOUS CHLORIDE SOLUTIONS 189

7.1. Chapter Overview 189
7.2. Thermodynamics 190
7.2.1. Tin 190
7.2.2. Lead 191
7.3. Transport and Kinetic Analyses 194
7.3.1. Determining the reduction kinetics of Sn^{IV} chloro- complexes 194
7.3.2. Determining the reduction kinetics of Sn^{II} chloro- complexes 197
7.3.3. Determining the molar ratio of tin complexes in solution 201
7.4. Modelling of the Mechanisms Occurring in the System 204
7.4.1. Electrochemical Reduction of Sn^{IV} Ions from Aqueous Chloride Electrolytes 204
7.5. Electrochemical Reactor Experiments 207
7.6. Chapter Summary 209
7.7. References 211

8. NICKEL-ZINC ELECTRO-CO-DEPOSITION 213

8.1. Chapter Overview 213
8.2. Precipitation of $Fe(OH)_3$ and $Fe(OH)_2$ 213
8.3. Speciation and Equilibrium Potentials 216
8.3.1. Nickel 216
8.3.2. Zinc 219
8.4. Electrolyte composition and complexation for the Zinc- Nickel- Chloride System 222
8.5. Determining the reduction kinetics of zinc(II) in 4 kmol m^{-3} HCl and 1 kmol m^{-3}

NaCl: 222
8.5.1. An experimental study 222
8.6. Interactions of Electrodeposition Potentials between Nickel and Zinc..... 229
8.7. Model Development 231
8.7.1. Electrochemical Reactions 231
8.7.2. Electrode Kinetics and Charge Efficiencies 233
8.7.3. Modelling of dissolved nickel (II) and zinc (II) concentration and potential profiles in the cathode | electrolyte boundary layer 234
8.7.4. Mathematical Model of a cation permeable membrane containing Na^+ and H^+ 239
8.8. Results and Discussion on the one-dimensional model of Ni^{II}-Zn^{II} electro-co-deposition 242
8.9. Chapter Summary 247
8.10. References 248

9. CONCLUSIONS 251

9.1. General Conclusions 251
9.2. Gold Electrodeposition 251
9.3. Copper Electrodeposition 252
9.4. Selective Electrodeposition of Tin from Aqueous Sn^{IV}-Pb^{II} Chloride Solutions 253
9.5. Nickel—Zinc Electro-co-deposition 254
9.6. Chapter Summary 255

10. FUTURE WORK 257

10.1. Experimental Work 257
10.2. Modelling Work 258

APPENDICES 259

Appendix A: Nernst Equations for all metals, used in the calculation for Figure 3.13 (pp 68) 259
Appendix B: Thermodynamic data 262
(a) Thermodynamic values for the Cl-H_2O system 262
(b) Thermodynamic values for the Au-Cl-H_2O system 263
(c) Thermodynamic values for the Cu-Cl-H_2O system 263
(e) Thermodynamic values for the Sn-Cl-H_2O system 265
(f) Thermodynamic values for the Pb-Cl-H_2O system 266
(g) Thermodynamic values for the Zn-Cl-H_2O system 267
(h) Thermodynamic values for the Ni-Cl-H_2O system 268
Appendix C: Reactions and E values 269
(a) Cl-H_2O system 269
(b) Au-Cl-H_2O system 270
(c) Cu-Cl-H_2O system 270
(d) Ag-Cl-H_2O system 271
(e) Sn-Cl-H_2O system 271
(f) Pb-Cl-H_2O system 272
Appendix D: Mechanistic studies 274
(a) Electrochemical Reduction of $AuCl_n^-$ Ions from Aqueous Electrolytes 274
Proposed Reduction Mechanism: 274
Appendix E: Maple^{TM} code 276
(a) Mechanism of electrochemical reduction of $AuCl_n^-$ 276
(b) Mechanism of electrochemical reduction of Cu^{II} in aqueous chloride solutions 277
(c) Mechanism of electrochemical reduction of Sn^{IV} Ions from Aqueous Chloride Electrolytes 279
(d) Modelling of dissolved nickel (II) and zinc (II) concentration and potential profiles in the cathode | electrolyte boundary layer. 280
Appendix F: Flow meter calibration 287
Appendix G: Costing 287
References 289

List of Figures

Figure 2-1. Schematic of Tafel plot $j_{0,c}$ and $j_{0,a}$ are the cathodic and anodic limiting current densities, respectively [1]. 35

Figure 2-2. Plot of Butler-Volmer equation for j_0 = 1 A m^{-2} [5]. 36

Figure 2-3. Current density operating regimes in under kinetic, mixed and mass transport control; k_m represents the mass transport rate coefficient. 36

Figure 2-4. Transport processes and distribution of electrical potential in an electrochemical reactor [5]. 40

Figure 2-5. The stages in the formation of a stable, growing nucleus of a metal on an electrode surface [2]. 42

Figure 2-6. Distribution of potential in an electrochemical cell. 44

Figure 2-7. Plug flow reactor operated in batch recycle mode with well-mixed reservoir [10]. 46

Figure 3-8. Material composition of WEEE [9]. 52

Figure 3-9. Printed Circuit Boards (PCBs). 53

Figure 3-10. PCB section [9]. 53

Figure 3-11. Composition of Metals in Electronic Scrap of PCBs [13]. 54

Figure 3-12. Metal recovery process of PCBs, showing the various materials in- and outflows in the different steps [18]. 60

Figure 3-13. Equilibrium potential of metals (vs. SHE) in 4 kmol m^{-3} HCl + 1 kmol m^{-3} NaCl leach solution at pH 0 [50]. 68

Figure 3-14. Metal recovery of Cu, Sn and Pb during potentiostatic electrowinning with carbon felt reactor [52]. 69

Figure 3-15. Metal recovery of Cu, Sn and Pb during galvanostatic electrowinning with carbon felt reactor [52]. 69

Figure 3-16. Predicted kinetics of hydrogen evolution on metals in 1 kmol m^{-3} H_2SO_4 [53].. 70

Figure 3-17. Undivided Chemelec cell consisting mesh electrodes and fluidised inert particles [111]. 81

Figure 3-18. Rotating cylinder electrode (RCE) [135]. 82

Figure 3-19. Schematic of graphite felt electrochemical reactor. 84

Figure 3-20. Schematic of typical spouted bed electrode [154]..... 85

Figure 3-21. Schematic diagram of the movement of the graphite particles in the circulating particulates bed reactor [157]. 87

Figure 4-22. Flow chart for mechanical processing of electronic waste [1]. 109

Figure 4-23. Magnetic and Eddy Current Separation Techniques [2]. 109

Figure 4-24. Rotating disc electrode assembly and electrochemical cell [4]. 112

Figure 4-25. Rotating ring-disc electrode assembly and electrochemical cell [4]. 114

Figure 4-26. RRDE experiment set-up (three-compartment glass cell, electrodes, rotating shaft, motor controller). 114

Figure 4-27. Photograph of the fluidised bed electrolyte of glass beads electrochemical reactor and the titanium mesh electrode. 117

Figure 4-28. Schematic diagram of the experimental set-up of the mesh electrode in a fluidised bed of inert particles electrochemical reactor. 118

Figure 4-29. Representation of components in a unit cell..... 120

Figure 4-30. Schematic diagram for the circulating particulates bed reactor. 120

Figure 4-31. Photograph of the circulating particulates bed reactor. 120

Figure 4-32. Schematic diagram of the experimental set-up of the circulating particulate bed cathode electrochemical reactor. 121

Figure 4-33. UV spectra for lead (II) chloride in NaCl/HCl. 123

Figure 4-34. UV spectra for tin (II) chloride in NaCl/HCl. 123

Figure 4-35. Absorption of tin (II) chloride and lead (II) chloride in NaCl/HCl. 124

Figure 4-36. Standard and flow-through cells for a spectrophotometer [8]. 125

Figure 4-37. Set-up for the fibre-optics. 125

Figure 5-38. Potential pH diagram for gold-water system. Activities: $Au^{3+} = 10^{-4}$; 298 K, 1 atm [3]. 130

Figure 5-39. Potential pH diagram for gold-chloride-water. Activities: $AuCl_n^- = 10^{-4}$, $Cl^- = 5$; 298 K, 1 atm [3]. 130

Figure 5-40. Electrode potential for $E_{AuCl_2^-/Au}$ and $E_{AuCl_4^-/Au}$ against gold and chloride concentrations..... 131

Figure 5-41. Predicted pH dependence of solubilities of Au^{3+} , $AuCl_2^-$ and $AuCl_4^-$ ions. Cl^- = 5; 298 K, 1 atm..... 131

Figure 5-42. Reduction of 0.5 mol m^{-3} Au^{III} at Pt rotating disc electrode in 4 kmol m^{-3} + 1 kmol m^{-3} NaCl, scan rate 10 mV s^{-1}..... 132

Figure 5-43. Cyclic voltammogram of a Pt rotating disc electrode rotating at 60-240 rpm in 0.5 mol m^{-3} Au^{III} in 4 kmol m^{-3} HCl + 1 kmol m^{-3} NaCl at a scan rate of 10 mV s^{-1}..... 133

Figure 5-44. Effect of rotation rate on current density for reduction of 0.5 mol m^{-3} Au^{III} at Pt rotating disc electrode in 4 kmol m^{-3} HCl + 1 kmol m^{-3} NaCl..... 134

Figure 5-45. Effect of electrode potential on current density for reduction of 0.5 mol m^{-3} Au^{III} on Pt and Au-plated Pt RDE in 4 kmol m^{-3} HCl + 1 kmol m^{-3}; scan rate 10 mV s^{-1}, rotation rate 960 rpm..... 135

Figure 5-46. Tafel plot for reduction of 0.5 mol m^{-3} Au^{III} at Au coated Pt RDE in 4 kmol m^{-3} + 1 kmol m^{-3} NaCl, scan rate 10 mV s^{-1} , rotation rate 960 rpm. 135

Figure 5-47. Linear potential sweep voltammogram for reduction of 0.5 mol m^{-3} Au^{III} at Pt rotating disc electrode in 4 kmol m^{-3} HCl + 1 kmol m^{-3} NaCl, scan rate 1 V s^{-1}; 60 rpm. 137

Figure 5-48. Prediction of potential-current relationship from the kinetic model solved with Maple™, compared to experimental data for the reduction of 0.5 mol m^{-3} Au^{III} in 4 kmol m^{-3} HCl +1 kmol m^{-3} NaCl..... 138

Figure 5-49. Predicted electrode potential dependence of surface concentrations of $AuCl_4^-$ and $AuCl_2^-$ and fractional coverages of Au(I)(θ_I) and Au(II)(θ_{II}) adsorbed species..... 139

Figure 5-50. Steady state current-potential behaviour for reduction of 0.5 mol $AuCl_4^-$ m^{-3} in CPBE reactor..... 140

Figure 5-51. Absorbance of solution during gold electrodeposition in CPBE at + 0.20 V (SCE); path length 1 mm measured via fibre optics, at time, t. 141

Figure 5-52. Current and gold concentration with time during electrodeposition on virgin graphite particles in CPBE reactor at + 0.20 V (SCE); flow rate = 0.25 dm^3 min^{-1}..... 142

Figure 5-53. Images of gold deposits in the CPBE: (a) on the feeder cathode electrode and (b) on the Au particulates inside the catholyte compartment. 143

Figure 5-54. Depletion of Au^{III} concentration and current with time during batch recycle electrowinning on gold metallised particles in CPBE reactor with feeder electrode at + 0.20 V (SCE); flow rate = 0.25 dm^3 min^{-1} 144

Figure 5-55. Depletion of dissolved Au^{III} concentration with time during batch recycle reduction in CPBE reactor with feeder electrode at +0.20 V (SCE); flow rate= 0.25 dm^3 min^{-1}. 145

Figure 5-56. Effects of flow rate on the time dependency of current, for gold deposition in a CPBE reactor at a feeder cathode potential of +0.20 V (SCE) and an initial gold concentration of 0.5 mol m^{-3}. 146

Figure 5-57. Depletion of dissolved gold concentration with time during batch recycle reduction in CPBE reactor with feeder electrode at + 0.20 V (SCE); flow rate = 0.25 dm^3 min^{-1}. 147

Figure 5-58. SEM image of virgin graphite particles (0.5- 1 mm) used as cathode in the CPBE. 148

Figure 5-59. SEM images of 10 μm gold deposits on virgin graphite particles..... 149

Figure 5-60. SEM image of gold deposits on a Au-pre plated graphite particulate in the CPBE operating at a feeder cathode potential of +0.20 V (SCE). 149

Figure 6-61. Potential pH diagram for copper-water system. Dissolved copper activities = 10^{-1}, 298 K, 1 atm..... 154

Figure 6-62. Potential pH diagram for copper-chloride-water. Activities: Dissolved copper and chloride activities = 10^{-1} and 5; 298 K, 1 atm..... 154

Figure 6-63. Predicted solubility of Cu^{I} species in aqueous chloride media at 298 K..... 154

Figure 6-64. Predicted solubility of Cu^{II} species in aqueous chloride media at 298 K..... 154

Figure 6-65. Predicted Ag^{I} species in aqueous chloride media at 298 K [7]. 156

Figure 6-66. Potential pH diagram for silver-chloride-water system. Dissolved Ag^{I} and chloride activities = 10^{-4} and 5; 298 K, 1 atm. [7]. 156

Figure 6-67. Effect of the RDE rotation rate on the cathodic polarization curves of 5 mol m^{-3} Cu^{II} in 4 kmol m^{-3} HCl + 1 kmol m^{-3} NaCl solutions, at Pt rotating disc electrode, scan rate 10 mV s^{-1}. 157

Figure 6-68. Reduction of 5 mol m^{-3} Cu^{II} at Pt rotating disc electrode in 4 kmol m^{-3} HCl + 1 kmol m^{-3} NaCl, scan rate 10 mV s^{-1}. 157

Figure 6-69. Tafel plot for reduction of 5 mol m^{-3} Cu^{II} at Pt rotating disc electrode in 4 kmol m^{-3} + 1 kmol m^{-3} NaCl, scan rate 10 mV s^{-1} , rotation rate of 36 s^{-1}. 159

Figure 6-70. Kinetics of 5 mol m^{-3} Cu^{II} reduction at Pt rotating disc electrode in 4 kmol m^{-3} HCl + 1 kmol m^{-3}. Experimental data (▲■) and Predictions (—) from Levich's equation [6-16]. 159

Figure 6-71. Predicted electrode potential dependence of surface concentrations of $CuCl_2$ (aq) and $CuCl_2^-$. 163

Figure 6-72. Model prediction of current density- electrode potential relationship from the kinetic model solved with Maple^{TM}, compared to experimental data for the reduction of 5 mol m^{-3} Cu^{II} in 4 kmol m^{-3} HCl + 1 kmol m^{-3} NaCl. 163

Figure 6-73. Absorbance spectra in the visible light region for solutions of 4 kmol m^{-3} HCl + 1kmol m^{-3} NaCl containing $CuCl_2$(aq), $CuCl_2^-$ and a mixture of the two [20]. 164

Figure 6-74. Reduction current and Experimental data (▲■) and Predictions (—) from Levich equation [6-16], for solutions of 4 kmol m^{-3} HCl + 1 kmol m^{-3} NaCl containing; (a,e)5 mol m^{-3} of $CuCl_2$(aq) + 5 mol m^{-3} $CuCl_2^-$, (b,f) 10 mol m^{-3} of $CuCl_2$ (aq) + 10 mol m^{-3} $CuCl_2^-$, (c,g) 50 mol m^{-3} of $CuCl_2$(aq) + 50 mol m^{-3} $CuCl_2^-$ and (d,h) 100 mol m^{-3} of $CuCl_2$(aq) + 100 mol m^{-3} $CuCl_2^-$, at a scan rate of 10 mV s^{-1}..... 166

Figure 6-75. (a) Reduction current and (b) Experimental data (▲■) correlated with Predictions (—) from Levich's equation [6-16] for the WEEE leachate (Chapter 4, section 4.2.2). 167

Figure 6-76. Cyclic voltammogram for negative scan alone for solutions of 4 kmol m^{-3} HCl + 1 kmol m^{-3} NaCl containing: (a) $CuCl_2$(aq), (b) $CuCl_2^-$ and (c) a mixture of $CuCl_2$(aq) and $CuCl_2^-$ at a scan rate of 10 mV s^{-1}..... 168

Figure 6-77. Cyclic voltammogram for solutions 4 kmol m^{-3} HCl + 1kmol m^{-3} NaCl containing $CuCl_2$(aq), $CuCl_2^-$ and a mixture of the two, obtained experimentally for rotation rate at; (a)1500 rpm and (b) 2160 rpm, scan rate 10 mV s^{-1}, compared against an averaged value calculated for the mixture..... 169

Figure 6-78. Voltammogram for the reduction of $CuCl_2$ (aq) and $CuCl_2^-$ and H_2 evolution on a Cu-coated Ti mesh cathode, in a fluidised bed of 590-840 μm glass beads, at a scan rate of 10 mV s^{-1}, at a flow rate of 0.85 dm^3 min^{-3}, bed expansion of 0.5 and initial copper concentration of 470 mol m^{-3}. 171

Figure 6-79. The optimal bed voidage for fluidised bed predicted by correlations in literature [16]. 171

Figure 6-80. Time dependence of the ($CuCl_2$(aq) and $CuCl_2^-$); ($[Cu^{II}]_0$ = 470 mol m^{-3}) concentration (red ◊) and reduction current density (blue ◊) in fluidised bed electrolyte reactor with 590-840 μm glass beads, batch recycle model at - 0.35 V (SCE) ; flow rate = 0.85 dm^3 min^{-1} , $k_m = 2.14\times10^{-5}$ m s^{-1}· 172

Figure 6-81. Time dependence of the ($CuCl_2$(aq) and $CuCl_2^-$); ($[Cu^{II}]_0$ = 470 mol m^{-3}) concentration (red ◊); model prediction (---) and reduction current density (blue ◊); model prediction (---) in fluidised bed electrolyte reactor with 590-840 μm glass beads, batch recycle model at -0.45 V (SCE); flow rate = 0.85 dm^3 min^{-1}, $k_m = 4.6\times10^{-5}$ m s^{-1}. 173

Figure 6-82. Image of copper deposits on a mesh electrode in the fluidised bed electrolyte reactor operating at a feeder cathode potential of -0.45 V (SCE). 174

Figure 6-83. Depletion of dissolved copper concentration with time during batch recycle reduction in fluidised bed electrolyte reactor with 590-840 μm glass beads; flow rate = 0.85 dm^3 min^{-3}; -0.45 V (SCE)..... 174

Figure 6-84. Images of copper pre-plating in the circulating particulate bed reactor: (a) on the feeder cathode electrode and (b) on the virgin graphite particles inside the catholyte compartment. Electrowinning from 1 kmol m^{-3} $CuSO_4$ acidified to pH 0.5 with H_2SO_4, operated for 1.5 hrs at 3 A. 176

Figure 6-85. Images of copper deposits after Cu deposition from the simulated WEEE leachate in the circulating particulates bed reactor: (a) on the feeder cathode electrode and (b) on the Cu pre-coated graphite particles inside the catholyte compartment. 177

Figure 6-86. Effects of cathode feeder potential on the time dependence of (a) copper concentration in the form of ln (c/c_0) and charge efficiency, and (b) current, for copper deposition in a circulating particulates bed reactor at a flow rate of 0.25 dm^3 min^{-1} and an initial copper concentration of 15 mol m^{-3}. 178

Figure 6-87. Effects of cathode feeder potential on time dependence of charge yield, for copper deposition in a CPBE reactor at a flow rate of 0.25 dm^3 min^{-1} and initial copper concentration of 15 mol m^{-3}. 180

Figure 6-88. Time dependences of tin, nickel, zinc, iron and lead ion concentrations, for copper deposition in a CPBE reactor at a flow rate of 0.25 dm^3 min^{-1} and initial copper concentration of 15 mol m^{-3}; cathode potential = -0.38 V. 180

Figure 6-89. SEM images of copper deposits on titanium mesh cathode with no fluidised inert particles. Image courtesy of Cheng et al.[21]..... 182

Figure 6-90. SEM images of copper deposits on titanium mesh cathode in a fluidised bed of glass beads at cathode potentials of: (a) -0.35 V (SCE), (b) -0.45 V (SCE). 183

Figure 6-91. XRD spectrum of Cu deposit samples at -0.35 V and -0.45 V (SCE) on Ti mesh electrode. 183

Figure 6-92. SEM image of copper deposits on a copper particle in the circulating particulate bed reactor operating at a feeder cathode potential of -0.38 V (SCE). 184

Figure 7-93. Solubility of Sn^{IV} species in aqueous chloride media at 298 K [12]. 191

Figure 7-94. Potential pH diagram for tin-chloride-water. Activities: Dissolved tin and chloride activities = 10^{-3} and 5 respectively; 298 K, 1 atm [12]. 191

Figure 7-95. Activity-pH diagrams for Pb^{II} species in equilibrium with PbO (red) and $Pb(OH)_2$ (ppt.) at 298 K, 1 atm [14]..... 192

Figure 7-96. Activity-pH diagram for Pb^{IV} species in equilibrium with PbO_2, at 298 K, 1 atm [14]. 192

Figure 7-97. Potential-pH diagram for lead-water system. Dissolved lead and chloride activities = 10^{-3} and 5 respectively; 298 K, 1 atm [14]. 192

Figure 7-98. Solubility of Pb^{II} species in aqueous chloride media at 298 K, 1 atm..... 194

Figure 7-99. Potential pH diagram for lead-chloride-water. Activities: Dissolved tin and chloride activities = 10^{-3} and 5 respectively; 298 K, 1 atm [14]. 194

Figure 7-100. Cyclic voltammogram of a vitreous carbon rotating disc electrode rotating at 16 s^{-1} in 1 mol m^{-3} Sn^{IV} in 4 kmol m^{-3} HCl + 1 kmol m^{-3} NaCl at a scan rate of 5 mV s^{-1}.195

Figure 7-101. Effect of the RDE rotation rate on the limiting current density for reduction of 1 mol m^{-3} Sn^{IV} at vitreous carbon rotating disc electrode in 4 kmol m^{-3} HCl + 1 kmol m^{-3} NaCl. 197

Figure 7-102. Cyclic voltammogram of a Sn-plated VC rotating disc electrode rotating at 16 s^{-1} in 1 mol m^{-3} Sn^{II} + 4 kmol m^{-3} HCl + 1 kmol m^{-3} NaCl at a scan rate of 5 mV s^{-1}. 198

Figure 7-103. Reduction of 1 mol m^{-3} Sn^{II} at Sn pre-plated VC rotating disc electrode in 4 kmol m^{-3} HCl + 1 kmol m^{-3} NaCl. 198

Figure 7-104. Effect of the RDE rotation rate on the limiting current density. 198

Figure 7-105. Tafel plot for reduction of 1 mol m^{-3} Sn^{II} at Sn pre-plated VC electrode in 4 kmol m^{-3} + 1 kmol m^{-3} NaCl, scan rate 10 mV s^{-1} , rotation rate of 36 s^{-1}. 200

Figure 7-106. Analysis using Tafel plots on hydrogen evolution at a Sn pre-plated VC electrode in 4 kmol m^{-3} HCl + 1 kmol m^{-3} NaCl at a scan rate of 5 mV s^{-1} and a rotation rate of 16 s^{-1}. 200

Figure 7-107. Schematic diagram of the rotating (Pt) ring- (vitreous carbon) disc electrode (RRDE) and possible electrode reactions..... 201

Figure 7-108. Cyclic voltammogram on glassy carbon in 1 mol m^{-3} Sn^{IV} + 4 kmol m^{-3} HCl and 1 kmol m^{-3} NaCl. Ring potential +0.6 V (SCE), pH 0, rotation rate 16 s^{-1}, scan rate 5 mV s^{-1}. 202

Figure 7-109. The apparent collection efficiency plots; $N_{app} = I_{ring}/ I_{disc.}$ 203

Figure 7-110. Prediction of potential-current relationship from the kinetic model solved with Maple™, compared to experimental data for the reduction of 1 mol m^{-3} Sn^{IV} in 4 kmol m^{-3} HCl +1 kmol m^{-3} NaCl..... 206

Figure 7-111. Model prediction of current density-electrode potential behaviour for reduction of $PbCl_4^{2-}$, $SnCl_6^{2-}$ and hydrogen evolution. 206

Figure 7-112. Model prediction of current efficiencies-electrode potential behaviour for Sn deposition ($\Phi^e_{Sn} = j_{Sn} / (j_{Sn} + j_{Pb} + j_{H2})$..... 207

Figure 7-113. Sn pre-plating in fluidised bed electrolyte reactor with 590-840 μm glass beads, batch recycle model at - 0.70 V (SCE), flow rate = 0.85 dm^3 min^{-1}, k_m = 5.36 x 10^{-5} , $V_{catholyte}$ = 2 dm^{-3} , together with PFER-CSTR model predictions. 208

Figure 7-114. Sn deposition in fluidised bed electrolyte reactor with 590-840 μm glass beads, batch recycle model at - 0.60 V (SCE) reversible potential of Pb^{2+}/Pb, flow rate = 0.85 dm^3 min^{-1}. 209

Figure 7-115. Time dependence of the Sn^{4+} ($[Sn^{4+}]_0$ = 2.85 mol m^{-3})and Pb^{2+} ($[Pb^{2+}]_0$ = 0.3 mol m^{-3}) concentration and reduction current density in fluidised bed electrolyte reactor with 590-840 μm glass beads, batch recycle model at - 0.60 V (SCE) reversible potential of Pb^{2+}/Pb, flow rate = 0.85 dm^3 min^{-1}..... 209

Figure 8-116. Solubility (activity-pH) diagram for $Fe(OH)_3$ (ppt) in equilibrium with aqueous Fe^{III} species at 298 K [1]. 214

Figure 8-117. Solubility (activity-pH) diagram for $Fe(OH)_2$ (ppt) in equilibrium with aqueous Fe^{II} species at 298 K [1]. 214

Figure 8-118. Potential pH diagram for iron-water system. Dissolved iron activity = 10^{-6}; 298 K, 1 atm [1]. 215

Figure 8-119. Potential pH diagram for aluminium- water. Activities: Al^{3+} = 10^{-6}; 298 K, 1 atm [2]. 215

Figure 8-120. Precipitation experiments in solutions contained 18 mol m^{-3} Ni^{II}, 30 mol m^{-3} Zn^{II} and 10 mol^{-3} Fe^{III} in 4 kmol m^{-3} HCl and 1 kmol m^{-3} NaCl..... 216

Figure 8-121. EDX reading for filtrate in sample pH 3.25. (Au being coated on the filtrate). 216

Figure 8-122. Potential pH diagram for nickel- water. Activities: Ni^{2+} = 10^{-3} kmol m^{-3}; 298 K, 1 atm. 217

Figure 8-123. Potential pH diagram for nickel-chloride-water. Activities: Dissolved nickel and chloride activities = 10^{-3} and 5; 298 K, 1 atm..... 217

Figure 8-124. Distribution curves of nickel species in 18 mol m^{-3} Ni^{II} and 5 kmol m^{-3} Cl^-; 298 K. Stability constant (*K*) values extracted from Ji and Cooper, 1996 [4]. 219

Figure 8-125. Potential pH diagram for nickel- water. Activities: Zn^{2+} = 10^{-3} kmol m^{-3}; 298 K, 1 atm [12]. 220

Figure 8-126. Potential pH diagram for nickel-chloride-water. Activities: Zn^{II} = 10^{-3}, Cl^- = 5; 298 K, 1 atm. 220

Figure 8-127. Distribution curves of zinc species in 20 mol m^{-3} Zn^{II} and 5 kmol m^{-3} Cl^-, 298 K. Stability constant (*K*) values extracted from Mathias et al., 1990 [13] and Baes and Mesmer, 1976 [14]. 221

Figure 8-128. Cyclic voltammogram of Pt in 30 mol m^{-3} Zn^{II} + 4 kmol m^{-3} HCl + 1 kmol m^{-3} NaCl solutions at pH 3.25; scan rate, 10 mV s^{-1}; rotating rate, 60- 1500 rpm; sweep reversal at -1.10 V (SCE). 224

Figure 8-129: Current time response for the reduction of 30 mol m^{-3} zinc chloride ions on a Pt stationary electrode in 4 kmol m^{-3} HCl + 1 kmol m^{-3} NaCl, at -1.10 V (SCE); 298 K, 1 atm. Diffusion coefficient value for Zn derived from the slope based on Cottrell equation [8-10]. 226

Figure 8-130: Disc voltammogram for Zn deposition and H_2 evolution on Zn-coated disc electrode in 30 mol m^{-3} Zn^{II} + 4 kmol m^{-3} HCl + 1 kmol m^{-3} NaCl at a scan rate of 2.5 mV s^{-1} and a rotation rate of 25 s^{-1}. 226

Figure 8-131. Koutecký- Levich plot of current density Zn deposition on Zn pre-plated Pt disc electrode in 30 mol m^{-3} Zn^{II} + 4 kmol m^{-3} HCl + 1 kmol m^{-3} NaCl at different disc potentials (E (SCE) / V). 227

Figure 8-132. Log kinetic current density of Zn deposition determined from Koutecký- Levich plot against overpotential ($E_{disc} - E_{Sn}$) for Zn deposition on Zn pre-plated Pt electrode in 30 mol m^{-3} Zn^{II} in 4 kmol m^{-3} HCl and 1 kmol m^{-3} NaCl. 227

Figure 8-133. Analysis using Tafel plots on hydrogen evolution current density on Ni wire working electrode (A = 1.5×10^{-4} A m^{-2}) in 4 kmol m^{-3} HCl and 1 kmol m^{-3} NaCl at pH 3.25; scan rate of 2.5 mV s^{-1} ,rotating rate 1500 rpm. 228

Figure 8-134. CV of (a) Zn-Ni deposition (b) Zn deposition on a Pt rotating disc electrode from 30 mol m^{-3} Zn^{II}, 18 mol m^{-3} Ni^{II} , 4 kmol m^{-3} HCl + 1 kmol m^{-3} NaCl solutions at pH 3.25 , scan rate, 10 mV s^{-1}; rotating rate, 1500 rpm and (c) H_2 evolution on Pt RDE 4 kmol m^{-3} HCl + 1 kmol m^{-3} NaCl solutions at pH 3.25. 230

Figure 8-135. Model prediction of current density and charge efficiencies ($\Phi^e_{Zn+Ni} = j_{Zn+Ni}$ / ($j_{Zn} + j_{Ni} + j_{H2}$) - electrode potential behaviour for reduction of Zn^{II}, Ni^{II} and hydrogen evolution. 234

Figure 8-136. Schematic diagram of the model geometry for the reactor with parallel plate electrodes. 236

Figure 8-137. Schematic of cation membrane transport process. 240

Figure 8-138. Time dependence of the Zn^{2+} ($[Zn^{2+}]_{t=0}$ = 30 mol m^{-3} ; ■)and Ni^{2+} ($[Ni^{2+}]_{t=0}$ = 18 mol m^{-3}; ▲) concentration and reduction current in fluidised bed electrolyte reactor with 590-840 μm glass beads, batch recycle model at – 1.10 V (SCE), flow rate = 6 x 10^{-5} m^3 s^{-1}. 243

Figure 8-139. Absorbance of solution during Zn^{II}-Ni^{II} electro-co-deposition in fluidised bed electrolyte reactor at -1.10 V (SCE); path length 1 mm measured via fibre optics. 243

Figure 8-140. Linear sweep voltammetry for Zn^{II}-Ni^{II} electro-co-deposition in fluidised bed electrolyte reactor; (○) and (□) represent linear sweep voltammetry before and after electro-co-deposition. 244

Figure 8-141. Time dependences of catholyte pH (▲) with 2% errors for each reading; (---) is the predicted catholyte pH; Ni-Zn charge yield, Φ^{e}_{Zn+Ni} (+). 244

Figure 8-142. Boundary layer concentration profiles for Zn^{2+}, Ni^{2+}, Cl^{-}, Na^{+}, H^{+} as predicted by the mass transfer model. 245

Figure 8-143. Magnification of the cathode boundary layer of the fluidised bed electrolyte reactor. 246

Figure 10-144. Schematic of electrochemical process for sequential selective metal recovery from multi-metal containing WEEE leachate. 256

Figure 11-145. Predicted potential drop in the reactor 285

Figure 11-146. Predicted pH profiles in the catholyte. 286

Figure 11-147. Flow meter calibration. 287

List of Tables

Table 3-1. Material composition (by weight) of six different categories of equipment [4]..... 52

Table 3-2. Metal content of PCBs. 54

Table 3-3. Price of base and PMs traded on the global market place [26]..... 62

Table 3-4. Leachate solution composition [25]. 64

Table 4- 5. Common reagents. 106

Table 4-6. Standard reagents. 107

Table 4-7. Electrode materials. 107

Table 4-8. Cation exchange membranes. 108

Table 4-9. Leachate solution composition [3]. 110

Table 5-10. Calculated δ_N and k_m values for different rotation rates..... 135

Table 6-11. Calculated δ_N and k_m values for different rotation rates..... 159

Table 6-12. A summary of the kinetic parameters obtained from literature [9,10] and RDE experiment. 160

Table 6-13. XRF analysis for copper deposition at -0.45 V (SCE). 175

Table 7-14. Calculated δ_N and k_m values for different rotation rates..... 199

Table 7-15. A summary of the kinetic parameters obtained from various sources..... 200

Table 8-16. Composition of the nickel-zinc plating baths used in this study. 222

Table 8-17. Calculated δ_N and k_m values for different rotation rates..... 225

Table 8-18: A summary of the kinetic parameters obtained from various sources..... 229

Table 8-19. A summary of initial metal ions concentration at pH 0 used in the models. 235

Table 8-20. A summary of diffusion coefficients of metal ions. 235

Table 11-21. Capital cost of recovery plant processing 1 tonne per day of shredded WEEE. 288

Nomenclature

Symbol	Definition	Unit
A	Electrode area	m^2
A_e	Geometric area	m^2
A_λ	Absorbance	1
c_i	Concentration of species *i*	mol m^{-3}
$c_{i,0}$	Inlet concentration of species *i*	mol m^{-3}
$c_{t=0}$	Initial concentration	mol m^{-3}
c_t	Concentration at time *t*	mol m^{-3}
d	distance	m
d_{cell}	Path length of cell	m
d_p	Diameter of particulates	m
D_i	Diffusion coefficient of species *i*	m^2 s^{-1}
E	Electrode potential	V
$E^{\ominus}$	Standard electrode potential	V
$E_{O/R}$	Reversible potential	V
E_r	Equilibrium electrode potential vs reference electrode	V
E_{disc}	Disc potential of rotating ring-disc electrode	V
E_{ring}	Ring potential of rotating ring-disc electrode	V
e^-	Electronic charge (1.602×10^{-19})	C
F	Faraday constant (96485)	A s mol^{-1}
f	Rotation rate	s^{-1}
ΔG	Gibbs free energy change	J mol^{-1}
ΔH	Enthalpy of formation	J mol^{-1}
I	Current	A
I_{disc}	Disc current of rotating ring-disc electrode	A
I_{ring}	Ring current of rotating ring-disc electrode	A
j	Current density	A m^{-2}
j_L	Mass transport limited current density	A m^{-2}
j_o	Exchange current density	A m^{-2}
k_m	Mass transport rate constant	m s^{-1}
k_c	Forward rate coefficient	variable
k_a	Reverse rate coefficient	variable
k_i	Heterogeneous rate constant	variable
$k_{i,0}$	Standard heterogeneous rate constant	variable
K	Equilibrium constant	1
M	Molar mass	g mol^{-1}
m	mass	kg
n	Number of electrons involved in a reaction	1
N_i	Flux of species i	mol m^{-2} s^{-1}
p	Partial pressure of gas	Pa
Q	Charge	C
q	Charge density	C m^{-2}
R	Universal gas constant (8.31441)	J K^{-1} mol^{-1}

R^2	R-square value: the fraction of variance in the data that is explained by a regression	1
r	Radius of micro-disc electrode	m
r_{rxn}	Reaction rate	mol m^{-2} s^{-1}
S	Entropy	kJ mol^{-1} K^{-1}
t	Prosess time	mol m^{-3}
T	Absolute temperature	K
u_i	Ionic mobility for species i	m^2 V^{-1} s^{-1}
U_{cell}	Cell voltage	V
$\dot{v}$	Volumetric flow rate	m^3 s^{-1}
$\mathbf{v}$	Electrolyte velocity	m s^{-1}
v	Superficial velocity	m s^{-1}
v_o	Inlet liquid velocity	m s^{-1}
v_{eff}	Effective liquid velocity (v/ε)	m s^{-1}
v_{mf}	Velocity of minimum fluidisation	m s^{-1}
v_t	Terminal velocity	m s^{-1}
V	volume	m^3
w	Specific electrical energy consumption (SEEC)	kW h kg^{-1} $product^{-1}$
x	Horizontal distance from electrolyte inlet	m
y	Vertical distance from electrolyte inlet	m
z_i	Electron stoichiometry or charge number of reaction	1
SHE	Standard Hydrogen Electrode	1
SCE	Saturated Calomel Electrode	1

Greek Symbols

Symbol	**Definition**	**Unit**
α	Transfer coefficient	1
β_a	Tafel coefficient for anodic reaction, $(1-\alpha)\, n\, F/(RT)$	V^{-1}
β_c	Tafel coefficient for cathodic reaction, $\alpha\, n\, F/(RT)$	V^{-1}
δ	Nernst diffusion layer thickness	m
ε_λ	Molar absorptivity	mol^{-1} m^2
ε	Voidage	1
ε_{emf}	Voidage of minimum fluidisation	1
η	Overpotential ($E-E_r$)	V
ϕ	Sphericity	1
ϕ_l	Liquid phase potential	V
ϕ_s	Solid phase potential	V
$\Delta\phi_{l,m}$	Liquid phase potential drop in the membrane	V
$\Delta\phi_{l,a}$	Liquid phase potential drop in the anolyte	V
κ_s	Effective solid phase conductivity	S m^{-1}
$\kappa_{s,o}$	Pure solid phase conductivity	S m^{-1}
κ_l	Effective liquid phase conductivity	S m^{-1}
$\kappa_{l,o}$	Pure liquid phase conductivity	S m^{-1}
κ_m	Conductivity of membrane	S m^{-1}
Φ	Charge yield	1

Φ_{ave}	Average charge efficiency	1
μ	Electrolyte dynamic viscosity	kg m^{-1} s^{-1}
ν	Electrolyte kinematic viscosity	m^2 s^{-1}
υ	Stoichiometric coefficient	1
ρ	Density	g m^{-3}
λ	Wavelength	nm
ω	Angular frequency	m s^{-1}

Sub- and superscript

0	start (t=0) (as subscript) or standard (as superscript)
a	anode
c	cathode
b	bulk
e	electrode
i	reacting species
s	solid phase
k	reaction
l	liquid phase
m	membrane
N	Nernst
O	oxidised form
R	reduced form
T	total

Dimensionless Groups

Symbol	Definition
Sh	Sherwood number= $\frac{k_m d_p}{D_i}$
Sc	Schmidt number= $\frac{\upsilon}{D_i}$
Re	Reynolds number= $\frac{\nu \rho d_p}{\mu}$

Abbreviations

ICP-OES	Inductively-coupled Plasma Optical Emission Spectroscopy
SEM-EDX	Scanning Electron Microscopy –Energy Dispersive X-Ray spectroscopy
XRD	X-Ray Diffraction Spectroscopy
XRF	X-Ray Fluorescence Spectroscopy
UV	Ultra Violet
SHE	Standard Hydrogen Electrode
SCE	Saturated Calomel Electrode

1. INTRODUCTION

This chapter includes the background of metal recovery using electrochemical technology, and the motivation, aims and objectives of this project.

1.1. Background

The production of electrical and electronic equipment (EEE) is known as one of the fastest growing businesses in the world [1]. New applications of EEE are increasing significantly at the same time as the average replacement process is accelerating. This rapid development has resulted in an increase of end-of-life or waste electric and electronic equipment (WEEE), which can be a valuable source of secondary raw materials if treated appropriately [2].

The Industry Council for Electrical & Electronic Recycling (ICER, 2008) estimated approximately a million tonnes (93 million items) of waste electrical and electronic equipment (WEEE) are discarded in the UK each year, though only large household appliances are presently being recycled at any scale. Furthermore, only ca. 20 % of the UK's 350,000 tonnes p.a. waste IT equipment is being reprocessed, the remainder being sent to landfills. The printed circuit board (PCB) content of that waste has been estimated at ca. 25 ktonnes p.a., comprising 4 ktonne Cu, 1 ktonne Sn, 1 ktonne Pb and 25 tonnes of precious metals (PMs) [3]. Currently, only those boards with sufficient PM content are subjected to metal recovery; the smaller volume, higher grade material is treated hydrometallurgically by precious metal refiners, while the lower grade material is exported to foreign copper smelters, the nearest to the UK being in Belgium (Umicore), which charges ca. £1000 per tonne for PCB smelting and metal refining [3]. This is less than charged by precious metal refiners, which achieve higher recoveries from a much lower throughput.

Technologies that are able to combine metal removal with metal recovery are becoming increasingly important. This is because they are able to convert wastes from an economic liability to a saleable resource, which results in the production of little or no waste, and simultaneously protects the environment. Current recycling processes are mainly pyrometallurgical, the WEEE being smelted at high temperatures which consists of the thermal treatment of minerals and metallurgical ores and concentrates to bring about physical and chemical transformations in the materials to enable recovery of valuable metals [2]. The cost effectiveness of pyrolytic recycling for WEEE, apart from those with relatively high precious metal content, coupled with increasing ecological concerns has cast doubt over the

long-term viability of this methodology and has provided impetus for the development of more sustainable approaches embracing mechanical and hydrometallurgical technologies. Although the majority of metals can be recovered by pyrometallurgical processes, the organic yields are combusted and subsequently produce noxious gases that are harmful to the environment [3]. Hydrometallurgical processes allow a more environmentally benign and energy efficient route which requires two stages of process to metal reclamation from shredded WEEE; metal dissolutions into an aqueous media and followed by recovery of metal ions [4].

The work at Imperial College London has demonstrated the feasibility of removing a high percentage of metals in electronic scrap [3,8].The non-selective dissolution obviates the need for expensive and waste streams of multiple dissolution steps. The process could be important in terms of meeting targets set by the WEEE Directive [6] because not only does it remove precious metals, but also all hazardous metals from the WEEE. Conversely, selective recovery or further processing of the metals is required to obtain the most value from electronic scrap.

Several techniques, which may compete and / or complement each other, have been developed for the removal of metal ions from solution including electrodeposition, adsorption, ion exchange, extraction, precipitation, membrane separation, and biochemical treatment. Each of these technologies has found industrial applications. The selection criterion include, but is not limited to, discharge standards, waste volume, contaminant concentration and composition, capital and operating costs, maturity and reliability of the technology. At times, a combination of the technologies may yield the best results [7,8].

Precipitation of metals is the most used and studied method for metal removal from, for example, industrial wastewaters. This usually consists of precipitating them with lime in the form of hydroxides, although carbonates or sulphides are also possible. Precipitation for the removal of metals from solution is inexpensive, but little selectivity for individual metals. Waste streams that require further treatment are also generated [9].

Ion exchange is well known for its ability to maintain the outlet stream quality, especially for low concentration heavy metal effluent. Nonetheless, it is difficult to find a suitable resin for treatment of a waste solution containing mixed metal ions, as most commercially available resins are non-selective. Regeneration of the resin and treatment of effluents generated

(concentrated metal solutions) is also expensive [9].

Reverse osmosis, other than the high operating pressure, requires pre-treatment of the wastewater (e.g. iron and oxidant removal, pH control, carbon filtration, biocide addition) to avoid plugging or damage to the membrane [9]. This will make the method complicated as well as costly, especially for small facilities.

The metallurgical industry has used solvent extraction for many years for a broad range of separations including the removal of soluble metals (Cd, Cr, Co, Cu, Ni, Mo, U, V, Zn, etc.) from solution [9]. Separation is carried out in contact with an immiscible organic phase, such as carboxylic acids, amines, and phenols, to form salts or complex compounds that give a favourable solubility distribution between the aqueous and organic phases. Although liquid-liquid extraction may concentrate the metals, its recovery from the solvent stream demands additional costs.

The use of electrochemical techniques for the recovery of metal ions from solution has a number of advantages which could possibly solve the problem raised in several techniques highlighted here. Firstly, electrolytic recovery units can operate continuously and yield a very high purity product in a metallic form that is suitable for re-use or resale. Furthermore, electrodeposition at a two-dimensional cathode is most suitable for relatively high metal concentrations; a high surface area three-dimensional electrode is required for more dilute solutions with metals concentrations less than 100 ppm [10-12]. In addition, electrodeposition does not generally require a supply of chemical reagents and hence does not generate large numbers of additional waste streams with disposal problems which may cut the operational cost [10]. However, there are a few major hurdles too. The equipment used in this process has a relatively high capital cost, and, depending on the cathode efficiency, may have a high energy cost [13-15]. Apart from these, the high purity product that can be obtained, without the generation of numerous waste streams, make electrodeposition a promising option for the recovery of metals from the leachates of WEEE. Taking all aspects into consideration, electrodeposition was chosen as the best option as this route produces an efficient, environmental friendly process involving theoretically no waste products/residual products/residue.

Therefore, this Ph.D. investigation describes a novel process to recover metals selectively by electrodeposition by pumping aqueous acidic chloride solutions produced by leaching of

shredded WEEE through the potentiostatically controlled cathode of an electrochemical reactor. The WEEE solutions contained low concentrations of precious metals, including Ag, Au, Pd and high concentrations of Cu [16].

1.2. Project Motivation and Aims

The WEEE leachate solutions, with which this PhD project is concerned, arise from WEEE scrap mainly from printed circuit boards. Samples from several sources of end-of-life printed circuit boards, mother boards, graphic cards etc., shredded with rotary shears to < 8 mm, were characterised physically and chemically and found to contain ca. (wt%): 22% Cu, 2% Zn, 1% Al, 0.2% Ni, 5% Sn, 3% Pb, 0.1% Fe, 0.02% Au, 0.04% Pd, 0.08% Ag, and 66.7% non-metallics; aluminium and iron concentrations depend on whether eddy current and magnetic separations had been used to remove them during pre-concentration, respectively. Shredded scrap material had been leached by electrogenerated chlorine in acidic aqueous solutions of high chloride ion activity. This has produced a multi metal leach solution, containing nearly all of the available metal in the scrap as mentioned above [16].

The motivation to provide effective recycling of electronic scrap for retrieval of the many different constituent metals is not only regulatory but also financial. The metal content in the electronic scrap represents a significant cost of raw materials for the manufacturer of the unit. The possibility of recovering even a fraction of this investment represents a saving for the company involved. For example, the price of copper (purity of $> 99.99\%$) which is predominant in shredded electronic scrap is currently around ca. £5.5k tonne^{-1} (www.lme.com). A comparison with the specific electrical energy consumption (SEEC) of electrodeposition, which is ca. 2×10^3 kWh tonne^{-1} of copper, corresponding to £100 tonne^{-1}, shows that recovery of copper from WEEE leaching solutions is economically feasible.

The design of a suitable electrochemical reactor for metal ion recovery is an essential part of this PhD project. In particular, a critical evaluation of the suitability of different types of electrodes is important due to a variety of metal ions concentrations that need to be recovered. Moreover, appropriate operating conditions for metals electrodeposition must be determined by electrochemical kinetic measurements and batch electrowinning experiments, supported by thermodynamic predictions and reactor modelling to achieve high charge yield and selective metal electrodeposition. For electrodeposition of all metals studied, the effects were determined of cathode potential and solution flow rate on electrodeposition rates, charge yields, specific electrical energy consumptions, and deposit morphologies. Hence, this

research project aimed to produce detailed information about the electrochemical separation and purification of metals, to enable future development of closed loop processes for recovery of dissolved metals from solutions resulting from leaching WEEE.

1.3. Thesis Organization

In Chapter 2, the basic principles of a simple electrochemical system which complement the experimental work are discussed. This includes the definitions of the main components in an electrochemical cell, the factors that control homogeneous and heterogeneous reactions in the cell (thermodynamics) and the factors that control the rates of these reactions (kinetics).

In the Literature Review chapter (Chapter 3), besides providing details for the facts cited above (section 1.1), a fairly extensive survey starting from the basic definitions of waste electrical and electronic equipment (WEEE), overview of the current situation and electrochemical metal recovery of each designated metal ions presented to set the stage for more specific chapters that follow. Related studies in selected literature are also highlighted.

In the Materials and Experimental Methods chapter (Chapter 4), a full description of the system configuration and methodology employed are given.

The Result and Discussions section can be read as four major Chapters (Chapter 5 to 8). Chapter 5 explores the electrodeposition of gold from solutions with concentrations < 10 mol m^{-3} in the WEEE leachate, using a three-dimensional cathode consisting of a circulating particulate bed of 0.5-1.0 mm diameter graphite particles, on which ($Au^{III}Cl_4^-$ + $Au^{I}Cl_2^-$) ions were reduced. The temporal decay of the solution absorbance of $AuCl_4^-$ ions at 312 nm was recorded on-line by quartz flow cell connected to a UV-visible spectrophotometer using fibre optics, enabling its time dependent concentration to be determined in real time. Chapter 6 presents an investigation of copper electrodeposition which is the dominant element in WEEE leachate. The crucial part is to achieve target purities of ≥99.99 in order to be a saleable resource. Chapter 7 and Chapter 8 discuss the fate of other metals present in the waste solutions, specifically Sn^{IV}-Pb^{II} , Al^{III}, Fe^{II}, Zn^{II} and Ni^{II} electrodeposition.

The Conclusions (Chapter 9) summarizes the results of the whole exercise, followed by a list of recommendations for future work in Chapter 10.

1.4. References

[1] Babu, B.R., Parande, A.K. and Basha, C.A., 2007, Electrical and electronic waste: a global environmental problem. *Waste Manage. & Res.*, 25: 307-318.

[2] Ongondoa, F.O., Williams, I.D. and Cherretta, T.J., 2011, How are WEEE doing? A global review of the management of electrical and electronic wastes. *Waste Manage.,*31 (4): 714-730.

[3] Pilone, D. and Kelsall, G.H., 2006, Prediction and measurement of multi-metal electrodeposition rates and efficiencies in aqueous acidic chloride media. *Electrochim. Acta*, 51 (18): 3802-3808.

[4] Encyclopedia Britannica, 2002, Pyrometallurgy - Smelting. 15th Edition, Chicago.

[5] Burkin, A.R., 2001, Chemical Hydrometallurgy. Imperial College Press.

[6] Goosey, M. and Kellner, R.A., 2002, Scoping Study: End-of-life Printed Circuit Boards, Department of Trade and Investment, Shipley Europe Limited.

[7] Jackson, E., 1986, Hydrometallurgical Extraction and Reclamation. John Wiley & Sons.

[8] Brandon, N.P., Kelsall, G.H., Müller, T., Olijve, R., Schmidt, M. and Yin, Q., 2001, Metal Recovery from Electronic Scrap by Leaching and Electrowinning in: Comninellis, C., Doyle, M. and Winnick, J., Editors, Proc. Electrochem. Soc., Vol. 2001-23, Energy and Electrochemical Processes for a Cleaner Environment, Electrochem. Soc., N.J.: 323-338.

[9] DTI, Sustainable Development Group, 2007, EC Directive on Waste Electrical and Electronic Equipment (WEEE) and EC Directive on the Restriction of the Use of Certain Hazardous Substances in Electrical and Electronic Equipment (RoHS).

[10] Scott, K., 1995, Electrochemical processes for clean technology. Royal Society of Chemistry, Cambridge, UK.

[11] Janssen, L.J.J. and Koene, L., 2002, The role of electrochemistry and electrochemical technology in environmental protection. *Chem. Eng. J.*, 85 (2-3): 137-146.

[12] Juttner, K., Galla, U. and Schmieder, H., 2000, Electrochemical approaches to environmental problems in the process industry. *Electrochim. Acta*, 45 (15-16): 2575 - 2594.

[13] Pletcher, D. and Walsh, F.C., 1990, Industrial Electrochemistry, 2nd ed., Chapman and Hall, London. UK.

[14] Berkowitz, J.B., Funkhouser, J.T., Steven, J.I., 1978, Unit Operations for Treatment of Hazardous Industrial Wastes, Noyes Data.

[15] Adcock, P.A. and Adeloju, S.B., 1999, Removal and Recovery of Metals by Electrodeposition. *Electrochem. News*, 3 (1): 2-4.

[16] Cheng, C.Y., Kelsall, G.H. and Robson, A., 2006, Model Predictions of Metal Leaching from Waste Electrical and Electronic Equipment (WEEE) in Chlorine-containing Acidic Aqueous Chloride. *ECS. Trans*., 2 (3): 231-242.

2. PRINCIPLES OF ELECTROCHEMICAL SYSTEMS

2.1. Chapter Overview

This chapter discusses the basic principles of electrochemical systems used in the analysis of the experimental results reported in subsequent chapters. This includes the fundamental definitions of electrochemical processes, electrochemical thermodynamic and kinetics, transport processes in electrochemical system and several electrochemical figures of merit, such as charge yield and specific electrical energy consumption (SEEC). The description of the modes of operation for electrochemical reactors utilized in this work i.e. mesh cathode in a fluidised bed of inert particles and circulating particulate bed electrode conclude this chapter.

2.2. Fundamental Definitions

In general, electrochemical reactions are heterogeneous chemical reactions which occur via the transfer of charge across the interface between an electrode and an electrolyte [1]. The general form of such processes is given in equation [2-1], where the redox couple O and R represent the oxidised and reduced component respectively:

$$O + ne^- \underset{\text{anodic oxidation}}{\overset{\text{cathodic reduction}}{\rightleftharpoons}} R \qquad [2\text{-}1]$$

The minimum components that are necessary for an electrochemical cell are an anode, a cathode, electrolyte to allow ionic contact between those electrodes and a power supply. The electrodes are usually good electronic conductors such as solid metals and carbon whilst the electrolyte is generally an effective ionic conductor. It should be noted that, in most laboratory experiments, a three electrode cell is employed. This allows a single electrode reaction (occurring at the "working" electrode) to determine the cell response and also permits automatic correction for most of the *IR* drop between the two electrodes where oxidation and reduction are occurring. The third electrode is normally a reliable reference electrode such as standard hydrogen electrode (SHE) and saturated calomel electrode (SCE)

2.3. Electrochemical Thermodynamics

Thermodynamic properties, such as the Gibbs free energy, of the products and reactants determine whether a reaction will proceed spontaneously or whether it requires an external driving force. The equilibrium potential of an electrochemical reaction is part of the number

of electrons involved governed by its Gibbs free energy (ΔG) following the equation:

$$\Delta G^0 = -nFE^0{}_{O/R} \qquad [2\text{-}2]$$

The Gibbs free energy is negative for a spontaneous reaction (a galvanic cell) and is positive for a non-spontaneous reaction (an electrolytic cell). The latter requires the input energy to proceed. Potentials are at equilibrium when no overpotential is applied and no current is exchanged between the electrodes. Equilibrium potentials for the case of non-standard conditions are determined by the Nernst equation:

$$E = E^{\ominus} + \frac{RT}{nF}\ln\left\{\frac{(O)}{(R)}\right\} \qquad [2\text{-}3]$$

For the generalised charge transfer reaction represented by the following reaction equation:

$$pA_q + rH^+ + ne^- \leftrightarrow qB_p + cH_2O \qquad [2\text{-}4]$$

As with most chemical reactions, thermodynamics predicts the possibility of a reaction to occur under specified conditions. In the case of electrode reactions, the determining factor is equilibrium electrode potential for a particular reaction on a specified electrode surface. This potential is given by the Nernst equation [2-5], in which the parentheses denote the activities of the oxidised and reduced species:

$$E_{B/A}/V = E^{\ominus}{}_{B/A} + \frac{RT}{nF}\ln\left\{\frac{(A_q)^p(H^+)^r}{(B_p)^q(H_2O)^c}\right\} \qquad [2\text{-}5]$$

where at 298.15K, the quotient:

$$\frac{2.303RT}{F} = 0.0591 \text{ V} \qquad [2\text{-}6]$$

Equation [2-5] can be expressed as:

$$E_{B/A}/V = E^{\ominus}{}_{B/A} - \frac{0.0591rpH}{n} + \frac{0.0591}{n}\log\left\{\frac{(A_q)^p}{(B_p)^q}\right\} \qquad [2\text{-}7]$$

At electrode potentials more positive than that given by equation [2-7], the electro-active species R, if present, will be oxidised; conversely, at potentials more negative than $E_{O/R}$, species O, if present, will be reduced. Hence, at electrode potentials other than that

corresponding to the equilibrium value, an oxidation or reduction current, a direct measure of the reaction rate implies.

Thus, when several reactions are possible, the electrochemical behaviour of aqueous systems can be depicted using potential-pH (Pourbaix) diagrams. Such diagrams represent the stability of a metal in a given environment by showing predominant species and phases for a fixed temperature and total dissolved activity. Examples of potential-pH diagrams are presented in Chapters 5 to 8.

2.4. Electrochemical Kinetics

The fact that a reaction is thermodynamically possible does not necessarily mean that it may occur, nor does it give any information about the rate at which it occurs, which is governed instead by the reaction kinetics. Rates of chemical reaction are normally expressed in terms of a rate over an interfacial area, mol m^{-2} s^{-1}. For an electrochemical process this is given in terms of current density in Faraday's Law [1]:

$$r_{rxn} = \frac{j}{nF} \qquad [2\text{-}8]$$

At the equilibrium potential for a reaction, the net current density j (A m^{-2}) due to the partial oxidation j_a and reduction j_c current densities is zero. When a potential not equal to $E_{O/R}$ is applied to the system, a current will flow. The expression relating the current density to the overpotential called the Butler-Volmer equation [2]:

$$j = j_0 \left[\exp\left\{ \frac{\alpha_A n_i F}{RT} \eta \right\} - \exp\left\{ -\frac{\alpha_C n_i F}{RT} \eta \right\} \right] \qquad [2\text{-}9]$$

The constant α_A and α_C are the transfer-coefficients for the anodic and cathodic reactions; they represent the fraction of the applied overpotential (η) used in providing a driving force for the reaction which is:

$$\eta = E - E_{O/R} \qquad [2\text{-}10]$$

The first exponential term in equation [2-9] represents the contribution of the anodic reverse reaction to the overall current. At cathodic overpotentials of greater than about 10 mV, the rate of the anodic reverse reaction becomes negligible, and simplifies to:

$$-j_C = j_0 \exp\left\{\frac{-\alpha_C n_i F}{RT}\eta\right\} \qquad [2\text{-}11]$$

$$\log(-j_C) = \log(j_0) - \frac{\alpha_C nF}{2.303RT}\eta \qquad [2\text{-}12]$$

where

$$\beta = \frac{\alpha_c nF}{RT} \qquad [2\text{-}13]$$

[2-12] is the Tafel equation, used to calculate rates of reaction well away from their reversible potentials. Figure 2-1 shows semi-logarithmic plots of the data that depict the linear regions corresponding to [2-12] and can be extrapolated to zero overpotential, to obtain the exchange current density (j_o). The slopes of the linear portions describe the Tafel region where β is the Tafel coefficient. The experimentally determined coefficient, β, may be used to determine the cathodic transfer coefficient (α_c). Once these values are known for a particular solution, kinetically controlled current densities can be predicted as a function of overpotential. Values of kinetic parameters such as j_0 and β for some reactions can sometimes be found in the literature; otherwise they can be determined experimentally.

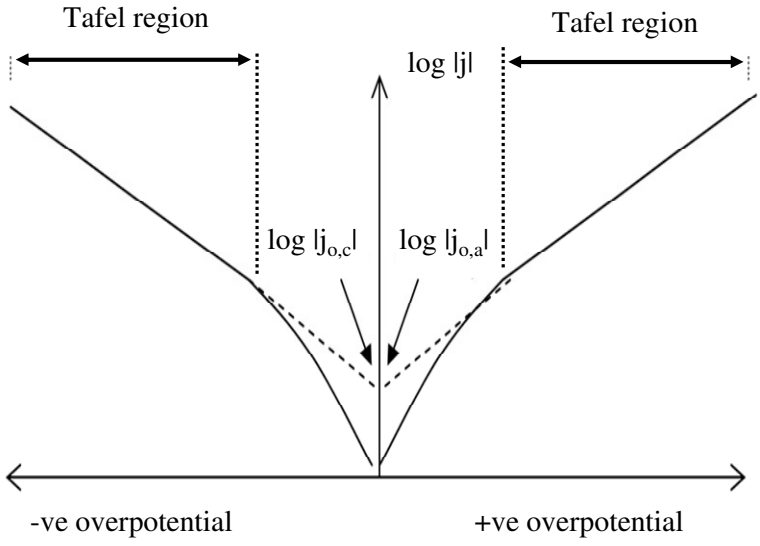

Figure 2-1. Schematic of Tafel plot $j_{0,c}$ and $j_{0,a}$ are the cathodic and anodic limiting current densities, respectively [1].

For kinetically controlled reactions, the rate of reaction at the electrode surface is slower than the rate of diffusion of species to the surface. At larger overpotentials and high current densities, mass transport effects cannot be neglected as the species at the electrode react

faster than the reactants can diffuse from the bulk to the reaction zone. Therefore, reactants are depleted at the reaction surface, and the current becomes mass transport limited. The mass transport limiting current, j_L, depends on the speed of diffusion of species to the electrode:

$$j_L = nF\frac{D_i}{\delta}c_i = n_i F k_{m,i} c_i \qquad [2\text{-}14]$$

The extended Butler-Volmer equation [2-15], accounts for both kinetic and mass transport limitations, and as shown in Figure 2-2, defines the complete current density - potential relationship for 'simple' electrode reactions [1].

$$j = \frac{j_0\left[\exp\left\{\frac{(1-\alpha)n_i F}{RT}\eta\right\} - \exp\left\{-\frac{\alpha n_i F}{RT}\eta\right\}\right]}{\left[1+\left(\frac{j_0}{j_L^R}\right)\exp\left\{\frac{(1-\alpha)n_i F}{RT}\eta\right\} + \left(\frac{j_0}{j_L}\right)\exp\left\{-\frac{\alpha n_i F}{RT}\eta\right\}\right]} \qquad [2\text{-}15]$$

The region exhibits kinetic, then a mixed control system where the rate of reaction is influenced by both the charge transfer reactions and the mass transport regimes in the system and followed by transport control, with increasing magnitude of overpotential as shown clearly in Figure 2-3.

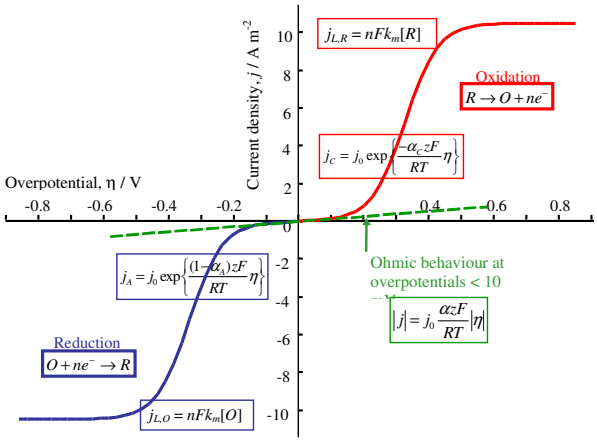

Figure 2-2. Plot of Butler-Volmer equation for j_0 = 1 A m^{-2} [5].

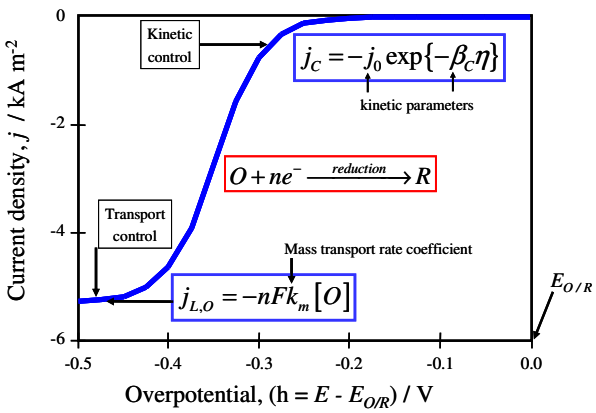

Figure 2-3. Current density operating regimes in under kinetic, mixed and mass transport control; k_m represents the mass transport rate coefficient.

In conditions where there is a single step determining the rate of an electrode reaction, its kinetics may be determined from a measurement of the steady state current density. As explained in section 2.4, determination of the steady state current density as a function of overpotential (η), has been commonly used to investigate the mechanism and kinetics of electron transfer reactions as well as reaction that involve chemistry of species adsorbed on the electron surface. Steady state measurements may also be used to study some homogeneous chemical reactions [2].

A special electrode geometry, the rotating disc electrode (RDE) is frequently employed in laboratory studies due to its well known velocity behaviour as a function of rotation speed, the ability to maintain laminar flow over a wide range of rotational speed and well established mass transport characteristics [2]. The RDE method is explained in the following section.

2.5. Rotating Disc Electrode (RDE)

The rotating disc electrode (RDE) is a simple and convenient method of examining electrode reactions under conditions where there is a well defined, steady state mass transport regime. In 1962, Levich [7] solved analytically the hydrodynamics of a downward-facing horizontal disc, immersed in a liquid and rotating about a vertical axis. The resulting (laminar) flow is axially up towards the disc and radially out across its surface. The mass transport limited current density given by Levich equation is:

$$j_L = nF\mathbf{N}_i = 1.554nFD_i^{2/3}\nu^{-1/6}c_i f^{1/2} \qquad [2\text{-}16]$$

The mass transport rate to the disc was predicted to increase with the square root of the rotation rate. For a known c_i, linear plots of j_L vs. $f^{0.5}$ passing through the origin provide an important diagnostic test for processes the rate of which is controlled by transport in solution to the electrode. Furthermore, if $j_L \propto c_i$, the diffusion coefficient (D) may be determined provided the kinematic viscosity (ν) can be estimated; an accurate value is unnecessary because a small error in ν has little effect on the value of D [2].

If the current increases are not constant, the Koutecký-Levich plot ($\frac{1}{j}$ vs. $\frac{1}{f^{1/2}}$) is used to determine the electrochemical rate constant by extrapolation to infinite rotation rate [8]. The Koutecký-Levich equation is [9]:

$$\left|-\frac{1}{j}\right| = \frac{1}{\nu_e F k_i C_i} + \frac{1.61 \upsilon^{1/6}}{\nu_e F C_i D_i^{2/3}} \cdot \frac{1}{f^{1/2}} \qquad [2\text{-}17]$$

The Koutecký-Levich plot describes the system in the mixed kinetics regime. For totally irreversible processes, j_L is independent of $f^{0.5}$.

2.6. Rotating Ring-Disc Electrode (RRDE)

The ring-disc electrode is an extension of RDE where it incorporates a ring electrode concentric with the disc, but electronically isolated from it and controlled independently with a second potentiostatic circuit, enabling the disc and ring electrode currents to be measured independently. The rotating ring-disc electrodes (RRDE) are powerful tools for the investigation of the kinetics and mechanisms of electrode reactions involving soluble products and/or intermediates. The ring electrode sits downstream of the solution flow, so by controlling its potential using a bi-potentiostat it can oxidise or reduce any species which are generated at the disc. The hydrodynamics have been solved so the current experienced at the ring when collecting species made at the disc is shown to depend only on geometric factors provided that the ring is operating in the mass transport limiting regime. The relation is expressed as collection efficiency (N_0) [7]:

$$N_0 = 1 - F(\alpha/\beta) + \beta^{2/3}[1 - F(\alpha)] - (1 + \alpha + \beta)^{2/3}[1 - F(\{\alpha/\beta\}\{1 + \alpha + \beta\})] \qquad [2\text{-}18]$$

Where:

$$F(\theta) = \frac{3^{1/2}}{4\pi} \ln\left[\frac{(1+\theta^{1/3}}{1+\theta}\right] + \frac{3}{2\pi} \arctan\left(\frac{2\theta^{1/3} - 1}{3^{1/2}}\right) + \frac{1}{4} \qquad [2\text{-}19]$$

$$\alpha = (r_2 / r_1)^3 - 1 \qquad [2\text{-}20]$$

$$\theta = (r_3 / r_1)^3 - (r_2 / r_1)^3 \qquad [2\text{-}21]$$

N_0 can also be determined experimentally for a given electrode even if the species formed at the disc electrode are completely stable and totally soluble, only a fraction of the species formed at the disc electrode reach the surface of the ring. These are detected as an oxidation or reduction current, depending on the ring electrode potential; the remaining species are dispersed into the bulk solution.

For the system:

$$O + ne^- \xrightarrow{disc} R \qquad [2\text{-}22]$$

$$R \xrightarrow{ring} O + ne^- \qquad [2\text{-}23]$$

in which the reactions at both ring and disc are mass transport controlled, the collection efficiency, N_0, is defined by:

$$N_0 = \frac{I_r}{I_d} \qquad [2\text{-}24]$$

and was shown mathematically to depend only on the radii of the ring (r) and the disc (d), being independent of the electrode rotation rate.

2.7. Non-steady State Systems

The reversible case arises when the couple O/R, has sufficiently fast kinetics that the electron transfer process at the surface appears to be in equilibrium. When either (a) a reaction with a poorer kinetics is investigated or (b) the potential scan rate is increased high enough to a rate of a non-steady state diffusion that the electron transfer reaction cannot remain in equilibrium, the kinetics of the couple must be considered. The slow electron transfer reactions would cause distortion to the plot in Figure 2-2 during electrodeposition i.e. the peak for an oxidation process is shifted to more positive potentials and that for a reduction to more negative potentials [2]. Hence, Cottrell equation can be used as an alternative means of estimating diffusion coefficients (D) of electro-active reactants by using a non-steady state technique in quiescent solutions.

Cottrell equation was derived by Frederick Gardner Cottrell in 1903 [2] which is given as:

$$i_d(t) = \frac{nFAD_i^{1/2}C_i}{\pi^{1/2}t^{1/2}} \qquad [2\text{-}25]$$

For a simple redox event, such as the ferrocene/ferrocenium couple, the current measured depends on the rate at which the analyte diffuses to the electrode. That is, the current is said to be "diffusion controlled." The Cottrell equation describes the case for an electrode that is planar but can also be derived for spherical, cylindrical, and rectangular geometries by using the corresponding laplace operator and boundary conditions in conjunction with Fick's second law of diffusion [2-26] [4].

$$\frac{\partial c}{\partial t} = D\frac{\partial^2 c}{\partial x^2} \qquad [2\text{-}26]$$

2.8. Transport Processes in Electrochemical Systems

As mentioned earlier, the rate of an electrochemical reaction may be influenced by the kinetics and cell potential difference, including the rate of transport of chemicals from the reaction. Ionic species in an electrolyte will instinctively move in response to electric fields, concentration gradients and bulk fluid motion. Therefore, the three forms of mass transport that can effect electrolysis reactions are diffusion, migration and convection [5]. This is illustrated schematically in Figure 2-4.

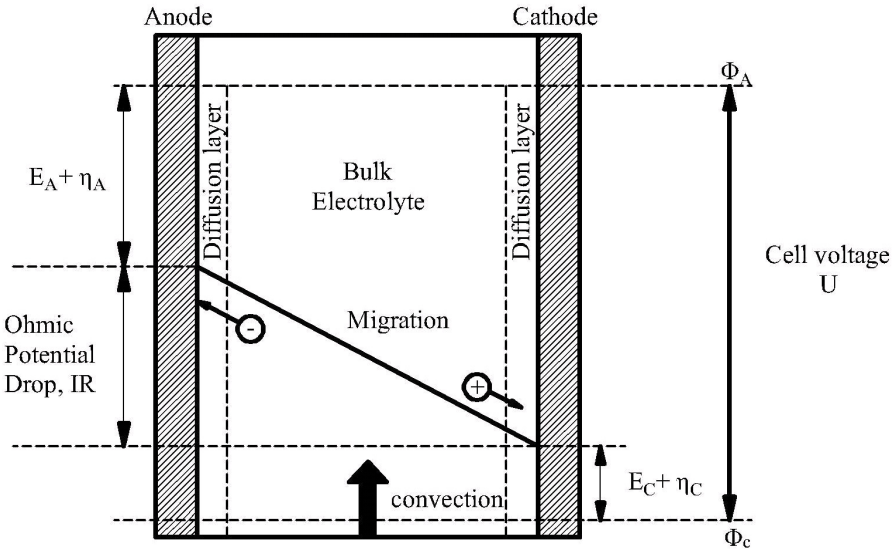

Figure 2-4. Transport processes and distribution of electrical potential in an electrochemical reactor [5].

The rate of movement of material by diffusion can be predicted at steady state by Fick's first law [2-27]. This law states that the diffusional flux to a surface depends on the diffusivity of the species in the electrolyte, D_i, and is proportional to the concentration, activity or chemical potential gradient existing across that plane.

$$N_i = - D_i \nabla c_i \qquad [2\text{-}27]$$

where the Del (∇) operator for gradients in three dimensions is:

$$\nabla = \frac{\partial}{\partial x} + \frac{\partial}{\partial y} + \frac{\partial}{\partial z} \qquad [2\text{-}28]$$

The rate of migration from regions of higher to lower electrochemical potential is proportional to the potential gradient [2-29]:

$$N_i = z_i F u_i c_i \nabla \phi \qquad [2\text{-}29]$$

The convection of species is a product of the bulk concentration and the bulk fluid velocity.

$$N_i = c_i \mathbf{v} \qquad [2\text{-}30]$$

Therefore, the total flux of a charged electro-active solute species to an electrode surface is [6]:

$$N_i = -D_i \nabla c_i - z_i F u_i c_i \nabla \phi + c_i \mathbf{v} \qquad [2\text{-}31]$$

where the ionic mobility, u_i, is the velocity per unit electric field and is related to the diffusion coefficient (D_i) by the Nernst-Einstein equation for species with z elementary charges:

$$u_i = \frac{D_i}{RT} \qquad [2\text{-}32]$$

According to Faraday's law, the current density is then given by:

$$\boldsymbol{j} = F \sum_i z_i \boldsymbol{N_i} \qquad [2\text{-}33]$$

where current densities at an electrode of geometric area, A_e, are related to the current (I) by:

$$j = I / A_e \qquad [2\text{-}34]$$

When concentration gradients can be ignored, substitution of equation [2-33] into equation [2-31] gives Ohm's law:

$$j = -\kappa \nabla \phi \qquad [2\text{-}35]$$

where

$$\kappa = F^2 \sum_i \left| z_i^2 \right| u_i c_i \qquad [2\text{-}36]$$

κ is the conductivity of the solution, and where the convective terms sum to zero by the electro-neutrality requirement:

$$\sum_i z_i c_i = 0 \qquad [2\text{-}37]$$

Electrode reactions involve a series of steps, the transport of the reactants to the reaction interface where charge (electrons) is transfered, and the transport of the products formed away from the surface.

2.9. Phase Formation and Growth

The mass transport of electroactive ions, for example copper ions in WEEE leachate, transfers copper ions from the bulk catholyte towards the surface of the electrode by diffusion. As a result of the mass transport process, electrodeposition of copper occurs, in which copper metal is produced. Electrodeposition takes place via the reduction of a cation on the substrate surface of a cathode to form an ad-atom with an applied potential or current. A rather idealised cathode surface, smooth even on an atomic level and free of defect will be assumed. The mechanism of deposition starts with the nucleation process between the electroactive cation and the surface of the electrode [2].

The ad-atom is formed by electron-transfer to the electroactive cation which is drawn towards the substrate surface of the cathode as an atom adsorbed onto this surface. The surface diffusion of ad-atom over the electrode surface to an energetically favourable site, in which the active of ad-atom aggregates forming a new electrodeposited phase. The nucleus grows parallel and/or perpendicular to the electrode surface. Eventually, nucleation starts when a number of nuclei form and grow on the surface. As the surface is covered by at least a monolayer of the metal, deposition occur on the same metal rather than a different metal substrate. The overall process is illustrated in Figure 2-5.

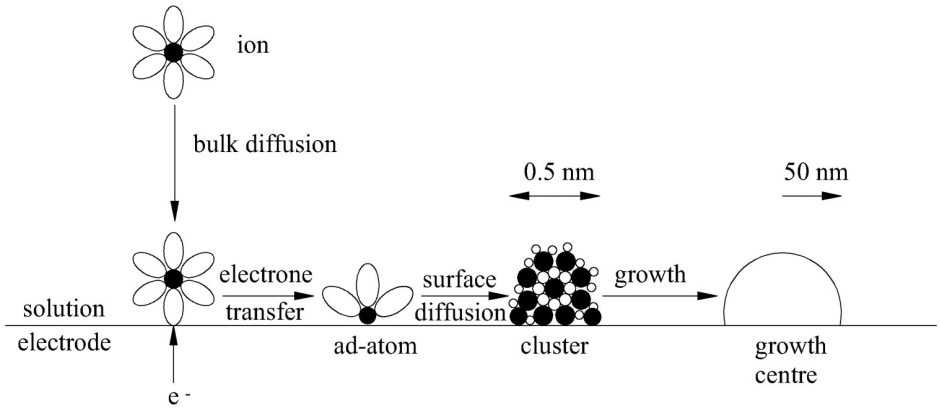

Figure 2-5. The stages in the formation of a stable, growing nucleus of a metal on an electrode surface [2].

2.10. Electrochemical Figures of Merit

2.10.1. Cell Voltage

The anode and cathode have reversible potentials of E_a and E_c, respectively. These are the electrode potentials at which the electrochemical reactions on each electrode are in thermodynamic equilibrium. Any deviation from these potentials will result in a reaction occurring. The overpotentials η_a and η_c are the deviations from the reversible potential on the anode and cathode respectively, which drive the reactions.

The rate of reaction in a given cell is determined by the overall cell voltage, U_{cell}. In a cell in which a current is flowing, which is a reaction occurring and it is not in thermodynamic equilibrium, U_{cell} has at least five components [5] which are depicted in Figure 2-6.

(i) The thermodynamic potential E_a requirement for the anode reaction,

(ii) The anode overpotential, $\eta_{a,}$ which provides the driving force for the anode reaction to depart from thermodynamic equilibrium,

(iii) The thermodynamic potential E_c requirement for the cathode reaction,

(iv) The cathode overpotential, $\eta_{c,}$ and,

(v) ohmic potential drop *IR*, due to resistance in the electrolyte(s)+membrane+ busbars.

Therefore,

$$U_{cell} = -\left(E_A + \eta_A - E_C - \eta_C + IR\right) = -\left(E_A + \eta_A - E_C - \eta_C + \sum_i \frac{j \cdot d_i}{\kappa_{eff,i}}\right) \qquad [2\text{-}38]$$

For which negative sign represents the cell voltage for an electrolytic reactor.

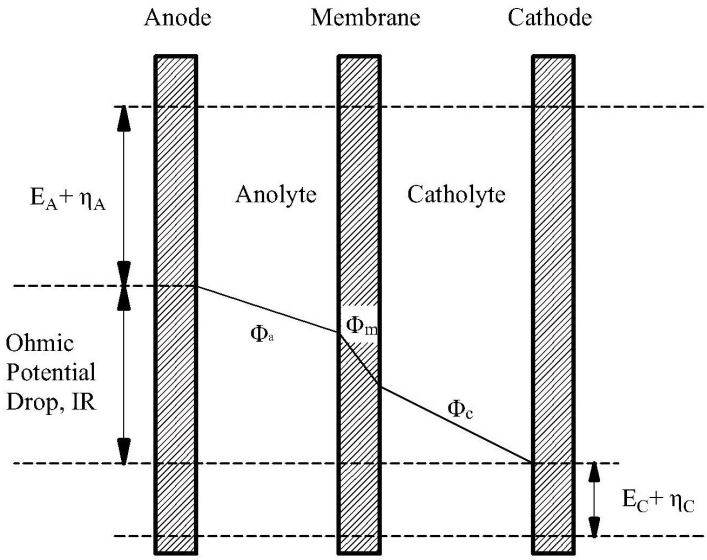

Figure 2-6. Distribution of potential in an electrochemical cell.

2.10.2. Charge Yield

A key parameter of an electrochemical process is the charge yield, Φ^e_P for product P. The charge yield is the ratio of the theoretical charge required for the amount of product obtained (Q_P) to the total charge (Q) passing through an electrolytic cell during the electrolysis time [5]:

$$\Phi_P^e = \left| Q_P / Q_T \right| \qquad [2\text{-}39]$$

The theoretical amount of charge required for the amount of product P obtained (Q_P) is calculated from the stoichiometry of the half-cell reaction using Faraday's law:

$$Q_P = \left| \frac{m_P \upsilon_e F}{\upsilon_P M_P} \right| = \left| \frac{n_P \upsilon_e F}{\upsilon_P} \right| \qquad [2\text{-}40]$$

where m_P is the mass and n_P is the amount (mol) of the product P formed during the electrolysis, M_P is the molar mass of P, F is the Faraday constant. υ_e represents the stoichiometric number of electrons for the electrode reaction yielding P. The total amount of charged passed through an electrochemical cell can be calculated from the current (I) passed during the electrolysis over time (t) [5]:

$$Q_T = \int I \, dt \qquad [2\text{-}41]$$

A low charge yield indicates that a large fraction of the total charge is due to loss reaction and vice versa.

2.10.3. Specific Electrical Energy Consumption (SEEC)

Another figure of merit is the SEEC (w_P^e) which is defined as the electrical energy required to form a unit mass/mole of the desired product P in an electrochemical cell [5]. This is typically measured in kWh tonne^{-1}, and is required for the estimation of operational costs of an electrochemical process or reactor.

$$w_P^e \text{ / kWh (tonne P)}^{-1} = \left(\frac{\nu_e F}{\Phi_P^e} \right) \cdot \frac{U}{3.6 M_P} \qquad [2\text{-}42]$$

2.11. Electrochemical Reactors for Metal Recovery

Electrochemical reactors have been utilised for many years to deposit metals from aqueous wastes for reuse. Pletcher et al. [10] cited a long list of 17 companies providing various electrochemical reactors for metal recovery. A review of the use of electrochemistry in waste removal by Bockris et al. in 1994 [11] also included a packed bed reactor for metals recovery, complete with design equations. Metal recovery via electrochemical reactors has the advantages that:

a) additional chemicals are not required,

b) selective metal recovery is possible taking into consideration thermodynamic and kinetic requirements of each species involved,

c) the metals can be recovered in their metallic form, and,

d) the processes tend to operate at low temperature and pressure, specifically at room temperature and pressure of 25°C and 1 atm.

Electrochemical reactors are often individually designed for a specific application, in order to maximise metal recovery and minimise running costs. Factors that affect these include cell voltage, cell current, electrode area, flow, ohmic drops in the cell (discussed in section 2.10.1) and associated connections, and the required form of the deposited metal (e.g. powder or sheet). For this Chapter, approximate and rigorous models are presented as follows for a circulating particulate bed reactor and mesh cathode in a fluidised bed of inert particles, which operates with continous recirculation of the electrolyte in the mass transport controlled

region.

2.11.1. Mode of operation and model description of the electrochemical reactor

The mode of operation for this kind of electrochemical reactor is depicted in Figure 2-7. The reservoir is considered as a well mixed tank (CSTR), while the reactor is considered as a plug flow reactor (PFER) [12]. It is important in the design of such processes to be able to predict the variation of concentration of the metal ion with time; in particular the application to a fluidised bed reactor operating for the cathodic selective removal of metals.

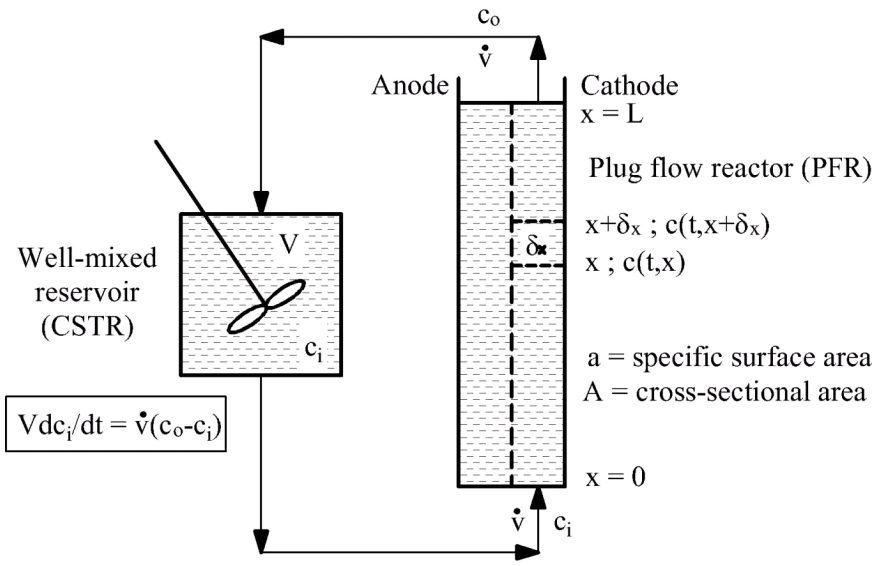

Figure 2-7. Plug flow reactor operated in batch recycle mode with well-mixed reservoir [10].

The basic assumptions involved in the ensuing derivation are outlined as follows:

a) Idealized plug flow exists in the reactor,

b) the reservoir is a perfect back-mix system,

c) the transport of the reactive ions in the reactor occurs under convective-diffusion control,

d) the mass transfer coefficient is constant throughout the reactor, and,

e) electrolyte temperature and hence physical properties are constant both in space and time.

By integration of the local current:

$$dI_x = nFk_m Aac_x dx \quad [2\text{-}43]$$

in the volume element Adx, over length L and substituting $c_o = c_i \exp\left(-\frac{k_m AaL}{\dot{\mathrm{v}}}\right)$, results in the predicted transport limited current for the reactor:

$$I_t = nF\dot{\mathrm{v}}c_i\left[1-\exp(-k_m AaL/\dot{\mathrm{v}})\right] \quad [2\text{-}44]$$

Substitution of the steady state concentration profile for the reactor, coupled with a mass balance on the CSTR reservoir.

$$Vdc_i/dt = \dot{\mathrm{v}}(c_0 - c_i) \quad [2\text{-}45]$$

results in an approximate equation predicting the time evolution of the concentration $c_{i,t}$ in the well mixed reservoir:

$$c_{i,t} = c_{i,t=o}\exp\left\{-\frac{\dot{\mathrm{v}}t}{V}\left[1-\exp\left(-\frac{k_m AaL}{\dot{\mathrm{v}}}\right)\right]\right\} \quad [2\text{-}46]$$

Substitution of equation [2-46] into equation [2-44] results in the time dependence of reactor current for a fixed flow rate and an initial $c_{i,t=0}$:

$$I_{L,t} = nF\dot{\mathrm{v}}c_{i,t=0}\left[1-\exp\left(-\frac{k_m AaL}{\dot{\mathrm{v}}}\right)\right]\exp\left\{-\frac{\dot{\mathrm{v}}t}{V}\left[1-\exp\left(-\frac{k_m AaL}{\dot{\mathrm{v}}}\right)\right]\right\} \quad [2\text{-}47]$$

In addition, selective ion exchange membranes are used in electrochemical reactors to create two hydraulically separated compartments for anolyte and catholyte as shown in Figure 2-7. The membrane functions as a barrier to convection and diffusion while permitting the selective migration of ions. Generally, an ion exchange membrane is a sheet of polymer with bound ionic species. Negatively-charged groups are fixed to cation exchange membranes in which anions are rejected by the negative charges and cannot permeate through, and vice versa for the anion exchange membrane. Membranes are used, for example, to block redox reaction loops in which species re-oxidise at an anode after being reduced at the cathode because that reduces the efficiency of the desired reactions [13].

2.11.2. Mass transport properties for a mesh cathode in a fluidised bed of inert particles of an electrochemical reactor

The minimum fluidisation velocity (v_{mf}) and terminal velocity (v_t) of the fluidised bed with inert glass beads were estimated by the following set of correlations [2-48]- [2-50][14]:

Voidage of minimum fluidisation (ε_{mf}):

$$\frac{1}{\phi\varepsilon_{mf}^3} \cong 14 \qquad [2\text{-}48]$$

ϕ is sphericity, $\phi = 1$ in this case and $\varepsilon_{mf} = 0.415$.

Velocity for minimum fluidisation (v_{mf}) for Re_p (vd_p/ν) < 20:

$$v_{mf} = \frac{\left(\phi d_p\right)^2}{150}\frac{g\left(\rho_s - \rho_l\right)}{\mu}\left(\frac{\varepsilon_{mf}^3}{1-\varepsilon_{mf}}\right) \qquad [2\text{-}49]$$

Terminal velocity (v_t) for spherical particles for $0.4 < Re_p < 500$:

$$v_t = \left[\frac{4}{225}\frac{\left(\rho_s - \rho_l\right)^2 g^2}{\rho_l \mu}\right]^{1/3} d_p \qquad [2\text{-}50]$$

The relationship between the bed voidage and flow rate was estimated by equations [2-51] - [2-53][15]:

$$v = v_t \cdot \varepsilon^n \qquad [2\text{-}51]$$

$$n = \left(4.4 + 18\frac{d_p}{d_t}\right)\mathrm{Re}_t^{-0.1} \qquad [2\text{-}52]$$

$$\mathrm{Re}_t = \frac{v_t d_p}{\nu} \qquad [2\text{-}53]$$

The mass transfer coefficient was estimated by correlations [2-54] –[2-55][16]:

$$St_p = \frac{k_m \varepsilon}{v} \qquad [2\text{-}54]$$

$$St_p = 1.24 \cdot Sc^{-0.667} \cdot \left[\mathrm{Re}_p / \left(1-\varepsilon\right)\right]^{-0.52} \qquad [2\text{-}55]$$

St_p was the Stanton number and u was the superficial velocity.

2.12. Chapter Summary

This chapter has described the theoretical studies of electrochemical process principles which complement the experimental work in the following chapters.

2.13. References

[1] Walsh, F.C., 1993, A First Course in Electrochemical Engineering. The Electrochemical Consultancy, Romsey, Hants.

[2] Pletcher, D., 1991, A First Course in Electrode Processes. The Electrochem. Consultancy, Romsey, UK.

[3] Bard, A.J., Parsons, R. and Jordan, J., 1985, Standard potentials in aqueous solution. Marcel Dekker, New York.

[4] Bard, A.J. and Faulkner, L.R., 2002, Electrochemical Methods: Fundamentals and Applications, 2nd ed., John Wiley & Sons, New York.

[5] Kelsall, G.H., in Lecture notes of Electrochemical Engineering elective course, Imperial College London, 2008.

[6] Newman, J. and Thomas-Alyea, K.E., 2004, Electrochemical Systems, 3rd ed., Wiley Inter-Science, New York.

[7] Albery, W.J. and Hitchman, M.L., 1971, Ring-Disc Electrodes. Clarendon Press.

[8] Levich, V.G., 1962, Physiochemical Hydrodynamics, 2nd ed., Prentice-Hall, Englewood Cliffs, New Jersey.

[9] Treimer, S., Tanga, A. and Johnson, D.C., 2001, A Consideration of the Application of Koutecký-Levich Plots in the Diagnoses of Charge-Transfer Mechanisms at Rotated Disk Electrodes: A Review. *Electroanalysis*, 14(3):165-171

[10] Pletcher, D., Walsh, F.C. and Whyte, I., 1990, The Application of Electrochemical Techniques to the Treatment of Industrial Process Liquors, IChemE Symposium Series No. 116 , Effluent Treatment and Waste Disposal, Hemisphere Pub Co., 195.

[11] Bockris, J.O'M, Conway, B.E., Yeager, E. and White, R.E. (editors), 1981, Comprehensive Treatise of Electrochemistry, Vol. 2, Electrochemical Processing, Plenum Press.

[12] Walker, A.T.S. and Wragg, A.A., 1980, Mass transfer in fluidised bed electrochemical

reactors. *Electrochim. Acta*, 25 (3): 323-330.

[13] Davis, T.A., Genders, J.D. and Pletcher, D. 1997, A first course in Ion Permeable Membranes, The Electrochemical Consultancy, Romsey, Hants, England, UK.

[14] Kunii, D. and Levenspeil, O., 1991, Fluidization Engineering, Butterworth-Heinemann, 2nd Edition.

[15] Coeuret, F., 1967, Proc. Int. Symp. Fluidization (Edited by Druikenburg). Netherlands Univ. Press, Eindhoven, 537.

[16] Cabin D.C. and Gabe D.R., 1974, Electrodeposition from a fluidised bed electrolyte- I. The mass transport correlation. *Electrochim. Acta*, 19: 645-652.

3. LITERATURE REVIEW

3.1. Chapter Overview

Electrical and Electronic Equipment is defined and typical material compositions of main equipment groupings are presented, followed by an overview of legislation, economic perspectives and common technologies to treat waste electrical and electronic equipment (WEEE). A review of electrochemical recovery for precious metals (PMs) such as gold (Au) and base metals such as copper, iron, lead, nickel, tin and zinc is then presented, with an emphasis on the thermodynamics, (micro-) kinetics, modelling of the reduction mechanisms and reactor design requirements. The chapter concludes with the objectives of the Ph.D. project.

3.2. Electrical and Electronic Equipment (EEE)

3.2.1. Definition of EEE

EEE is defined by the WEEE Directive [1] as 'equipment which is dependent on electric currents or electromagnetic fields in order to function properly and equipment for the generation, transfer and measurement of such currents and fields'. In addition, an upper voltage limit of 1000V/1500V for alternating and direct current is used to ensure that large industrial equipment is not covered by the legislation. In their interim report for the Environment Protection Agency (EPA), Wilkinson et al. [2] gave a simpler definition of EEE as equipment that uses electricity or through which electricity flows, and/or which contains an electronic circuit, i.e. a circuit with active and passive components.

A broad range of goods and appliances are classified as EEE, including large and small household appliances, IT equipment, lighting, radio & audio equipment, electrical tools and telecommunication equipment. When such products reach the end of their useful life they become WEEE [3].

3.2.2. Characterisation of WEEE

In order to enable development of a suitable physical or chemical process of metal recovery from WEEE, it is essential to understand three major factors [4]:

(a) the materials that are present in WEEE,
(b) their location, and
(c) the concentration in which they are present.

As previously defined, WEEE includes a variety of equipment that are disparate in both function and composition (Table 3-1), and their generalised material composition has been summarised by a number of studies [5-8].

Table 3-1. Material composition (by weight) of six different categories of equipment [4].

Equipment category	Ferrous metals / %	Non-ferrous metals / %	Glass / %	Plastics / %	Other / %
Large household appliances	61	7	3	9	21
Small household appliances	19	1	0	48	32
IT equipment	43	0	4	30	20
Telecommunications	13	7	0	74	6
Television, Radio etc	11	2	35	31	22
Gas discharge lamps	2	2	89	3	3

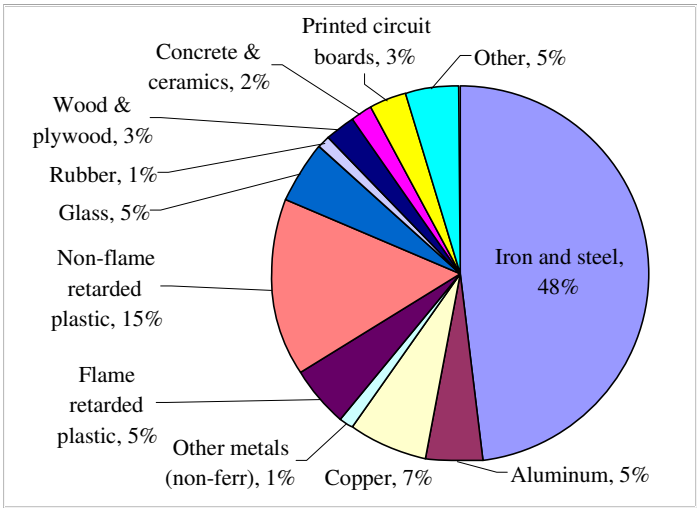

Figure 3-8. Material composition of WEEE [9].

The cost and efficiency of WEEE recycling will depend on the amount and number of different materials present, as well as the complexity of their arrangements. It is likely that the principal application of chemical recycling will be in the treatment of electronic components such as populated circuit boards, examples of which are shown in Figure 3-9. In order to optimise the efficiency of such a process, it is important that the electronic scrap and printed circuit boards (PCBs) are separated from WEEE as a whole. For the purpose of this project, it was assumed that the WEEE would have undergone some degree of pre-treatment to remove bulk metal, plastic and glass components and that the electronic components such as printed circuits boards and wires are to be recycled.

According to Duan et al.[5], the largest sources of scrap PCBs are from mobile phone (21.30%), computers (18.76 %), stereos (11.2 %) and televisions (7.04%). The location and quantity of metals in electronic components will vary depending on the design, application, and type of function required. Hence any system for chemical recycling of WEEE should be able to process a range of materials. Consequently, it will be useful to gain an understanding of the typical composition of such units.

PCBs are typically constructed from base layers of reinforced polymers, which range from glass fibre reinforced epoxy resins to chemically stable polymers, such as polytetrafluoroethylene (PTFE). Copper metal is usually deposited between the polymer layers and etched onto the polymer surface, while interconnector holes drilled through the board are filled with copper and palladium to join the metal layers. Other metals including Pb, Sn, Ni, Au, Ag, and Pd may be deposited onto the copper layers to create a solderable finish. Metal containing components are then attached to the unpopulated board with lead (no longer being used as the new regulation implemented, explained in section 3.3.1), tin and silver solder. The electronic components added to bare PCBs contain an even wider mix of materials. Aluminium is present in cooling parts of the active semiconductor elements and capacitors, while iron is found in cabinets, heat sinks, transformers and electromechanical components. Gold is used as connector wires and pins, whereas resistors contain mixed metal oxides. Small quantities of tantalum, gallium, indium, titanium, silicon, germanium, antimony, tellurium, and a large proportion of the periodic table may also be present [9]. A schematic of a section through typical PCBs is shown in Figure 3-10.



Figure 3-9. Printed Circuit Boards (PCBs).

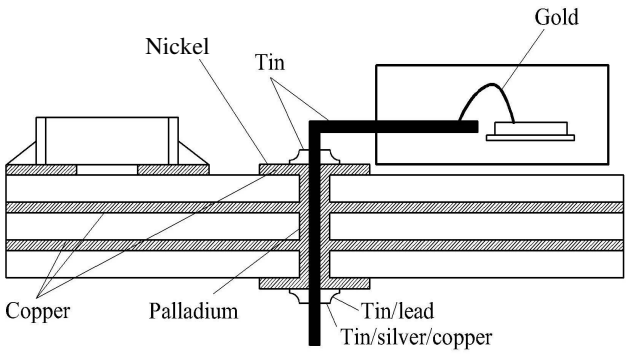

Figure 3-10. PCB section [9].

Several studies [9-13] have analysed the general metal content in PCBs (Table 3-2) while Brandon et al. [13] reported the typical content after the use of eddy current and magnetic separations during the pre-concentration process (Figure 3-11).

Table 3-2. Metal content of PCBs.

	Weight % of Metals in Electronic Scrap / PCBs					
Cu	7.20	19.19	23.47	10.00	16.00	14.20
Fe	2.19	3.56	1.22	-	5.00	8.18
Ni	0.26	1.65	2.35	0.85	2.00	0.52
Sn	1.63	2.03	1.54	-	4.00	1.99
Pb	2.35	1.01	0.99	1.20	2.00	1.03
Al	5.80	7.06	1.33	7.00	5.00	3.64
Zn	0.21	0.73	1.51	1.60	1.00	1.11
Au	-	0.07	0.05	0.03	0.01	0.01
Ag	0.07	0.10	0.30	0.01	0.05	0.08
Pd	-	-	0.02	-	0.01	0.02
Ref:	[Duan et al., 2011]	[Yoo et al., 2009]	[Ogunniyi and Vermak, 2009]	[Kim et al., 2004]	[Goosey and Kellner, 2003]	[Brandon et al., 2002]

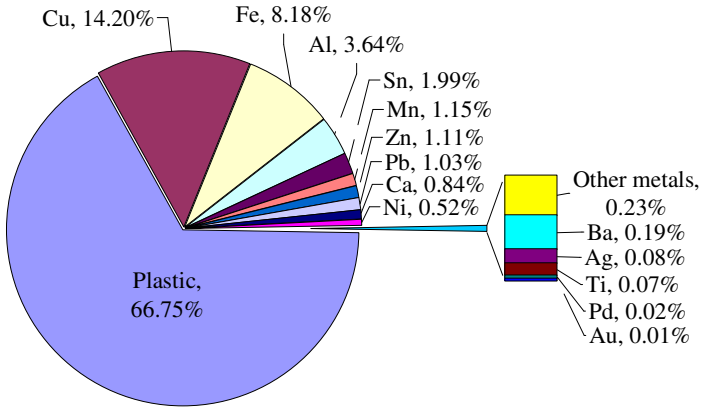

Figure 3-11. Composition of Metals in Electronic Scrap of PCBs [13].

3.3. Overview on Current Situation

The increased use of electronics and technology in society brings the challenge of protecting human health and the environment from potentially harmful effects due to improper handling and disposal of these products. Every year, an estimated one million tonnes of WEEE are discarded by householders and commercial groups in the UK [14]. Of these, 43 % is sent

directly to landfill and more than 90 % is landfilled, incinerated or recovered with no pre-treatment [8]. Hence, considerable quantities of valuable material are wasted and hazardous material released into the earth from landfill or into the air from smelters.

For PCBs alone, it was reported that 50 ktonnes per annum of PCB scrap is generated within the UK, of which an estimated 40 ktonnes per annum comprises populated boards. The remaining 10 ktonnes is either composed of unpopulated boards or associated board manufacturing scrap such as off-cuts. Of this 50 ktonnes per annum of estimated PCB scrap, it is further estimated that only 15 % is subjected to any form of recycling, while the remainder is consigned to landfill. Approximately 60 % of the estimated landfill demand of 43 ktonnes per annum is believed to be consigned within the total redundant equipment package [9].

The majority of PCB scrap that enters the recycling route involves recovery of the metals and PMs by smelting. There are few smelters in the world capable of doing this (Umicore in Belgium, Boliden in Sweden and Noranda in Canada; reviewed in section 3.3.2), and the costs involved are such that only boards with a high PM content are recycled. Approximately 90 % of the intrinsic value of scrap PCBs lies in the PM content, and as the basic charges levied by commercial smelters are between £500-1000, processing of low grade electronic waste by smelting is not economic [9].

The rapid escalation of WEEE is also a global concern. The growth of WEEE in Europe is about three times higher than the growth of the average municipal waste. In the EU, 6 million tonnes of WEEE were generated in 1998 and with the volume of WEEE increasing by at least 3 to 5 % per annum, it is estimated to reach 24 million tonnes by 2020 [8]. In 2007, it was reported that 2.25 million tonnes of WEEE were generated in the USA, about 18 % of which was collected for recycling and the remainder largely sent to landfills [2]. In terms of PCBs, only 29 ktonnes of metal were recovered and the remainder was sent to foreign smelters for extraction of copper and other PMs [16]. In Asia, especially China, it was reported that the total amount of PCBs that will be discarded in the near future may reach 526 ktonnes every year, which will account for almost 5 % of the total hazardous waste generation in China [5]. This number is in an order of magnitude higher compared to waste generated in the UK.

In order to tackle this global issue, implementation of emerging legislation such as the WEEE and Restriction on Hazardous Substances (RoHs) Directive will necessitate the increasing recovery and recycling of materials found in scrap PCBs.

3.3.1. Legislative Issue for WEEE

The awareness of the danger caused by WEEE to life and the environment is reflected in environmental legislation and regulations. Considering the current waste management and the rapid growth and the hazardous content of EEE in particular, the European Commission adopted two draft directives in June 2000 on WEEE and on the Restriction of the use of certain hazardous substances in EEE (RoHS) [1].

3.3.1.1 Waste Electrical and Electronic Equipment (WEEE) Directive

The UK regulations implementing the WEEE Directive were laid before Parliament on 12 December 2006 and were enforced on 2 January 2007 [3].The objective of the WEEE directive is to prevent the generation of WEEE, increase reuse, recycling and to reduce the environmental burden associated with end-of-life management of these waste streams [3]. The directive states that member countries shall encourage the design and production of EEE which takes into account and facilitates the dismantling, recovery, and in particular the reuse and recycling, of WEEE, their components and materials. Producers are then required to increase the use of common components and material coding standards. On the other hand, member states must set up separate WEEE collection facilities (to achieve a minimum of 4 kg per person per year) to minimise the disposal of WEEE as unsorted waste. New equipment put onto the market are obliged to be marked with the symbol indicating separate collection for EEE (a crossed-out wheeled bin). Producers need to set up and finance systems to provide necessary treatment of the separately collected WEEE using the best available treatment, recovery and recycling techniques. The minimum requirements for the treatment of WEEE are disassembly, fluid removal, and selective treatment of components containing printed circuit boards, batteries, mercury, chlorofluorocarbons, brominated flame retardants, cathode ray tubes, asbestos, and polychlorinated byphenols [3].

3.3.1.2 Restriction on Hazardous Substances (RoHS) Directive

Certain materials that are frequently present in EEE are hazardous in nature, and considered to pose risks to human health and the environment. Taking into account current technical and economic feasibility, substitution of hazardous materials in EEE by a safer material, is the most effective way of ensuring significant reductions of risks to health and the environment. The RoHS Directive has banned the placing on the EU market of new EEE containing more than agreed levels of lead, cadmium, mercury, hexavalent chromium, and polybrominated biphenyl (PBB) or polybrominated diphenyl ether (PBDE) flame retardants since 1 July 2006

[3].

Mercury is mainly used in fluorescent tubes as well as in batteries, switches, sensors, and relays. In fact, 22 % of the world consumption of mercury is in EEE.[9] Mercury and its compounds are highly toxic and long-term exposure may be fatal; they produce biological transformations in the environment and living organisms [3]. Cadmium is highly toxic and many of its compounds are carcinogenic. Cadmium is mostly found in batteries, but is also used as a pigment and stabiliser in plastics and as a fluorescent [2]. Currently consumer electronics contribute 9 % of the cadmium present in municipal waste streams [3]. Lead is found in solder, cathode ray tubes (CRT) in television and computer screens and batteries (40 % of lead is present in the municipal waste stream because of EEE [18]). Lead and lead compounds are bio-accumulative, carcinogenic, teratogenic, has negative effects on the human nervous system, blood and kidneys.[18]. Hexavalent chromium is highly toxic and is used as corrosion protector coating. Brominated flame retardants (BFR) are used for flammability protection of PCBs. However they accumulate in the environment, and may produce dangerous dioxins and furans upon heating during recycling processes [17].

It should be noted that while these hazardous chemicals have been banned in new EEE from 2006 by the RoHS directive, the WEEE chain will continue to contain them for some years to come, and so any recycling process should be designed accordingly.

3.3.2. Review on Industrial Metal Recovery

In order to comply with the current legislation on WEEE which emphasises recycling, current industrial metal recovery was reviewed. In recent years, separate collection systems for the recycling of WEEE have been established in several countries. The recycling systems are set-up so that the WEEE is collected and transported to dismantling facilities, where manual separation of the waste into different fractions occurs, in most cases, to remove hazardous substances before other materials can be recycled or treated in a safe and suitable way. The fractions containing PCBs, low and high-grade fractions, are thereafter sold to copper smelters, which feed the material into their process to recover predominantly precious metals (PMs) and copper.

Copper smelters process electronic scrap especially from PCBs to recover Cu, Au, Ag, Pt and Pd [9]. From an economic viewpoint, PCB waste is seen as a PM source, which is the reason that the smelters receive and process this type of waste. Copper, in itself, is normally seen as a

usable by-product that comes along with the PMs. On the global market, there are only four large copper smelters that process WEEE including PCBs [18]:

(a) Boliden, Rönnskärsverken, in Skellefteå, Sweden,

(b) Noranda, Rouyn-Noranda, in Quebec, Canada,

(c) Umicore, Hoboken, in Antwerp, Belgium, and

(d) Norddeutsche Affinerie (NA), in Hamburg, Germany.

Although there are more than 160 copper smelters in the world, of which some process copper scrap, these treat mainly waste products with high percentages of pure copper such as electrical cables, copper rods and tubes. However, some smaller copper smelters in Asia, mainly in Japan, China and India, might also process PCBs, but these smelters normally do not stay on the market for very long [18].

Within the UK, Johnson Matthey accepts scrap PCBs through their smelters, but the drawback is such that only boards with very high PM content are processed, whilst the others are shipped abroad for subsequent retrieval of the economic components and disposal of the hazardous materials. This represents a significant loss for the economy. In addition, Engelhard Sales Ltd., Cinderford, UK which is a wholly-owned subsidiary of BASF has been actively developing the recycling facilities to process a wide variety of WEEE, including IT and telecommunications equipments, CRT monitors and other display screen equipment. In addition, they claimed to have a wealth of experience of PMs and catalyst refining which employ pyrometallurgical, hydrometallurgical, and physical methods [19] to reclaim over 3000 different types of PM bearing materials including Au, Ag, Pt, Pd, Rh and Ir. [20] The full process description has not been disclosed, and cannot be found in the open literature.

3.3.2.1 Johnson Matthey

Johnson Matthey began as a refinery in Hatton Garden, London in 1817. Two basic processes are used: the Miller Process, employing chlorine as the purifying agent; or electrolysis, a technique originally developed in the 1870s by Dr. Emil Wohlwill and since then, much modernised. Using chlorine, gold can be refined up to a fineness of 995 parts per thousand but for fineness up to 999.9, electrolysis is essential. More recently, solvent extraction technology has been developed and applied in primary refining of ore. In small refineries, processing scrap from jewellery, dental production and other similar items other may be used. In

particular, the aqua regia process, which involves dissolving the gold scrap in aqua regia acid and then selectively precipitating pure gold with a chemical reducing agent such as ferrous sulfate or sodium hydrogen sulfate. This can produce Au of up to 99.99% purity [21].

3.3.2.2 Boliden

Currently, Boliden (Rönnskärsverken) recycles about 30 ktonnes of WEEE scrap per year of which some 2 ktonnes comes from Sweden, while the rest is imported. PCBs constitute about 50-60% of the total amount processed. In 2000, Boliden produced approximately 240 ktonnes of copper, in the form of copper cathodes, of which about 30 % came from recycled materials such as electronic and metal scrap, residues and slag. Additionally, about 40 % of the 14 kg Au produced and 90 % of the 41 ktonnes of Zn clinkers produced also came from recycled materials [22].

Principally, Boliden [22] adopted pyrometallurgical and electro-refining techniques in their process. Following smelting of PCBs, the copper anodes are refined in an electrolysis treatment, using sulfuric acid and copper sulfate as the electrolyte. The anode plates are placed in electrolyte tanks, with a cathode sheet put in-between every copper anode. The cathodes are made of stainless steel. During the process, a current of about 20 kA is used in order for the copper to be transferred to the cathodes. The PMs and impurities that remain on the anodes, settle as anode slime. This slime is then pumped to a PMs plant for further refining. The end product of the electrolytic refinery is 99.99% pure copper cathodes, which are ready to be sold on the market. In the PM refinery, gold, silver, platinum, palladium and selenium are recovered. The process chemistry involved in the processing of PCBs is shown schematically in Figure 3-12.

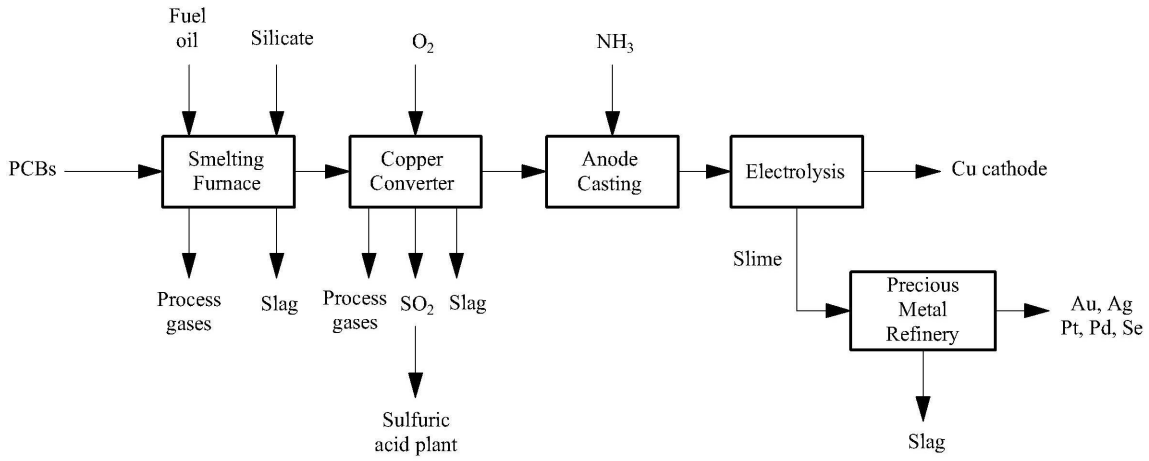

Figure 3-12. Metal recovery process of PCBs, showing the various materials in- and outflows in the different steps [18].

3.3.2.3 Noranda

Currently at the Noranda's copper smelter (the Horne smelter, Rouyn-Noranda, Quebec, Canada), approximately 150 ktonnes of metal recyclables is processed annually, of which 50 ktonnes is WEEE. In 1999, the copper production was 200 ktonnes of which 15 % contributed from recycled electronic and metal scrap. The Horne smelter produces copper anode, which are sent to Noranda-CCR copper refinery in Montreal-East, Quebec, for the final refinery of copper into copper cathodes and of PMs [18].

3.3.2.4 Umicore

Umicore's facility in Hobroken, Belgium, under the head of the business unit Umicore PMs, processes Cu, Pb, Ni containing materials to recover those metals and PMs. In 2001, 96 % of the raw materials processed were secondary material, of which about 16 ktonnes were WEEE [18]. The recovery process involved copper electrowinning in sulfuric acid (H_2SO_4) plant, whilst the PMs are collected in residue which is further refined at the precious metal refinery. It was reported that the recovery process of PMs combines classical methods (cuppelation) with in house developed processes (silver refinery) to allow the in-house recovery of all PMs. The 'cuppelation' process is whereby ores or alloyed metals are treated under controlled high temperature in order to extract the PMs [23].

3.3.2.5 Norddeutsche Affinerie

Norddeutsche Affinerie, Hamburg, Germany processes about 4 ktonnes of WEEE, which

consists almost exclusively of PCBs. The circuit boards (i.e. without capacitors, batteries, components containing mercury and hazardous materials) are mechanically shredded, resulting in two fractions of materials: coarse circuit card pellets and absorbed filter dust. The latter is utilised in the copper smelting process of the Norddeutsche Affinerie, while the plastic parts of the circuit cards burn nearly residue-free. The non-ferrous and precious metals are concentrated in multiple-stage refinery processes and are then reprocessed to copper products and by-products. The by-products which include Au, Ag, Pd and Pt in the formed of anode slime are then precipitated in a multiple-stage process. It was reported that the overall process especially Cu refining has a very high overall recycling rate, which resulted in a yearly production of Cu as approximately 370 ktonnes [18].

Generally, the recycling systems in operation today for end-of-life EEE in the industries are directed towards the recovery of high purity (99.99%) copper and PMs; however, there is no direct focus on recycling of Sn-Pb solders. PCBs, which contain considerable quantities of valuable metals, are, after separation at dismantling facilities, delivered to copper smelters for the recycling of PMs and copper, whilst most of the Sn and Pb contained in the PCB fractions are discharge from the process [18]. On the other hand, Ag and Cu are refined as separate end products. Sn and Pb consequently, follow the process gases and are predominantly trapped in the cleaning devices as filter dust. At the present situation, at one site, approximately one quarter of this filter dust is subsequently sent to other smelters, where the metals contained in the dust are recovered. However, the remaining three quarters are temporarily stored onsite awaiting final disposal [22]. Consequently, large amounts of raw material resources in today's operation are lost in the process. Apart from environmental compliance, the driving force of metal recovery is the economic value of the PMs and copper recovered. From an economic viewpoint, PCB waste is seen as a PM source, which is the reason that the smelters receive and process these types of wastes.

As per this review, current recycling methods for copper are mainly pyrometallurgical and only those boards with adequate PM content are subjected to metal recovery; the smaller volume, higher grade material is treated hydrometallurgically by PM refiners, while the lower grade material is sent to foreign copper smelters. The nearest copper smelter to the UK is in Belgium (Umicore), which charges ca. £1k per tonne for PCB smelting and metal refining [24]. This is less than the amount charged by PM refiners, which achieve higher recoveries from a much lower throughput. The Printed Circuit Industry Federation estimated the cost of waste management for the UK printed circuit board industry (ca. 5 km^2 p.a.) at > £27 million

p.a., mostly in PCB production [24]. As there is just a small fraction of PM content and the contained copper value (ca. £5.5k per tonne Cu [26]) will not cover the costs of conventional pyrometallurgical recovery, a lower cost hydrometallurgical process is required to recover metals, as from WEEE. This would assist to remove the contained metals from the landfill stream, with consequential economic and environmental benefits, and enable a less centralised reprocessing of such wastes than in foreign copper smelters [24].

3.4. Economic Perspectives

The drive to provide effective recycling of electronic scrap for retrieval of the many different constituent metals has not only political and regulatory consequences, but also financial. The metal content in the electronic scrap represents a significant cost of raw materials for the manufacturer of the unit. The possibility of recovering even a fraction of this investment represents a saving for the company involved. For the purpose of this report 10 metals, 6 base and 4 precious, were analysed as shown in Table 3-3, based on weight % scrap [13] shows recent trading prices [26] of these metals in the global markets.

Table 3-3. Price of base and PMs traded on the global market place [26].

Element	Weight % Scrap	Price	
		£ / tonne	£ / tonne scrap
Cu	14.19	6,140	871.00
Pb	1.03	1,518	15.60
Ni	0.52	13,195	68.61
Sn	1.99	5,022	99.94
Zn	1.11	1,550	17.05
Au	0.013	33.3m	4329.00
Ag	0.076	875,000	665.00
Pd	0.016	19.1m	3056.00
Fe	8.18	756	61.84
Pt	0.005	39.7m	1985.00

The cost effectiveness of pyrolytic recycling for scrap board assemblies, apart from those with relatively high PMs content, coupled with increasing ecological concerns, has cast doubt over the long-term viability of this methodology. Subsequently this has provided impetus for the development of more sustainable approaches embracing mechanical and hydrometallurgical technologies. To significantly elevate the levels of recycling being undertaken, it is clear that any approaches must embrace a cost effective manner and be environmentally benign.

Hydrometallurgical approaches do offer a treatment alternative to smelting and the possibility of realising higher metal recovery yields. This latter point is of great significance when dealing with high value scrap. Two stages are generally involved in hydrometallurgical approaches to metal reclamation from shredded electronic systems where metal dissolution into an aqueous media is followed by recovery of the metal ions. The dissolution consists of a series of selective and/or non-selective acid and/or caustic leaches of finely divided solid material. The solutions are then subjected to separation procedures such as electrodeposition, solvent extraction, precipitation, cementation, ion exchange, filtration, and distillation to isolate and concentrate the metals of interest [27].

3.5. Research at Imperial College London on hydrometallurgical process

Existing recycling methods are mainly pyrometallurgical, which involve smelting of the WEEE at high temperatures and the production of polluting noxious gases. Alternative technologies that are economically viable and eco-efficient will be necessary to meet the demands of the WEEE directive. Therefore, the work at Imperial College London has demonstrated the feasibility of removing a high percentage of metals in electronic scrap using hydrometallurgical processes. The non-selective dissolution obviates the need for expensive and waste streams generation of multiple dissolution steps. The process could be important in terms of meeting targets set by the WEEE Directive because it removes all the hazardous metals from WEEE and not just the valuable PMs. On the other hand, selective recovery or further processing of the metals is required to obtain the most value from electronic scrap [13,25]. The WEEE leachate solutions, with which this project was concerned, arise from WEEE scrap mainly from PCBs. Samples from several sources of end-of-life PCBs, mother boards, graphic cards etc., shredded with rotary shears to < 8 mm, were characterised physically and chemically and found to contain ca. (wt%): 22% Cu, 2% Zn, 1% Al, 0.2% Ni, 5% Sn, 3% Pb, 0.1% Fe, 0.02% Au, 0.04% Pd, 0.08% Ag, and 66.7% non-metallics; Al and Fe concentrations depending on whether eddy current and magnetic separations had been used to remove them during pre-concentration. Shredded scrap material has been leached by electrogenerated chlorine in acidic aqueous solutions of high chloride ion activity which was at 4 kmol m^{-3} HCl+ 1 kmol m^{-3} NaCl [25]. This has produced a multi metal leach solution, containing nearly all of the available metal in the scrap as mentioned above. The concentrations of each metal ion are summarised in Table 3-4.

Table 3-4. Leachate solution composition [25].

Element	Concentration / mol m^{-3}	Element	Concentration / mol m^{-3}
Cu	475.99	Ni	15.75
Zn	37.97	Ag	1.62
Al	27.31	Pd	0.187
Fe	0.10	Au	0.0522
Sn	28.12	Mg	3.35
Pb	10.48	Ba	0.002

The metal ions contained in the WEEE leachate are subjected to selective or non-selective metal recovery. Considerable amounts of reviews [28-30] have been made on metal recovery from effluent such as wastewater and industrial waste, which include WEEE. The techniques are adsorption [31,32], ion exchange [33,34], precipitation [35,36], extraction [37,38], membrane separation [39,40], biochemical treatment [41,42], and electrodeposition [13,44,45]. Each of these technologies has found industrial applications. The selection criterion include, but not limited to, discharge standards, waste volume, contaminant concentration and composition, capital and operating costs, maturity and reliability of the technology. At times, a combination of the technologies may yield the best results [42]. Since the main aims of this Ph.D. project is to produce an efficient, environmentally friendly electrochemical process involving theoretically no waste products, only electrodeposition will be discussed in detail here.

As summarised briefly in the Introduction (Chapter 1), electrochemical techniques such as electrowinning and electrodeposition are well-established technologies that are used extensively in metallurgical processes for the extraction or purification (electrorefining) of metals from ores, and in the electrical and electronics industry for the deposition of metals from solution [44]. Pletcher et al. [13], cited a list of 17 companies providing various electrochemical reactors for metal recovery. The use of electrochemical techniques for the recovery of metal ions from solution has a number of advantages and disadvantages. Firstly, electrolytic recovery units can operate continuously and obtain a very high purity product in a metallic form that is suitable for re-use or resale. Electrodeposition at a two-dimensional cathode is most suitable for relatively high metal concentrations; a high surface area three-

dimensional electrode is required for more dilute solutions with metals concentrations less than 100 ppm [11,12,108,109]. In addition, electrodeposition does not generally require a supply of chemical reagents and hence does not generate additional waste streams with disposal problems [108]. However, there are a few major hurdles too. The equipment used in this process has a relatively high capital cost, and, depending on the cathode efficiency, may have a high energy cost [109]. Apart from these, the high purity product that can be obtained, without the generation of numerous waste streams, make electrodeposition a promising option for the recovery of metals from the leachates of WEEE.

Taking all aspects into consideration, electrodeposition technique was chosen as the best option as this route produces an efficient, environmentally benign process involving theoretically no waste products. A number of groups in the UK [46-49] have investigated the use of such a process from different electrolytes, briefly reviewed in the following section.

3.6. Electrochemical Metal Recovery for PM (Au) and Base Metals (Cu, Sn, Pb, Ni, Zn, Al)

In the UK, there have been three potentially significant development projects undertaken on hydrometallurgical approaches to the recycling of scrap PCBs and subsequent recovery including researchers from the University of Newcastle, University of Cambridge and Imperial College London. The feasibility of electrodeposition of copper and lead at different concentrations of HNO_3 has been investigated by Meccuci and Scott [46] by preliminary galvanostatic electrolysis from simulated leaching solutions. The process to recover tin on the other hand, is somewhat complicated and the energy consumption will be considerably higher than that for copper. Having dissolved the copper, lead, and tin from PCBs using HNO_3, the tin was precipitated as stannic oxide. The precipitate was separated from the stripping solution by filtration and then dissolved in 10 % HC1 heated to 90 °C for 15 min. When the concentration of tin in the resulting solution was 30-60 g dm^{-3}, a coherent deposit of tin was obtained by electrodeposition at a potential of -0.60 V (SHE) with a current efficiency of 70-85 %. The electrochemical recycling of copper from the stripping solution was found to be efficient and feasible because of good current efficiencies, low deposition potentials, and high purity of the copper deposit achieved. For the electrowinning of lead, the dendritic deposit morphology and subsequent metal re-dissolution, together with hydrogen evolution, resulted in a low current efficiency. In addition, Pb^{II} tends to form an oxide deposit on the anode, an ionic exchange membrane has to be applied to separate the cathodic and anodic compartments

when copper or lead is electrodeposited, and hence the cost of the cells will be high. The maximum charge efficiency, obtained in the more dilute acid solutions (0.5 kmol m^{-3} HNO_3) was 43 % for copper and 27 % for lead.

A systematic method to determine the feasibility of metal recovery from various concentrations of spent tin stripping solution has been successfully applied as reported by Buckle and Roy [47]. The thermodynamics of the waste, particularly on Cu-NO_3-H_2O , Sn-NO_3-H_2O and Fe-NO_3-H_2O, were then investigated to determine the regions where the metals are in solid and dissolved forms. The strategies outlined were to recover HNO_3 until the proton (H^+) concentration in solution was 0.6 kmol m^{-3}, and subsequently separate SnO_2 from the dissolved copper via filtration at a pH between -0.4 and 2.4. The concentration of H^+ and NO_3^- were reported to affect the charge yield of copper deposition such that a lower NO_3^- concentration resulted in a higher charge yield of copper deposition which the author recommended for a higher degree of acid recovery prior to copper deposition. It was reported that copper can be recovered with a charge yield of 0.95 from a 300 mol m^{-3} Cu^{2+} in 1 kmol m^{-3} NO_3^- solution at a current density of 1250 A m^{-2}. However, it was elucidated that the charge yield would be decreased to 0.77 if the copper concentration was reduced by an order of magnitude from the starting solution, thus the current densities decrease due to the kinetics of nitrate reduction was deemed to be slow. In addition, the charge yield for copper deposition was lower for Cu^{2+} in a HNO_3 bath containing Fe^{3+} and trace amount of SnO_2 , ca. 0.24, applied current of -47mA. This is mainly due to the reduction of Fe^{3+} to Fe^{2+}. Thus, it was suggested that careful control and monitoring were required of Fe^{3+} concentrations arising from the stripping waste which in turn could decrease charge yields for copper electrodeposition [48].

The lead and tin from solder that was leached by fluoroborate solutions by Fray et al. [49] was also recovered by electrodeposition in a membrane-divided electrochemical reactor; at the anode, Ti^{IV} oxidant was regenerated from Ti^{III}. The nature of the metallic lead deposit depended on the current density used varying from an excellent metal foil deposit at 100 A m^{-2} to a powdery / dendritic deposit at 400 A m^{-2}. Performing the electrolysis under anaerobic conditions was found to be essential to prevent the continual re-oxidation of the titanium as it was pumped around the circuit, however under these conditions, the charge yield was greater than 0.90. The electrodeposition of tin was also found to occur at good charge yields at high tin concentrations. Lower current densities were suggested to remove the tin down to very low residual levels, probably in a second electrolysis stage. It was not possible to electrodeposit all

the tin from solution, because stannous ions underwent aerial oxidation to stannic ions, which proved impossible to reduce electrochemically. Hence, it is important to prevent the formation of stannic ions by leaching and electrowinning under anaerobic conditions. However, air and/or electrochemical oxidation in the presence of very low tin concentration is then required to regenerate the Ti^{IV} oxidizing agent for use in the anaerobic leach [49].

A previous project in Imperial College London has demonstrated the feasibility of electrowinning of Ag, Au, Cu, Pb, Pd and Sn from leach solutions (4 kmol m^{-3} HCl + 1 kmol m^{-3} NaCl) at pH 0 onto the graphite felt cathode of a membrane-divided electrochemical reactor [13]. The leach solution composition was previously shown in Table 3-4 . The carbon felt reactor was operated for a total of twelve hours under both potentiostatic and galvanostatic control. The cathode feeder electrode potential was controlled with respect to a saturated calomel electrode (SCE) at potentials -0.40 V, -0.50 V, -0.60 V, -0.65 V, and -0.75 V. The equilibrium potential of reactions for different metals/metal chloride ions in 4 kmol m^{-3} HCl + 1 kmol m^{-3} NaCl leach solution, estimated by the Nernst equation, is summarised in Figure 3-13. Equations used [50] for individual electrochemical reaction and the metal ions concentrations assumed can be found in Appendix A.

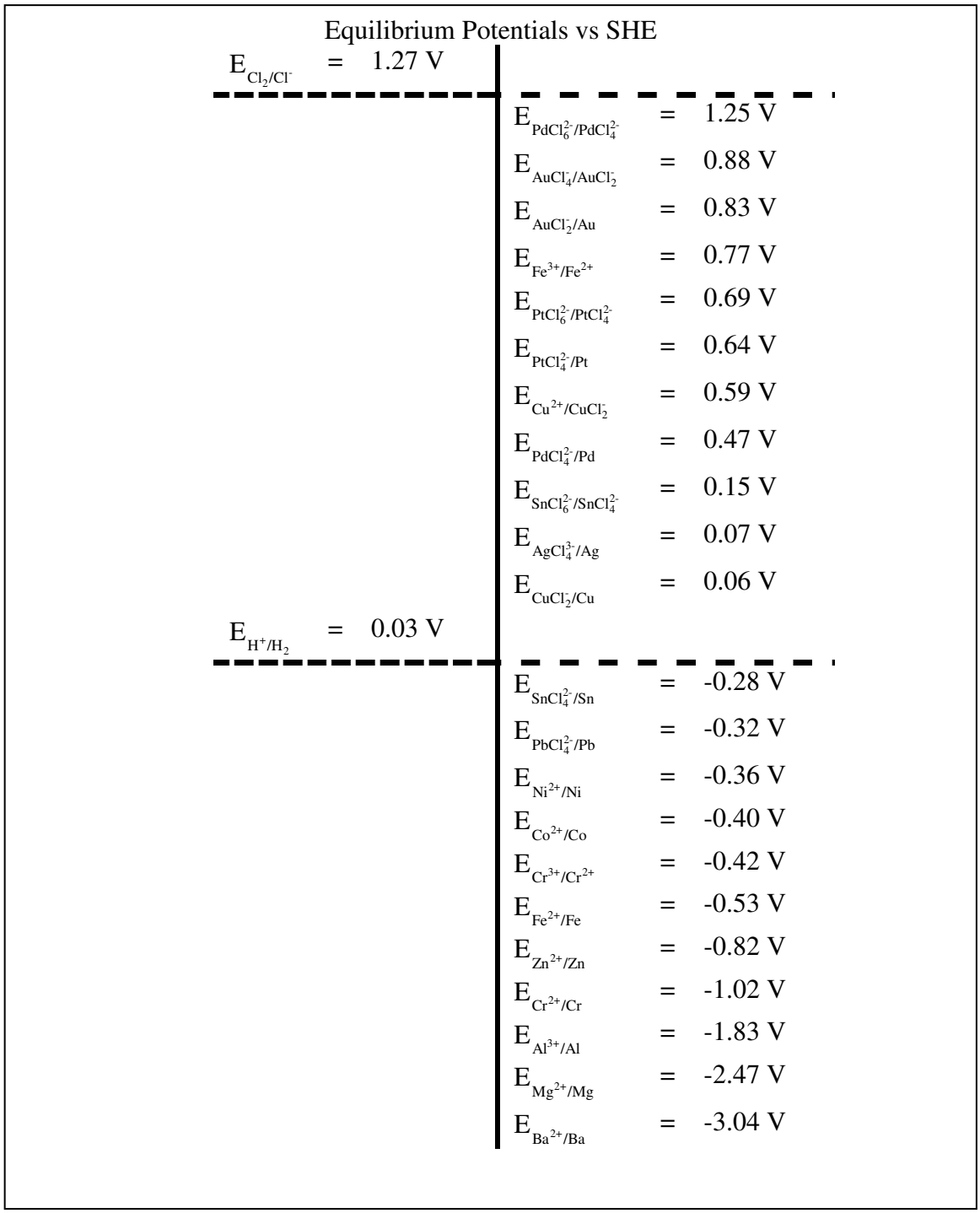

Figure 3-13. Equilibrium potential of metals (vs. SHE) in 4 kmol m^{-3} HCl + 1 kmol m^{-3} NaCl leach solution at pH 0 [50].

For galvanostatic control, the total current was fixed at 9 A and the potential range was from -0.50 V to -0.85 V (SCE). The feasibility of using graphite-felt cathodes has been established experimentally and theoretically for simultaneous deposition of the range of metals in the leach solutions.

It was reported that the recovery of considerable amounts of Sn and Pb was possible after the copper had been eliminated. The deposition of Cu, Sn and Pb under both galvanostatic and potentiostatic control are compared in Figure 3-14 and Figure 3-15. Operating under constant current allows semi-selective deposition of the metals on the cathode. As can be seen from the figures, the main drawback of the galvanostatic method is that the metals deposit at lower potentials and hence a lower current efficiency results. For metals with multiple oxidation states, initially partial reduction of the metals occurs if $E > E_{M^{z+}/M}$. Potentiostatic control allows the choice between selective or non-selective deposition, although setting the potential at a value (E = -0.70 V (SCE)) that would allow deposition of most metals would result in a considerable amount of hydrogen evolution at the cathode, which would again decrease the current efficiency. From the results obtained, it was thought that semi-selective electrowinning at a variety of potentials (e.g. E_1 = -0.50 V (SCE), E_2 = -0.70 V (SCE)) is the most efficient method of metal recovery [52].

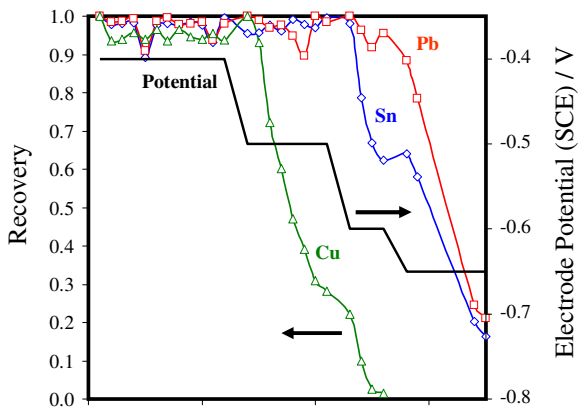

Figure 3-14. Metal recovery of Cu, Sn and Pb during potentiostatic electrowinning with carbon felt reactor [52].

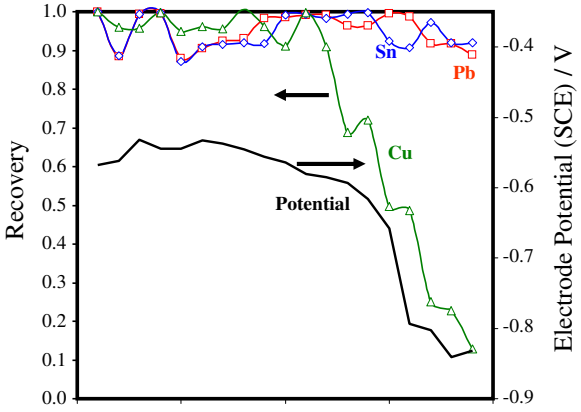

Figure 3-15. Metal recovery of Cu, Sn and Pb during galvanostatic electrowinning with carbon felt reactor [52].

It was also acknowledged that the largest loss of efficiency during electrodeposition from aqueous solutions was hydrogen evolution. As can been seen from Figure 3-16, the current density for hydrogen evolution varies over many orders of magnitude for different metals. This is because the hydrogen bonds should not be too weak such that the hydrogen is unstable on the surface nor too strong leaving few sites available for H + H recombination. Metals such as Pt, Fe, Ni are good catalysts for hydrogen evolution, but other metals like Pb inhibit the reaction [53].

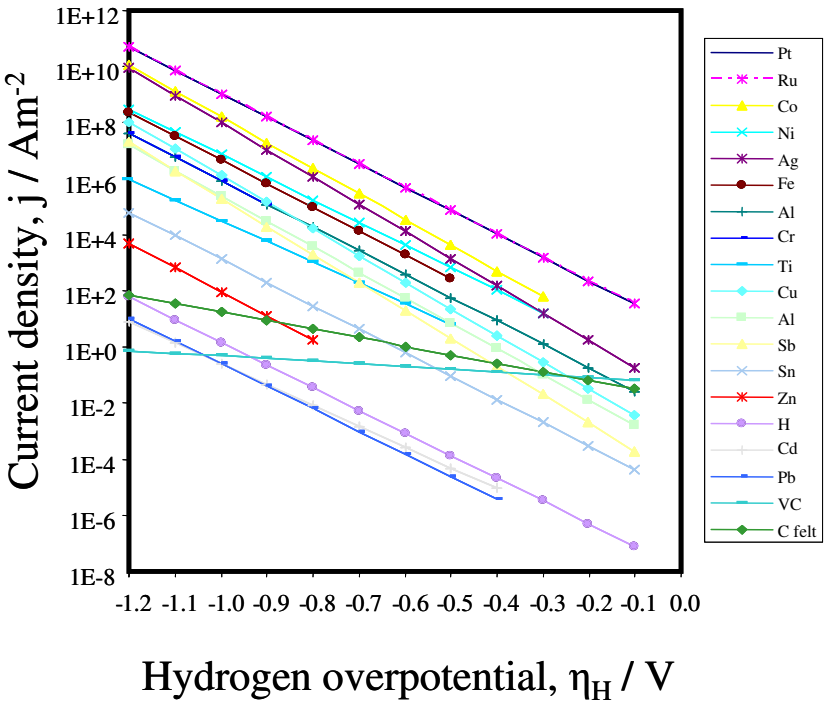

Figure 3-16. Predicted kinetics of hydrogen evolution on metals in 1 kmol m^{-3} H_2SO_4 [53].

The initial work at Imperial College to dissolve shredded WEEE in an external leach reactor and subsequently recover the dissolved metals at a graphite felt cathode was quite promising and has provided some useful observations for the improvement of the cathode selection and the understanding of the process chemistry. In addition, potentiostatic control allows the choice between selective or non-selective deposition, although setting the potential at a value (E = -0.70 V (SCE)), that would allow deposition of most metals, would result in a considerable amount of hydrogen evolution at the cathode which would again decrease the charge yield.

The following section reviewed the specific work on electrodeposition on certain metals which are dissolved in aqueous chloride solutions.

3.6.1. Gold Electrodeposition

A number of papers [55-59], including a more recent one [60], has been written on the electrodeposition of gold and particularly from chloride complexes. However, in each case, it is from a solution at different concentration several orders of magnitude greater than would be expected from a gold concentration in WEEE leachate which was around 0.05 mol m^{-3}(refer Table 3-4). Nicol et al. [56] have studied gold deposition in acidic chloride media and found gold deposition to be transport controlled and the limiting current proportional to the Au^{III}

concentration. Nonetheless, they were able to detect Au^{I} intermediates by oxidation at a Pt ring electrode.

Harrison and Thomson [57] also studied gold deposition from chloride electrolytes using a rotating disc electrode but unfortunately neglected the presence of Au^{I} species. Diaz et al.[59] studied the effects of Au^{I}: Au^{III} molar ratio, pH and Cl^- concentration on the voltammetric behaviour of a Pt electrode to enable the kinetics and mechanism of gold dissolution and deposition to be determined. Most of the thermodynamic data used in this paper was pre-determined by Kelsall et al. [61]. According to their investigations, at + 0.80 V (SCE), Au dissolved exclusively as $AuCl_2^-$ ions, the proportion of $AuCl_4^-$ ions increasing at higher potentials. On the other hand, a steady state kinetic model of the coupled electrochemical and chemical reactions resulting in gold dissolution as $AuCl_n^-$ ions, was shown to be capable of predicting the experimentally determined reaction order (≈ 1.7) with respect to chloride ion concentration and the Tafel slope (≈ 80 mV $decade^{-1}$ at pH 0).

Gold deposition is reported to be transport controlled and the limiting current is proportional to Au^{III} concentration. Diaz et al. [59] investigation on the kinetics of the Au-Cl-H_2O system showed that in certain potential ranges, the $AuCl_4^-$ ion could be reduced by the following reaction:

$$AuCl_4^- + 2e^- \rightleftarrows AuCl_2^- + 2Cl^- \qquad [3\text{-}1]$$

And although there is expected to be only a small quantity of the $AuCl_2^-$ present, this can be reduced to elemental gold by reaction:

$$AuCl_2^- + e^- \rightleftharpoons Au + 2Cl^- \qquad [3\text{-}2]$$

Removing gold from chloride solution specifically produced from WEEE was further investigated by Cheng et al. [60] using a packed bed cathode operated in batch recycle mode with a stirred tank reservoir. The packed bed cathode of 2-3 mm graphite particles was able to deplete ($[AuCl_4^-]$ + $[AuCl_2^-]$) in 1 kmol m^{-3} aqueous HCl from 0.5 mol m^{-3} (10^2 g m^{-3}) to $< 5\times10^{-3}$ mol m^{-3} (< 1 g m^{-3}), essentially under mass transport control, with current efficiencies of < 4 F $(mol\ Au)^{-1}$ and specific electrical energy consumptions of ca. 400 kW h $(tonne\ Au)^{-1}$. The investigation established that as the ($[AuCl_4^-]$ + $[AuCl_2^-]$) concentration decayed, the $[AuCl_2^-]$: $[AuCl_4^-]$ molar ratio decayed from an initial value of ca. 0.3 to < 0.05 over the first ca. 500 s which then increased passing through a maximum after 500 – 1500 s depending on the flow rate. In addition, a multi-step mechanism for reduction of

$AuCl_4^-$ ions involving adsorbed Au^{II} and Au^{I} species was proposed to explain this behaviour in terms of changing overpotentials for $AuCl_4^-$ and $AuCl_2^-$ reduction as the total dissolved gold concentration decreased and changing $[AuCl_2^-]$: $[AuCl_4^-]$ molar ratios. The developed reduction mechanisms model is more complex than the basic electrode reactions used for the Butler-Volmer equation proposed by Nicol [56] and Harrison and Thomson [57].

Most of the literature on electrodeposition of Au in aqueous chloride solutions involved lab-scale rotating disc electrode, except for the investigation done by utilizing packed bed electrochemical reactor which will be reviewed in section 3.7.

3.6.2. Copper Electrodeposition

Much has been written on the voltammetric studies on copper deposition/dissolution reactions in aqueous chloride solutions particularly from chloride complexes [65-68]. However, in each case, solutions with varying chloride concentration as well as different electrochemical reactors were utilised. Most investigations were performed in a glass cell. To summarise, although different processes have been proposed for the copper electrodeposition from chloride solutions, the following general deposition mechanism has been widely accepted in recent years; a two-step, single electron transfer is the most likely path for Cu ions as found by multiple authors [65,75,76,77] in the literature. And of all possible reaction paths for a two-step reaction of Cu^{2+} complex to Cu the following path is the most likely [75]:

$$Cu^{2+} + Cl^- + e^- \rightleftharpoons CuCl_{ads} \qquad [3\text{-}3]$$

$$CuCl_{ads} + e^- \rightleftharpoons Cu(s) + Cl^- \qquad [3\text{-}4]$$

Where the adsorbed copper chloride complex can react with adsorbed chloride ions to the dissolved $CuCl_2^-$ complex:

$$CuCl_{ads} + Cl^- \rightleftharpoons CuCl_2^- \qquad [3\text{-}5]$$

A single rate-determining step, which is the cupric-cuprous transition, for the whole two-step process was reported based on numerous publications [76,77] on copper deposition in chloride media. In addition, voltammetry experiments show two reduction waves corresponding to the two reduction steps [70]. However, in the recent papers by Powell et al.[79] which discussed Cu-Cl-H_2O highlighted different predominant species of Cu^{II} in aqueous chloride; this will be discussed further in the Results and Discussion chapter

(Chapter 6).

The main source for Tafel slopes and exchange current density (j_0) of copper deposition related to this project was investigated by Winter et al. [78], who measured Tafel slopes for the separate reactions of Cu in 4 kmol m^{-3} NaCl + 1 kmol m^{-3} NaCl. For the reduction of Cu^{II} to Cu^{I}, a value of 125 mV dec^{-1} and j_0 = 7.94 A m^{-2} was found on a glassy carbon cathode. This value is equal to the Tafel slope found for the overall reaction. For the subsequent reaction in which Cu^{I} becomes solid Cu, the authors found a Tafel slope of 40 mV dec^{-1} and j_0 =5.01 A m^{-2} on fresh deposited copper.

As per the discussion in section 3.7, a series of reports by Brandon et al. [71] on multi- metal electrodeposition at the graphite felt electrochemical reactor including copper which was predominant in the WEEE leachate have been successfully demonstrated .It was reported that selectivity can be achieved, if required, by electrode potential control.

Parthasarady [80], reported that in the absence of complicating factors like complexation, mixed cations behave individually, i.e. their electrodeposition potentials do not change. He noted that those which have close deposition potentials may interfere with each other, i.e. the selectivity is affected. Hence, copper purity is the main issue in the multi-metal contained WEEE leachate as it needs to achieve the 99.99% purity of commercial grade copper.

The electrodeposition of copper from concentrations containing Fe^{II} or Fe^{III} in sulphate media was investigated by Dew and Phillips in two papers [81,82] who used a Chemelec cell, a commercially available fluidized bed of glass beads with titanium based mesh electrodes. The reduction of Fe^{III} to Fe^{II} at the cathode had very negative effects on the charge efficiency of copper electrowining. However, co-deposition of Cu-Fe was not reported.

Referring to the equilibrium potential of metals (vs SHE) in 4 kmol m^{-3} HCl + 1 kmol m^{-3} NaCl leach solution at pH 0 (Figure 3-13),iron and silver might disrupt the copper deposition efficiency at some stage due to the close electrodeposition potential. However, as aluminium and iron concentrations were pre-removed using eddy current and magnetic separations, the current efficiency problem was partially eliminated. The low concentration of silver which exist in the WEEE leachate is discussed in detail in Chapter 6.

3.6.3. Selective Recovery of Tin by Electrodeposition from Tin-Lead Solutions

None of selective deposition of tin and lead in chloride acidic solution had been found so far For one thing, it is not easily achieved, and sometimes it is the co-deposition that is desired. However, certain selectivity may be achieved possibly by electrode potential control which was not a practice in industrial electrochemical waste recovery. Therefore, the review focuses on single metal kinetics and the recovery utilising electrochemical reactors.

The reduction of tin-chloride complexes has a multifaceted reaction route. A two wave reduction route from Sn^{IV} to Sn^{II} to Sn metal is most likely in electrolytes composed with strong acidic aqueous solutions. Two reduction current waves are detected [95,96] in voltammetry experiments, the reduction of Sn^{IV} in solutions of 1 kmol m^{-3} HCl [95] and 4 kmol m^{-3} NH_4Cl [96] concentration. First, the Sn^{IV} reduces to Sn^{II} according to:

$$SnCl_6^{2-} + 2e^- \rightleftharpoons SnCl_4^{2-} + 2Cl^- \qquad [3\text{-}6]$$

It is believed that reaction [3-6] is kinetically controlled and is irreversible in a strong hydrochloric acid solution [97]. In a second wave the $SnCl_4^{2-}$ reduces to elemental tin:

$$SnCl_4^{2-} + 2e^- \rightleftharpoons Sn + 4Cl^- \qquad [3\text{-}7]$$

The reduction of Sn^{II} to Sn is a fast reaction in most electrolytes. Most publications on tin electrochemistry report the behaviour of the Sn^{4+}/Sn^{2+} and Sn^{2+}/Sn couples separately. Hence, sources of the values of kinetic parameters were different [98]. Monien [99] investigated Sn electrodeposition from 1 kmol m^{-3} HCl and 3 kmol m^{-3} NH_4Cl solutions at a planar mercury electrode, but did not suggest two consecutive reaction steps for the reduction of Sn^{IV} to Sn^{II}. They reported that the overall reduction reaction was irreversible and complicated by chemical complex reactions before the electrode reaction.

The Tafel slope for Sn^{II}-chloride to Sn^{IV}-chloride was found to be 137 mV dec^{-1} by Lerner et al. [99] on a carbon electrode. For the reduction of Sn^{II}-chloride to solid tin, Galus et al. [96] reported a cathodic Tafel slope value of 54 mV dec^{-1} which was close to the value recorded by Stirrup et al. [97] which was 64 ± 5 mV dec^{-1}. Monien [99] and Lerner et al. [100] presented experimental values of the exchange current density for the Sn^{IV} to Sn^{II} oxidation. Since the latter authors measured the exchange current density in a 4 kmol m^{-3} HCl solution at a pyrolytic carbon electrode, which is similar to the condition described in this project, these values will be the main references for further comparison. Monien [99] reported that the higher the chloride concentration, the higher the exchange current for Sn^{IV} reduction. While

the oxidation of Sn^{II} in 4 kmol m^{-3} HCl gives a limiting current, the reduction of Sn^{IV} shows only a single wave, not completely separated from hydrogen reduction [101].

Few publications have been found on the electrolytic recovery of tin from dilute solutions. García-Gabaldón et al. [102] investigated the potentiostatic recovery of tin using an electrochemical reactor with two compartments separated by a ceramic diaphragm, reporting that the charge yield was approximately 1 within the potential range of -0.60 V to -0.80 V (SCE). The major interfering reaction during tin deposition on the cathode surface was hydrogen evolution which was reported to occur at ca. < - 0.65 V (SCE), below which both space-time yield and specific electrical energy consumption (SEEC) increased. Hence, the choice of the applied electrode potential depended on a compromise between initial investment costs and energy costs.

The same authors [103] reported results for a similar electrochemical reactor to electrodeposit Sn galvanostatically from activating solutions of the electroless plating of polymers. Based on their previous results of differential pulse polarographic measurements [103] on the same waste solution, most tin occurred in the form of Sn^{IV} rather than of Sn^{II}. Hence, 10^{-2} kmol m^{-3} Sn^{IV} in 1 kmol m^{-3} HCl was prepared and used in this study. Hydrogen evolution occurred at applied current densities of below 303 Am^{-2}, However, the mass transfer coefficient (k_m) was enhanced due to the turbulence contributed by H_2 bubbles. The charge yield was 0.83 and SEEC of 3530 kW h $tonne^{-1}$ of tin deposited. At higher current densities than ca. 380 Am^{-2}, the rate of hydrogen evolution became excessive, decreasing the charge yield to 0.55 and increasing the SEEC to ca. 5960 kWh $(tonne\ Sn)^{-1}$.

According to Ponce and Pletcher [105], electrodeposition of Pb in chloride is expected to have an intermediate state of $PbCl_2$(ads) which was believed to be dissolve back from the cathode to $PbCl_3^-$. Hence, the following equation of cathodic reduction of the dominant lead-chloro complex in solution [105]:

$$PbCl_3^- \rightleftharpoons PbCl_2(ads) + Cl^- \qquad [3\text{-}8]$$

$$PbCl_2(ads) + 2e^- \rightleftharpoons Pb(s) + 2Cl^- \qquad [3\text{-}9]$$

Ponce and Pletcher [105] also carried out a voltammetry experiment of 7 ppm Pb^{II} in 0.5 kmol m^{-3} NaCl at pH 2 which demonstrated a one wave deposition for Pb^{II} on reticulated vitreous carbon cathode for which the $E_{O/R}$ was reported at -0.64 V (SCE) and the reverse scan was determined as electrodissolution of $PbCl_2$ (ads). To date, only Tafel slopes and j_0 for 8.5 x 10^{-}

^{4} kmol m^{-3} Pb^{II} in 10^{-1} kmol m^{-3} $HClO_4$ solutions [106] were found from the scarce literature of Pb rotating disc electrode (RDE) deposition in chloride media. The Tafel slope and j_0 were reported as 30 mV dec^{-1} and 0.7 Am^{-2} respectively [106].

3.6.4. Fate of other metals not recovered at pH 0

While low or zero charge yields would be expected Ni^{II}, Zn^{II} and $Fe^{III/II}$ in 4 kmol m^{-3} HCl and 1 kmol m^{-3} NaCl, based on the equilibrium potentials in Figure 3-13, charge yields would be expected to increase at pHs > 0. For other metals such as Al^{III} dissolved in the WEEE leachate, their reduction is impossible in aqueous media. Hence, the fate of these metals and possible recovery routes are discussed below.

3.6.5. Metal Precipitation

Precipitation of metals is the most widely used and studied method for metal removal. This is evident in industrial wastewaters, most usually with lime forming metal hydroxides, which is an inexpensive process, but with little selectivity for individual metals. The pH dependence of the solubilities of Ni^{II}, Fe^{III}, Zn^{II} and Al^{III} hydroxides are predicted in Chapter 8. Precipitation of '$Al(OH)_3$' is possible at pH 5-9 and the particles recovered by e.g. filtration.

3.6.6. Electro-co-deposition

Selective deposition is not easily achieved and sometimes co-deposition is desired. The electrodeposition of binary alloys is a process of great practical importance. One aspect of particular interest is anomalous co-deposition, in which the alloy is found to be much richer in the less-noble component than would be expected on the basis of single-metal deposition rates. Many attempts to explain this phenomenon via mathematical models have been made, but there is still no consensus. Nowadays, many new industrially important alloys are produced via co-deposition, e.g. magnetic Ni-Fe [83] and the corrosion resistant Ni-Zn alloy [84]. In producing Ni-Fe alloys, sufficiently negative electrode potentials cause Ni^{II} and Fe^{II} co-reduction.

The earliest investigation on the electrodeposition of zinc-nickel alloy coatings from a chloride bath containing NH_4Cl using different plating solutions was reported by Fratesi and Roventi [86]. They showed the strong influence of parameters of current density, temperature and nickel percentage in the baths on the composition of the deposits and the morphology. At low current densities, transition from anomalous to normal co-deposition occurs. When the nickel percentage of the deposit becomes higher than that present in the bath, current

efficiencies for alloy deposition decreases and the potential shifts towards less negative values. Anomalous co-deposition of zinc-nickel alloys was found to be attributed to the intrinsically slow nickel(II) reduction kinetics. Normal co-deposition with very low current efficiency occurred at potentials close to the free corrosion potential of zinc and zinc-nickel alloys. This suggests that the occurrence of normal co-deposition probably occurred at insufficiently negative potentials to ensure zinc(II) reduction, causing partial dissolution of the metal already deposited [85].

In the Ni- Zn system, the presence of zinc will shift the potential of nickel to more negative values , and both metals tend to discharge together [87] with zinc being more copious than the solution Zn^{II} : Ni^{II} molar ratio in solutions. The latter phenomenon is commonly known as anomalous deposition. This does not only present complication for selective electrodeposition where required, but also complicates the Ni-Zn alloy deposition control [88]. It is commonly agreed that the decreased nickel content is due to the slow kinetics of nickel deposition relative to that of Zn [84]. Hence, at the potentials at which zinc can deposit ($E^{\theta}_{Zn^{2+}/Zn}\ (\mathrm{SHE}) = -0.82\ \mathrm{V}$) (Figure 3-13), with its less negative electrode potential ($E^{\theta}_{Ni^{2+}/Ni}\ (\mathrm{SHE}) = -0.36\ \mathrm{V}$) (Figure 3-13), the driving force for Ni deposition is far greater than that for Zn deposition. However, as surveyed by Swathirajan [91], the retardation of nickel discharge was reported due to zinc hydroxide/oxide formation.

Mathias and Chapman [88] studied the composition of electrodeposited zinc-nickel alloy films deposited on a rotating disc electrode and developed a one-dimensional transport-reaction model, including the effect of migration and complexation of zinc by chloride, for an un-divided electrochemical cell. It was found that migrational transport can enhance the interfacial concentrations of nickel(II) to values exceeding that in the bulk solution. A simple electrode kinetics model was postulated to describe the partial current density of each metal reduction reaction in terms of electrode potential, interfacial concentrations, and temperature. Kinetics parameters appearing in the model were estimated from experimental deposit composition data. The resulting model was able to predict alloy composition over a range of plating conditions, but electrode polarization was not accurately predicted [88]. A more complete kinetic model, describing zinc-nickel interactions, is still needed.

In another paper, Mathias and Chapman [90] reported the effect of zinc-nickel alloy electrodeposition kinetics model from thickness and composition measurements on the rotating disc electrode. They also investigated the effects of radial variations of the

compositions as well as the thickness of electrodeposited zinc-nickel alloys on the rotating disc electrode for deposits obtained from steady state chloride electrolytes at different bath compositions, electrode rotation rates, and applied voltages. Nickel was predicted not to complex significantly [90], contrary to speciation calculations for Ni^{II} in chloride aqueous solutions as reported by Ji and Cooper [92]. In addition, they reported that anomalous deposition can be attributed simply to the zinc exchange current density being five orders of magnitude higher than that of nickel and, at practical total current densities, the kinetically facile zinc deposits much more rapidly than the sluggish nickel. The effect of changing the pH from 1.6 to 3.6 was found to be small [90].

Overall, the review of thermodynamics, (micro-) kinetics, reduction mechanisms model from various metals contained in WEEE have provided some useful observations for the improvement of each metal recovery. Appropriate designs of electrochemical reactors for metal recovery are reviewed below.

3.7. Electrochemical Reactor Design

Ideally, a reactor for industrial deployment should be designed to deplete the dissolved metal in the effluent to the target concentration for discharge to sewer and such that it could be operated continuously. Scott [108] and Walsh [109] have written excellent reviews on some of the specifications of reactor design, which ensure energy efficient reactor operation including:

(a) High charge yield

(b) High mass transport rates (k_m)

(c) High current density

(d) Low potential drop (φ), over electrodes and membranes

(e) High surface area (A) electrodes per unit reactor volume

(f) Uniform potential distribution

(g) Acceptable operating cost, lifetime and practicality

Janssen and Koene in their review paper [110] explained that the main parameters for an electrolysis reaction in the removal of impurities were the current density, charge and space-time yield. However, for dilute solutions the effectiveness of the reactor was strongly determined by the mass transfer of the reacting species, the effective surface area of the

electrode and the occurrence of side reactions.

As reported in Chapter 2, the above criteria are inter-related and increment or decrement of each parameter would affect the others. It is apparent that a high charge yield is desirable in any reactor operation, not only to minimize the energy requirement, but also to diminish the problems related to secondary reactions such as precipitation and gas evolution [108-109]. According to Juttner et al. [111], improved mass transport can be achieved by setting the electrodes in motion or by applying turbulence promoters. Increased mass transport rates enables increased current densities for transport controlled conditions. However, as the current density increases, the cell voltage increases and therefore corresponding so do the operating costs. As reported by Scott [108], to suppress this effect, the inter-electrode gap can be decreased and conductive electrodes should be used. Examples are the pump cell [113,114], the Chemelec cell [115-117], the rotating cylinder electrode (RCE) cell [119,121], the beat rod cell [122], and cells with vibrating electrodes or electrolytes [123].

Attempts to accommodate large electrode area in a small cell volume resulted in developments such as the multiple cathode cell [124], the Swiss roll [125-126], or the extended surface electrolysis (ESE) cells [127]. Improved mass transfer coefficients and enlarged specific electrode area are provided by the use of three-dimensional electrodes. Examples are the porous flow-through cell, the packed-bed cell, the fluidized bed cell, and the rolling tube cell.

Generally, electrodes can be categorized into two groups: two-dimensional (2-D) static and moving, and three-dimensional (3-D) static and moving. Generally, reactors with 2-D electrodes are favorable electrode configuration, due to their ability to treat effluents with high reactant concentrations ca $\geq$ 10 mol m^{-3}, which is common industrially [108,112,129]. However, 3-D electrodes offer higher specific surface areas compared to 2-D electrodes and the feasibility of their treating diluted effluent is well established [108,109].

Due to the sheer volume of reactor designs, the literature review presented here will focus on selected designs of reactors available in the Electrochemical Engineering Group, of Imperial College London that are suitable for depleting ca 500 mol m^{-3} of copper, the predominant species in the WEEE leachate, to analytically undetectable concentrations.

3.7.1. Electrochemical Reactor with 2-D electrodes

The simplest electrode 2-D shapes and favorably used industrially are plates and cylinders [128]. For the parallel plate electrode reactor configuration, this is due to the easy operational set-up, relatively low production costs, feasible for continuous operation and simple to maintain [109,118]. Generally, stationary parallel plate electrodes are used in flow-by reactors in which electrolyte is pumped between the plates such that the solution flow is perpendicular to the current, which is believed to minimize the ohmic losses within the reactor [111].

Due to growing demands in economy and maintenance of industrial metal recovery processes, electrode materials of various special shapes have also been introduced into industrial practice to an increasing degree. For example, the perforated plate, extended metal, slitted, grooved, louvered, or other regularly deformed electrode surfaces do not really increase the geometric surface of the electrode, however intended for different purposes depending on the needs and requirement of the process [128].

The specific surface area of plates is considerably low compared to a 3-D electrode, however mass transport rates may be enhanced by using a variety of turbulence promoters such as inert particles, electrolyte distributors or adjusting solution pumping rates. As in a Chemelec cell [115,116], turbulence in the electrolyte can be promoted using inert fluidised particles [130-132] to enhance mass transfer and modify the electrodeposit at immersed conventional plate [131] or mesh electrodes [133]. Expanded mesh cathodes were used to ensure there was a flow of fluidised beads around and through the cathodes as shown Figure 3-17. It was envisaged that the fluidised bed in a membrane divided reactor with a mesh cathode enabled a six-fold increase in mass transport rates [133] and subsequently produced an adherent and coherent tin deposit with a charge yield of >0.9, cell voltages of 2-3 V and specific electrical energy requirement of 1000-1500 kWh (tonne Sn^{-1}), depending on the current density during batch depletion in the fluidised bed electrolyte [133].

Chaudary et al. [134] investigated the performance of fluidised bed cell of inert glass beads to recover tin from dilute solution (concentration range 0.25-1.00 g dm^{-3}). The results show that the combination of high mass transport conditions and a moderately high electrode surface area per unit electrode volume provides a system for continuous removal of metal from dilute solutions; tin was depleted to 0.001 g dm^{-3} with charge yield of 0.88.

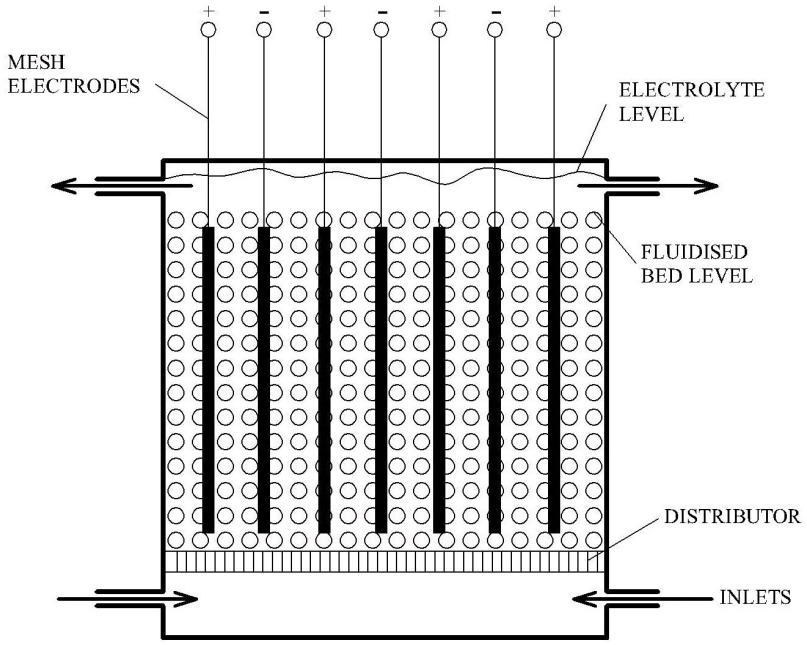

Figure 3-17. Undivided Chemelec cell consisting mesh electrodes and fluidised inert particles [111].

On the other hand, the application of rotating cylinder electrodes (RCEs) for metal electrodeposition has progressed significantly over the last few decades [111,119,121]. Low et al. [121], in their review paper reported that new tools for experimental and theoretical study have been developed and improved throughout the years. As explained by Koene and Janssen [129] and Chen [135], the RCE utilizes a rotating inner cylinder electrode as cathode and stationary concentric outer cylinder as the counter electrode. The reactor has a well defined hydrodynamics which features establishing turbulent flow at low rotation speed resulted in a higher mass transport rate [121]. Furthermore, mass transport can be enhanced through roughened surfaces [136], jet electrolyte flow [137] and expanded mesh [121]. In addition, the potential and current distributions can be uniform or non-uniform depending on the position and geometry of the working and counter electrodes [121]. Scraping devices (e.g. scraper blade) can be included in the design to remove the deposited metal, hence the process can be operated continuously [129]. Figure 3-18 shows a schematic of a RCE.

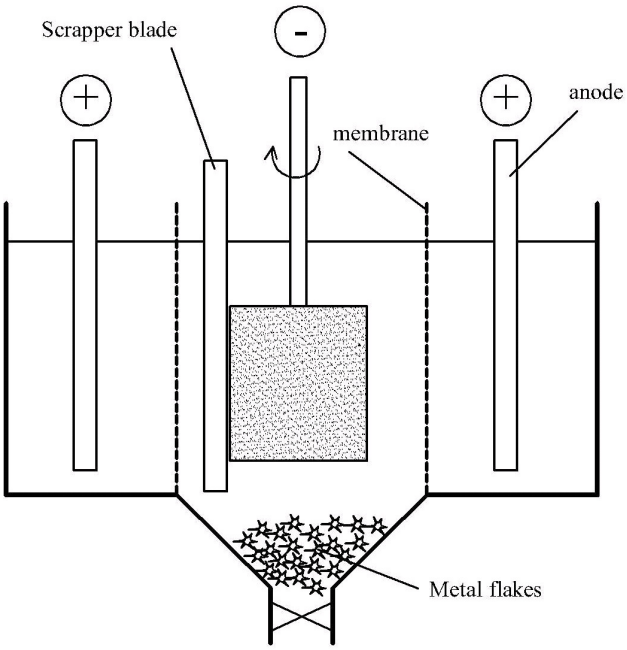

Figure 3-18. Rotating cylinder electrode (RCE) [135].

With the new development of RCE, it was found that this system can reduce a variety of metal content in effluent such as copper [138,139], silver [140], cadmium [141] and tin [142] with a high current density and charge yield. Nonetheless, as discussed in several papers, RCE design suffers some limitations. In fact, Walsh [109] has summarized a long list of possible fault conditions as experienced in industrial RCE reactors specifically for photographic silver removal over a period of 20 years which resulted in fractional conversion per pass in a single reactor much less than 0.6 under industrial conditions. A few set-back of RCE configurations are the continuous removal of deposit from the cylinder leaves particles in the solution and resulted re-dissolution of metal, hydroxide formation can occur for some metal ions e.g Ni and diameter of the cylinder is limited especially for a divided concentric reactor [144].

Compared to RCEs, the scale-up of a parallel plate reactor is easier to achieve by increasing the electrode size or by forming electrode arrays, without affecting reactor performance. This is advantageous when the reactor is initially designed on a laboratory scale but then has to be transferred to a pilot plant scale. However, due to their low specific surface area, plate electrodes cannot be used to fully purify low metal content such as gold and palladium in the WEEE leachate since it is not feasible to increase mass transport rates to the order of magnitude required to deplete the reactant concentration below 1 mol m^{-3}. Moreover, parallel

plate reactors do not easily allow for continual harvesting of deposit compared to a 3-D electrode as described in the following section.

3.7.2. Electrochemical Reactor with 3-D electrodes

A reactor with a 3-D electrode structure is required to deplete WEEE leachates with metal ion concentrations < 1 mol m^{-3} down to analytically undetectable limits. A high surface area cathode can be achieved in a variety of ways, due to the numerous references on the 3-D electrodes; only 3 types of such electrodes will be reviewed for comparison reasons, which are:

(a) Highly porous electrodes i.e. graphite felt

(b) Spouted bed electrode

(c) Fluidized particulate bed electrode

3.7.2.1 Highly porous electrodes

Porous electrodes have the advantage of a high specific surface area, allowing them to operate at low current densities at the electrode-electrolyte interface, but at relatively high currents per unit volume of reactor [111]. Gonzalez-Garcia et al. [149] reported that the specific surface area of a carbon felt (Le Carbone Lorraine, RVC 4002) was found to be 22100-22700 m^2 / m^3 with a porosity ca. 0.98 and a fairly low (2.7×10^{-3} Ω m) electrical resistivity. This is highly desirable for metal electrowinning in order to achieve the very low metal concentrations of industrial emissions, as required by legislation, e.g. < 1 ppm limits for most metals discharge to sewer. Considerable experimental work has demonstrated the effectiveness of graphite felt, for recovering a wide range of heavy metal from dilute solutions [145-148].

A membrane (Nafion)–divided reactor with graphite felt electrode was used to remove copper from dilute cyanide solution by direct electrowinning by Lu et al.[147]. Based on the experimental results, 40 % recovery of copper was achievable from a solution of 1 - 2 g dm^{-3} Cu, with a current efficiency of 50 – 80 %. Ragnini et al. [150] demonstrated that lead in aqueous solution being depleted to a concentration of 0.5 mg dm^{-3} and a 99 % charge yield of lead from aqueous solution could be achieved with residence times ranging from 94 – 150 min, using a highly porous felt electrode in a flow-through cell. In addition, Tricoli et al. [148] reported recovery of silver from diluted silver chloride aqueous solutions in a flow-through reactor with graphite felt cathode and attributed the successful process to the usage of high surface area materials.

Based on the previous work at Imperial College London which utilized the readily available electrochemical reactors (Figure 3-19), the feasibility of using graphite-felt cathodes has been established experimentally and theoretically for simultaneous deposition of the range of metals in the leach solutions [13,146]. In addition, a degree of selective deposition from multi-metal solutions was also demonstrated [146]. Nonetheless, it was reported that the reactor configurations using graphite felt electrode suffer from several limitations [154]:

(a) Require mechanical support and feeder electrodes,

(b) Are difficult to remove from a reactor to harvest the powdery alloy product,

(c) Have low loadings prior to dendrite growth beyond the felt,

(d) Suffer increasing pressure drop across the felt with time, and

(e) Rapid loss of surface area due to clogging.

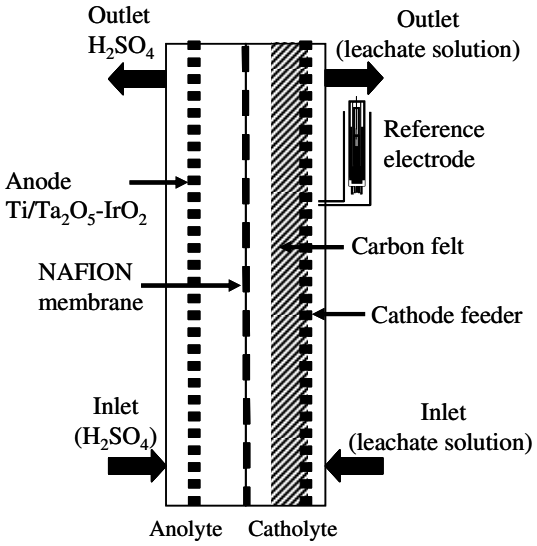

Figure 3-19. Schematic of graphite felt electrochemical reactor.

3.7.2.2 Spouted bed electrode

An alternative 3-D reactor design incorporates a spouted particulate bed cathode that had been used previously at Imperial College London for palladium and platinum recovery from spent catalyst leach solutions [154]. Scott [151-152] who first patented the design of spouted bed electrode listed several advantages of particulate cathode in the form of a spouted bed which are:

(a) High specific surface area

(b) High mass transport rates

(c) Good electrical conductivity through the bed

(d) Particles in constant motion

Many papers [151-156] have been published on spouted bed electrochemical reactors. Dawson [154] made a comprehensive review on patents and papers relating to spouted bed for electrodeposition of heavy metals from effluent. The basic operation of a spouted electrode is as follows [154]:

(i) The flow of electrolyte in the cathode compartment enters the base as a jet.

(ii) This jet entrains particles up the rectangular draft tube in the centre.

(iii) At the top of the tube, the flow of particles hit a deflector which subsequently falls down on the descending beds of particles either side.

(iv) The descending sections have a similar voidage to packed beds on their way down to the base of the draft tube where they repeat the process again.

Figure 3-20 shows schematically a common design of spouted bed electrode.

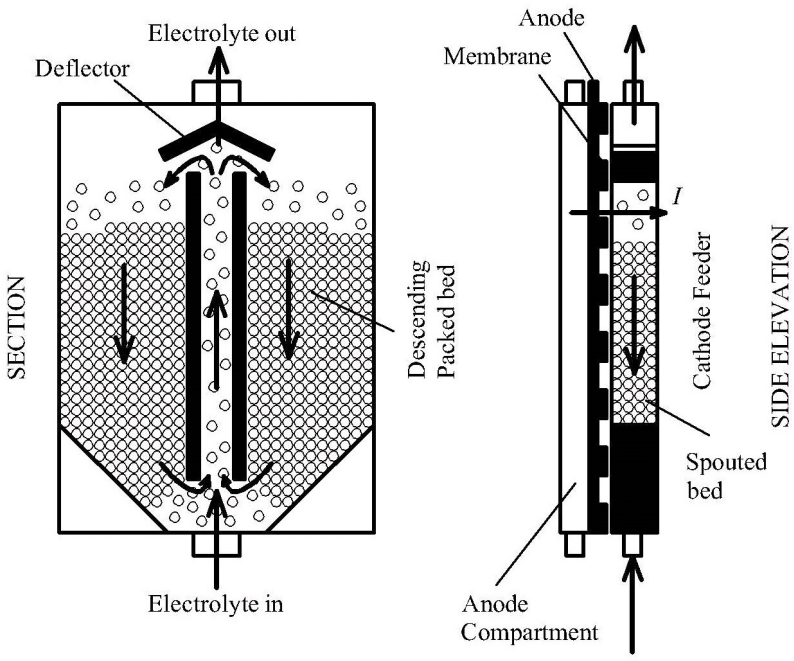

Figure 3-20. Schematic of typical spouted bed electrode [154].

It was reported that good electrical conductivity is achieved through the bed with nearly all particles in electrical contact with the feeder all the time (except for the brief period when they are being levitated up the draft tube) [154]. However, particle contact resistance can affect electrode conductivity. As tested in the lab for recovery of Pt and Pd from iodide solutions, Dawson discovered some disadvantages to the design which are listed below [154]:

(a) Instability between the two sides with bed heights and descending velocity changing constantly on each side.

(b) Dead areas where particles appear stationary around inlet nozzle and against interface between triangular inserts and membrane (also at feeder probably) which leads to particle bridging.

(c) Slow descending velocities in bed (partly due to small density difference between electrolyte and carbon), which can lead to bridging but reduces the uniformity of plating since particles do not change places with each other with enough frequency.

(d) Flow up the draft tube was inefficient with particles seen to be descending towards the extremes of the tube.

To address these problems, a single sided spouted bed type electrochemical reactor was developed incorporating a circulating particulate bed cathode.

3.7.3. Circulating particulate bed electrode

As an alternative reactor design, the behavior of a single sided circulating particulate bed cathode reactor was investigated by several researchers at Imperial College London [154,157] as shown in Figure 3-21.

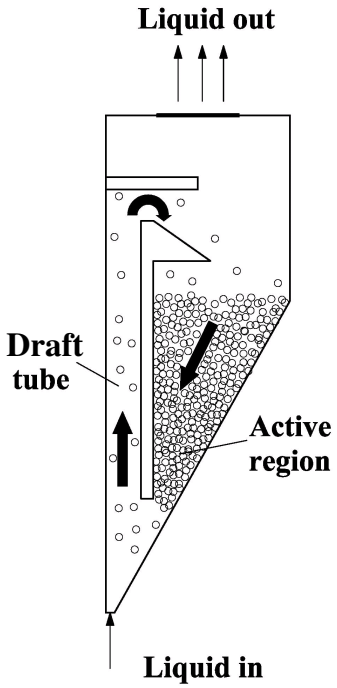

Figure 3-21. Schematic diagram of the movement of the graphite particles in the circulating particulates bed reactor [157].

An advantage of this design, as compared to the carbon-felt reactor, is that it can be more readily adapted for continual removal of the metals by increasing the liquid flow rate and blowing the beads out of the reactor. Moreover, the movement of the particles could inhibit the formation of dendrites and the subsequent re-dissolution of the metal, a problem encountered with the carbon felt reactor. Metals with such a low concentration such as, platinum and palladium were successfully recovered via this reactor [154] as it offers higher conductivity of pre-metallised beads and the improved mass transport characteristics as compared to the carbon felt. However, the process demonstrated a higher current density, thus higher specific electrical energy consumption was attained. Dawson [154] reported a depletion of 1 mol m^{-3} Pd^{IV} solution containing a residue of 0.05 m mol^{-3} I_3^-, in 4 kmol m^{-3} iodide; at a feeder electrode of 0 V (SHE), the overall charge yield was 0.6 and the specific electrical energy consumption was 368 kW h $tonne^{-1}$.

Robson [157] did a preliminary experiment using the newly designed electrochemical reactor which, at a cathode feeder potential of -0.50 V (SCE) depleted 10 mol m^{-3} copper in 4 kmol m^{-3} + 1 kmol m^{-3} NaCl solutions rapidly to analytically undetectable concentrations by electrodeposition onto (growing) copper beads; dendrite formation was limited. Due to the higher conductivity of the copper beads and the improved mass transport characteristics as

compared to the carbon felt, the current densities required was higher for this reactor design.

At the potentials required to reduce gold(III), the copper particles used as the cathode to electrodeposit copper [151,157] would dissolve, so another electrically conducting material is required. It would be possible to plate gold onto gold particles, but the very high cost of gold metal, and hence the value of the reactor inventory would be too high to make this a feasible option; its density of 19.3 g cm^{-3} may also cause particle transport problems in the draft tube of the reactor. Other choices available as the electrode are glass beads, vitreous carbon particles and graphite particles.

Glass beads are readily available, but they are not electrically conductive and so require pre-treatment, such as electroless metal deposition, to make them conductive. Graphite particles [60] are relatively cheap, widely available and have a higher density (ca. 2.5 g cm-3) than vitreous carbon, so are easier to fluidise. Hence, graphite particles were chosen as the cathode for the CPBE reactor and the results will be reported in Chapter 5 and 6.

As overall views, the results obtained from the three reactors (carbon felt reactor, circulating particulate bed reactor, fluidised bed electrolyte) are quite promising and have provided some useful observations for the application of metal recovery. In addition, potentiostatic control allows the choice between selective or non-selective deposition, although setting the potential at a value (E = -0.70 V (SCE)) that would allow deposition of most metals would result in high rates of hydrogen evolution at the cathode, that would again decrease charge yields.

The feasibility of a mesh cathode in fluidised bed of inert particles and circulating particulate bed have been established, providing the starting point for this project. Moreover, appropriate operating conditions for metals electrodeposition must be determined by electrochemical kinetic measurements and batch electrowinning experiments, supported by thermodynamic predictions and reactor modelling to achieve high charge yield and selective metal electrodeposition. For electrodeposition of all metals studied, the effects were determined of cathode potential and solution flow rate on electrodeposition rates, charge yields, specific electrical energy consumptions, and deposit morphologies. Hence, this research project aimed to produce detailed information about the electrochemical separation and purification of metals, to enable future development of closed loop processes for recovery of dissolved metals from solutions resulting from leaching WEEE.

3.8. Project Objectives

The three primary objectives and associated tasks by which they could be achieved were:

(a) Design of a technically and economically viable, energy efficient process for the selective electrochemical recovery of the precious metal (Au) and base metal (Cu, Sn, Pb Ni, Zn) in an overall close-looped process for metal recovery from WEEE.

- Determine the deposition (micro-) kinetics of the metal components (Au, Cu, Sn, Zn) from acidic aqueous chloride solutions.
- Determine the suitable electrochemical reactor design (circulating particulate bed electrode and mesh cathode in fluidised bed of inert particles electrochemical reactor) to optimise metal recovery from the WEEE leachate, including low concentration of precious metals.
- Determine the effect of cathode potential and solution flow rate on electrodeposition rates, charge yields, specific electrical energy consumptions, on the reduction of the various metals (Au, Cu, Sn, Pb, Ni, Zn) in the solutions.
- Development of on-line metal ions concentration measurement by quartz flow cell connected to UV spectrophotometer using fibre optics, enabling time dependent concentrations to be determined in real time.
- Determine the possibility of selective electrodeposition of tin from synthetic Sn^{IV}-Pb^{II} aqueous chloride solutions, from which Pb could be electrodeposited subsequently.
- Determine the pH at which to precipitate '$Fe(OH)_3$', to be recovered by filtration; this option should also enable subsequent electro-co-deposition of Ni and Zn with high charge yields, as the higher pH will decrease the driving force for hydrogen evolution.
- Verification of the metal morphologies produced at the cathode are adherent and coherent, using analytical technique such as scanning electron microscopy (SEM), and purities determined by X-ray fluorescence (XRF) and X-ray diffraction spectroscopy (XRD).

(b) Establish a copper electrodeposition process to achieve 99.99%, as required for commercial purity Cu in order to be a saleable product.

- Determine what dark coloured mixed oxidation state intermediate species are formed in partially reduced leach solutions and whether they constitute a problem for copper recovery, hence affect the purity of copper recovered.
- Determine the suitable electrochemical reactor design (circulating particulate bed electrode and mesh cathode in fluidised bed of inert particles electrochemical reactor) to optimise the electrodeposition of high concentration of Cu in WEEE leachate, subsequently recovered diluted Cu concentrations in a three dimensional cathode electrochemical reactor to ensure complete recovery and investigate whether target purities can be met, for copper, or whether an electrorefining step will be required.
- Determine the effect of cathode potential and solution flow rate on electrodeposition rates, charge yields, specific electrical energy consumptions, and deposit morphologies, imaged subsequently by scanning electron microscopy (SEM), and purities determined by X-ray fluorescence spectroscopy (XRF); qualitatively by X-Ray diffraction spectroscopy (XRD).

(c) Develop mathematical models to predict the micro- and reactor-scale kinetics for the electrochemical reduction of Au, Cu, Sn and Zn which will then be validated experimentally

- Establishing mathematical model for general application to optimise the metal recovery, based on a detailed understanding of the (micro-) kinetics and mechanism of electrodeposition and electro-co-deposition of metals.
- Develop a one-dimensional model in MAPLE^{TM} to predict the kinetics of Ni-Zn electro-co-deposition, which was validated experimentally. The model also considered the potential and concentration profiles in the cathode | electrolyte boundary layer for conditions in which migration and convective diffusion all contribute to overall transport rates, to predict the behaviour and optimize the process parameters of the electrochemical reactors.

3.9. References

[1] European Parliament, 2003, Directive 2002/96/EC of the European Parliament on Waste Electrical and Electronic Equipment (WEEE*).O. J. Eu Commun.*, 46 (L37): 24-38.

[2] Wilkinson, S., Duffy, N. and Crowe, M., 2001, Waste from Electrical and Electronic Equipment in Ireland, A Status Report. Environmental Protection Agency, Ireland.

[3] Department of Trade & Industry (DTI), Sustainable Development Group (SDG), 2007, EC Directive on Waste Electrical and Electronic Equipment (WEEE) and EC Directive on the Restriction of the Use of Certain Hazardous Substances in Electrical and Electronic Equipment (RoHS).

[4] Industry Council for Electronic Equipment Recycling (ICER), 2000, UK Status Report on Waste from Electrical and Electronic Equipment.

[5] Duan, H., Hou, K., Li, J. and Zhu, X., 2010, Examining the technology acceptance for dismantling of waste printed circuit boards in light of recycling and environmental concerns. *J. Environ. Manage.*, 92 (3): 392-399.

[6] Kim S., Hwang, T. and Overcash, M., 2001, Life cycle assessment study of color computer monitor. *Int. J. Life Cycle Assess*., 6: 35–43.

[7] Taberman, S.-O., Carlsson, B., Erichson, H., Brobech, J. and Gregersen, J. C., 1995, Vol. TemaNord report to the Nordic Council of Ministers, Copenhagen.

[8] AEA Technology, 2004, WEEE & Hazardous Waste, A Report by DEFRA. http://www.defra.gov.uk/environment/waste/producer/electrical/document/weee-hazwaste.pdf.

[9] Goosey, M. and Kellner, R., 2003, Recycling technologies for the treatment of end of life printed circuit boards (PCBs). *Circuit World*: 33–37.

[10] Yoo, J., Jeong, J., Yoo, K., Lee. J., and Kim, W., 2009, Enrichment of the metallic components from waste printed circuit boards by a mechanical separation process using a stamp mill. *Waste Manage.*, 29: 1132–1137.

[11] Ogunniyi, I.O. and Vermaak, M.K.G., 2009, Investigation of froth flotation for beneficiation of printed circuit board comminution fines. *Minerals Engineering*, 22 (4): 378–385B.

[12] Kim, B.S., Lee, J., Seo, S., Park, Y. and Sohn, 2004, H., A process for extracting precious metals from spent printed circuit boards and automobile catalysts. *J. Minerals, Metals & Materials Soc.* (TMS), 56: 55–58.

[13] Brandon, N. P., Kelsall, G. H., Schmidt, M. and Yin, Q., 2002, Metal recovery from electronic scrap by leaching and electrowinning. in TMS Meeting on Recycling and Waste Treatment in Mineral and Metal Processing: Technical and Economic Aspects, vol. 2002, The Metals Society, Warrendale, PA, USA, 359-368.

[14] WasteOnline, 2010, Electrical and Electronic Equipment Recycling. Wasteonline Website:http://www.wasteonline.org.uk/resources/InformationSheets/ElectricalElectronic.htm.

[15] Ongondoa, F. O., Williams, I. D. and Cherretta, T. J., 2011, How are WEEE doing? A global review of the management of electrical and electronic wastes. *Waste Manage*., 31 (4): 714-730.

[16] Kang, H. Y. and Schoenung, J. M., 2005, Electronic waste recycling: A review of U.S. infrastructure and technology options Resources. *Conserve & Recycling*, 45 (4): 368-400.

[17] Cui, J. and Forssberg, E., 2003, Mechanical recycling of waste electric and electronic equipment: a review. *J. Hazard. Mat.*, 99: 243—263.

[18] Kindesjö, U., 2002, Phasing out lead in solders: An assessment of possible impacts of material substitution in electronic solders on the recycling of printed circuit boards. Master Thesis, Lund University, Lund.

[19] BASF Global, 2011, BASF-The Chemical Company, Corporate Website: http://www.basf.co.uk/ecp1/Group_companies_UK_Ireland/Englehard_Sales_Ltd.

[20] Setchfield, S. H., General Manager Refining, Engelhard Sales Ltd, Valley Road, Cinderford, UK, 2006, Catalyst recycling essential for the environment An International Newsletter Monitoring Technical and Commercial Developments in the Manufacture and Use of Catalysts, Proceedings of the European Workshop on Spent Catalyst Recycling, Regeneration, and Re-use, Frankfurt (Dechema) (4): 1-2.

[21] Johnson Matthey, 2007, Precious Metal Products Division - Research & Development Website: http://www.matthey.com/about/preciousmetals.htm.

[22] Boliden, 2002, Mining Technology - Boliden Zinc, Copper, Gold and Silver Mine

Myra Falls, Canada. Website: http://www.boliden.com/www/en/bolidenen.nsf.

[23] Hagelüken, C., 2006, Recycling of electronic scrap at Umicore's integrated metals smelter and refinery, World of Metallurgy, *ERZMETALL* 59(3):152–161.

[24] Goosey, M. and Geraghty, K., 2004, in Sustainable Electronic & Electrical Systems for the Automotive Sector (SEES Consortium).

[25] Cheng, C.Y., Kelsall, G.H., Umi, M.A. and Robson, A.C. 2008, Metals leaching from waste electrical and electronic equipment (WEEE) in chlorine-containing acidic aqueous chloride- Part II. Experimental. Personal Communication.

[26] London Metal Exchange, (http://www.lme.co.uk/nickel.asp), viewed on 21 May 2011, 09:20 GMT.

[27] Burkin, A. R., 2001, Chemical Hydrometallurgy. Imperial College Press.

[28] Scott, K., 1995, Electrochemical processes for clean technology. Royal Society of Chemistry, Cambridge.

[29] Chen, G., 2004, Electrochemical technologies in wastewater treatment. *Sep. & Purif. Technol*., 38 (1): 11-41.

[30] Wang, L.K., Hung, Y.T. and Shammas, N.K., 2007. Advanced physicochemical treatment technologies, Handbook of Environmental Engineering Vol. 5, Humana, New Jersey.

[31] Jusoh, A., Su Shiung, L., Ali, N.A. and Noor, M.J., 2007, A simulation study of the removal efficiency of granular activated carbon on cadmium and lead. *Desalination*, 206 (1-3): 9-16.

[32] Park, H.G., Kim, T.W., Chae, M.Y. and Yoo, I.K., 2007, Activated carbon-containing alginate adsorbent for the simultaneous removal of heavy metals and toxic organics. *Process Biochem*., 42 (10): 1371-1377.

[33] Doula, M.K. and Dimirkou, A., 2008, Use of an iron-overexchanged clinoptilolite for the removal of Cu^{2+} ions from heavily contaminated drinking water samples. *J. Hazard. Mater.,* 151 (2-3): 738-745.

[34] Alyuz, B. and Veli, S., 2009, Kinetics and equilibrium studies for the removal of nickel and zinc from aqueous solutions by ion exchange resins. *J. Hazard. Mater*., 167 (1-3): 482-488.

[35] González-Muñoz, M.J., Rodríguez, M.A., Luquea, S. and Álvareza, J.R., 2006, Recovery of heavy metals from metal industry waste waters by chemical precipitation and nanofiltration. *Desalination*, 200:742–744.

[36] Alvarez, M.T., Crespo, C. and Mattiasson, B., 2007, Precipitation of Zn(II), Cu(II) and Pb(II) at bench-scale using biogenic hydrogen sulfide from the utilization of volatile fatty acids. *Chemosphere*, 66 (9): 1677-1683.

[37] Cox, M., 1992, Solvent extraction in hydrometallurgy. in: Rydberg, J., Musikas, C. and Choppin, G.R., Editors, Principles and Practices of Solvent Extraction, Marcel Dekker Inc., New York: 357–412.

[38] Mihaylov, I., 2003, Solvent Extractants for Nickel and Cobalt: New Opportunities in Aqueous Processing. *JOM*, 55 (7): 38-42.

[39] Landaburu-Aguirre, J., Pongrácz, E., Perämäk, P. and Keiski, R.L., 2010 Micellar-enhanced ultrafiltration for the removal of cadmium and zinc: use of response surface methodology to improve understanding of process performance and optimisation. *J. Hazard. Mater*.,180: 524–534.

[40] Molinari, R., Poerio, T. and Argurio, P., 2008, Selective separation of copper (II) and nickel(II) from aqueous media using the complexation-ultrafiltration process. *Chemosphere*, 70 (3): 341-348.

[41] Amini, M., Younesi, H. and Bahramifar, N., 2009, Statistical modeling and optimization of the cadmium biosorption process in an aqueous solution using Aspergillus niger. *Coll. & Surf.*, 337 (1-3): 67-73.

[42] Apiratikul, R. and Pavasant, P., 2008, Batch and column studies of biosorption of heavy metals by Caulerpa lentillifera. *Bioresource Tech.*, 99 (8): 2766-2777.

[43] Pletcher, D. Walsh, F.C., 1990, Industrial Electrochemistry, 2nd. ed., Chapman and Hall, London.

[44] Adcock, P.A. and Adeloju, S.B., 1999, Removal and Recovery of Metals by Electrodeposition. *Electrochem. News*, 3 (1).

[45] Pletcher, D., Walsh, F.C. and Whyte, I., 1990. The Application of Electrochemical Techniques to the Treatment of Industrial Process Liquors. IChemE Symposium Series No. 116, Effluent Treatment and Waste Disposal, Hemisphere Pub Co., 195.

[46] Mecucci, A. and Scott, K., 2002, Leaching and electrochemical recovery of copper, lead and tin from scrap printed circuit boards. *J. Chem. Tech. & Biotech.*, 77 (4): 449-457.

[47] Buckle, R. and Roy, S., 2008, The recovery of copper and tin from waste tin stripping solution: Part I. Thermodynamic analysis. *Sep. & Purif. Tech.*, 62 (1): 86-96.

[48] Roy, S. and Buckle, R., 2009, The recovery of copper and tin from waste tin stripping solution: Part II: Kinetic analysis of synthetic and real process waste. *Sep. & Purif. Tech.*, 68 (2): 185-192.

[49] Fray, D.J., Gibson, R.W., Sunderland, J.G. and Dalrymple, I.M., 2003, in Electrochemistry in Mineral and Metal Processing VI, vol. 2003-18, Proceedings – Electrochem. Soc. 346-354.

[50] Bard A.J., Parsons, R. and Jordan, J., 1985, Standard potentials in aqueous solutions, New York, Marcel Dekker.

[51] Dawson, R., 2006. Electrochemical recovery of platinum and palladium from alumina-supported catalysts, PhD Thesis, Imperial College London.

[52] Robson, A, 2005. Metal Recovery from End-of-Life Electrical and Electronic Systems. MPhil/PhD Report, Imperial College London.

[53] Kelsall, G., 2007, CE408 - Electrochemical Engineering and Technology Lecture Notes, Imperial College London.

[54] Appleby, A.J., Chemla, M., Kita, H. and Bronoel, G. in Encyclopedia on Electrochemistry of the Elements, Ch.IX-A3, Vol.IX, A.J.Bard (Ed.) Marcel Dekker, New York, 1982: 383-597.

[55] Schalch, E., Nicol, M.J., Diggle, J.W., Charlton, B.D. and Vaessen, J.P.H., 1976. An Electrochemical and Kinetic Investigation of the Behaviour of Gold in Chloride Solutions. I. The Cathodic Deposition of Gold, Report No. 1848, *Natl. Inst. Metallurgy, Mineral Process Chem. Div.*, Johannesburg, South Africa.

[56] Nicol, M.J., 1976, An Electrochemical and Kinetic Investigation of the Behaviour of Gold in Chloride Solutions. III. The Gold(III)/ Gold(I) Reaction on Platinum and the Disproportionation of Gold(I), Report No. 1846, *Natl. Inst. Metall. Mineral Process Chem. Div.*, Johannesburg, South Africa.

[57] Harrison, J.A. and Thompson, J., 1975. The kinetics of gold deposition from chloride solution. *Electroanal. Chem*., 59: 273–280.

[58] Muir, R.D., Stett, C.W.A., Priddle, C.J., 1982, Hydrometallurgy - Research, Development and Plant Practice, AIME, Warrendale, Pa., 825-838.

[59] Diaz, M. A., Kelsall, G. H. and Welham, N. J., 1993, Electrowinning coupled to gold leaching by electrogenerated chlorine. I. Au (III)-Au (I)/Au kinetics in aqueous Cl_2/Cl^- electrolytes. *J. Electroanal. Chem*., 361 (1/2): 25.

[60] Cheng, C-Y., Diaz, M.A., Kelsall, G.H. and Robson, A.C., 2006, Gold Electrowinning from Acidic Aqueous Chloride in a Packed Bed Electrode. *ECS Trans*., 2 (3): 317-328.

[61] Kelsall, G.H., Welham, N.J. and Diaz, M.A., 1993, Thermodynamics of Cl-H_2O, Br-H_2O, I-H_2O, Au-Cl-H_2O, Au-Br-H_2O and Au-I-H_2O systems at 298 K. *J. Electroanal. Chem.,* 361 (1/2): 13-24.

[62] Walker, A.T.S. and Wragg, A.A., 1977, The modelling of concentration—time relationships in recirculating electrochemical reactor systems. *Electrochim. Acta*, 22 (10): 1129-1134.

[63] Yoshida, F., Ramaswami, D. and Hougen, O.A., 1962. Temperatures and partial pressures at the surfaces of catalyst articles. *AIChE J*., 8 (1): 5–11.

[64] Sakai, T., Takenaka, H. and Torikai, E., 1986, Gas diffusion in the dried and hydrated Nafion. *J. Electrochem. Soc*., 133: 88-92.

[65] Abrantes, L. M., Araujo, L. V. and Levi, M. D., 1995, Voltammetric studies on copper deposition/dissolution reactions in aqueous chloride solutions. *Minerals Eng*., 8 (12): 1467-1476.

[66] Crousier, J.P. and Pardessus, 1988, Voltammetry study of copper in chloride solution. *Electrochim. Acta*, 33 (8): 1039–1042.

[67] Oishi, T., Koyama, K. S. Alam, Tanaka, M. and Lee, J.C., 2007, Recovery of high purity copper cathode from printed circuit boards using ammoniacal sulfate or chloride solutions. *Hydromet.*, 89 (1-2):82-88.

[68] Ovchinnikova, S.N., Aleksandrova, T.P. and Vais, A.A., 2004, Copper in acid chloride solutions electrochemical behaviour by quartz microgravimetry and voltammetry.

Russian J. Electrochem., 40 (7):755–759.

[69] Sum, E.Y.L., 1991, The recovery of metals from electronic scrap. *JOM*, 43 (4): 53-61.

[70] Winand, R., 1991, Chloride hydrometallurgy. *Hydromet.*, 27 (3): 285–316.

[71] Brandon, N.P., Kelsall, G.H., Müller, T., Olijve, R., Schmidt, M. and Yin, Q., 2001, Metal Recovery from Electronic Scrap by Leaching and Electrowinning. 200th Electrochemical Society Meeting, San Francisco, Proc. Electrochem.Soc., Vol.2001-23, Energy and Electrochemical Processes for a Cleaner Environment, ed. C.Comninellis, M.Doyle and J.Winnick, (Electrochem.Soc., N.J., 2001):323-338.

[72] Brandon, N.P., Kelsall, G.H., Schmidt, M.J. and Yin, Q., 2002, Metal recovery from electronic scrap by leaching and electrowinning II. TMS Meeting on Recycling and Waste Treatment in Mineral and Metal Processing: Technical and Economic Aspects, , Luleå, Sweden, B.Björkman, C.Samuelsson, J-O.Wilkström (Eds.), TMS, Warrendale, PA, 2002: 359-368.

[73] Brandon, N.P., Kelsall, G.H., Olijve, R., Schmidt, M. and Yin, Q., 2002, Metal Recovery from Electronic Scrap by Leaching and Electrowinning III, in "Chloride Metallurgy 2002, Proceedings of the International Conference on the Practice and Theory of Chloride/Metal Interaction", Vol. II, Peek, E., van Weert, G. (Eds.), CIM, Montréal, Canada: 743-757.

[74] Brandon, N.P., Kelsall, G.H. and Yin, Q., 2000, UK Patent Application 0026390.5.

[75] Bockris, J.O. and Enyo, M., 1962, Mechanism of electrodeposition and dissolution processes of copper in aqueous solutions. *Trans. Faraday Soc*., 58: 1187-1202.

[76] Diard, J. P., Le Canut, J. M., Le Gorrec, B. and Montella, C., 1998, Copper electrodissolution in 1 M HCl at low current densities. I. General steady-state study. *Electrochim. Acta*, 43 (16/17): 2469-2483.

[77] Lee, H.P. and Nobe, K., 1986. Kinetics and mechanisms of Cu dissolution in chloride media. *J. Electrochem. Soc*., 133 (10): 2035-2043.

[78] Winter, D.G., Covington, J.W. and Muir, D.M., 1982, Studies related to the electrowinning of copper from chloride solutions. In: P.D. Parker, Editor, Chloride Electrometallurgy, *AIME*, New York: 167–188.

[79] Powell, K.J., Brown, P.L., Byrne, R.H., Gajda, T., Hefter, G., Sjoberg, S. and Wanner,

H., 2007, Chemical speciation of environmentally significant metals with inorganic ligands. Part 2: The Cu^{2+}-OH^-,Cl^-, CO_3^{2-} , SO_4^{2-}, and PO_4^{3-} systems (IUPAC Technical Report). *Pure & App. Chem*., 79: 895-950.

[80] Parthasardhy, N.V., Practical Electroplating Handbook, Prentice Hall, 1989.

[81] Dew, D.W. and Phillips, C.W., 1985, The effect of Fe(II) and Fe(III) on the efficiency of copper electrowinning from dilute acid Cu(II) sulphate solutions with the Chemelec cell. Part I. Catholic and anodic polarisation studies. *Hydromet*., 14 (3): 331–349.

[82] Dew, D.W. and Phillip, C.V., 1985, The effect of Fe(II) and Fe(III) on the efficiency of copper electrowinning from dilute acid Cu(II) sulphate solutions with the chemelec cell. Part II. The efficiency of copper electrowinning from dilute liquors. *Hydromet.*, 14 (3): 351-367.

[83] Krause, T.T., 2003, Model for nickel-iron alloy electrodeposition on a rotating disk electrode. *J. Electrochem. Soc*., 144 (3): 960.

[84] Lin, Y.P. and Selman, J.R., 1999, Electrodeposition of Corrosion-Resistant Ni-Zn Alloy. I. Cyclic Voltammetric Study. *J. Electrochem. Soc*., 140 (5): 1299.

[85] Roventi, G., Fratesi, R., Guardia, R.A.D. and Barucca, G., 2000, Normal and anomalous code-position of Zn-Ni alloys from chloride bath. *J. App. Electrochem.*, 30 (2): 173-179.

[86] Fratesi, R. and Roventi, G., 1991, Electrodeposition of zinc-nickel alloy coatings from a chloride bath containing NH_4Cl. *J. App. Electrochem.*, (22): 657-662.

[87] Pushpavanam, M. and Balakrishnan, K., 1996, Zinc-nickel alloy electrodeposition from uncomplexed acid bath. *J. App. Electrochem.*, 26 (3): 283-290.

[88] Mathias, M.F. and Chapman, T.W., 1987, The composition of electrodeposited Zinc-Nickel Alloy Coatings. *J. Electrochem. Soc.*, 134 (6): 1408-1415.

[89] Mathias, M.F. and Chapman, T.W., 1990, A Zinc-Nickel alloy electrodeposition kinetics model from thickness and composition measurements on the rotating disc electrode. *J. Electrochem. Soc.*, 137 (1): 102-110.

[90] Mathias, M.F., Villa, C.M. and Chapman, T.W., 1990, A model of zinc-nickel alloy electrodeposition in an industrial-scale cell. *J. App. Electrochem.*, 20(1):1-10.

[91] Swathirajan, S.S., 1987, Electrodeposition of zinc + nickel alloy phases and

electrochemical stripping studies of the anomalous codeposition of zinc. *J. Electroanal. Chem. & Interfacial Electrochem.*, 221 (1): 211.

[92] Ji, J. and Cooper, W.C., 1996, Nickel speciation in aqueous chloride solutions. *Electrochim. Acta*, 41 (9): 1549-1560.

[93] Walsh, F.C., 2001, Electrochemical technology for environmental treatment and clean energy conversion. *Pure Appl. Chem.*, 73(12): 1819 – 1837.

[94] Cheng, C.Y. and Kelsall, G.H., 2008, Recovery of Metals from 4 M HCl and 1 M NaCl Solutions by Circulating Particulates Bed Reactor and Mesh Cathode in a Fluidised Bed of Inert Particles - Part II. Experimental. Personal Communication.

[95] Shvab, N.A., Kazdobin, K.A., Klimenko, L.A., Dzyazko, Y.S., 1992, Cathode processes in electrochemical extraction of palladium and tin from hydrochloric combined solutions of activation. *Ukrainskii Khimicheskii Zhurnal*, 58 (7): 547-550.

[96] Galus, Z., 1975, Chapter IV-5: tin, In: [ed] A.J. Bard.- Encyclopedia on Electrochemistry of the Elements, vol. IV, New York: Marcel Dekker.

[97] Stirrup, B.N.and Hampson, N.A., 1976, The active dissolution of tin in acidic chloride electrolyte solutions: a rotating disc study. *J. App. Electrochem.*, 6 (4): 353-360.

[98] Stirrup, B.N. and Hampson, N.A., 1977, Review paper: Electrochemical reactions of tin in aqueous electrolytic solutions. *Surf. Tech.*, 5: 429-462.

[99] Monien, H., 1969, Electrochemical and reaction kinetics of the tin(IV) reduction in chloride medium at a planar mercury electrode. *Electroanal. Chem. & Interface. Electrochem.*, 20: 119-128.

[100] Lerner, H., Austin, L.G., 1965, The kinetics of the stannous/ stannic redox reaction at carbon electrodes. *J. Electrochem. Soc.*, 112 (6): 636-638.

[101] Kiekens, P., Verplaetse, H., Temmerman, E., 1981. Electrochemical study of the oxidation of tin(II) at glassy carbon electrodes. *Talanta,* 28: 192-194.

[102] García-Gabaldón, M., Pérez-Herranz, V., Garcia-Anton, J. and Guiñón, J.L., 2005, Electrochemical recovery of tin and palladium from the activating solutions of the electroless plating of polymers- potentiostatic operation. *Sep. Purif. Tech.*, 45 (3): 183-191.

[103] García-Gabaldón, M., Pérez-Herranz, V., Garcia-Anton, J. and Guiñón, J.L., 2006,

Electrochemical recovery of tin from the activating solutions of the electroless plating of polymers- galvanostatic operation. *Sep. Purif. Tech*., 51 (2): 143-149.

[104] Pérez-Herranz, V., García-Gabaldón, M., Guiñón, J.L. and Garcia-Anton, J., 2003, Effect of citric acid and hydrochloric acid on the polarographic behaviour of tin. *Analyt. Chim. Acta*, 484 (2): 243-251.

[105] Ponce de Leon, C. and Pletcher, D., 1996, The removal of Pb(II) from aqueous solutions using a reticulated vitreous carbon cathode cell: the influence of the electrolyte medium. *Electrochim. Acta,* 41(4): 533-541.

[106] Gioda, A.S., Giordono, M.C. and Macagno, V.A., 1977, The Pb/Pb^{2+} exchange reaction in perchlorate acid solutions. *J. Electrochem. Soc*., 124: 1324-1329.

[107] Ambrose, J., Barradas, R. G., Belinko, K. and Shoesmith, D. W., 1974, Reactions at the lead electrode/hydrochloric acid interface. *J. Colloid & Interface Sci*., 47 (2): 441-454.

[108] Scott, K., 1993, Electrochemical Methods for the Treatment of Industrial Process Streams and Effluents. Part I: Cell Design and the Recovery of Dissolved Metals by Electrodeposition. *Develop.Chem. Eng. and Mineral Process.*, 1 (4): 185-197.

[109] Walsh, F.C., 2001, Electrochemical technology for environmental treatment and clean energy conversion. *Pure Appl. Chem*., 73 (12): 1819-1837.

[110] Janssen, L.J.J., and Koene, L., 2002, The role of electrochemistry and electrochemical technology in environmental protection. *Chem. Eng. J*., 85(2-3): 137-146.

[111] Juttner, K., Galla, U. and Schmieder, H., 2000, Electrochemical approaches to environmental problems in the process industry. *Electrochim. Acta*, 45 (15-16): 2575 - 2594.

[112] Koene, L. and Janssen, L.J.J., 2001, Removal of nickel from industrial process liquids *Electrochim. Acta*, 47 (5): 695-703.

[113] Jasson, R.E.W., Marshall, R.J. and Rizzo, J.E., 1978, The rotating electrolyser. I. The velocity field. *J. Appl. Electrochem*, 8: 281–285.

[114] Jasson, R.E.W., Marshall, R.J. and Rizzo, J.E., 1978, The rotating electrolyser. II. Transport properties and design equations. *J. Appl. Electrochem*, 8 *:*287–291.

[115] Lopez-Cacicedo, C.L., 1975. The recovery of metals from rinse waters in “Chemelec”

electrolytic cells. *Trans. Inst. Met. Finish.*, 53: 74–77.

[116] Backhurst, R., Coulson, J.M., Goodridge, F., Plimley, R.E. and Fleischmann, M., 1969, A preliminary investigation of fluidised bed electrodes. *J. Electrochem. Soc.*,116 (11): 1600-1607.

[117] Campbell, D.A., Dalrymplea, I.M., Sunderland, J.G. and Tilstona, D., 2003, The electrochemical recovery of metals from effluent and process streams. *Resources, Conserve. & Recycling*, 10 (1-2): 25-33.

[118] Pletcher, D. and Walsh, F., 1993, Industrial Electrochem., Second, Chapman & Hall

[119] Gabe, D.R. and Walsh, F.C., The rotating cylinder electrode—a review of development. *J. Appl. Electrochem.*, 13(10): 3–22.

[120] Kreysa, G., Pionteck, S. and Heitz, E., 1974, Comparative investigations of packed and fluidized bed electrodes with non-conducting and conducting particles. *J. App. Electrochem.*, 5 (4): 305-312.

[121] Low, C. T. J., de Leon, C. P. and Walsh, F. C., 2005, The Rotating Cylinder Electrode (RCE) and its Application to the Electrodeposition of Metals. *Aus. J. Chem.*, 58: 246-262.

[122] Kammel, R. and Lieber, H. W., 1977, Possibilities of treating electroplating effluents without the formation of residues; metal recovery in place of sludge disposal. *Galvanotechnik*, 68 (8): 710-715.

[123] Bruhn, D., Dietz, W., Müller, K-J. and Reynvaan, C., 1986, EPA 86109265.8.

[124] Storck, A., Robertson, P.M. and Ibl, N., 1979, Mass transfer study of three-dimensional electrodes composed of stacks of nets. *Electrochim. Acta*, 24 (4): 373-380.

[125] Patzer, J.F., Yao, S.J. and Wolfson Jr., S.K., 1996, In Situ Electrode Formation in a Swiss Roll Reactor. *Ind. & Eng. Chem. Res.*, 35 (4): 1316-1321.

[126] Saba, A.E., El Sherif, A.E. and Elsayed, E.M., 2007, The electroremoval of copper from dilute waste solutions using Swiss-roll electrode cell. *JOM*, 59 (10): 53-57.

[127] Keating, K.B. and William, J.M., 1976, The recovery of soluble copper from an industrial chemical waste. *Resource Recovery & Conserve.*, 2 (1): 39-55.

[128] Ullmann's Encyclopedia of Industrial Chemistry.

[129] Koene, L. and Janssen, L.J., 2001, Removal of nickel from industrial process liquids. *Electrochim. Acta*, 47 (5): 695-703.

[130] Walker, A.T.S. and Wragg, A.A., 1980, Mass transfer in fluidised bed electrochemical reactors. *Electrochim. Acta*, 25 (3): 323-330.

[131] Carbin, D.C. and Gabe, D.R., 1974, Electrodeposition from a fluidised bed electrolyte-I. The mass transport correlation. *Electrochim. Acta*, 19 (10): 645-652.

[132] Kreysa, G., Pionteck, S. and Heitz, E., 1974, Comparative investigations of packed and fluidized bed electrodes with non-conducting and conducting particles. *J. App. Electrochem.*, 5 (4): 305-312.

[133] Kelsall, G.H. and Gudyanga, F.P., 1991, Electrochechemical Reactor Design Consideration for Simultaneous Tin Electrowinning and Cr^{2+} Electrogeneration. *Dechema Monogr*, 123: 167.

[134] Chaudhary, A.J.S., Dando, S.O.V. and Grimes, S.M., 2001, Removal of tin from dilute solutions. *J. Chem. Tech. & Biotech.*, 76 (1): 47-52.

[135] Chen, G., 2004, Electrochemical technologies in wastewater treatment. *Sep. & Purif. Tech.*, 38 (1): 11-41.

[136] Recendiz, A., Leon, S., Nava, J.L. and Rivera, F.F., Mass transport studies at rotating cylinder electrode during zinc removal from dilute solutions. *Electrochim. Acta*, 56 (3): 1455-1459.

[137] Reade, G.W., Ponce-de-Leon, C. and Walsh, F.C., 2006, Enhanced mass transport to a reticulated vitreous carbon rotating cylinder electrode using jet flow. *Electrochim. Acta*, 51 (13): 2728-2736.

[138] Rivera, F.F., Gonzalez, I. and Nava, J.L., 2008, Copper Removal from an Effluent Generated by a Plastics Chromium-Plating Industry Using a Rotating Cylinder Electrode (RCE) Reactor. *Environ. Tech.*, 29:817-826.

[139] Masse, N., St-Pierre, J. and Bergeron, M., 1995, Copper removal from aerated solution containing various metal ions using an undivided rotating cylinder electrode reactor. *J. App. Electrochem.*, 25 (4): 340.

[140] Alonso, A.R., Lapidus, G.T. and GonzÃ¡lez, I., 2008, Selective silver electroseparation from ammoniacal thiosulfate leaching solutions using a rotating

cylinder electrode reactor (RCE). *Hydromet*., 92 (3-4): 115-123.

[141] Terrazas-Rodraguez, J.E., Gutiarrez-Granados, S., Alatorre-Ordaz, M.A., Ponce de LeÃn, C. and Walsh, F.C., The use of a rotating cylinder electrode to selective recover palladium from acid solutions used to manufacture automotive catalytic converters. *J. App. Electrochem*., 41 (1): 89-97.

[142] Grau, J.M. and Bisang, J.M., 2007, Electrochemical removal of cadmium from dilute aqueous solutions using a rotating cylinder electrode of wedge wire screens. *J. App. Electrochem*., 37 (2): 275-282.

[143] Recendiz, A., Gonzalez, I. and Nava, J.L., 2007, Current efficiency studies of the zinc electrowinning process on aluminum rotating cylinder electrode (RCE) in sulfuric acid medium: Influence of different additives. *Electrochim. Acta*, 52 (24): 6880-6887.

[144] Rivera, F.F., Nava, J.L., Oropeza, M.T., Recendiz, A. and Carreno, G., Mass transport studies at rotating cylinder electrode: Influence of the inter-electrode gap. *Electrochim. Acta*, 55 (9): 3275-3278.

[145] Kinoshita, K., and Leach, S.C., 1982, Mass-Transfer Study of Carbon Felt, Flow-Through Electrode. *J. Electrochem. Soc*., 129(9): 1993-1997.

[146] Pilone, D. Kelsall, G.H., 2006, Prediction and measurement of multi-metal electrodeposition rates and efficiencies in aqueous acidic chloride media. *Electrochim. Acta*, 51 (18): 3802-3808.

[147] Lu, J., Dreisinger, D.B. and Cooper, W.C., 2002, Copper electrowinning from dilute cyanide solution in a membrane cell using graphite felt. *Hydromet*., 64 (1): 1-11.

[148] Tricoli, V., Vatistas, N. and Marconi, P.F., 1993, Removal of silver using graphite-felt electrodes. *J. App. Electrochem.*, 23 (4): 390-392.

[149] Gonzalez-Garcia, J., Bonete, P., Exposito, E., Montiel, V., Aldaz, A. and Torregrosa-Macia, R., 1999, Characterization of a carbon felt electrode: structural and physical properties. *J. Mat. Chem*., 9 (2): 419-426.

[150] Ragnini, C.A.R., Di Iglia, R.A., Bizzo, W., and Bertazzoli, R., 2000, Recycled niobium felt as an efficient three-dimensional electrode for electrolytic metal ion removal. *Water Res*., 34(13): 3269-3276.

[151] Scott, K., 1981, Metal Recovery Using a Moving-Bed Electrode. *J. App. Electrochem*.,

11(3): 339-346.

[152] Scott, K., 1988, A consideration of circulating bed electrodes for the recovery of metal from dilute solutions. *J. App. Electrochem*., 18(4): 504-510.

[153] Stankovic, V. and S. Stankovic, 1991, An Investigation of the Spouted Bed Electrode Cell for the Electrowinning of Metal From Dilute Solutions. *J. App. Electrochem*., 21(2): 124-129.

[154] Dawson, R. J., 2006, Electrochemical Recovery of Platinum and Palladium from Alumina-Supported Catalysts. Ph.D. Thesis, Chemical Engineering, Imperial College London.

[155] Jiricny, V., Roy, A. and Evans, J. W., 2000, Electrodeposition of Zinc from Sodium Zincate/Hydroxide Electrolytes in a Spouted Bed Electrode. *Metall. & Mat. Trans. B*, 31 (4): 755-766.

[156] Uekawa, K., 2007, Spouted Bed Electrode (SBE). *J. Surf. Finish. Soc. Japan*, 58 (11): 641-643.

[157] Robson, A., 2005, Metal Recovery from End-of-Life Electrical and Electronic Systems. MPhil/PhD Transfer, Imperial College London.

4. MATERIALS AND EXPERIMENTAL METHODS

4.1. Chapter Overview

This chapter details the experimental methods used to obtain micro-kinetic data, which were not available from literature. These were required:

(i) as inputs to the mathematical model(s) for predicting reactor performance;

(ii) to investigate the electrodeposition of various metals from synthetic and actual waste electrical and electronic equipment (WEEE) solutions;

(iii) to characterize the deposit morphologies and to determine the electrodeposit metal purities.

From results of experiments with a vitreous carbon or platinum rotating disc electrode (PINE Instrument Company, MT28 series electrode- AFMT28GCPT), kinetic data required to refine the reactor model were derived for electrodeposition of Au, Cu, Sn and Ni-Zn electro-co-deposition and for evolution of H_2 thereon. Using a rotating Pt ring-vitreous carbon disc electrode, the mechanism for Sn electrodeposition was also investigated. To validate model predictions, metal concentrations and currents were measured as functions of time in batch recycle operation which utilized two types of electrochemical reactors: (a) mesh cathode in fluidised bed of inert particles; and (b) circulating particulates bed cathode. The operations of these two reactors were elucidated in this Chapter. During the experiment, samples of catholyte(s) were taken from the reservoir at fixed time intervals and was analysed off-line by Inductively-Coupled Plasma- Optical Emission Spectrometer (Perkin Elmer Instruments, Model Optima 2000 DV). Whilst for diluted metal ions concentration (< 1 mol m^{-3}), such as gold, the temporal decay of the solution absorbance of $AuCl_4^-$ ions at 312 nm was recorded on-line by quartz flow cell connected to UV spectrophotometer (Agilent 8453 UV-Visible system) using fibre optics, enabling its time dependent concentration to be determined in real time. The features of both techniques to analyse metal ions concentrations will be discussed in detail in this Chapter. Finally, experimental equipment for determining the deposit morphologies which was Scanning Electrons Microscopy, (SEM- JEOL 5610) and purities of deposit metals i.e. via X-ray fluorescence spectroscopy (XRF) as well as X-Ray diffraction (XRD) will be explained. Some details, notably the quantitative aspects are given in the Appendices.

4.2. Materials

4.2.1. Chemicals

The following tables are lists of the principal chemicals and materials which have been used during the course of this project, also included are their purities and their suppliers.

Table 4- 5. Common reagents.

Reagent	Reagent grade	Supplier
Hydrochloric Acid	GPR, 37%	Fisher
Copper (I) Chloride	AnalaR, 99%	Fisher
Copper (II) Chloride	AnalaR, 99%	Fisher
Tin (II) Chloride	AnalaR, 99%	Sigma Aldrich
Copper (II) Sulphate	AnalaR, 99%	Sigma Aldrich
Tin (IV) Chloride	AnalaR, 99%	Sigma Aldrich
Lead (II) Chloride	AnalaR, 99%	Sigma Aldrich
Aluminium Chloride	AnalaR, 99%	Sigma Aldrich
Gold (I) Chloride	AnalaR, 99%	Sigma Aldrich
Gold (III) Chloride	AnalaR, 99%	Sigma Aldrich
Zinc Chloride	AnalaR, ≥98%	Fluka
Nickel (II) Chloride	AnalaR, 99%	Sigma Aldrich
Iron (II) Chloride	AnalaR, 99%	Sigma Aldrich
Iron (III) Chloride	AnalaR, 99%	Sigma Aldrich

Table 4-6. Standard reagents.

Reagent	Reagent grade	Supplier
Sodium Hydroxide	AnalaR, 99%	VWH
Sodium Chloride	AnalaR, 99%	Sigma Aldrich
Lead and Tin standard solutions for ICP	1000 mg L^{-1} 30 % HCl /trace (tr)-HNO_3	SPEX CertiPrep
Silver standard solution for ICP	100 mg L^{-1} 30 % HCl/trace (tr)-HNO_3	SPEX CertiPrep
Copper, Iron, Nickel, Zinc standard solutions for ICP	1000 mg L^{-1} 10% HCl / 1% HNO_3	SPEX CertiPrep
Gold, Platinum, Palladium, Barium, Cobalt, Chromium, Beryllium and Magnesium standard solution	100 mg L^{-1} 10% HCl / 1% HNO_3	SPEX CertiPrep
Aluminium standard solution for ICP	1000 mg L^{-1} 2% HCl	SPEX CertiPrep

Table 4-7. Electrode materials.

Materials	Material grade	Supplier
Platinum foil	99.85%	Goodfellow
Nickel wire	99.98%	Goodfellow

Titanium Mesh	Not specified	Goodfellow
Nickel Mesh	99.9%	Goodfellow
Ti/Ta_2O_5-IrO_2 Mesh	Not specified	Magneto Special Anodes B.V.
Graphite particles	99.8%	Alfa Aesar

The electrodes were cut into appropriate sizes; 3 cm^2 for platinum flag which was used as the counter electrode, 135 cm^2 for both; titanium, nickel mesh cathode and Ti/Ta_2O_5-IrO_2 mesh anode. The Ti/Ta_2O_5-IrO_2 mesh anode was specially made suitable to be used in a highly acidic environment by Magneto Special Anode B.V. (Schiedam, Netherlands). The sizes for the graphite particles used were 0.5-1.0 mm in diameter.

Table 4-8. Cation exchange membranes.

Membrane	Membrane type	Supplier
Nafion 424	Perfluorinated acid based	Ion Power

The Nafion membranes were purchased from Ion Power Inc. (Newcastle, USA). Both membranes are highly acid based polymer sheets with sulfonic acid SO_3^- groups. The negative charge of the acid permits the passage of cations only. The membranes were cut into desired sizes and were conditioned in hot water at about 80^oC for 40 minutes for maximum swelling. After the conditioning process, the membrane was kept in de-ionised water at all times to maintain the performance of the membrane.

4.2.2. Electric and Electronic Equipment Waste

The waste electrical and electronic equipment (WEEE) in the course of this research were supplied by Precious Metal Industries Group Ltd., Neath, South Wales, UK (PMI). Initially, samples from several sources of end-of-life printed circuit boards, mother boards, graphic cards etc., shredded with rotary shears to < 8 mm, were characterised physically and chemically and found to contain ca. (wt%): 22% Cu, 2% Zn, 1% Al, 0.2% Ni, 5% Sn, 3% Pb,

0.1% Fe, 0.02% Au, 0.04% Pd and 0.08%.Ag. 66.7 % non-metallics and iron, were removed prior to metals leaching via mechanical separation processes which involve gravity separation (differentiate between plastics and metals), magnetic separation (to remove ferrous metals iron and steel) and eddy current separation (to separate metallic and non-metallic materials). An example of a mechanical treatment route is given in Figure 4-22 [1]. Magnetic and eddy current separation technologies are explained schematically in Figure 4-22 [2].

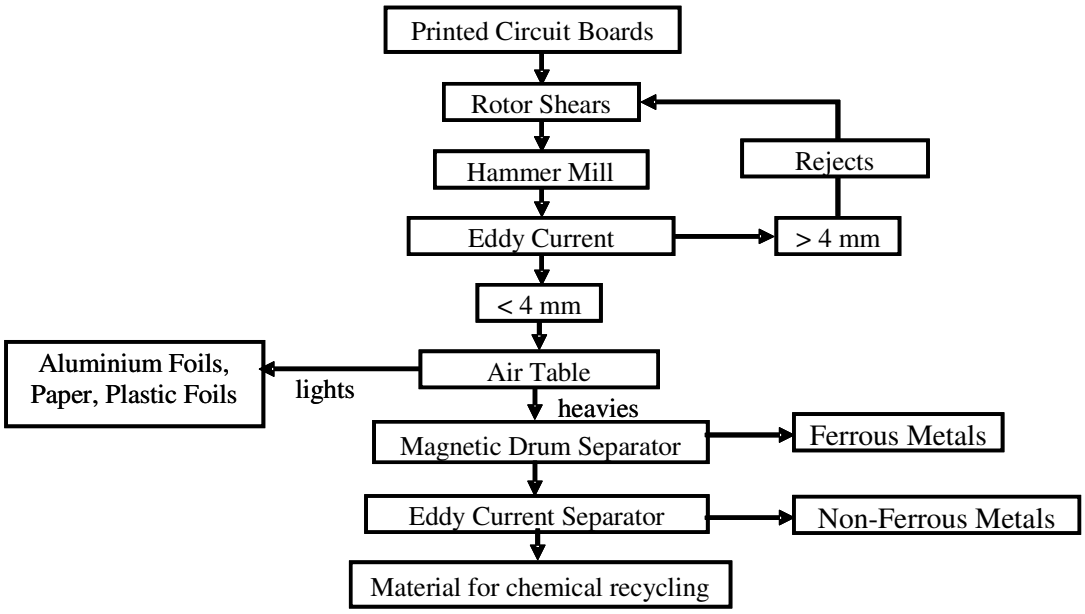

Figure 4-22. Flow chart for mechanical processing of electronic waste [1].

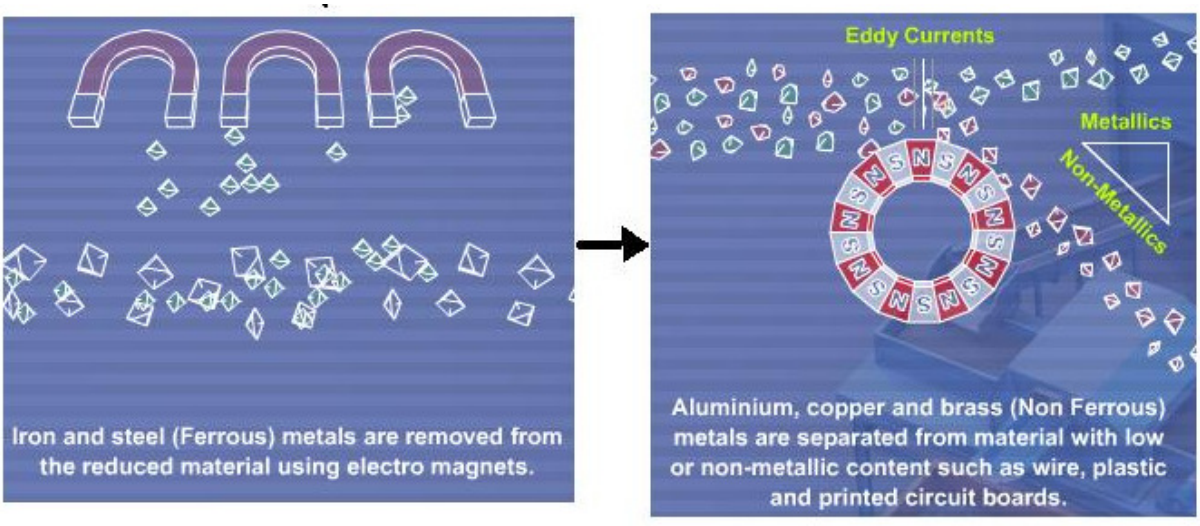

Figure 4-23. Magnetic and Eddy Current Separation Techniques [2].

In the previous project at Imperial College London [3], the metals were leached in dissolved chlorine, generated in an electrochemical reactor, in acidic aqueous chloride solutions (4 kmol m^{-3} HCl + 1kmol m^{-3} NaCl). Non-selective dissolution of metals present in WEEE was achieved with conversions of > 0.99 for base metals (Al, Zn, Cu, Fe, Sn, Pb) and > 0.95 for precious metals (Ag, Pd, Ni, Ba, Mg) in ca. 30 hours. The dissolved metal was analysed by Inductively Coupled Plasma Optical Emission (ICP) spectrophotometry. The leach solution composition is given in Table 4-9.

Table 4-9. Leachate solution composition [3].

Element	Concentration / mol m^{-3}	Element	Concentration / mol m^{-3}
Cu	475.99	Ni	15.75
Zn	37.97	Ag	1.62
Al	27.31	Pd	0.187
Fe	0.10	Au	0.0522
Sn	28.12	Mg	3.35
Pb	10.48	Ba	0.002

For all experiments conducted, the synthetic metal solutions were prepared in the presence of 4 kmol m^{-3} HCl and 1 kmol m^{-3} NaCl. All solutions were made from analytical grade chemicals and high purity water made by reverse osmosis (Elga Elgastat) and de-ionisation (Elga Prima) to give a resistivity of 1.6×10^5 Ω m. Metal solutions were prepared under the presence of nitrogen to avoid its oxidation by air.

4.3. Electrochemical Measurement Equipment.

4.3.1. General remarks

The electrochemical measurements in this work were mainly carried out with Autolab potentiostats PGStat 100 and PGStat 30 (Eco Chemie B.V., Utrecht (NL)). A Mettler-Toledo AG245 balance (Mettler-Toledo Ltd., Leicester (UK)) was used to weigh the chemicals (section 4.2.1) for solution preparation. A solution of 4 kmol m^{-3} HCl + 1 kmol m^{-3} NaCl

(leaching solutions) was used as the base electrolyte for all measurements, with the conductivity of ca. 65 S m^{-1}. Additionally, de-ionised water was used, supplied by a reverse osmosis system (Elgastat Prima; Elga, Marlow (UK)) with a typical conductivity of 1.6×10^{-3} S m^{-1} to dilute the leaching solutions to desired concentration. Saturated calomel electrodes (Cole-Parmer Instrument Co., Vernon Hills, IL (USA)) were used as reference throughout. All potentials are given in relation to saturated calomel (SCE).

4.3.2. pH and Conductivity

These measurements were carried out with a Hach-Lange Sension combined conductivity-pH meter (Hach-Lange, Manchester (UK)). The conductivity probe had a Pt electrode, whereas the pH meter employed a liquid gel and glass electrode. The meter had an RS232 interface to send its data to a computer, which used an appropriate LabView programme to read the data stream into an Excel spreadsheet. The meter was calibrated regularly; the pH probe was subject to a three-point calibration with pH buffers of values 4.0, 7.0 and 10.0. The conductivity probe was calibrated with a 0.05 S m^{-1} KCl standard (Sigma-Aldrich Company Ltd., Gillingham (UK)).

4.3.3. Rotating Disc Electrode (RDE)

Rotating disc experiments were carried out in a three-compartment glass cell, incorporating a platinum flag counter electrode, a saturated calomel reference electrode (SCE), a rotating vitreous carbon or platinum disc electrode, mounted in a cylindrical Teflon sheath ,as a working electrode. The catholyte was separated from the anolyte by an ion exchange membrane (Nafion-424). The cell was bubbled with nitrogen gas ('White Spot' grade, BOC Ltd) for 15 minutes before each experiment to remove any dissolved oxygen. In addition, the cell was slightly tilted in order to allow hydrogen bubbles to escape. The experiments were carried out at different rotation rates within a range 60- 3000 rpm which is controlled by an AFMSR modulated speed electrode rotator (Pine Instrument Company, Grove City,PA, USA). All experiments were conducted at room temperature and pressure.

The rotating disc (RDE) electrode diameter and surface area were recorded as 0.5 cm and 0.196 cm^2 respectively as supplied by Pine Instrument Company, Grove City, PA, U.S.A. The rotating disc electrode technique was used to investigate the electrode kinetics of gold (Au^{III}), copper (Cu^{II}), tin (Sn^{IV}) and zinc (Zn^{II}) reduction. Prior to each experiment the working electrode surface was mechanically polished with surface polishing equipment (Buehler Ltd., Lake Bluff, IL (USA)), using 300 nm and 0.05 μm alumina powder (Sigma Aldrich) which is

wetted with semi-pure water. The electrode was then thoroughly washed with distilled water and placed in an ultrasonic cleaning bath (Thermo Scientific) to remove any adhering alumina particles. Figure 4-24 shows schematic diagram of RDE systems.

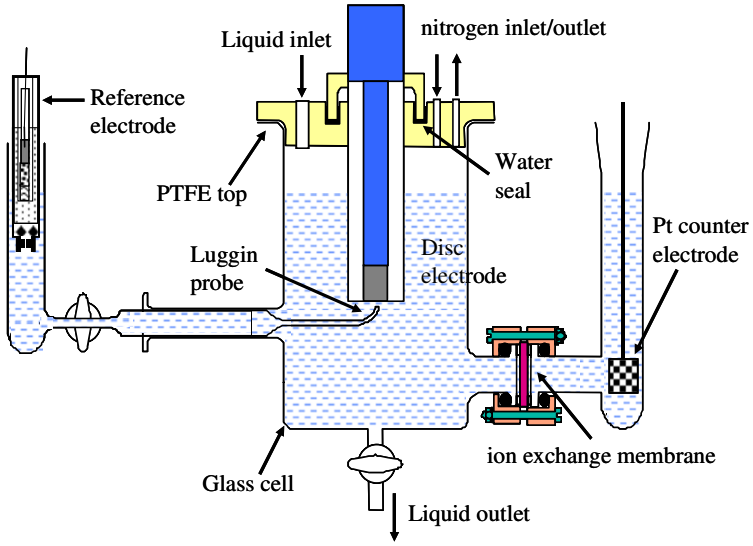

Figure 4-24. Rotating disc electrode assembly and electrochemical cell [4].

Electrochemical measurements were made using computer controlled Autolab PGStat as described in section 4.3.3.1 and different electrochemical methods were utilized, these included step, cyclic and linear sweep voltammetry and chrono-amperometry methods. The main parameters altered were the scan limits and scan rate. The following section summarizes the main electrochemical methods undertaken.

4.3.3.1 Cyclic Voltammetry

Cyclic voltammetry as the name suggests, sweeps across a preset range of potentials and then sweeps back to determine the oxidation reactions of the species previously reduced. The method requires Autolab cyclic voltammetry method (normal) setting, the parameters concerned were the scan rate in volts per second and the step potential. The scan rate must be such that the system is under steady-state, a value of 0.01 Vs^{-1} is sufficiently low for the system. The scan limits were set in accordance with the theoretical predictions of the extended Butler-Volmer Equation, and using the Pourbaix diagram of complex stability. By scanning across boundaries between different complexes will produce a voltammogram of current against potential which answer fundamental questions such as [4]:

- What oxidation/ reduction reactions occur?
- At what potentials do they occur?
- How many electrons are involved?
- Do the electron transfers occur all at once or at different potentials in steps?

Unless reported otherwise, the rotating disc electrode was rotated at 6 different rotation rates i.e. 60 rpm, 240 rpm, 540 rpm, 960 rpm, 1500 rpm and 2160 rpm. These speeds were chosen to verify diffusion limited phenomena.

4.3.3.2 Linear Sweep Voltammetry

Linear sweep voltammetry involves the same apparatus and set up as cyclic voltammetry, the only difference is the sweep is only in one direction.This uni-directional sweep is essential to primarily detect the reduction of the species involved.

4.3.3.3 Chrono-amperometry

A constant potential was applied to the system at a low overpotential in order to deposit metal on the surface of the electrode, and the current (density) recorded with time, so the charge passed could be determined by their integration.

4.3.4. Rotating Ring-Disc Electrode

A rotating platinum ring – vitreous carbon disc electrode (PINE Instrument Company, MT28 series electrode - AFMT28GCPT) was used to to determine the molar ratio of tin complexes in chloride solutions, particularly to detect Sn^{IV} species dissolved at the vitreous carbon disc electrode, by the oxidation of Sn^{II} species at the Pt ring electrode. For this experiment, synthetic 10^{-5} kmol m^{-3} Sn^{II}, and 10^{-3} kmol m^{-3} Sn^{IV} and 5x 10^{-4} kmol m^{-3} Pb^{II} solutions in the presence of 4 kmol m^{-3} HCl and 1 kmol m^{-3} NaCl as a supporting electrolyte were prepared. All solutions were made from analytical grade chemicals and high purity water made by reverse osmosis (Elga Elgastat) and de-ionization (Elga Prima) to give a resistivity of 1.6×10^{5} Ω m. Sn^{II} solutions were prepared under the presence of nitrogen to avoid its oxidation by air.

Technically the experimental set-up and procedures were similar to the rotating disc experiment however in rotating ring-disc experiment, the ring was connected to Bi-potentiostat (which is embedded with the PGstat30 Potentiostat/Galvanostat) .Dimensions of

the rotating ring-disc electrode (PINE Instrument Company documentation for MT28 series electrode) are listed below:

Disk Diameter / mm	5.00
Ring Inner Diameter / mm	4.93
Ring Outer Diameter / mm	5.38

The theoretical collection efficiency is defined as the ratio of the flux of soluble intermediate reaching the ring to the flux of soluble intermediate leaving the disc [5] which is given as 21.8%. Figure 4-25 and Figure 4-26 show schematic diagrams of RRDE systems

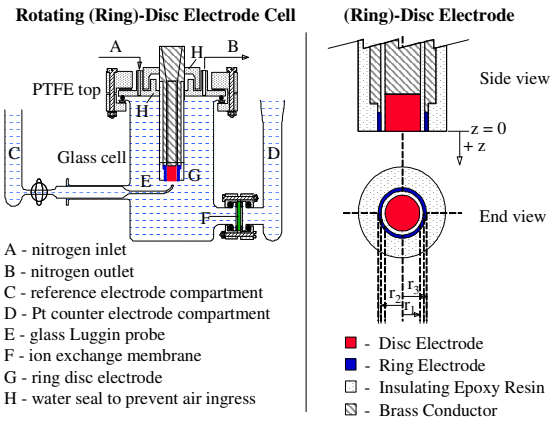

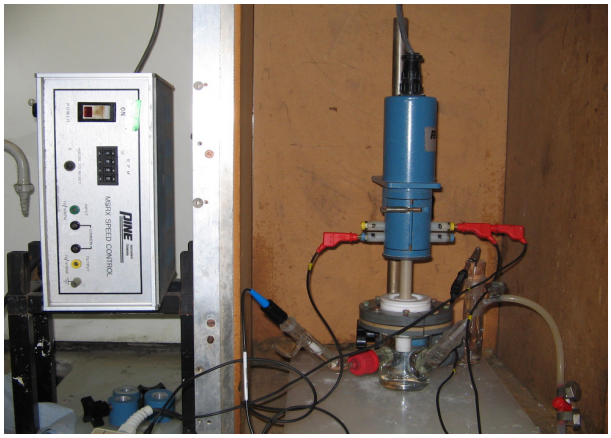

Figure 4-25. Rotating ring-disc electrode assembly and electrochemical cell [4].

Figure 4-26. RRDE experiment set-up (three-compartment glass cell, electrodes, rotating shaft, motor controller).

4.3.5. Special Precautionary Measures

The following is the list of precautions taken using the Rotating Disc Electrode (RDE) and Rotating Ring-Disc Electrode (RRDE):

(i) Positioning the test cell such that the liquid surface was reasonably still with the RDE or RRDE rotating which could minimizes premature turbulence,

(ii) Limiting the liquid volume between 5 and 10 ml; the minimum was to reduce splashing while the maximum was to avoid corrosive solutions seeping into the metallic joints of the RDE or RRDE.

(iii) Ensuring identical nitrogen pressure setting, including maintaining the liquid heights of the gas humidifiers (about 50 mm of water); this ensures similar flow rates,

(iv) Removing any bubbles trapped on the electrodes before the experiments,

(v) Regular checks on the solution level in the reference electrode and pH meter,

(vi) Storing the reference electrode and pH probe in their respective storage fluids to prevent plugging by crystallization,

(vii) Shaking off trapped solutions off the pH probe back into the test cell after any pH measurement to minimize test solution loss, and

(viii) Avoiding organic contaminants, like bare hands touching sensitive areas, or the use of tissue paper to mop glass ware.

4.3.6. Repeatability & Reproducibility

Due to the sheer number of experiments, each experiment was repeated three times unless a particular run went out of the trend. Where a new run happens to start with the same solution combination, it provided the opportunity to check for reproducibility. To avoid reported variability among vitreous carbon or platinum electrode, from even the same manufacturer, only one was used throughout the work. As it was subjected to relatively mild conditions and handling, electrode degradation was not expected nor observed.

Repeatability, i.e. the possibility of producing the same results on repeated runs with the same sample, was usually very good. Reasonable repeatability suggested that the polishing method for the vitreous carbon and platinum electrode was adequate, and restored it to its initial conditions. Where hydrogen evolution was severe, partly due to the random nature of the bubbles formed at the surface, repeatability of the current-potential profiles was not as good as expected.

Reproducibility, i.e. repeat runs using identical but different samples showed greater variability, was poorer. This was not restricted to low concentrations alone, where one might suspect concentration errors; since stock solutions usually also showed variability in the voltammograms. The errors did not have a trend such as shifting increasingly in a particular

direction, which would imply a drift in instrumentation, reference electrode ageing or even cation adsorption by the storage container.

4.4. Reactor Experiments

Perspex and polyvinyl difluoride (PVDF) were used to construct the electrolytic cells. The materials which were supplied by Porvair Technology were chosen to withstand the highly acidic medium such as metals leachate solution at pH 0. Two electrochemical reactors were fabricated (i.e. Mesh Electrode in a Fluidised Bed of Inert Particles and Circulating Particulate Bed Electrode) in the Chemical Engineering Workshop and the system of each are discussed as follows:

4.4.1. Mesh Electrode in a Fluidised Bed of Inert Particles

Figure 4-27 shows a schematic diagram of the reactor (340 mm (h) × 120 mm (w) × 100 mm (t)) with a mesh cathode in a fluidised bed of inert particles. The cathode was a Ti mesh with a surface area of 0.0135 m^2, immersed in a bed of 250 cm^3 of inert particulates (glass beads) with diameters ranged from 590 - 840 μm, which would fluidise with appropriate electrolyte flow rate to enhance mass transport of the reactants. A flow distributor was installed at the inlet (bottom) of the catholyte compartment to ensure even distribution of flow rate. The cathode potential was controlled with a Luggin capillary probe containing a saturated calomel reference electrode (SCE), assumed to have a potential of +0.245 V (SHE). The anode used to generate oxygen from an anolyte of 1 kmol m^{-3} H_2SO_4, was a mesh Ti/Ta_2O_5-IrO_2.

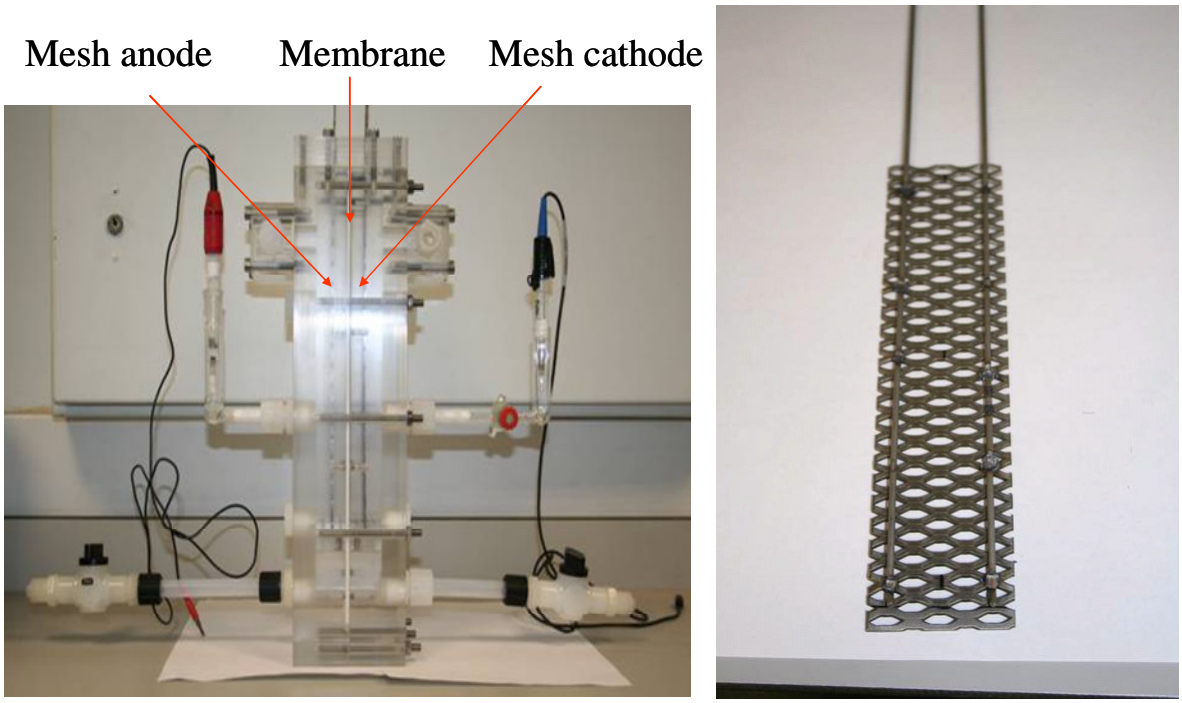

Figure 4-27. Photograph of the fluidised bed electrolyte of glass beads electrochemical reactor and the titanium mesh electrode.

The applied cathode potential in the fluidised bed reactor was controlled with respect to a saturated calomel electrode (SCE) by a computer-controlled AUTOLAB potentiostat and the current was measured. Anolyte and catholyte were separated by a Nafion N-424 permeable membrane and they were both operated in batch recycle mode with reservoirs. The volume of each of the anode and cathode compartments of the reactor was 0.5 dm^3, and the total volume of anolyte and catholyte circulating in each system was 2 dm^3.

A sample point was located immediately after the catholyte reservoir and samples of the catholyte were taken at fixed time intervals. The flow rate of the leach solutions was measured by a Titan 810- VOP-O-PTM flow meter and data was logged by data acquisition device NI DAQPad-6015 (National Instruments). The calibration curve for the flow meter is given in Appendix F. The schematic diagram of the experimental set-up is shown in Figure 4-28. The samples were diluted in a matrix of 4 kmol m^{-3} HCl before the metals concentration was analysed using the Inductively Coupled Plasma analyser (ICP-OES) (Perkin Elmer Instruments Optical emission spectrometer Model Optima 2000 DV). The metal deposits morphology on the Ti mesh obtained under different potentials, with and without fluidised inert particulates had been studied using SEM. The effects of applied feeder cathode potential and electrolyte flow rate on the performance of the fluidised bed reactor had also been

investigated.

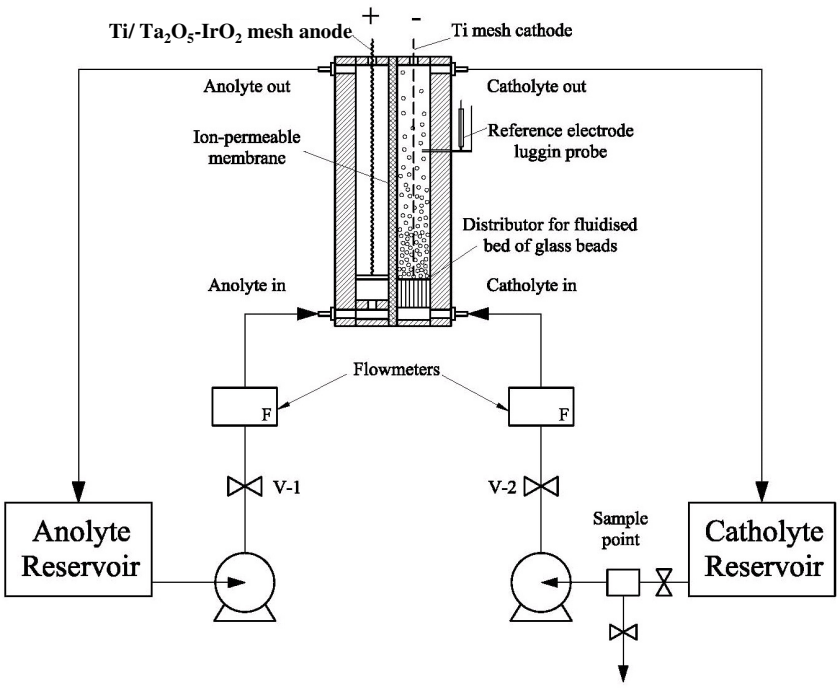

Figure 4-28. Schematic diagram of the experimental set-up of the mesh electrode in a fluidised bed of inert particles electrochemical reactor.

4.4.2. Circulating Particulate Bed Cathode

For a low concentration of metal ions in waste electronics such as gold, platinum and palladium, a three-dimensional cathode, with a high surface area per unit volume and a high mass transport rate coefficients, is the best option to be used for metal recovery. Initially, it has been described in Chapter 3, that a circulating particulate bed cathode (CPBE) reactor can be used to recover precious metals from chloride solutions by electrodeposition. However, because of the 3-D nature of the electrode, and the potential drop in the direction of current flow, for a 0.01 m deep cathode, it is necessary to keep the metal ion concentration below 10 mol m^{-3}. Since the concentrations of gold in leachate solutions from WEEE are likely to be below 1 mol m^{-3}, a CPBE reactor is attractive for the deposition of gold, due to the high specific surface area, high mass transport rates and improved deposit morphologies for such reactors.

Figure 4-29 shows the arrangement of the components in an individual unit cell, each contained by a Perspex frame (240 mm (h) × 145 mm (w)× 50 mm (t)), separated by a 2 mm

thick rubber gasket (Altec tubing (www.altectubing.co.uk)) to prevent short circuit by contacts between cathode, membrane and anode, while allowing electrolyte, and hence ionic current, to pass through. The electrolyte flowed from the bottom to the top of reactor and even distribution of the electrolyte. The unit cell were compressed together by two stainless steel plates on each side of the frame to ensure good electrical contacts between the Ti-feeder cathode and the graphite particles electrodes. The anode was a mesh Ti/Ta_2O_5-IrO_2 while the particulates bed cathode consisted of 40 cm^3 of graphite particles with an averaged diameter of 0.5- 1.0 mm and a total surface area of c.a. 0.2 m^2. The particulates travelled up the draft tube due to the force exerted on them by the flow of electrolyte, and down on the right hand side due to the force of gravity. The movements of the particulates resulted in two regions: a dilute upward moving region (draft tube) and a dense downward moving region as shown in Figure 3-20 (Chapter 3) and can be monitored by a small window constructed on the stainless steel plate. To enable charge transfer, the graphite particulates need to be in contact directly or indirectly with Ti- feeder electrode. The entire unit as schematically shown in Figure 4-30 was held together using steel frame made in the Chemical Engineering Workshop (Figure 4-31).

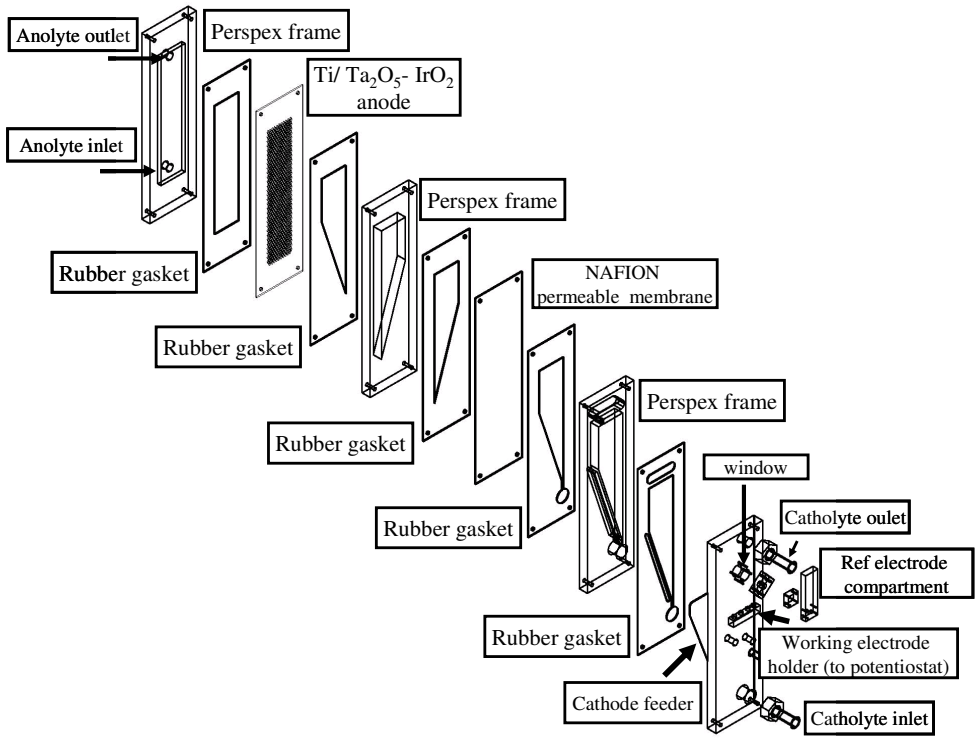

Figure 4-29. Representation of components in a unit cell.

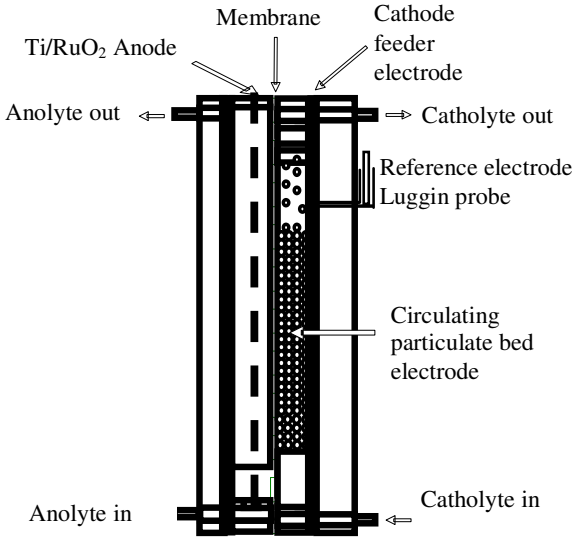

Figure 4-30. Schematic diagram for the circulating particulates bed reactor.

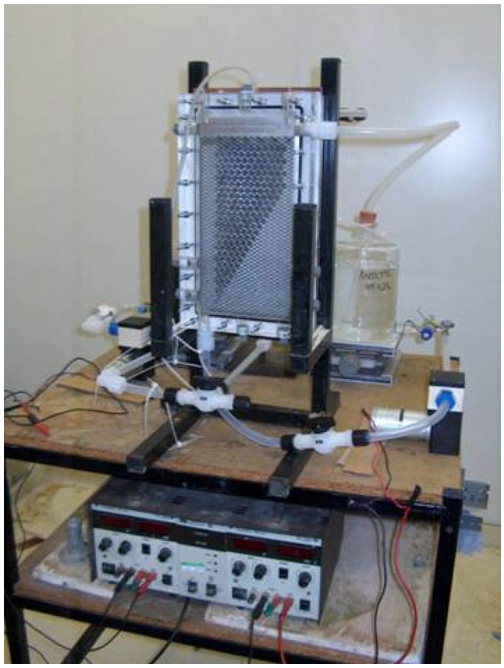

Figure 4-31. Photograph of the circulating particulates bed reactor.

The applied feeder cathode potential was controlled with respect to a saturated calomel reference electrode (SCE.) by a computer-controlled AUTOLAB PGSTAT30 potentiostat / galvanostat (coupled with a 10A current booster), which also measured the current through the reactor. The catholyte and anolyte compartment were separated by a Nafion-N424 membrane to prevent partially reduced metals ions from the cathode transferred to the anode, re-oxidised subsequently and reducing charge efficiency. The catholyte was 4 kmol m^{-3} HCl + 1 kmol m^{-3} NaCl solutions containing metal ions and the anolyte was 1 kmol m^{-3} H_2SO_4. Both catholyte and anolyte were operating in batch recycle mode with separate reservoirs. The catholyte flow rate was measured by a flow meter (Omega FTB603) and logged by data acquisition device (NI DAQPad-6015, National Instruments) and software (LabView^{TM}.) The reason for the flow of the anolyte was to aid the removal of gas bubbles evolved from the anode, since build-up of bubbles would reduce the effective conductivity of the anolyte and increase the cell voltage. A schematic of the flow circuit is shown below. The piping arrangement used was George Fischer PVDF piping. Two 12 V DC Totton pumps were used to pump the fluids from their reservoirs through the anode and cathode chambers and back to the reservoirs again. Two 10 L glass reservoirs were used as catholyte and anolyte reservoirs. The schematic diagram of electrochemical reactor flow circuit is shown in Figure 4-32.

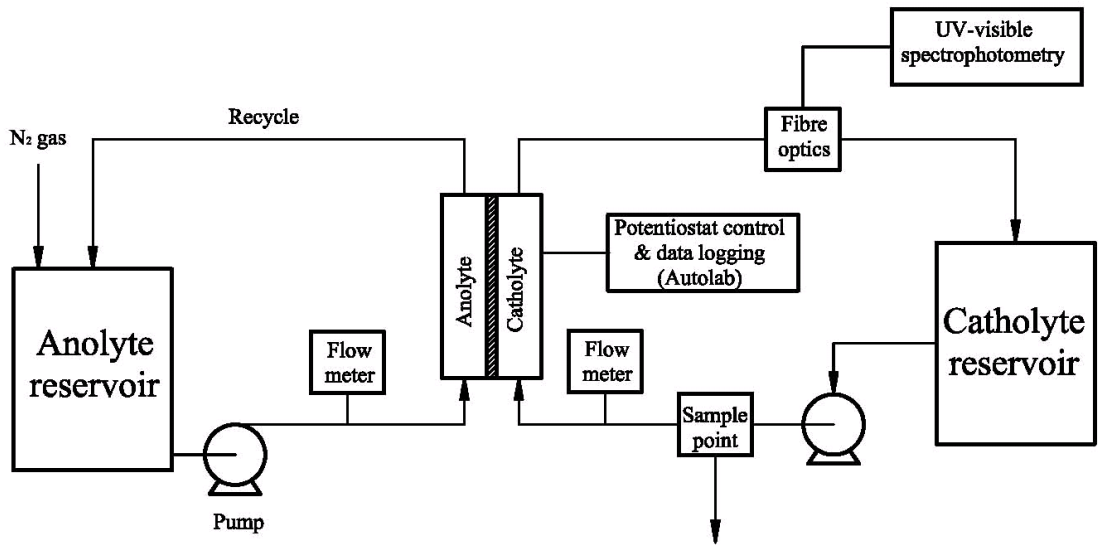

Figure 4-32. Schematic diagram of the experimental set-up of the circulating particulate bed cathode electrochemical reactor.

During the experiment, samples of catholyte were taken from the reservoir at fixed time intervals. Each sample was diluted at a ratio of 1:50 in 0.5 M HCl before metal ions

concentration was analysed by ICP (Inductively Coupled Plasma – Perkin Elmer Instruments Optical Emission Spectrometer Model Optima 2000 DV). In addition, the morphology of metal deposits on pre-metallised graphite particulates obtained under different potentials had been studied using SEM (Scanning Electrons Microscopy, SEM – JEOL 5610). The effects of applied feeder cathode potential and electrolyte flow rate on the Cu recovery rates and charge efficiency had also been investigated.

4.5. Precipitation Experiments

The pH was recorded using a pH probe. The pH probe was allowed to equilibrate for 10 mins before each reading was taken. Four 50 ml samples were prepared. NaOH was added until the sample pH spanned to the theoretical value given in the speciation diagram as per calculated prior to each experiment, preferably with at least one sample precipitated [47]. For example, if theory predicted that precipitation would occur at pH 3.5, then the sample could have been at pH 3.00, 3.25, 3.50 and 3.75. The samples were then left for at least a week to allow for the equilibration of slow reactions [47]. The pH of the samples was then re-measured.

4.6. Analytical Techniques

Various analytical techniques were used to monitor the components involved in determining the electrochemical efficiency of the process to recover metals from the waste electrical and electronic equipment (WEEE).

4.6.1. UV-Visible Spectrophotometry

To quantify the concentration of a metal in aqueous solution, it can be useful to apply spectrophotometer (Agilent 8453 UV-Visible system), where the adsorption of incoming light by a sample is measured. It is a quick and relatively simple method for measurement of metal concentrations, as many of metal chloride complexes present in the leachate absorbs in the UV range. In this method a light beam passes through a liquid sample. The equipment was used with a 1 mm wide quartz cuvette and 4 kmol m^{-3} HCl + 1 kmol m^{-3} NaCl as blank Dependent on the sample characteristics the beam will be attenuated by light absorption. The intensity of the beam after the sample is compared to a blank and the intensity change at specific wavelengths related to a contaminant concentration [7].

This technique uses the different intensities of absorption that species in solution have for different wavelengths (λ) of light in the UV-Visible region. The absorbance of light behaves

linearly with concentration over a region dependent on a particular system. This is written as Beer's Law [8]:

$$A_\lambda = \sum_{i=1}^{m} \varepsilon_{\lambda i} c_i d_{cell}$$

Where: A_λ = Absorbance

ε_λ = Molar absorbtivity / $mol^{-1}m^2$

c = concentration / mol m^{-3}

d_{cell} = Optical path length / m

In the present case, however, the UV-Vis spectrophotometer is sensitive towards measurement of the metal ion concentration in solutions that have almost the same wavelengths e.g. tin and lead. Figure 4-33 and Figure 4-34 indicate the absorption of single metal chloride complexes whilst Figure 4-35 clearly shows that tin and lead chloride could not be distinguished through UV spectrophotometry.

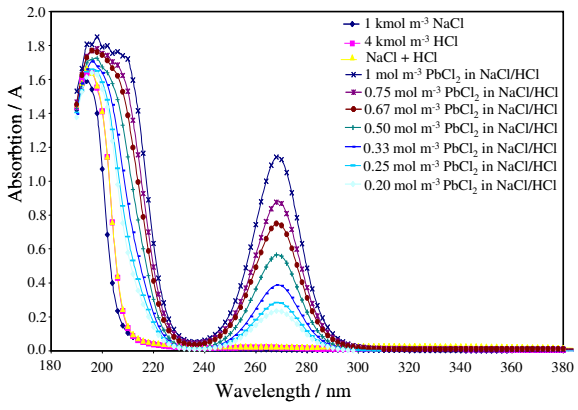

Figure 4-33. UV spectra for lead (II) chloride in NaCl/HCl.

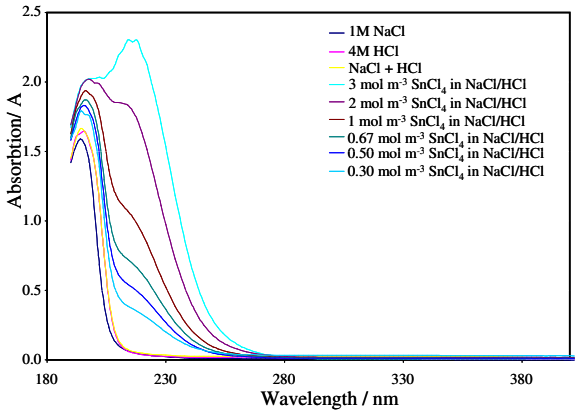

Figure 4-34. UV spectra for tin (II) chloride in NaCl/HCl.

Due to this difficulty, all sample measurements were performed by inductively coupled plasma (ICP) spectrometry (will be described in section 4.6.2), which is very accurate down to parts per billion levels, but involves taking samples and analysing the solutions after the experiments have been completed.

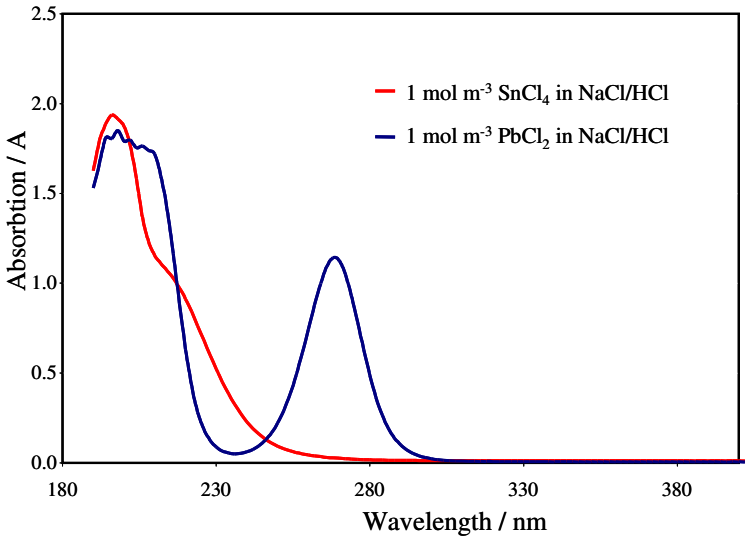

Figure 4-35. Absorption of tin (II) chloride and lead (II) chloride in NaCl/HCl.

Despite the inability to distinguish between multiple metal chloro-complexes ions concentration, the temporal decay of the solution absorbance of $AuCl_4^-$ ions alone at 312 nm (molar absorptivity, ε_{312} = 662.1 mol^{-1} m^2) was recorded on-line by quartz flow cell connected to UV spectrophotometer using fibre optics, enabling its time dependent concentration to be determined in real time.

4.6.1.1 Fibre Optics

Fibre-optics probes from HELLMA are precision measuring devices made from high- quality quartz glass. Direct contact of hard materials (glass, metal, ceramics, etc.) with the optical surfaces of a probe, especially in the area of the optical measuring section must be avoided. Dropping, knocking or forcing the probe in any way can cause breakage of the measuring head, thus making the probe unusable. Rapid and excessive temperature changes, especially shock-line cooling of the probe head, can lead to damage and thereby to failure of the probe.

The fibre cables attached to a probe contain thin quartz fibres, which must not be bent too tightly. For 600 µ fibres, the minimum bending radius for short periods of time is 60 mm. For long periods of time, the minimum bending radius is 100 mm. Bending of the fibre cables to radii smaller than these can cause breakage of the fibre and render the probe unusable [9]. During the experiments, one end of the fibre-optics probes was connected to the UV-Vis spectrophotometry, whilst the other end of the fibre-optics was in contact with the quartz

cuvettes which are available as flow through cells (see Figure 4-36 and Figure 4-37) for in-line analysis. Samples were recorded every 15 minutes interval which measure the absorbance of species in the solutions.

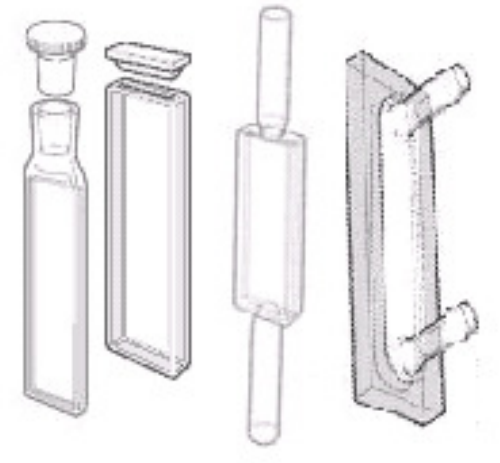

Figure 4-36. Standard and flow-through cells for a spectrophotometer [8].

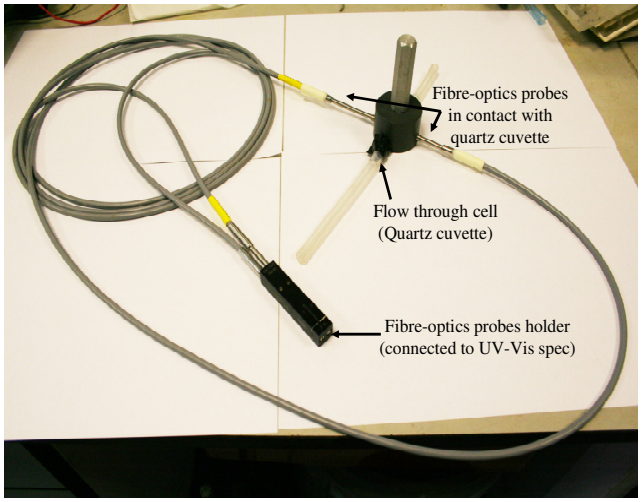

Figure 4-37. Set-up for the fibre-optics.

Any optical connectors on the fibre cables or probe must be protected against soiling. Soiled connections can cause distinct loss of signal and can strongly impair the efficiency of the probe [9]. Covers designed to keep the optical connectors clean should be put in place when the optical connectors are not being used. The probe was cleaned immediately after finishing a measurement. This is best done by immersing and careful swivelling of the probe head in a cleaning solution (such as undiluted solvent used for previous measurements). This process should be repeated several times with fresh solvent. After cleaning, the probe head must be rinsed several times with distilled water and subsequently dried with clean (oil-free) air. In no case should optical fibres on their connections come into contact with liquids (water, solvents, or cleaning solution). In order to maintain the efficiency of the probe, it is essential that the probe is cleaned at regular intervals.

4.6.2. Inductively Coupled Plasma Spectroscopy Optical Emission Spectroscopy (ICP-OES)

In this method, a high frequency, high energy magnetic field is applied by a coil to a gas stream, in this case Argon, so that the gas is excited and a plasma is created. A liquid sample is pumped into the system by a peristaltic pump, nebulised and sprayed into the plasma flame, which leads to the excitation of the sample. As a result, an emission spectrum can be

measured showing peaks at wavelengths characteristic for its composition. The concentration of the sample components at these wavelengths is determined by calibration of the emission intensity [7]. In the present project, ICP-OES (Perkin Elmer Optima DV 2000; Perkin-Elmer, Waltham, MA (USA)) was used to determine the metal ions concentration in a solution. Since particulate matter may block the nebuliser, the samples had to be acidified. Hence, all samples measured by ICP were subject to appropriate dilution (50 or 10 times depending on the metal ions concentration) in 4 kmol m^{-3} HCl. Prior to a measurement, a three-point calibration was carried out using a diluted ICP standard (Table 4-6) in concentrations below and above the expected metal ions concentration in the sample. Each sample concentration was measured three times and the arithmetic average computed.

4.6.3. X-Ray Fluorescence Spectroscopy (XRF)

After the copper electrodeposition experiments in two different electrochemical reactors, the electrode sample surfaces were rinsed in 1 kmol m^{-3} NaOH in order to minimise copper oxidation rates. The sample was subsequently analysed by X-ray fluorescence spectroscopy (Bruker, AXS, GmbH, Karlruhe, Germany) This equipment will determine quantitatively the metal presents and therefore the metal purity can be calculated. The sample is subjected to radiation by a powerful beam of short wavelength x-rays. This beam displaces an electron from the inner-most electron shells of an atom. To replace the lost electron, electron from the outer shell is promoted up into the core, and in doing so, releases energy in the form of x-rays. The resultant 'secondary' or 'fluorescent' x-ray radiation can be used to assess the amount of element giving rise to its presence in the sample [7].

4.6.4. X-Ray Diffraction (XRD)

X-ray powder diffractometry (X'Pert PRO model) was used in identification of the main metal phases present within the electrode sample after the electrodeposition process which utilized the two different electrochemical reactors. Output from the XRD diffractometer is in the form of line spacing intensity against 2Θ, where Θ is the angle of incidence of the x-rays to the stage containing the sample. The line spacing, d, can be calculated from Θ using Bragg's equation:

$$n\lambda = 2 \cdot d \cdot \sin\theta \qquad [3\text{-}10]$$

where n is equal to 1 for the 1st order of diffraction fringes and λ is the wavelength of the incident x-rays. The x-ray source used in the XRD diffractometer was copper, for which the

wavelengths of the $K\alpha_1$ and $K\alpha_2$ line spacing [7] are 0.1540562 nm and 0.1544390 nm, respectively. The d-spacings (equation [4.2]) at $2\Theta > 60^0$, the wavelength for the $\lambda_{K\alpha 1}$ should be used as this is twice as intense as the $\lambda_{K\alpha 2}$.

The resulting diffraction patterns were identified from the powder diffraction reference files of the International Centre for Diffraction Data [11]. Analysis was carried out on the sample of Cu electrodeposition on the Ti mesh cathode and Cu-pre metalized graphite particles in order to measure the deposit purity qualitatively.

4.6.5. Scanning Electron Microscopy (SEM) and Energy Dispersive X-ray microanalysis (EDAX)

The SEMs (Scanning Electrons Microscopy, SEM- JEOL 5610) of Imperial College Department of Materials, were used to image the surfaces of the Au and Cu electrodeposited graphite particles in order to determine the deposit morphologies. EDAX facility used to analyse the chemical composition of the top 1 μm.

4.7. Software

The following software packages (not including Microsoft Office) were used in the project.

1. Waterloo Maple™ version 13 - Symbolic mathematical programming language used for solving networks of equations and modelling the performance of the electrochemical reactor.
2. AutoCAD™ 2011 and SolidWorks™ 2011 – 3D Computer Aided Design (CAD) packaged used for the design of the electrochemical reactors and to produce the detailed process circuit.

4.8. Chapter Summary

This chapter has described the chemicals, apparatus, electrochemical equipment and procedures for the rotating disc and rotating ring-disc experiments required to determine the kinetic parameters for the reactions involved and for the experiments with two different electrochemical reactors. Finally, experimental equipment for determining the deposit morphologies and metal purities were also discussed.

4.9. References

[1] Cui, J. and Forssberg, E., 2003, Mechanical recycling of waste electric and electronic equipment: A review. *J. Hazard. Mat*., 99 (3): 243-263.

[2] SIMS Recycling, 2004, WEEE Recycling presentation. SIMS Recycling Solutions, http://simsrecycling.com/.

[3] Cheng, C-Y., Kelsall, G.H., Umi, M.A. and Robson, A.C. 2008, Metals leaching from waste electrical and electronic equipment (WEEE) in chlorine-containing acidic aqueous chloride- Part II. Experimental. Personal Communication.

[4] Kelsall, G.H., 2007, CE408 - Electrochemical Engineering and Technology Lecture Notes, Imperial College London.

[5] Albery, W.J., and Hitchman, M.L., 1971, Ring-Disc Electrodes. Clarendon Press Oxford, Chapter 3, 17-28.

[6] Buckle, R. and Roy, S., 2008, The recovery of copper and tin from waste tin stripping solution: Part I. Thermodynamic analysis. *Sep. & Purif. Tech*., 62 (1): 86-96.

[7] Kellner, R., Mermet, J.M., Otto, M., Valcarcel, M. and Widmer, H.M., 2004, Analytical Chemistry, 2nd ed., Weinheim, Wiley–VCH.

[8] Primer A., 1996, Fundamentals of modern UV-visible spectroscopy. Hewlett Packard.

[9] Fibre optics, 2011, HELLMA, http://www.hellma-analytics.com/text/161/en/fibre-optic-probes.html.

[10] R.C. Weast, CRC Handbook of Chemistry and Physics. 66th ed., 1985-1986. CRC Press, Florida.

[11] Powder Diffraction File, Inorganic Phases, X-ray powder diffractometry (X'Pert PRO model).

5. GOLD ELECTRODEPOSITION

5.1. Chapter Overview

This chapter is divided into five major sections. In the first, the thermodynamics of gold-water (Au-H_2O) and gold-chloride-water (Au-Cl-H_2O) systems are presented. In the second, the electrodeposition kinetics of $AuCl_n^-$ which demonstrates typical voltammograms for different rotation rates (60 – 2160 rpm) will be measured. This paves the way for the third section that involves the mathematical modelling of reduction kinetic measurements using MAPLE^{TM} software. Due to the low concentrations of gold in waste electronics and hence in the WEEE leachate solutions, ca. < 1 mol m^{-3}, a three-dimensional cathode i.e. circulating particulate bed electrode (CPBE), which has a high surface area per unit volume and high mass transport rate coefficients was used for the recovery of $AuCl_n^-$. In the last section, the results from the reactor experiments were modelled in terms of mass transport controlled reaction in a plug flow electrochemical reactor (PFER), operated in batch recycle with a continuous stirred tank reactor/reservoir (CSTR).

5.2. Thermodynamic Analysis

Comprehensively reviewed thermodynamic data [1] were used to calculate potential-pH and solubility diagrams for Au-H_2O and Au-Cl-H_2O systems [2,3], for which the full set of data and equations are given in Appendix B(b). From the potential-pH diagram shown in Figure 5-38, it is evident that for the Au-H_2O system, gold is soluble only as Au^{3+} ions at very low pH and under strongly oxidising conditions due to the low solubility of $Au(OH)_3$.

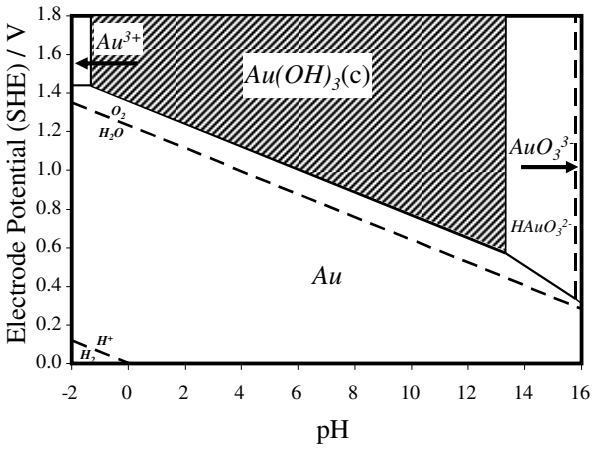

Figure 5-38. Potential pH diagram for gold-water system. Activities: Au^{3+} = 10^{-4}; 298 K, 1 atm [3].

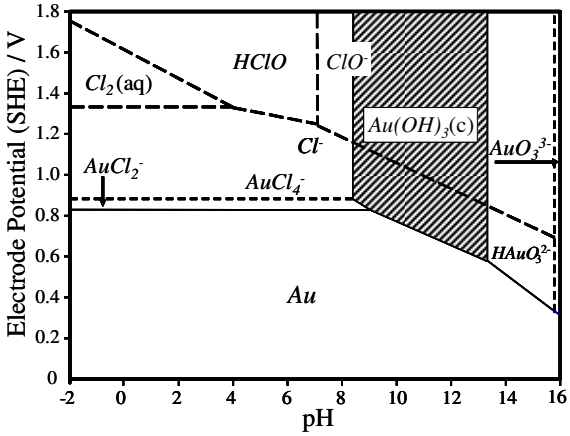

Figure 5-39. Potential pH diagram for gold-chloride-water. Activities: $AuCl_n^-$ = 10^{-4}, Cl^- = 5; 298 K, 1 atm [3].

The addition of chloride ions depassivates the gold hydroxide and significantly increases the potential-pH range in which gold species are stable in solution, due to the formation of gold chloride complexes [3]. Gold may be present in chloride solutions in the +1 and +3 oxidation states, depending on the potential and composition of the solution. At pH 0 the relevant equilibrium reactions are:

$$AuCl_2^- + e^- \rightleftharpoons Au + 2Cl^- \qquad [5\text{-}1]$$

$$E_{AuCl_2^-/Au}(\text{SHE}) / \text{V} = 1.152 + 0.0296 \log\left(AuCl_2^-\right) - 0.118 \log\left(Cl^-\right) \qquad [5\text{-}2]$$

$$AuCl_4^- + 3e^- \rightleftharpoons Au + 4Cl^- \qquad [5\text{-}3]$$

$$E_{AuCl_4^-/Au}(\text{SHE}) / \text{V} = 1.0006 + 0.0197 \log\left(AuCl_4^-\right) - 0.0789 \log\left(Cl^-\right) \qquad [5\text{-}4]$$

Inspite of the standard electrode potential for reaction [5-1] is greater than that for reaction [5-3] which suggests that the gold metal is oxidised to $AuCl_4^-$ ions, the equilibrium potentials of the two reactions depend differently on the gold ion and chloride ion concentrations. Hence, at low gold concentrations and high chloride concentrations, there is a potential window in which $AuCl_2^-$ ions are also stable, as predicted by Figure 5-40. In such a case, the reduction of $AuCl_4^-$ ions could occur sequentially by reactions [5-5] and [5-1].

$$AuCl_4^- + 2e^- \rightleftharpoons AuCl_2^- + 2Cl^- \qquad [5\text{-}5]$$

$$E_{AuCl_4^-/AuCl_2^-}(SHE)/V = 0.925 + 0.0296\log\left\{\left(AuCl_2^-\right)/(AuCl_2^-)\right\} - 0.059\log\left(Cl^-\right) \quad [5\text{-}6]$$

Although the solubility of gold (I) chloride ions is significantly higher than gold (III) ions, it should be noted that gold (I) chloride ions are unstable at high gold concentrations and disproportionate to form gold and gold (III) chloride ions at activities above those given by the reactions [5-7].

$$3AuCl_2^- \rightleftarrows AuCl_4^- + Au + 2Cl^- \quad [5\text{-}7]$$

$$3\log\left(AuCl_2^-\right) = -7.66 + \log\left(AuCl_4^-\right) + 2\log\left(Cl^-\right) \quad [5\text{-}8]$$

The predicted solubilities of Au^{3+}, $AuCl_2^-$ and $AuCl_4^-$ ions solution are plotted in Figure 5-41.

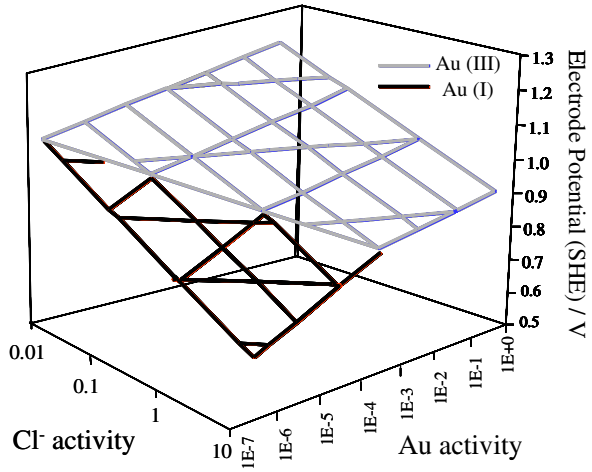

Figure 5-40. Electrode potential for $E_{AuCl_2^-/Au}$ and $E_{AuCl_4^-/Au}$ against gold and chloride concentrations.

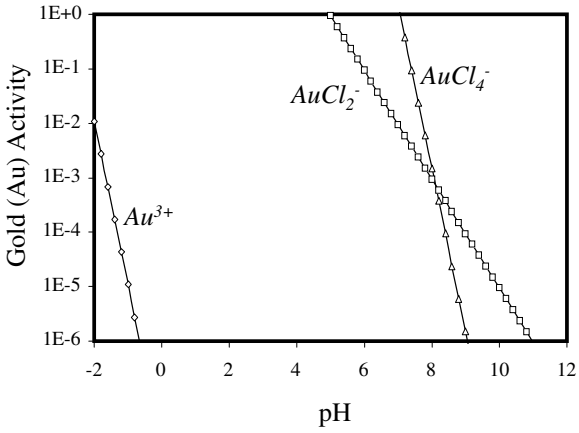

Figure 5-41. Predicted pH dependence of solubilities of Au^{3+} , $AuCl_2^-$ and $AuCl_4^-$ ions. Cl^- = 5; 298 K, 1 atm.

5.3. Transport and Kinetic Analyses

For a solution containing 0.5 mol m^{-3} gold (III) chloride in 4 kmol mol^{-3} HCl + 1 kmol m^{-3} NaCl, the equilibrium potential for reaction [5-1] and [5-3], are +0.639 V (SCE) and +0.616 V (SCE), respectively. At potentials below these values, Au^{III} and Au^{I} ions will be reduced. The voltammetric behaviour of gold chloride species were investigated using platinum (Pt) rotating disc electrode (RDE). Figure 5-42 illustrates the results of the negative-going linear potential sweep from +0.60 V (SCE) to 0 V (SCE) for rotation rates from 60 rpm to 2160 rpm

(1 to 36 s^{-1}).

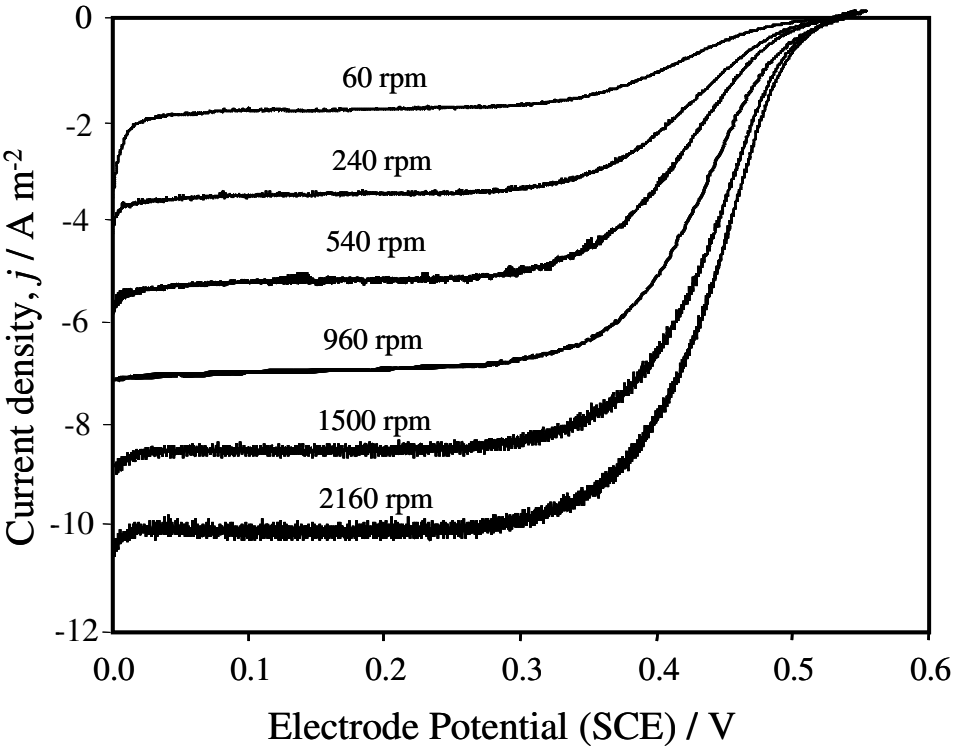

Figure 5-42. Reduction of 0.5 mol m^{-3} Au^{III} at Pt rotating disc electrode in 4 kmol m^{-3} + 1 kmol m^{-3} NaCl, scan rate 10 mV s^{-1}.

Although both $AuCl_2^-$ and $AuCl_4^-$ ions are predicted to be stable in solutions containing 5 kmol m^{-3} chloride ions and 0.5 mol m^{-3} gold chloride ions, two distinct reduction current waves for the successive reduction of $AuCl_4^-$ and $AuCl_2^-$ ions are not evident in Figure 5-42. Nonetheless, two oxidation peaks ($E_{AuCl_2^-/AuCl_4^-} \simeq 0.65\,\mathrm{V}$, $E_{Au/AuCl_2^-} \simeq 0.63$ V (SCE), for Au^{III} and Au^{I} activity of 0.5 respectively) are to some extent apparent at the positive going and potential sweeps to +1.0 V (SCE) as depicted in Figure 5-43 which illustrates the cyclic voltammogram of a Pt RDE rotating at 60,240, and 540 rpm. This may be due to the similar reversible potential for the Au^{III}/Au^{I} couple and the Au^{I}/Au.

Once the Pt disc is coated with a monolayer of gold atoms the rate of gold deposition increases. It was calculated that 5×10^{-6} C of charge need to be passed in order to coat the Pt disk with a monolayer of gold. Moreover, the anodic and cathodic charge, Q_A and Q_C at 240 rpm were measured by integration of the area beneath potential/time dependent plots giving values of 1.04×10^{-3} C and 1.10×10^{-3} C over the range of the potential used, respectively. Hence, the charge yield for gold deposition may be estimated as ca. 0.95.

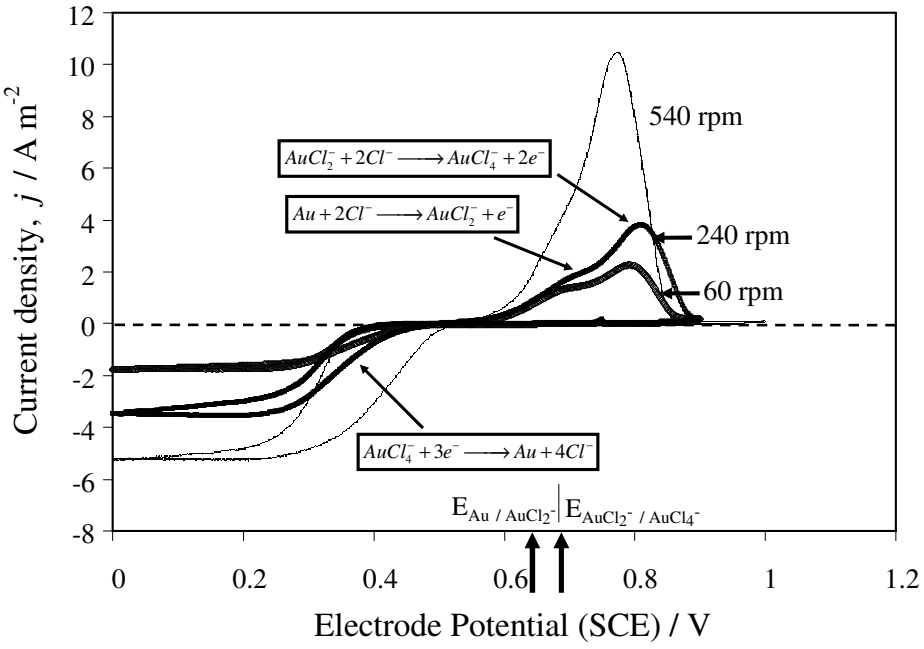

Figure 5-43. Cyclic voltammogram of a Pt rotating disc electrode rotating at 60-240 rpm in 0.5 mol m^{-3} Au^{III} in 4 kmol m^{-3} HCl + 1 kmol m^{-3} NaCl at a scan rate of 10 mV s^{-1}.

Since the kinetics of Au^{III} to Au^{I} reduction were fast, there was no clear Tafel region on semi-logarithmic plot of current density against overpotential.

When the potential was stepped from a value at which no electrochemical reactions occur, to a region where the reduction or oxidation is mass transfer controlled, the concentration of reactant is depleted, the diffusion layer thickness increases and the current decreased with time to its steady state value. The mass transport limited current is proportional to the square root of the rotation rate, and should be given by the Levich equation [5-9].

$$j_L = 1.554 n F D_i^{2/3} \nu^{-1/6} f^{1/2} c_i \qquad [5\text{-}9]$$

At +0.2 V (SCE), the electrodeposition of $AuCl_4^-$ ions onto gold metal was mass transport controlled, with current densities and deposition rates in agreement with those predicted with the Levich equation as shown in Figure 5-44 and the reaction occurred is represented by equation [5-10].

$$AuCl_4^- + 3e^- \longrightarrow Au + 4Cl^- \qquad [5\text{-}10]$$

At higher rotation rates, the experimental results may be slightly higher than the theoretical predictions, because gold deposition from chloride solutions onto a planar electrode may

result in a non-smooth surface of higher surface area. Nonetheless, this should not matter for conditions under which the scale of surface roughness is smaller than the diffusion layer thickness. The $D_{AuCl_4^-}$ calculated from the slope is 7.16×10^{-10} m^2 s^{-1}. This value is almost similar to that obtained by Diaz et al. [3] for a solution containing 0.823 mol m^{-3} total gold (0.625 mol Au^{III} +0.918 mol Au^{I} + 1 kmol HCl m^{-3}), and using platinum as electrode material which was 6.8 $x10^{-10}$ m^2 s^{-1} at room temperature.

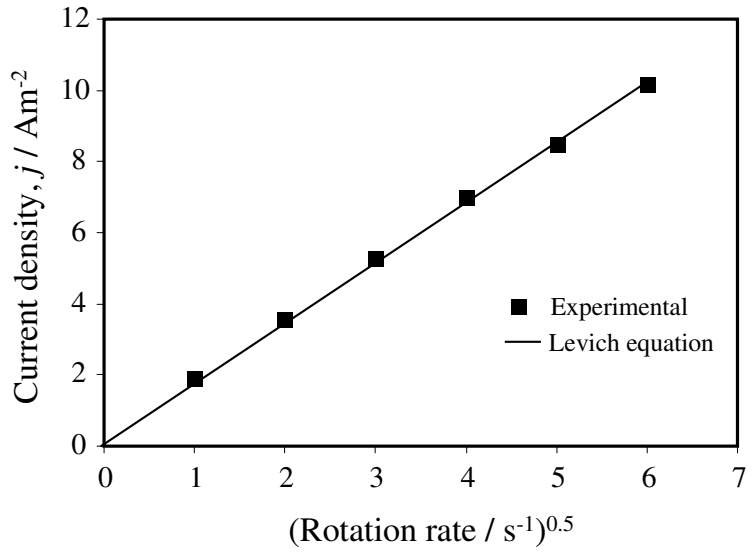

Figure 5-44. Effect of rotation rate on current density for reduction of 0.5 mol m^{-3} Au^{III} at Pt rotating disc electrode in 4 kmol m^{-3} HCl + 1 kmol m^{-3} NaCl.

This diffusion coefficient value, D_i is then used to determine the Nernst diffusion layer thickness, δ_N, , for each rotation rate and subsequently k_m values was calculated by knowing that $k_m = \frac{D_{Zn^{2+}}}{\delta_N}$ and are tabulated in Table 5-10 below.

Table 5-10. Calculated δ_N and k_m values for different rotation rates.

Rotation rate / s^{-1}	Square root of rotation rate / $s^{-0.5}$	$\delta_N \times 10^{-5}$ / m	$k_m \times 10^{-5}$ / m s^{-1}
1	1	5.45	1.31
4	2	2.66	2.69
9	3	1.79	4.01
16	4	1.44	4.97
25	5	1.19	6.22
36	6	0.91	7.90

Figure 5-45 shows the overpotential required to nucleate the gold deposit onto the Pt disc. The Tafel coefficient, β and the exchange current density j_0 (Figure 5-46) or the reduction of gold (III) chloride ions to gold onto gold disc are 35.4 V^{-1} and 8.5×10^{-2} A m^{-2} respectively. On the other hand, a Tafel plot for the electrodeposition of gold from a solution gold (III) chloride ions on a Pt surface, has a lower value Tafel coefficient, β of 10.2 V^{-1}. This value is expected because more energy is required to nucleate gold on a Pt substrate than on a gold substrate.

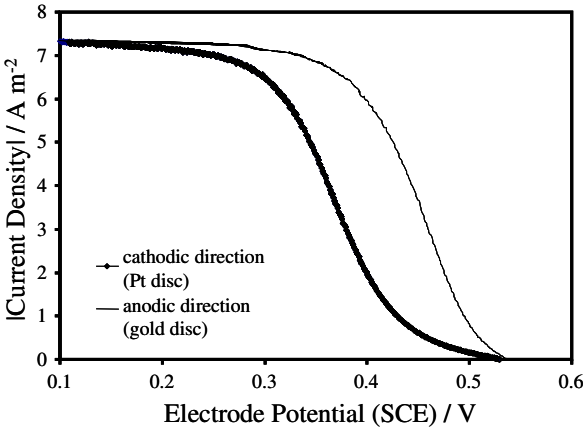

Figure 5-45. Effect of electrode potential on current density for reduction of 0.5 mol m^{-3} Au^{III} on Pt and Au-plated Pt RDE in 4 kmol m^{-3} HCl + 1 kmol m^{-3}; scan rate 10 mV s^{-1}, rotation rate 960 rpm.

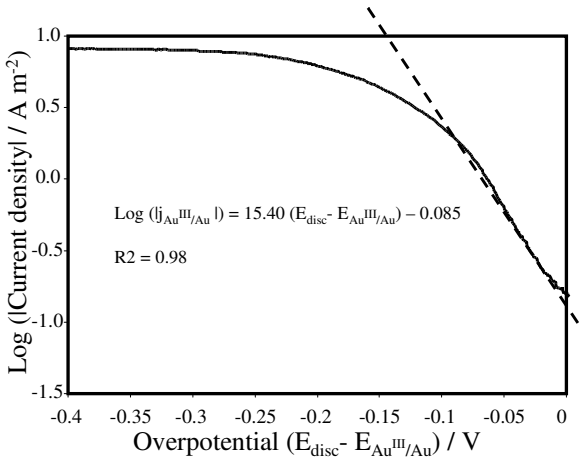

Figure 5-46. Tafel plot for reduction of 0.5 mol m^{-3} Au^{III} at Au coated Pt RDE in 4 kmol m^{-3} + 1 kmol m^{-3} NaCl, scan rate 10 mV s^{-1}, rotation rate 960 rpm.

Initially, it was found that two separate reduction current waves for the reduction of $AuCl_4^-$ and $AuCl_2^-$ ions were not apparent during a linear sweep voltammogram at a low scan rate (10 mV s^{-1}) with the system at steady state. Therefore, the potential sweep rate was increased to investigate the mechanism of gold (III) reduction. At the voltammetry steady state, as the potential swept to a more negative potential in value than the equilibrium potential of gold chloride, it will be reduced with an initial exponential increase in the rate with the potential. When the kinetically controlled rate is fast enough to deplete the concentration of gold chloride at the electrode surface to zero, the reaction rate becomes limited by the mass transport (diffusion) of gold to the electrode surface. As the scan rate increases, it takes less time to sweep the electrode potential as less time is available for electrochemical reactions to occur. Hence, at the same potential, the depletion of the reactant at the electrode surface is lower than the steady state distribution, resulting in a steeper concentration gradient and a higher current. A maximum is reached as a result of the balance between the increasing rate constant and the decreasing surface concentration with time, the current of which is given by Randles-Sevcik equation [5-11] for solution phase reactants and products. Once the peak has been reached, the current decays with $time^{-2}$ (or $potential^{-2}$).

$$i_p = 0.4463nFAC_i\left(\frac{nF}{RT}\right)^{1/2} \nu_s^{1/2} D_i^{1/2} \qquad [5\text{-}11]$$

Figure 5-47 shows that two current peaks became evident during the reduction of gold (III) chloride ions to gold when the electrode potential was scanned at 1 V s^{-1}, implying that there are at least two steps involved in the mechanism. From the magnitude of the current peaks, the reduction process probably involved a two electron reduction $Au^{III}Cl_4^-$ to $Au^{I}Cl_2^-$ followed by a one electron reduction of $AuCl_2^-$ to Au^0. $D_{AuCl_2^-}$ is derived to be 1.9×10^{-9} m^2s^{-1} which echoed the value of 1.3×10^{-9} m^2s^{-1} that has been reported previously by Diaz et al.[3] Futhermore, $D_{AuCl_4^-}$ is calculated as 9.9×10^{-10} m^2 s^{-1}.

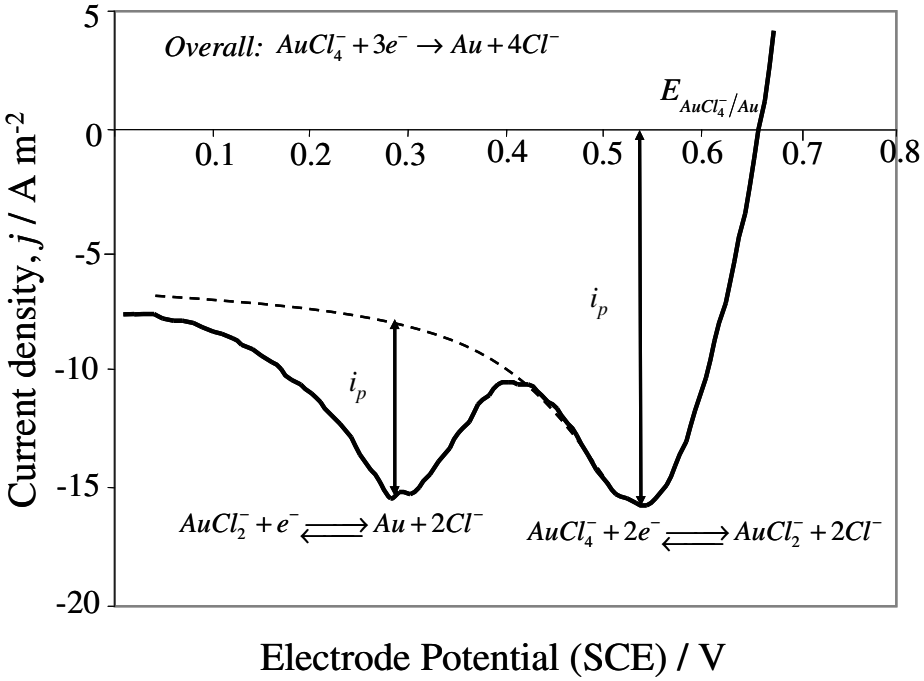

Figure 5-47. Linear potential sweep voltammogram for reduction of 0.5 mol m^{-3} Au^{III} at Pt rotating disc electrode in 4 kmol m^{-3} HCl + 1 kmol m^{-3} NaCl, scan rate 1 V s^{-1}; 60 rpm.

5.4. Kinetic Model of $AuCl_n^-$ reduction

The rotating disc experiments show that for an electrolyte containing 0.5 mol m^{-3} Au^{III} and 5 kmol m^{-3} Cl$^-$ ions, the reduction and electrodeposition of gold is likely to proceed by the sequential reactions:

$$AuCl_4^- + 2e^- \rightleftharpoons AuCl_2^- + 2Cl^- \qquad [5\text{-}12]$$

$$AuCl_2^- + e^- \rightleftharpoons Au + 2Cl^- \qquad [5\text{-}13]$$

However, due to the small difference in equilibrium potentials for the reduction of $AuCl_2^-$ and $AuCl_4^-$ ions, it was not possible to determine the reduction kinetics experimentally. Therefore, a mathematical model for the reduction of gold chloride was developed, to compare the experimental results, and improve the values of kinetic parameters used in the modelling process. At potentials positive of the potential of zero charge, the electrode is likely to adsorb negatively charged species [4]. The kinetic model mechanism for the reduction of $AuCl_n^-$ ions from aqueous chloride electrolytes are given in Appendix C(b).

Nevertheless $[AuCl_2^-]_{surf}$ is not defined, so it may be necessary to adjust kinetic parameters for forward and reverse reactions. The mass balance equations (Appendix D(a)) were solved

using the '*solve*' function in Maple™ software (www.maplesoft.com). A predetermined mass transfer coefficient, k_m of disc electrode at various rotation rates (Table 5-10) was used in the model. The rate coefficients ($k_{c1} = k_{c2} = 6\times10^{-7}$ s^{-1}, $k_{c3} = 4\times10^{-7}$ s^{-1}, $k_{ads} = 1\times10^{-8}$ s^{-1} , $k_{des} = 1\times10^{-7}$ s^{-1}) being selected from the published data by Cheng et. al [4] and being fitted according to the experimental data obtained from the Au^{III} rotating disc experiment as shown in Figure 5-42. The full algorithm and mathematical codes to solve the equations are provided in Appendix E(a). Figure 5-48 shows the current density - potential behaviour. The rate of overall reduction of $AuCl_4^-$ ions to elemental gold becomes totally mass transport controlled at potentials < + 0.30 V (SCE). Figure 5-49 shows the corresponding dependence on electrode potential of the concentrations of gold species at, and adsorbed on, the electrode surface.

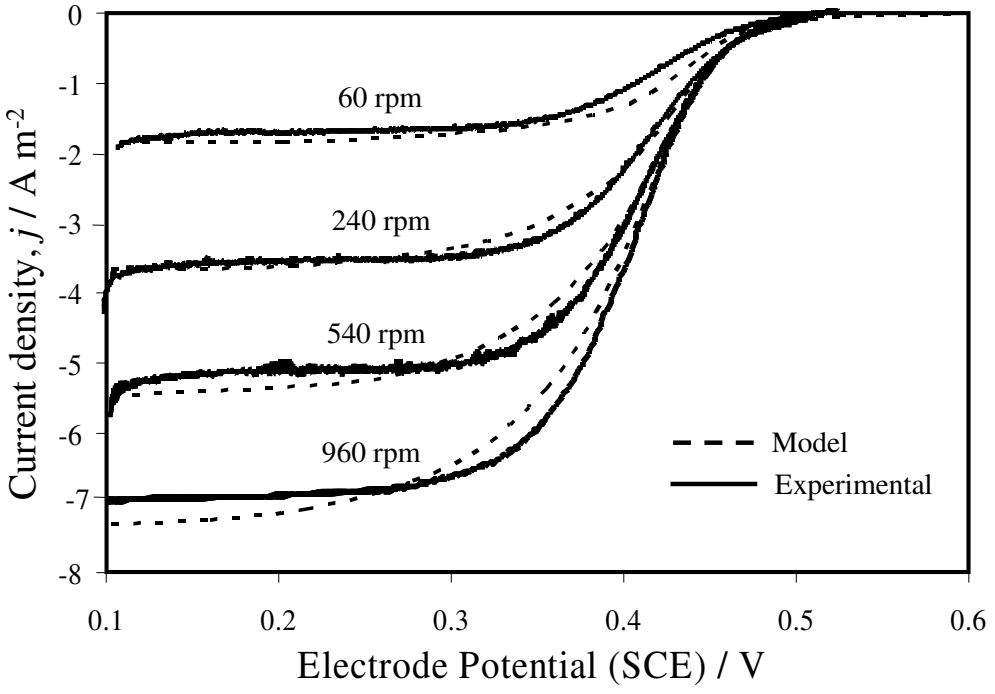

Figure 5-48. Prediction of potential-current relationship from the kinetic model solved with Maple™, compared to experimental data for the reduction of 0.5 mol m^{-3} Au^{III} in 4 kmol m^{-3} HCl +1 kmol m^{-3} NaCl.

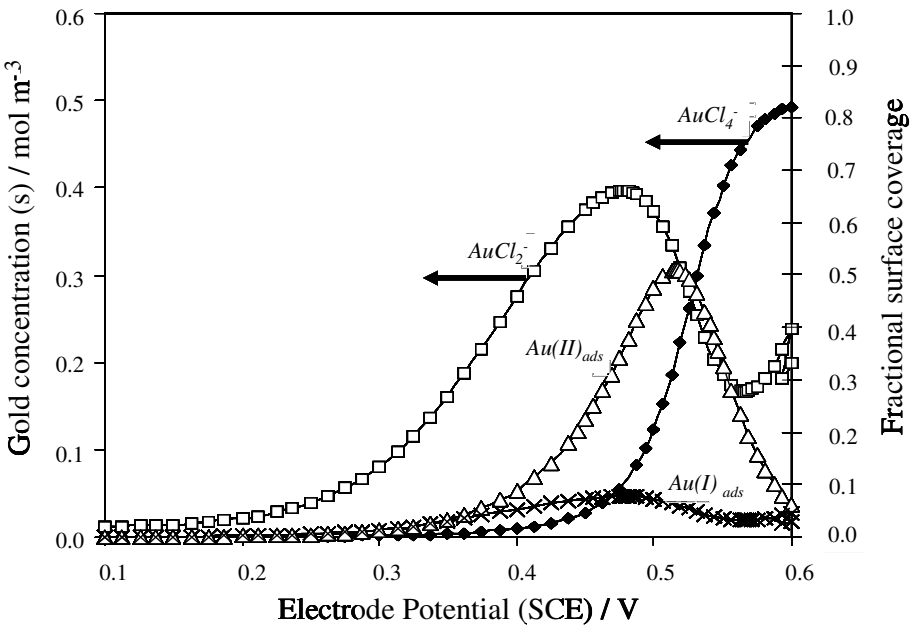

Figure 5-49. Predicted electrode potential dependence of surface concentrations of $AuCl_4^-$ and $AuCl_2^-$ and fractional coverages of Au(I)(θ_I) and Au(II)(θ_{II}) adsorbed species.

5.5. Gold Electrodeposition in Circulating Particulate Beds Electrode (CPBE) Reactor

It has been discussed in the Literature Review (Chapter 2), that a CPBE reactor can be used to recover copper from chloride solutions by electrodeposition. However, because of the 3-D nature of the electrode, and the potential drop in the direction of current flow, for a 0.01 m deep cathode it is necessary to keep the metal ion concentration below 10 mol m^{-3}. Since the concentrations of gold in leachate solutions from WEEE are likely to be below 1 mol m^{-3}, a CPBE reactor is attractive for the deposition of gold due to the high specific surface area and/or high mass transport rates coefficients.

As has been explained in Chapter 3 (Materials and Experimental Methods), graphite particles in 0.5-1 mm spheres were used as the cathode to electrodeposit gold in the CPBE reactor. The density of the graphite particles of ca. 2.5 g cm^{-3} was found to be low in comparison to the density of the electrolyte, and hence the particles were too sensitive to inlet flow rate and liable to float in the electrolyte. This problem would occur only during the start-up phase, because the average density of the particles will increase as they are metallised. Thus, a layer of gold of at least 5 μm thick was required to increase the effective density enough to prevent the particles floating in a 5 kmol m^{-3} Cl^- solution.

As has been reported previously by Cheng et al.[4], about 10 % of the $AuCl_4^-$ ions in solution

were removed by adsorption onto the virgin graphite particles. A solution of 0.5 mol m^{-3} (ca. 98 g m^{-3}) gold chloride in 1 kmol m^{-3} HCl was pumped through the packed bed reactor with no potential applied to the cathode feeder for 1 hour, and the gold concentration was reduced to 90 g m^{-3}. This phenomenon has been exploited for the recovery of gold from chloride solutions in CPBE, but the rate of adsorption of gold onto graphite is low and the maximum loading of the graphite by this method is also lower than by electrowinning.

Figure 5-50 shows the results of the negative-going linear potential sweep from +0.60 V (SCE) to 0 V (SCE) for the reduction of $AuCl_4^-$ ions in the CPBE reactor, at a flow rate of 0.25 dm^3 min^{-1}. The current was noisier than for a planar rotating disc, due to the small potential drop in the 3D electrode and the noise due to the variation in number of particles in contact with the feeder at any time. However, it was possible to see that the reduction of gold is mass transport controlled at +0.20 V (SCE). The mass transport controlled current when the particles were circulating, was about half the initial current with no particles, suggesting that about 50 % of the particles were active at any one time. While it would have been possible to deposit gold as a packed bed, if the particles were not moving, there was the risk of forming bridging deposits and poor deposit morphologies. With no flow to replenish reactants, the gold would also have been depleted and the reaction rate would have decreased quickly in a packed bed reactor, and so overall the gold deposition rate was unlikely to be faster than for the CPBE reactor.

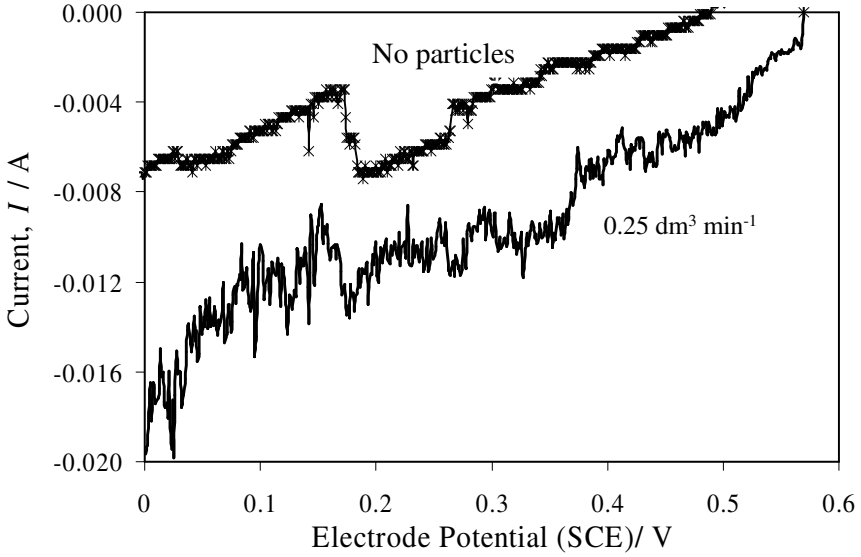

Figure 5-50. Steady state current-potential behaviour for reduction of 0.5 mol $AuCl_4^-$ m^{-3} in CPBE reactor.

During the electrodeposition process of gold onto the unseeded graphite particles, the Au^{III} concentration was calculated from the solution absorption, measured by UV-Vis spectrophotometry through fibre optics apparatus, using the absorptivity for Au^{III} concentrations (λ_{max} = 312 nm, molar absorptivity, ε_{312} = 662.1 mol^{-1} m^2), so enabling Au^{III} / Au^{I} molar ratios to be determined. The total of gold concentration of each sample was also analysed using ICP (Inductively Coupled Plasma – Perkin Elmer Instruments Optical Emission Spectrometer Model Optima 2000 DV). Figure 5-51 depicts the reading of the absorbance of solution during gold electrodeposition in CPBE for ca. 3 hours. The peak at ca. 225 nm was contributed by the concentration of aqueous chlorine in the sample.

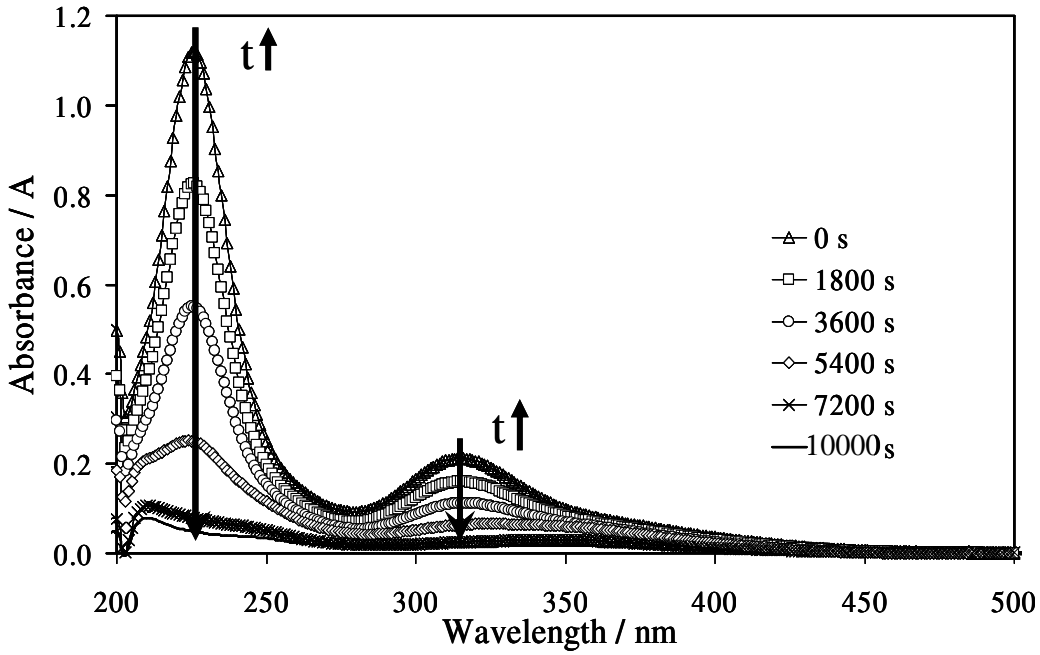

Figure 5-51. Absorbance of solution during gold electrodeposition in CPBE at + 0.20 V (SCE); path length 1 mm measured via fibre optics, at time, t.

As can be seen in Figure 5-52, and as was expected from the kinetic measurements at the planar RDE, the reduction of $AuCl_4^-$ ions was faster than that of $AuCl_2^-$ ions on carbon due to the additional overpotential driving force required for the nucleation of a new phase. This resulted in an initial accumulation of $AuCl_2^-$ ions during the first electrodeposition process onto fresh graphite.

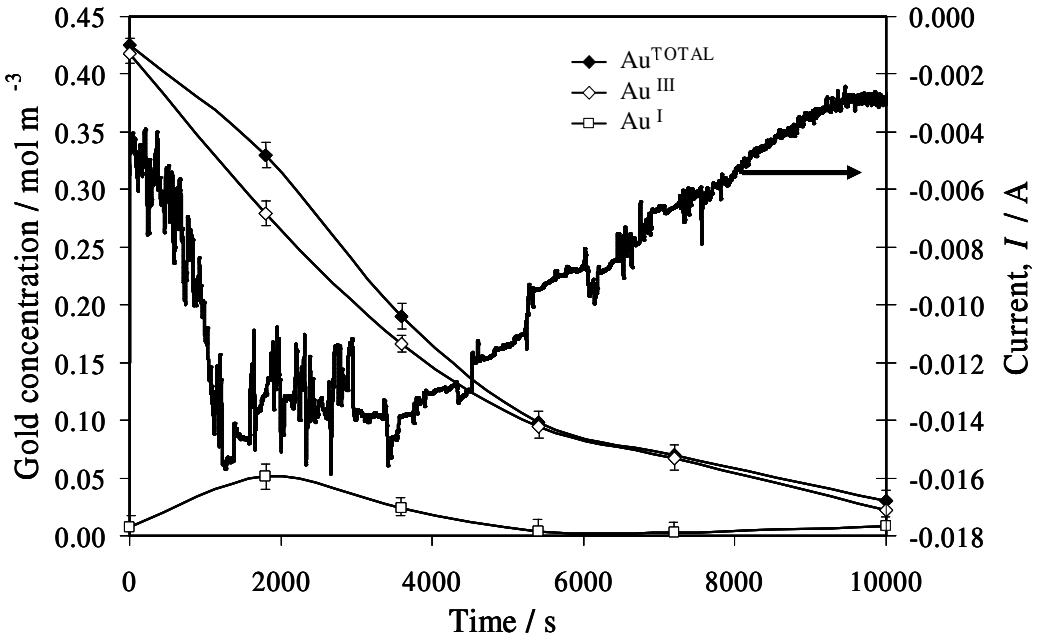

Figure 5-52. Current and gold concentration with time during electrodeposition on virgin graphite particles in CPBE reactor at + 0.20 V (SCE); flow rate = 0.25 dm^3 min^{-1}.

Figure 5-53 shows images of Au deposits in the CPBE(a) on the feeder Ti cathode and (b) on the graphite particulates in the catholyte compartment. Even Au deposition was observed on the feeder cathode unlike in the packed bed of graphite particulates. On the feeder cathode, the majority of Au deposition occurred along the area corresponding to the draft tube as well as on the feeder cathode area corresponding to the particulates packed bed. Since the voidage in the draft tube and above the packed bed was higher with respect to that in the packed bed, the effective conductivity of electrolyte in those areas was higher, and hence became the preferred paths for the current flow. In order to ensure maximum amount of current passing through the particulates packed bed and to fully utilise the large surface area provided by the graphite particulates to ensure high Au removal rates, the feeder cathode areas corresponding to the draft tube and above the packed bed were insulated (lacquered) with acrylic to block the current routes by-passing the packed bed [6].



(a) Au plated on Feeder Electrode



(b) Au particulates inside the catholyte compartment

Figure 5-53. Images of gold deposits in the CPBE: (a) on the feeder cathode electrode and (b) on the Au particulates inside the catholyte compartment.

The increase in reaction rate of gold deposition and particle conductivity as the virgin graphite was plated in gold can be seen by the increase in measured current (Figure 5-53). The peak in the magnitude of the (negative) reduction current after 3500 s was as a result of the interfacial area increasing with time until the growing nuclei coalesced, while the concentration of dissolved gold in solution decreased. Having metallised the graphite particles, in further electrodeposition experiments at +0.20 V (SCE), >99 % of the gold was recovered from solution in just over 2 hours (Figure 5-54). The initial current was nearly double that with the bare graphite, even though the initial concentration current was lower (0.33 mol m^{-3} against 0.44 mol m^{-3}), probably because the kinetics of gold reduction are slower on graphite than on gold. Therefore, while the reduction of $AuCl_4^-$ ions to Au on a gold surface is mass transport controlled at +0.20 V (SCE), this is not the case on graphite. The conductivity of the particles would also have increased once coated with gold, so more of the bed would have been electrically active.

It can also be seen in Figure 5-54 that on gold, the reduction of $AuCl_4^-$ ions occurs at the same

rate as the reduction of $AuCl_2^-$ ions. Hence since Au^I does not appear in solution, it is possible to follow the electrowinning of gold, at potentials where the reduction is mass transport controlled online via fibre optics by measuring the Au^{III} concentration with UV-Vis spectrometry. However, online measurement is only applicable for a diluted gold concentration (< 1 mol m^{-3}).

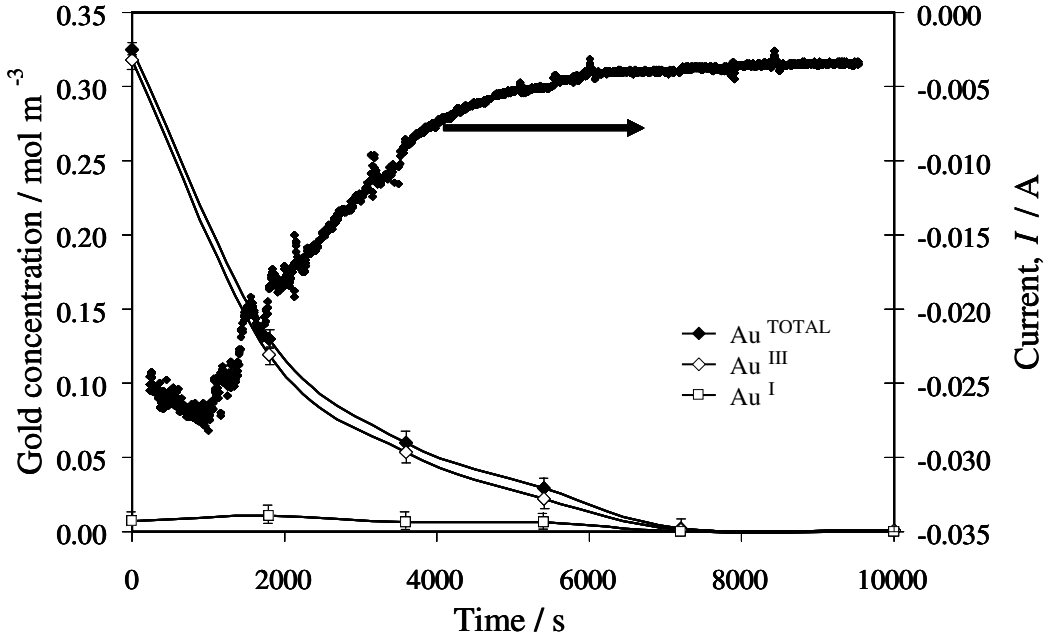

Figure 5-54. Depletion of Au^{III} concentration and current with time during batch recycle electrowinning on gold metallised particles in CPBE reactor with feeder electrode at + 0.20 V (SCE); flow rate = 0.25 dm^3 min^{-1}.

The plateau in current of about 4 mA after ca. 8000 s (Figure 5-54), is probably due to reduction of dissolved oxygen by:

$$O_2 + 4H^+ + 4e^- \rightarrow 2H_2O \qquad [5\text{-}14]$$

The main source of dissolved oxygen was the aqueous H_2SO_4 anolyte, which would have been supersaturated with oxygen and for which Nafion membranes have been reported to have high solubility and diffusion coefficients [8]. For typical Nafion membranes, of 1.78×10^{-5} m thickness [7], the diffusion coefficient of oxygen was 5×10^{-11} m^2 s^{-1} and the solubility was 15 mol m^{-3}[5]. As oxygen was generated at the anode of the CPBE reactor, the anolyte dissolved oxygen concentration would have increased and because of the diffusion across the membrane, the catholyte dissolved oxygen concentration would have also increased with time. The maximum current at the 0.1 m^2 area graphite cathode, from the reduction of

dissolved oxygen, limited by diffusion across a typical Nafion membrane, was predicted to be 3.3 mA. This reduction of dissolved oxygen decreased the charge efficiency for gold electrowinning to ca. 0.90. However, this loss of efficiency will be less of a problem if the leaching and electrochemical reactors are coupled, since the anolyte will be a chloride solution to generate chlorine which has a much lower solubility and diffusion coefficient through Nafion membranes [5].

The concentration decay during the electrodeposition of gold under mass transport control can be approximated to the general form expected for a model steady-state plug flow reactor (PFR), coupled to a CSTR. Hence, for a mass transport controlled reaction, the concentration should decay exponentially with time according to equation [5-15], and as shown experimentally in Figure 5-55. The $k_m A_a$ values were measured as 1.1×10^{-5} m s^{-1} for deposition on virgin graphite particles and 1.3×10^{-5} m^3 s^{-1} for deposition on Au-plated graphite particles.

$$c_t = c_o \exp\left\{-\frac{\dot{v}t}{V}\left[1-\exp\left(-\frac{k_m AaL}{\dot{v}}\right)\right]\right\} \qquad [5\text{-}15]$$

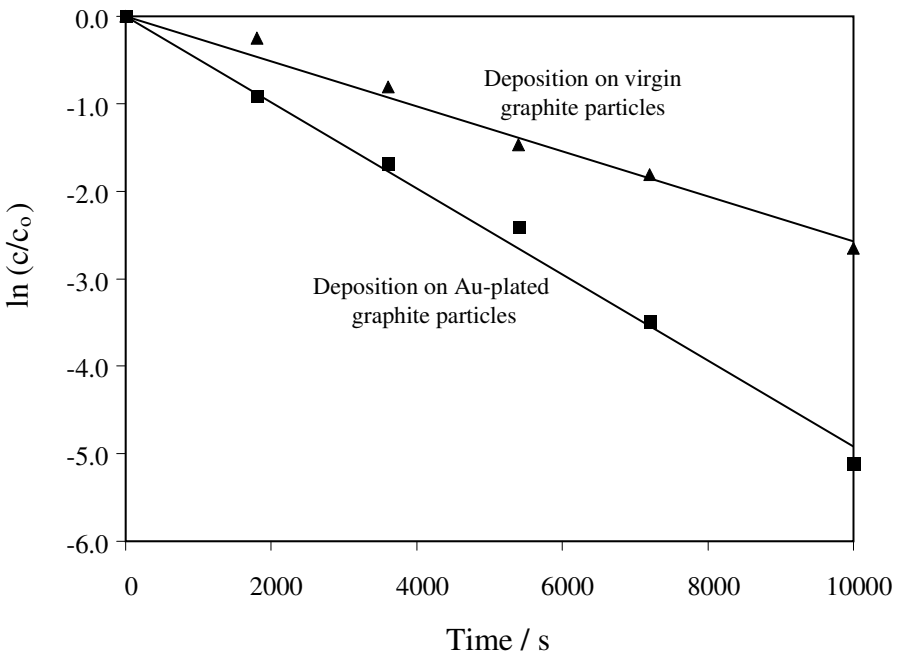

Figure 5-55. Depletion of dissolved Au^{III} concentration with time during batch recycle reduction in CPBE reactor with feeder electrode at +0.20 V (SCE); flow rate= 0.25 dm^3 min^{-1}.

It was considered that increasing the inlet flow rate increased the mass transfer rate within the CPBE and therefore, may increase electrodeposition rates. However, at higher flow rates, the graphite particles were entrained up the draft tube from the bottom of the particle bed faster than they could be replaced by the falling particles from above. Hence, the lower part of the bed was not a descending packed bed in contact with the feeder electrode and was unable to deposit gold at the electrode. Therefore, the overall electrodeposition current at higher flow rates was lower as shown in Figure 5-56.

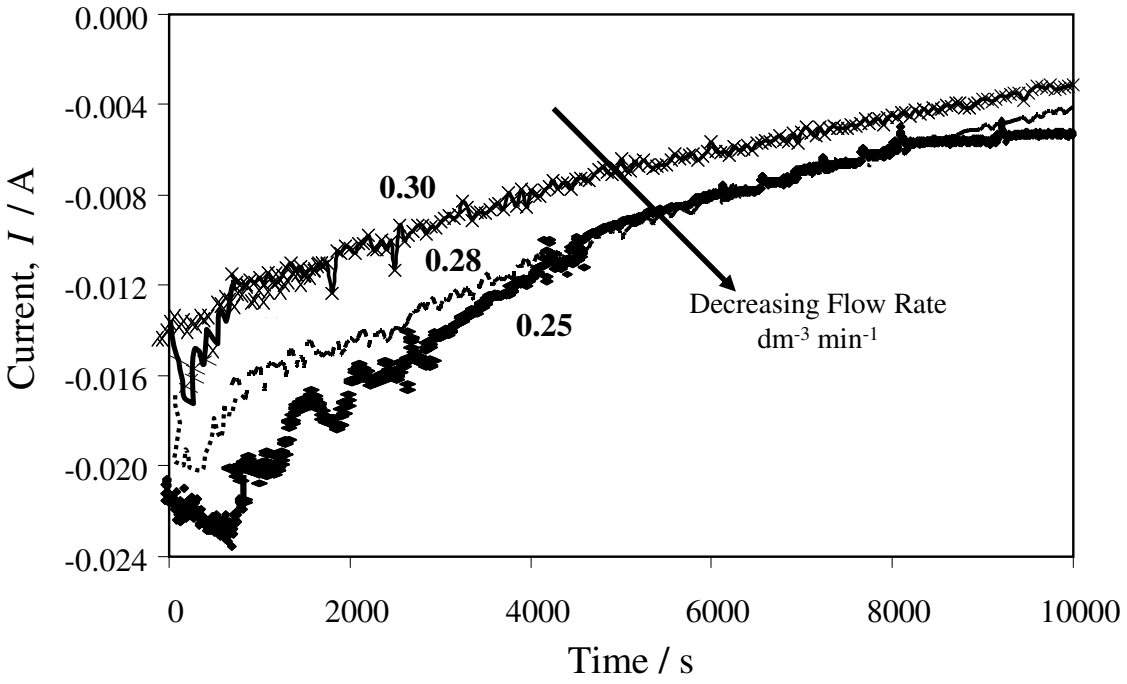

Figure 5-56. Effects of flow rate on the time dependency of current, for gold deposition in a CPBE reactor at a feeder cathode potential of +0.20 V (SCE) and an initial gold concentration of 0.5 mol m^{-3}.

It has been shown that gold chloride ions can be depleted from solution by electrodeposition, to concentrations that were analytically undetectable. Gold was recovered with high current efficiencies (Figure 5-57) and very low specific electrical energy consumption (equation [5-16]) of 800-1300 kW h (tonne Au)$^{-1}$ for cell voltages (U) of 2.0-3.0 V and fractional current efficiencies of ca. 0.95.

$$w \ / \text{kW h (tonne } Au)^{-1} = \frac{\nu_e F}{\Phi_i^e} \cdot \frac{U}{3.6 M_{Au}} \qquad [5\text{-}16]$$

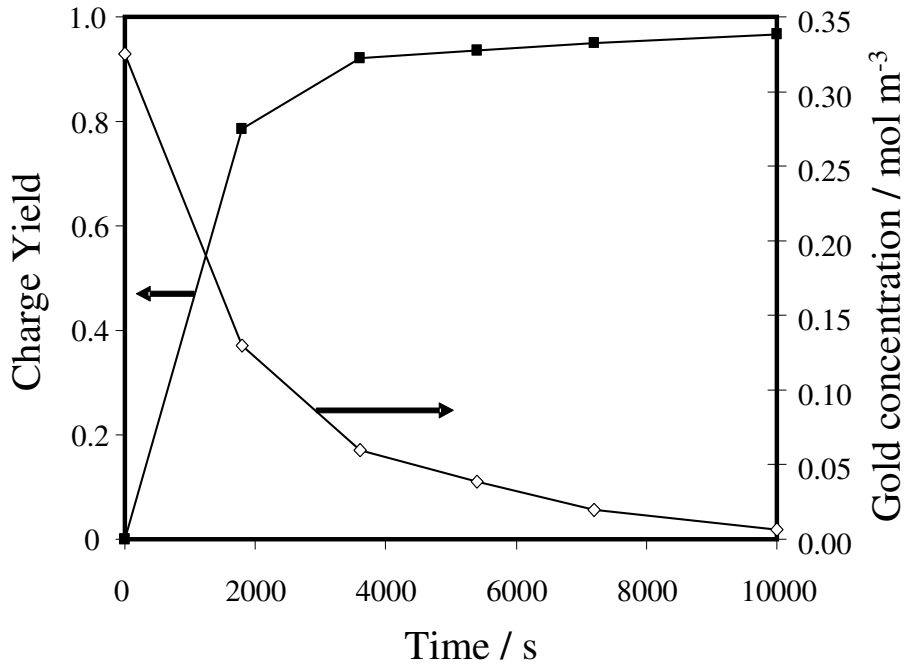

Figure 5-57. Depletion of dissolved gold concentration with time during batch recycle reduction in CPBE reactor with feeder electrode at + 0.20 V (SCE); flow rate = 0.25 dm^3 min^{-1}.

5.6. Deposit morphologies

The morphology of the Au deposits was one of the major factors that determine if the CPBE was feasible for the recovery of Au from the catholyte (leach solution). Au deposits formed from a chloride media tend to be dendritic [9,10], which break from the electrode's surface easily, re-dissolve in the catholyte and hence, reducing current efficiency. Coherent and adherent Au deposit was essential for maintaining a high current efficiency, achieving a reasonable Au loading on the electrode and enabling the transfer of metals-coated electrode to the electro-refining stage [4].

Figure 5-58 shows a SEM image of virgin graphite beads which will be used as a cathode in the CPBE. As the density of the graphite particles is recorded ca. 2.5 g cm^{-3}, it is essential to metallise the virgin graphite particles. Thus, a layer of gold of at least 5 μm thick was required to increase the effective density enough to prevent the particles floating in a 5 kmol m^{-3} Cl^- solution.

Figure 5-60 depicts a SEM image of Au deposits on a graphite particulate in the CPBE, operating mass transport control, at a feeder cathode potential of +0.20 V (SCE). The average

diameter of graphite particulates before and after Au deposition, measured under a microscope, was 520 and 530 μm, respectively which are shown in Figure 5-59. Therefore, the thickness of the Au deposits was ca. 10 μm.

Subsequently, the metallised graphite particulates were used to deposit Au from the actual WEEE leachate. The morphology obtained at +0.20 V (SCE), Au deposited under total mass transport control were adherent to the particulates and depicts a compact cauliflower structure and little voidage. Random samples of Au particulates had been chosen from the packed bed cathode showed similar structure to that of Figure 5-60, which proved that the constant collusions between the Au particulates in the CPBE were able to improve the morphology of the deposits.

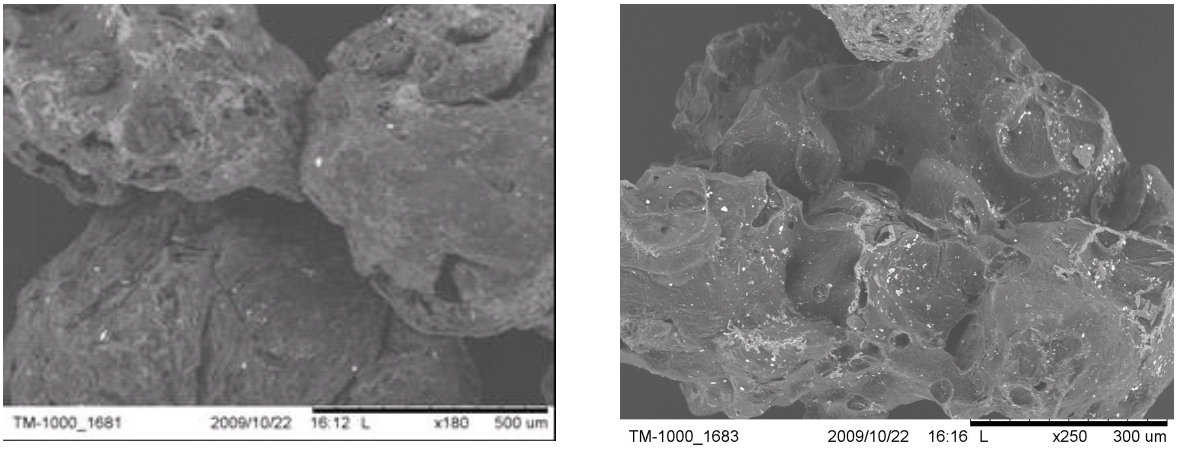

Figure 5-58. SEM image of virgin graphite particles (0.5- 1 mm) used as cathode in the CPBE.

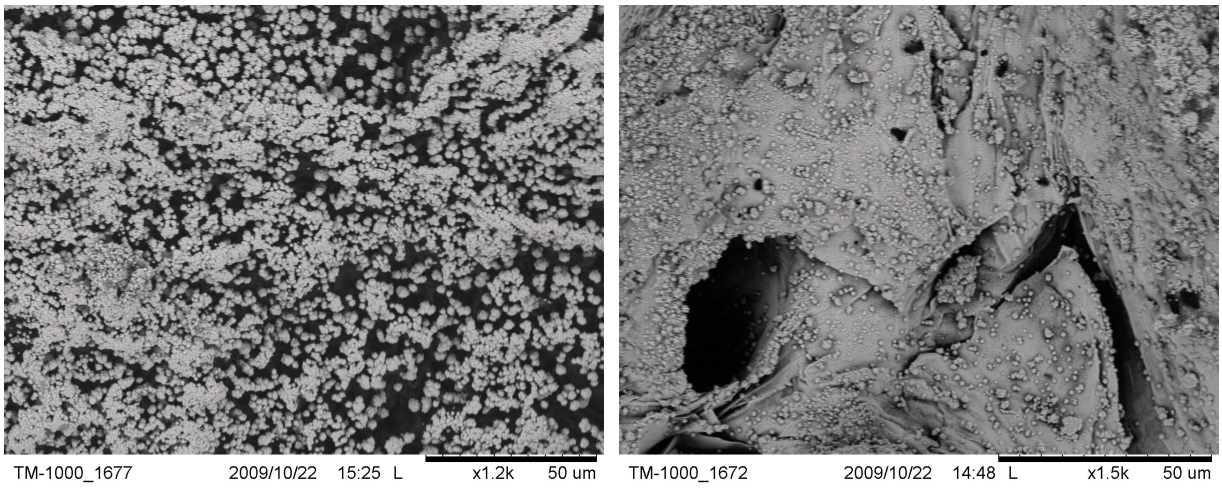

Figure 5-59. SEM images of 10 µm gold deposits on virgin graphite particles.

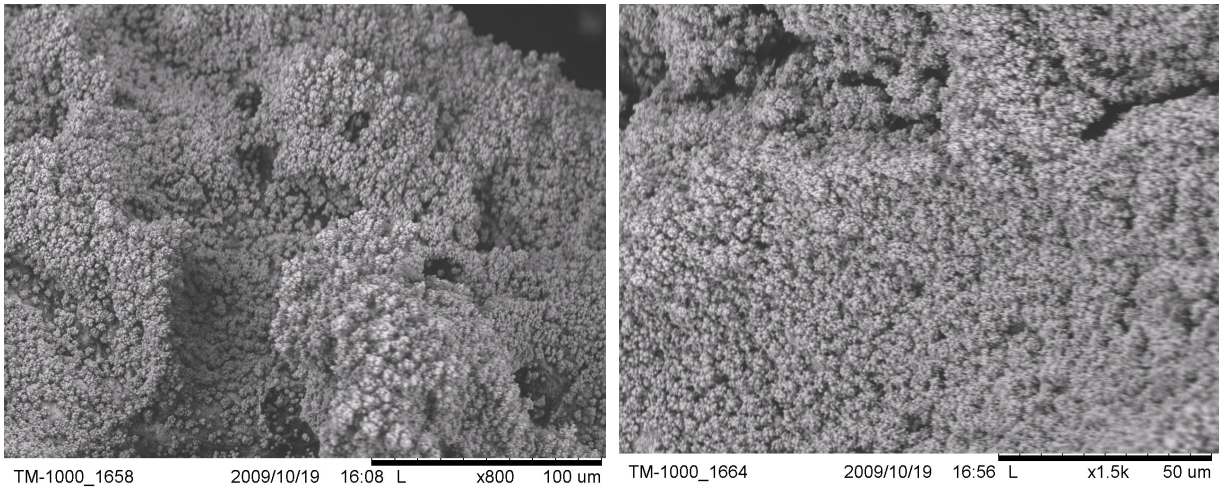

Figure 5-60. SEM image of gold deposits on a Au-pre plated graphite particulate in the CPBE operating at a feeder cathode potential of +0.20 V (SCE).

5.7. Chapter Summary

Experimental results demonstrated that the CPBE was suitable for the recovery of Au from the leach solution produced by leaching metals from WEEE. Concentrations <0.5 mol m^{-3} (< 10^2 g m^{-3}) of $AuCl_4^-$ and $AuCl_2^-$ ions in 4 kmol m^{-3} HCl + 1 kmol m^{-3} NaCl in aqueous electrolyte were successfully reduced to elemental gold in CPBE of 0.5-1 mm graphite particles, in an electrochemical reactor incorporating a cation- permeable membrane and operated in bath recycle mode. Depletion to concentrations < 5 x 10^{-3} mol m^{-3} (< 1 g m^{-3}) appeared to be mass transport controlled at an applied potential of +0.20 V (SCE) and specific electrical energy consumption (SEEC) of ca. 800-1300 kW h (tonne Au)$^{-1}$ for cell voltages (U) of 2.0-3.0 V and fractional current efficiencies of ca. 0.95. However, atomic absorption and UV spectrophotometry established that, as the ($[AuCl_4^-]$+ $[AuCl_2^-]$) concentration decayed, the $[AuCl_2^-]$:$[AuCl_4^-]$ molar ratio changed. A multi-step mechanism for reduction of $AuCl_4^-$ ions proposed by Cheng et al. explained this behaviour in terms of changing overpotentials for $AuCl_4^-$ and $AuCl_2^-$ reduction as total dissolved gold concentrations decreased. In addition, SEM images confirmed that adherent and coherent Au deposits were achieved with CPBE for Au deposition under mass transport control, which is at +0.20 V (SCE).

5.8. References

[1] Bard, A.J., Parsons, R. and Jordan, J., 1985, Standard potentials in aqueous solutions, Marcel Dekker, New York.

[2] Kelsall, G. H., Welham, N.J. and Diaz, M.A., 1993, Thermodynamics of Cl-H_2O, Br-H_2O, I-H_2O, Au-Cl-H_2O, Au-Br-H_2O and Au-I-H_2O systems at 298 K. *J. Electroanal. Chem.*, 361 (1/2): 13-24.

[3] Diaz, M.A., Kelsall, G.H. and Welham, N.J., 1993, Electrowinning coupled to gold leaching by electrogenerated chlorine. I. Au(III)-Au(I)/Au kinetics in aqueous Cl_2/Cl^- electrolytes. *J. Electroanal. Chem.*, 361 (1/2): 25.

[4] Cheng, C-Y., Diaz, M.A., Kelsall, G.H. and Robson, A.C., 2006, Gold Electrowinning from Acidic Aqueous Chloride in a Packed Bed Electrode. *ECS Trans.*, 2 (3): 317-328.

[5] Davis, T.A., Genders, J.D. and Pletcher, D., 1997, A first course in ion permeable membranes Electrochemical Consultancy, Romsey, England.

[6] Dawson, R.J., 2006, Electrochemical Recovery of Platinum and Palladium from Alumina-Supported Catalysts. Ph.D. Thesis, Chemical Engineering, Imperial College London.

[7] Ion Power website (http://www.ion-power.com/res/98-05_Nafion_N-424.pdf).

[8] Sakai, T., Takenaka, H. and Torikai, E., 1986, Gas Diffusion in the Dried and Hydrated Nafions. *J. Electrochem. Soc.*, 133 (1): 88-92.

[9] Schalch, E., Nicol, M.J., Diggle, J.W., Charlton, B.D. and Vaessen, J.P.H., 1976. An Electrochemical and Kinetic Investigation of the Behaviour of Gold in Chloride Solutions. I. The Cathodic Deposition of Gold, Report No. 1848, *Natl. Inst. Metallurgy, Mineral Process Chem. Div.*, Johannesburg, South Africa.

[10] Nicol, M.J., 1976, An Electrochemical and Kinetic Investigation of the Behaviour of Gold in Chloride Solutions. III. The Gold(III)/Gold(I) Reaction on Platinum and the Disproportionation of Gold(I), Report No. 1846, *Natl. Inst. Metall. Mineral Process Chem. Div.*, Johannesburg, South Africa.

6. COPPER ELECTRODEPOSITION

6.1. Chapter Overview

This chapter is divided into five major sections. In the first section, the thermodynamics of copper-water (Cu-H_2O) and copper-chloride-water (Cu-Cl-H_2O) systems are presented. In the second, the rotating (Pt) disc electrode has been used to determine the reduction (micro-) kinetic data for copper in solutions of 4 kmol m^{-3} HCl + 1 kmol m^{-3} NaCl which were subsequently modelled using MAPLE^{TM} software. Metal chloride ions in the leach solutions can be partially reduced to form dark coloured intermediate species of mixed oxidation states, under potentiostatic or galvanostatic operation. The existence of copper chloride complexes had been confirmed by spectrophotometry [1]. Therefore, in the third section, we attempted to determine the concentration of these mixed oxidation states species and to investigate if the partially reduced mixed oxidation state species, constitute a problem for copper electrodeposition; using cyclic voltammetry. In the fourth section, copper electrodeposition was investigated using an electrochemical reactor with a Ti/Ta_2O_5-IrO_2 anode, cation-permeable membrane and a Ti mesh cathode in a fluidised bed of 590-840 μm glass beads to enhance mass transfer rates and to improve copper deposit morphologies. The effects were ascertained by the cathode deposition rates, charge yields, specific electrical energy consumptions, and deposit morphologies which were further scrutinized by scanning electron microscopy (SEM), and purities were determined by XRD and XRF spectroscopy. On the other hand, for low concentrations of copper in WEEE leachate, a three dimensional cathode i.e. the circulating particulate bed cathode was utilized and found to deplete Cu^{II} solutions rapidly from < 10 mol m^{-3} Cu^{II} ca. 100 ppm. Finally, in the fifth section, the results from the reactor experiments were modelled in terms of mass transport controlled reaction in a plug flow electrochemical reactor (PFER) operated in batch recycle with a continuous stirred tank reactor/ reservoir (CSTR).

6.2. Thermodynamics

6.2.1. Copper

Critically reviewed thermodynamic data [2] were used to calculate potential-pH and solubility diagrams for copper-water (Cu-H_2O) and copper-chloride-water (Cu-Cl-H_2O) systems for which the full set of data and equations are given in Appendix B(c). It can be seen from the potential-pH diagram in Figure 6-61, that for a copper-water system, copper is soluble only as

Cu^{2+} ions. Dissolution of copper metal leads to the formation of cuprous (Cu^{I}) as well as cupric species (Cu^{II}) [2], which form complexes with chloride ions. Based on thermodynamic data for Cu^{II} species reviewed subsequently by Powell et al.[3], Cu^{II} generally tends to form four consecutive chloro-complexes in chloride concentrations which are:

$$Cu^{2+} + Cl^{-} \rightleftharpoons CuCl^{+} \quad [6\text{-}1]$$

$$Cu^{2+} + 2Cl^{-} \rightleftharpoons CuCl_2(aq) \quad [6\text{-}2]$$

$$Cu^{2+} + 3Cl^{-} \rightleftharpoons CuCl_3^{-} \quad [6\text{-}3]$$

$$Cu^{2+} + 4Cl^{-} \rightleftharpoons CuCl_4^{2-} \quad [6\text{-}4]$$

According to Powell et al.[3], the complexes $CuCl^{+}$ and $CuCl_2$(aq) are weak, while the higher order complexes are extremely weak in fresh water and seawater, however are formed at a very high chloride concentrations. Hence, using the stability constants, log *K* (Appendix B(c)), for species critical to the speciation of Cu^{II} in chloride aqueous solutions [3], it was found that $CuCl_2$(aq) predominates, for which the reaction is given by:

$$CuCl_2(aq) + e^{-} \rightleftharpoons CuCl_2^{-} \quad [6\text{-}5]$$

$$E_{CuCl_2(aq)/CuCl_2^{-}}\textbf{(SHE) / V} = 0.4917 + 0.0591\log\left\{\left(CuCl_2(aq)\right)/\left(CuCl_2^{-}\right)\right\} \quad [6\text{-}6]$$

In addition, cuprous ions also form strong complexes with chloride ions. With an exception for $CuCl_2^{-}$ and $CuCl_3^{2-}$ [4], there is some disagreement about the species formed because Cu^{+} ions are easily oxidised to Cu^{2+} ions. The presence of mixed oxidation state Cu species were investigated and addressed in detail in section 6.5. At high chloride activity of 5, the predominant species for Cu^{I} is $CuCl_2^{-}$ for which the electrochemical reaction is as follows:

$$CuCl_2^{-} + e^{-} \rightleftharpoons Cu + 2Cl^{-} \quad [6\text{-}7]$$

$$E_{CuCl_2^{-}/Cu}\textbf{(SHE) / V} = 0.2240 + 0.0591\log\left(CuCl_2^{-}\right) - 0.118\log\left(Cl^{-}\right) \quad [6\text{-}8]$$

Figure 6-62 illustrates the potential- pH diagram for copper-chloride-water; the dissolved copper and chloride activities are 10^{-1} and 5 respectively, at room temperature and pressure.

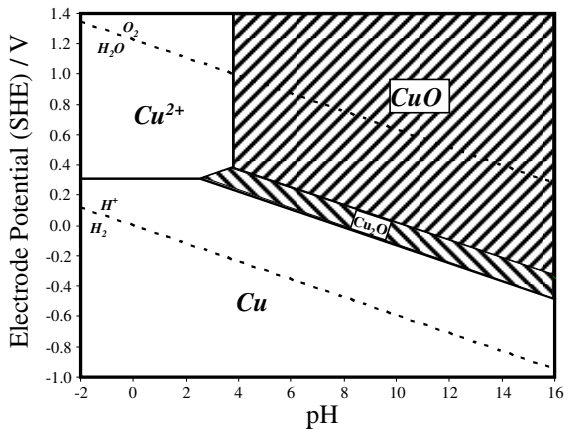

Figure 6-61. Potential pH diagram for copper-water system. Dissolved copper activities = 10^{-1}, 298 K, 1 atm.

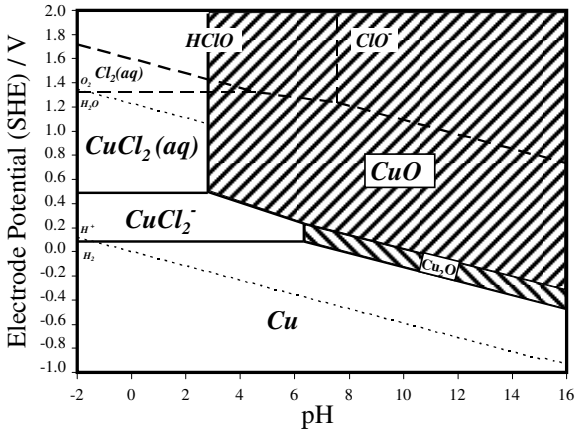

Figure 6-62. Potential pH diagram for copper-chloride-water. Activities: Dissolved copper and chloride activities = 10^{-1} and 5; 298 K, 1 atm.

The solubility of copper (I) chloride and copper (II) chloride are given in Figure 6-63 and Figure 6-64 respectively. Copper (I) chloride has a limited solubility compared to copper (II) chloride especially at low chloride activity [5], in which the insoluble solid is CuCl at low pH and Cu_2O at high pH as shown in Figure 6-63.

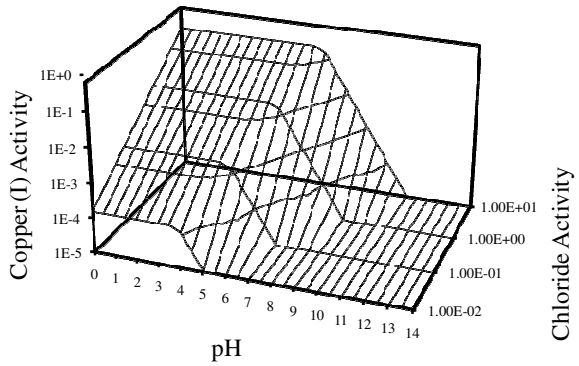

Figure 6-63. Predicted solubility of Cu^I species in aqueous chloride media at 298 K.

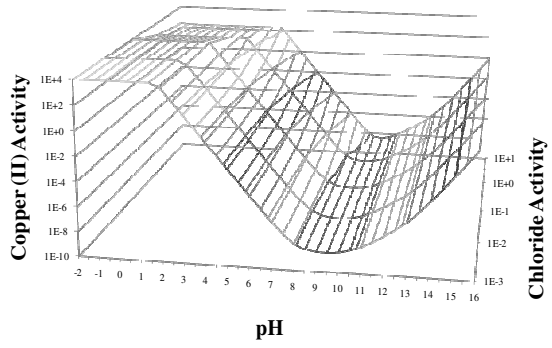

Figure 6-64. Predicted solubility of Cu^{II} species in aqueous chloride media at 298 K.

6.2.2. Silver

Silver dissolves predominantly in the Ag^I state, although some occurrences of Ag^{II} and Ag^{III}

have been reported [6]. For chloride complexes the following Ag^{I} species are in general considered to be present as the following species AgCl(s), $AgCl_2^-$, $AgCl_3^{2-}$, $AgCl_4^{3-}$ [7]. Although Ag^{I} exist in a very small amount in the WEEE leachate ca. 0.001 mol m^{-3}, it dissolved in chloride and was present in the solution as silver chloro- complexes. As shown in, Figure 6-65, the $AgCl_n^{(n-1)-}$ solubility increases as the chloride activity increases. Dependent on the mixed potential present in the leach solution the following leach reactions describe the leaching behaviour for a $[Cl^-]$ concentration of 5 kmol m^{-3} for the silver-chloride system:

$$Ag^+ + 2Cl^- \rightleftharpoons AgCl_2^- \quad [6\text{-}9]$$

$$Ag^+ + 3Cl^- \rightleftharpoons AgCl_3^{2-} \quad [6\text{-}10]$$

$$Ag^+ + 4Cl^- \rightleftharpoons AgCl_4^{3-} \quad [6\text{-}11]$$

From speciation calculations undertaken by Welham et al. [7], it was reported that the main species present in a solution in which $[Cl^-] > 4$ kmol m^{-3}, are $AgCl_3^{2-}$ and $AgCl_4^{3-}$ with percentages of about 40% and 60%, respectively. The silver chloro-complexes can be reduced at the electrode to elemental silver according to the following reaction equations:

$$AgCl_2^- + e^- \rightleftharpoons Ag + 2Cl^- \quad [6\text{-}12]$$

$$AgCl_3^{2-} + e^- \rightleftharpoons Ag + 3Cl^- \quad [6\text{-}13]$$

At high chloride activity of 5, the predominant species for Ag^{I} is $AgCl_4^{3-}$ [7] as shown in Figure 6-66 for which the electrochemical reaction is as follows:

$$AgCl_4^{3-} + e^- \rightleftharpoons Ag + 4Cl^- \quad [6\text{-}14]$$

$$E_{AgCl_4^{3-}/Ag}\,\mathbf{(SHE)\ /\ V} = 0.4743 + 0.059\log\left(AgCl_4^{3-}\right) - 0.237\log\left(Cl^-\right) \quad [6\text{-}15]$$

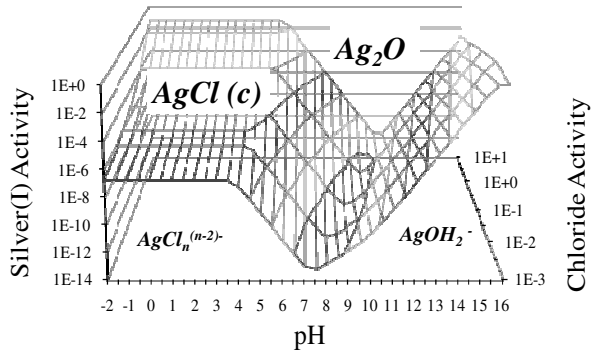

Figure 6-65. Predicted Ag^I species in aqueous chloride media at 298 K [7].

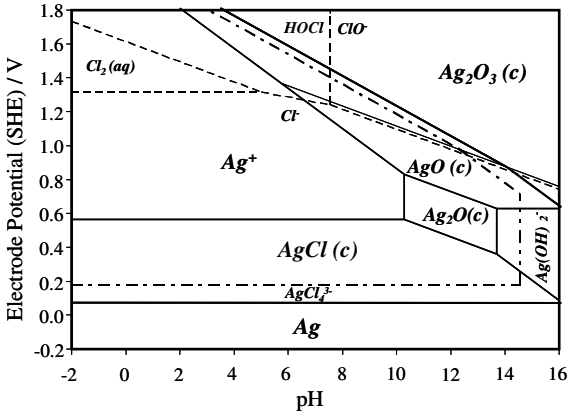

Figure 6-66. Potential pH diagram for silver-chloride-water system. Dissolved Ag^I and chloride activities = 10^{-4} and 5; 298 K, 1 atm. [7].

6.3. Transport and Kinetic Analyses

6.3.1. Cu-Cl-H_2O

The voltammetric behaviour of copper chloride species were investigated using a platinum (Pt) rotating disc electrode (RDE). Figure 6-67 illustrates the results of the negative-going linear potential sweep from +0.80 V (SCE) to -0.60 V (SCE) for rotation rates from 240 rpm to 2160 rpm (4 to 36 s^{-1}). Although two distinct reduction current waves for the successive reduction of $CuCl_2$(aq) and $CuCl_2^-$ ions are evident in Figure 6-67, the concentration of these chloro-complexes species could not be distinguished easily. According to Powell et al.[3], the formation of chloro-complexes have different electronic absorption bands, therefore several research investigated the existence of these species mostly by UV-vis spectrometry [1,3]. However, the bands are strongly overlapping [3] and thus require a significant number of additional measurements and the use of deconvolution software [8]. For $CuCl_2$ (aq)/ $CuCl_2^-$ ratio between 100 and 0.02, the reversible potential for the reduction of $CuCl_2$ (aq) to $CuCl_2^-$ measured using equation [6-6] was estimated between +0.37 V and +0.15 V (SCE). On the other hand, for $CuCl_2^-$ concentration between 5 and 10^{-3} mol m^{-3}, the reversible potential was estimated between -0.23 V and -0.45 V (SCE). Figure 6-68 illustrates that the reduction of $CuCl_2$ (aq) to $CuCl_2^-$ and the consecutive reduction of $CuCl_2^-$ to Cu were within the estimated range of electrode potential vs SCE.

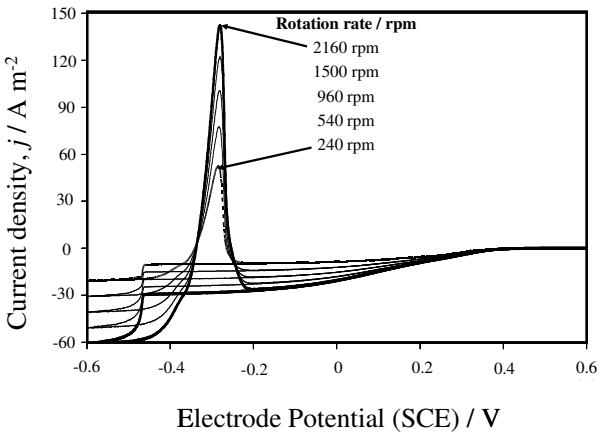

Figure 6-67. Effect of the RDE rotation rate on the cathodic polarization curves of 5 mol m^{-3} Cu^{II} in 4 kmol m^{-3} HCl + 1 kmol m^{-3} NaCl solutions, at Pt rotating disc electrode, scan rate 10 mV s^{-1}.

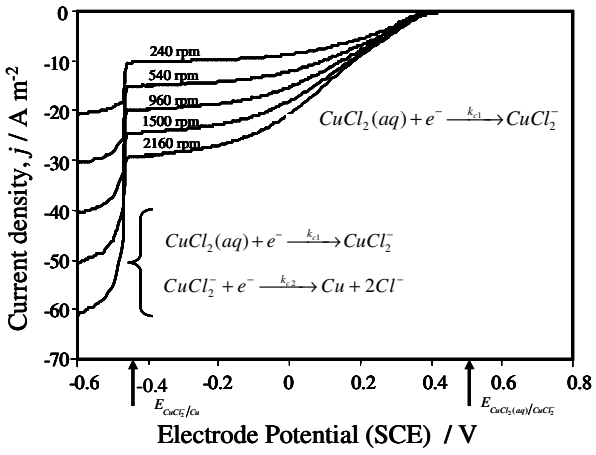

Figure 6-68. Reduction of 5 mol m^{-3} Cu^{II} at Pt rotating disc electrode in 4 kmol m^{-3} HCl + 1 kmol m^{-3} NaCl, scan rate 10 mV s^{-1}.

The current loop between the negative-going and positive-going potential sweeps was due to nucleation and growth of Cu on the Pt substrate, which increased the surface area. As the potential was swept from +0.60 V to -0.60 V (SCE), the Cu deposited was stripped from the electrode surface showing a well defined Cu oxidation peak at ca. -0.35 V (SCE). Nevertheless, only one peak appeared which is considered to represent the stripping of copper metal to $CuCl_2^-$. However the oxidation of $CuCl_2^-$ to $CuCl_2$ (aq) was not apparent here as it is not stable at < ca. +0.26 V (SCE) as according to Figure 6-62. Its large size compared with the reduction waves is possible due to the absence of mass transport limitation (the Cu is already on the surface and does not need to be transported to the site of reaction). Note that the current returns to the limiting current for the reduction of $CuCl_2$(aq) to $CuCl_2^-$ since the reaction continues at a mass transport controlled rate during the oxidation of Cu to $CuCl_2^-$. The anodic and cathodic charge densities, q_A and q_C at 25 s^{-1} were measured by integration of current density - time dependent plots giving values of 2.04×10^{-6} C m^{-2} and 2.25×10^{-6} C m^{-2}, respectively, over the range of the potential used. Hence, the charge yield for copper deposition may be estimated as ca. 0.91, the balance being due to hydrogen evolution, for which the equilibrium potential was estimated at < ca. -0.5 V (SCE) in the solutions used.

An exchange current density, j_o of 10^{-2} A m^{-2} and Tafel slope as 57 mV $decade^{-1}$ were estimated for the reduction of $CuCl_2$ (aq) ions to $CuCl_2^-$, under the conditions used (Figure 6-

69). This value of the Tafel slope is close to the value of 60 mV decade^{-1} reported by Lee and Nobe [10] for reaction [6-5] as is measured on a glassy carbon electrode in a 5 kmol m^{-3} HCl + 1 mol m^{-3} NaCl electrolyte. For the subsequent reaction where Cu^{I} becomes a solid Cu^{0} deposition which is shown in equation [6-7], it was not possible to measure the values in this work as the accessible range of current was restricted to less than an order of magnitude below the limiting current, which restricted the accuracy of the Tafel slope and exchange current density derived. Most of the studies in the literature [11,12] reported Tafel slope and exchange current density on copper electrode for the total reaction of Cu^{II} to Cu metal, except for Winter et al.[9] who measured for the separate reactions of Cu^{II} reductions, reactions [6-5] and [6-7]. Hence, the values for the exchange current density and Tafel slope for the reduction of Cu^{I} to Cu^{0} documented by Winter et al. [9] were used ; j_o = 5.01 A m^{-2} and Tafel slope = 40 mV decade^{-1} for 0.125 kmol m^{-3} Cu^{II} in 4 kmol m^{-3} NaCl + 1 kmol m^{-3} HCl electrolyte.

At -0.3 V (SCE), the reduction of $CuCl_2$(aq) ions to $CuCl_2^-$ was mass transport controlled, with current densities and deposition rates in agreement with those predicted with the Levich equation as shown in [6-16] and the reaction occurred is represented by equation [6-5]. The $D_{Cu^{II}}$ calculated from the slope is 6.5×10^{-10} m^2 s^{-1} (Figure 6-70) which is in agreement with data reported by Winter et al. [9] that was 5×10^{-10} m^2 s^{-1} considering the kinematic viscosity, υ as 1.17×10^{-6} m^2 s^{-1} taken from Majima et al [13].

$$j_L = 1.554 n F D_i^{2/3} \nu^{-1/6} f^{1/2} c_i \qquad [6\text{-}16]$$

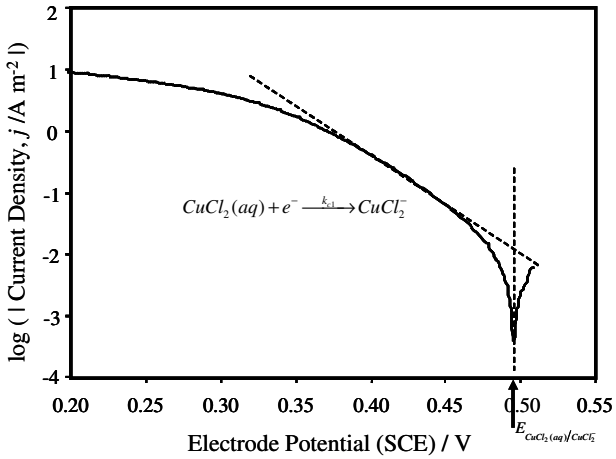

Figure 6-69. Tafel plot for reduction of 5 mol m^{-3} Cu^{II} at Pt rotating disc electrode in 4 kmol m^{-3} + 1 kmol m^{-3} NaCl, scan rate 10 mV s^{-1}, rotation rate of 36 s^{-1}.

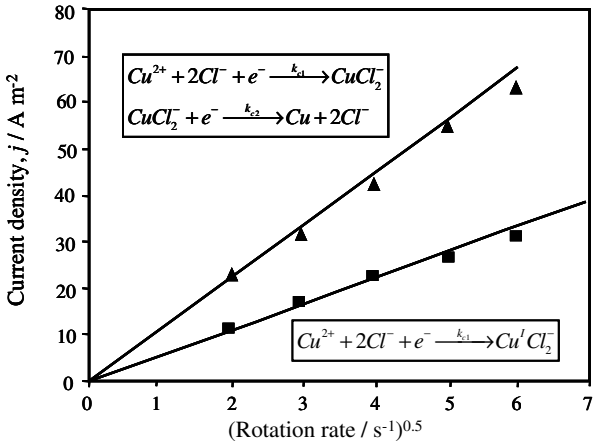

Figure 6-70. Kinetics of 5 mol m^{-3} Cu^{II} reduction at Pt rotating disc electrode in 4 kmol m^{-3} HCl + 1 kmol m^{-3}. Experimental data (▲■) and Predictions (—) from Levich's equation [6-16].

This diffusion coefficient value was then used to determine the Nernst diffusion layer, δ_N, and k_m values for each rotation rates, which are tabulated in Table 6-11 below.

Table 6-11. Calculated δ_N and k_m values for different rotation rates.

Rotation rate / s^{-1}	Square root of rotation rate / $s^{-0.5}$	$\delta_N \times 10^{-5}$ / m	$k_m \times 10^{-5}$ / m s^{-1}
4	2	2.85	1.98
9	3	1.96	3.05
16	4	1.49	4.18
25	5	1.21	5.37
36	6	1.01	6.43

Table 6-12 summarises the kinetic parameters obtained from various sources as reported in the text.

Table 6-12. A summary of the kinetic parameters obtained from literature [9,10] and RDE experiment.

Reactions	Exchange current density and Tafel slope	Literature	Rotating disc
$CuCl_2(aq)/CuCl_2^-$	$j_{o,_{CuCl_2(aq)/CuCl_2^-}}$ / A m^{-2}	7.94	10^{-2}
	Tafel slope / mV decade^{-1}	60	57
		Source: Lee and Nobe [10]	
$CuCl_2^-/Cu$	$j_{o,_{Cu}}$ / A m^{-2}	5.01	-
	Tafel slope / mV decade^{-1}	40	-
		Source: Winter et al. [9]	

Due to the difficulty in reproducibility and discrepancies between the kinetic parameters reported here and those in literature, the kinetic parameters calculated here should be used only for similar conditions as per reported. The electrochemical kinetic parameters for deposition of Cu that have been determined will be used to adjust model parameters in Maple™.

6.3.2. Ag-Cl-H_2O system

Tafel slopes for silver reduction and oxidation in HCl or NaCl containing electrolytes were scarce in literature. The theoretical cathodic Tafel slope for silver reduction was calculated as 120 mV dec^{-1} based on the assumption that the silver reduction is a straightforward reduction process in electrolytes containing perchlorate ($HClO_4$) [15]. Perchlorate ions do not complex silver ions, so that kinetic parameter values derived in this kind of solutions are not really comparable to those for HCl solutions [16].

6.4. Modelling of the Mechanisms Occurring in the System

Models have been developed in Maple™ (Appendix E(b)) to predict current densities-potential relationships of the copper chloro-complexes in solution. For multi-steps reductions (Cu), the current densities were predicted by steady state balance of surface concentrations.

From experimental data obtained previously (section 6.3.1) for $CuCl_2$(aq) reduction, kinetic

values of j_0 and Tafel coefficient were derived as 10^{-2} A m^{-2} and 57 mV dec^{-1} respectively, for a concentration of 5 mol m^{-3}. Hydrogen evolution kinetics on the Cu surface was also included in the model predictions; $j_0 = 3.98\times10^{-4}$ and Tafel slope= 105 m V $decade^{-1}$ [20]. Using Maple™, it was possible to determine the unknown surface concentrations in terms of electrode potential, using estimates for the rate coefficients.

6.4.1. Electrochemical Reduction of Cu^{II} Ions from Aqueous Chloride Electrolytes

The electrode reactions defined for the different metals given in Appendix C (b-f) are used to calculate the current density vs. potential but even if the reaction mechanism is known, it is not always possible to fit the current potential relation in Butler-Volmer form. The Butler-Volmer equation assumes a simple electrode reaction and does not compensate for other processes that can retard the overall rate for example: adsorption at the cathode, a different charge transfer or dissolution of intermediate products. The solution is to develop a specialised equation for the current-potential relation based on a detailed description of the reaction mechanism to fit the model with the reality. In most cases an assumption is made for the likely reaction mechanism, since for most systems the detailed reaction mechanism is not known.

To find a more fitting current density vs. potential relation for the copper electrode reactions, a mechanistic study is applied. A reaction mechanism is proceeded by a set of postulated elementary reactions. The main reactions at the cathode are the electrodeposition of metals, such as the multi-step reduction of the predominant species in the conditions used (section 6.3.1), $CuCl_2$ (aq) to $CuCl_2^-$ and the reduction of $CuCl_2^-$ to Cu:

$$CuCl_2(aq) + e^- \rightleftharpoons CuCl_2^- \qquad [6\text{-}17]$$

$$E_{CuCl_2(aq)/CuCl_2^-}\textbf{(SHE) / V} = 0.4917 + 0.0591\log\left\{\left(CuCl_2(aq)\right)/\left(CuCl_2^-\right)\right\} \qquad [6\text{-}18]$$

$$CuCl_2^- + e^- \rightleftharpoons Cu + 2Cl^- \qquad [6\text{-}19]$$

$$E_{CuCl_2^-/Cu}\textbf{(SHE) / V} = 0.2240 + 0.0591\log\left(CuCl_2^-\right) - 0.118\log\left(Cl^-\right) \qquad [6\text{-}20]$$

The mechanism of these reactions can be described by equation [6-21] - [6-24]

$$CuCl_{2(aq)} \underset{k_m}{\overset{k_m}{\rightleftharpoons}} CuCl_{2(aq)}(surface) \qquad [6\text{-}21]$$

$$CuCl_{2(aq)}(surface) + 2Cl^- + e^- \xrightarrow{k_{c1}} CuCl_2^-(surface) \qquad [6\text{-}22]$$

$$CuCl_2^-(surface) \underset{k_m}{\overset{k_m}{\rightleftharpoons}} CuCl_2^- \quad [6\text{-}23]$$

$$CuCl_2^-(surface) + e^- \xrightarrow{k_{c2}} Cu + 2Cl^- \quad [6\text{-}24]$$

The steady state mass balances for the surface concentrations of $CuCl_2$ (aq) and $CuCl_2^-$, i.e. $\left(\frac{d\left(CuCl_{2(aq)}\right)_{surface}}{dt}\right) = 0$ and $\left(\frac{d\left(CuCl_2^-\right)_{surface}}{dt}\right) = 0$:

$$k_m\left(CuCl_{2(aq)}\right) - k_m\left(CuCl_{2(aq)}\right)_{surface} - k_{c1}\left(CuCl_{2(aq)}\right)_{surface} = 0 \quad [6\text{-}25]$$

$$k_{c1}\left(CuCl_{2(aq)}\right)_{surface} - k_{c2}\left(CuCl_2^-\right)_{surface} - k_m\left(CuCl_2^-\right)_{surface} + k_m\left(CuCl_2^-\right) = 0 \quad [6\text{-}26]$$

The current densities due to the reduction of $CuCl_2$ (aq) to $CuCl_2^-$ ($j_{CuCl_2(aq)}$) and of $CuCl_2^-$ to elemental Cu ($j_{CuCl_2^-}$) are given respectively by:

$$j_{CuCl_{2(aq)}} = -nFk_{c1}\left(CuCl_{2(aq)}\right)_{surface} \quad [6\text{-}27]$$

$$j_{CuCl_2^-} = -nFk_{c1}\left(CuCl_2^-\right)_{surface} \quad [6\text{-}28]$$

where:

$$k_{ci} = k_{i,0}\exp\left\{\frac{-\alpha_i F(E - E_i^0)}{RT}\right\} \quad [6\text{-}29]$$

The mass balance equations ([6-25] and [6-26]) were solved using the '*solve*' function in Maple™ software (www.maplesoft.com). A predetermined mass transfer coefficient, k_m of disc electrode at various rotation rates (Table 6-11) was used in the model. The rate coefficients ($k_{1,0} = 1\times10^{-8}$ s^{-1}, $k_{2,0} = 5\times10^{-10}$ s^{-1}) were selected from data adjusted according to experimental data obtained from the Cu^{II} rotating disc experiment as shown in Figure 6-68. The full mathematical codes to solve the equations are provided in Appendix E(b). Figure 6-71 illustrates the predicted electrode potential dependence of surface concentrations of $CuCl_2$ (aq) and $CuCl_2^-$. As the cathode potential decreased from +0.80 to +0.20 V (SHE), the surface concentrations of $CuCl_2$(aq) decreased and for potentials < +0.20 V (SHE), the surface concentrations of $CuCl_2^-$ was predominant. Figure 6-72 shows the model prediction of potential-current relationship from the kinetic model, compared to the experimental data for 5 mol m^{-3} Cu^{II} reduction in 4 kmol m^{-3} HCl + 1 kmol m^{-3} NaCl. The model shows good correlation with experimental results.

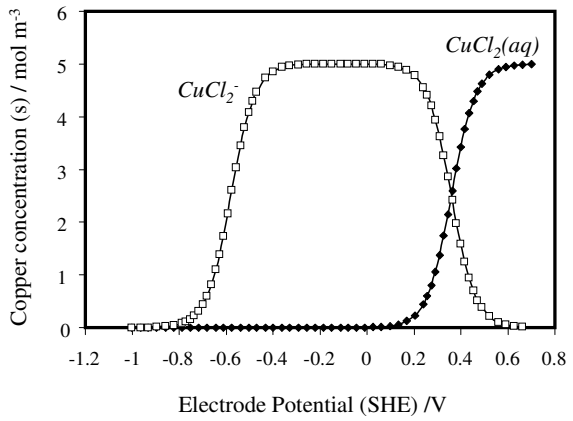

Figure 6-71. Predicted electrode potential dependence of surface concentrations of $CuCl_2$ (aq) and $CuCl_2^-$.

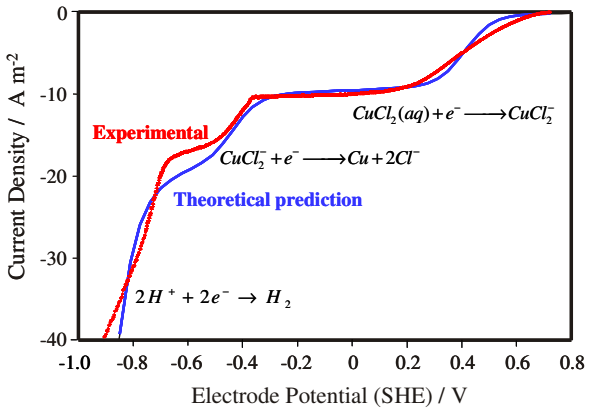

Figure 6-72. Model prediction of current density- electrode potential relationship from the kinetic model solved with Maple™, compared to experimental data for the reduction of 5 mol m^{-3} Cu^{II} in 4 kmol m^{-3} HCl + 1 kmol m^{-3} NaCl.

6.5. Determination of dark coloured intermediate (mixed metal and mixed oxidation state of Cu)

Metal chloride ions in the leach solutions can be partially reduced to form dark coloured intermediate species of mixed oxidation states, under potentiostatic or galvanostatic operation. The colour of 4 kmol m^{-3} HCl + 1 kmol m^{-3} NaCl solutions containing $CuCl_2$ (aq), $CuCl_2^-$ and a mixture of the two ions are vibrant green, colourless and dark green, respectively. Cheng et al.[20] had reported that valleys were observed between 500 and 600 nm for all three spectra as shown in Figure 6-73. At 550 nm, the absorbance for the solutions containing 50 mol m^{-3} of $CuCl_2^-$ only and 50 mol m^{-3} of $CuCl_2$ (aq) only were c.a. 0 and 0.002, respectively. If Beer's law (equation [6-30]) was obeyed, the absorbance at 550 nm for the solution containing 50 mol m^{-3} $CuCl_2$ (aq) + 50 mol m^{-3} $CuCl_2^-$ should be c.a. 0.002.

$$A_\lambda = \sum_{i=1}^{m} \varepsilon_{\lambda i} c_i d \qquad [6\text{-}30]$$

The absorbance at 550 nm measured experimentally for this solution was 0.012 [20], much higher than the value expected if Beer's law was obeyed. This was explained by the formation of mixed oxidation states species (chloro-Cu^I-Cu^{II} complexes [1,3]), which was in equilibrium with $CuCl_2$ (aq) and $CuCl_2^-$. As this species was unstable, the equilibrium constant and the

molar absorptivity ($\varepsilon_{\lambda i}$) of this mixed oxidation states species were unknown and it would be difficult to determine its concentration. In the following section (6.5.1), the concentration of these mixed oxidation states species are determined and investigated if the partially reduced mixed oxidation state species, constitute a problem for copper electrodeposition; using cyclic voltammetry.

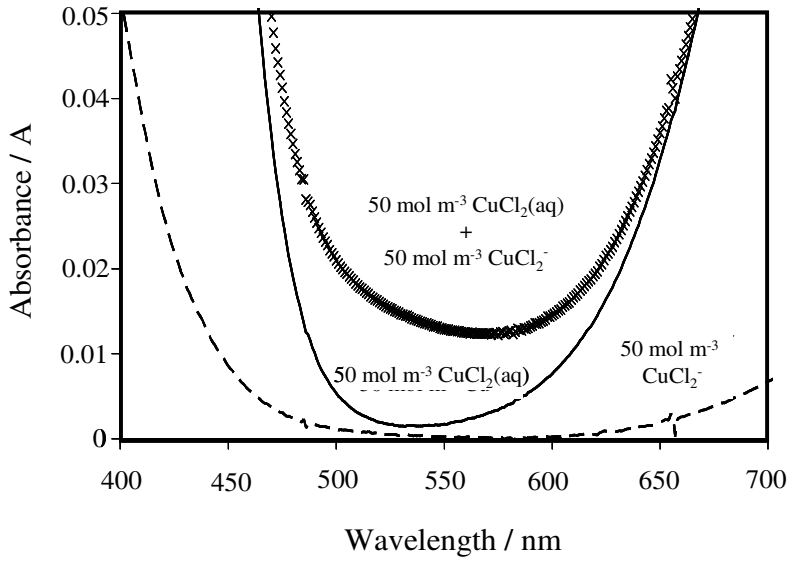

Figure 6-73. Absorbance spectra in the visible light region for solutions of 4 kmol m^{-3} HCl + 1kmol m^{-3} NaCl containing $CuCl_2$(aq), $CuCl_2^-$ and a mixture of the two [20].

6.5.1. Voltammetry Analyses

4 kmol m^{-3} HCl + 1 kmol m^{-3} NaCl solutions containing $CuCl_2$ (aq), $CuCl_2^-$ and a mixture of the two ions were prepared from analytical grade chemicals and high purity water which had been described in Chapter 4 (Materials and Experimental Methods). As $CuCl_2^-$ ions are easily oxidised to $CuCl_2$ (aq) ions, a number of precautions were required which include N_2 gas was bubbled through the 4 kmol m^{-3} HCl + 1 kmol m^{-3} NaCl solutions to remove any dissolved O_2 (aq) prior to dissolution of CuCl(s) and all the experimental procedures took place inside a N_2(g) filled glove bag.

Figure 6-74(a)-(d) show the reduction current (negative-going scan) alone and Figure 6-74(e)-(h) illustrate the experimental data and predictions according to Levich's equation for 4 kmol m^{-3} HCl + 1 kmol m^{-3} NaCl solutions containing stimulated $CuCl_2$ (aq) and $CuCl_2^-$ at different ratios, scan rate of 10 mV s^{-1} and at rotation rates for 60, 240, 540, 960, 1500, 2160 and 2940

rpm, with all scans starting at the open circuit potentials. When plotted against the square root of the rotation rate, the mass transport limiting current densities in Figure 6-74(e)-(h) exhibited a linear dependence, as predicted by Levich's equation [6-16]. Using $D_{Cu^{II}}$ = 6.5×10^{-10} m^2 s^{-1}, calculated from the experimental data, and a kinematic viscosity value, ν = 1.17×10^{-6} m^2 s^{-1} [13], the concentrations calculated from Levich equation were in good agreement with the prepared $CuCl_2(aq)$ and $CuCl_2^-$ concentrations in 4 kmol m^{-3} HCl + 1 kmol m^{-3} NaCl. This demonstrated that the concentration of $CuCl_2^-$ can be determined providing that the Cu^{II} solutions are free from O_2, which would otherwise be co-reduced.

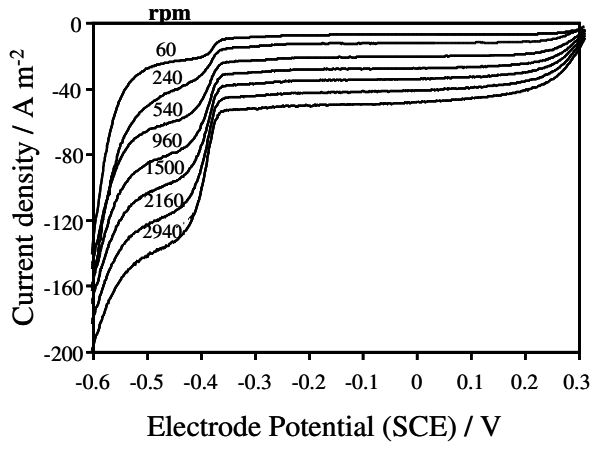

(a)

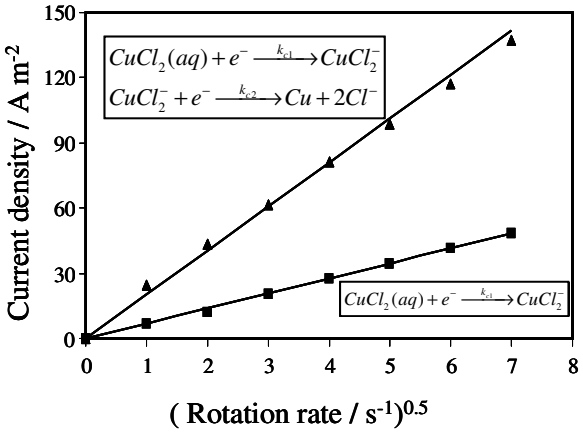

(e)

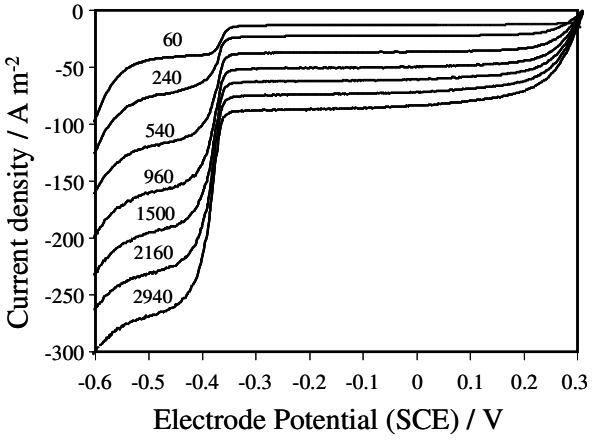

(b)

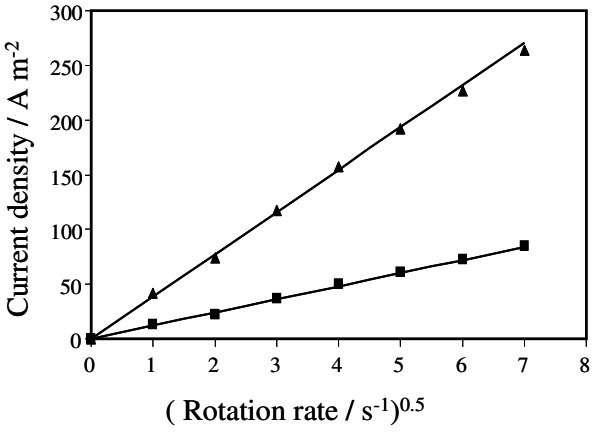

(f)

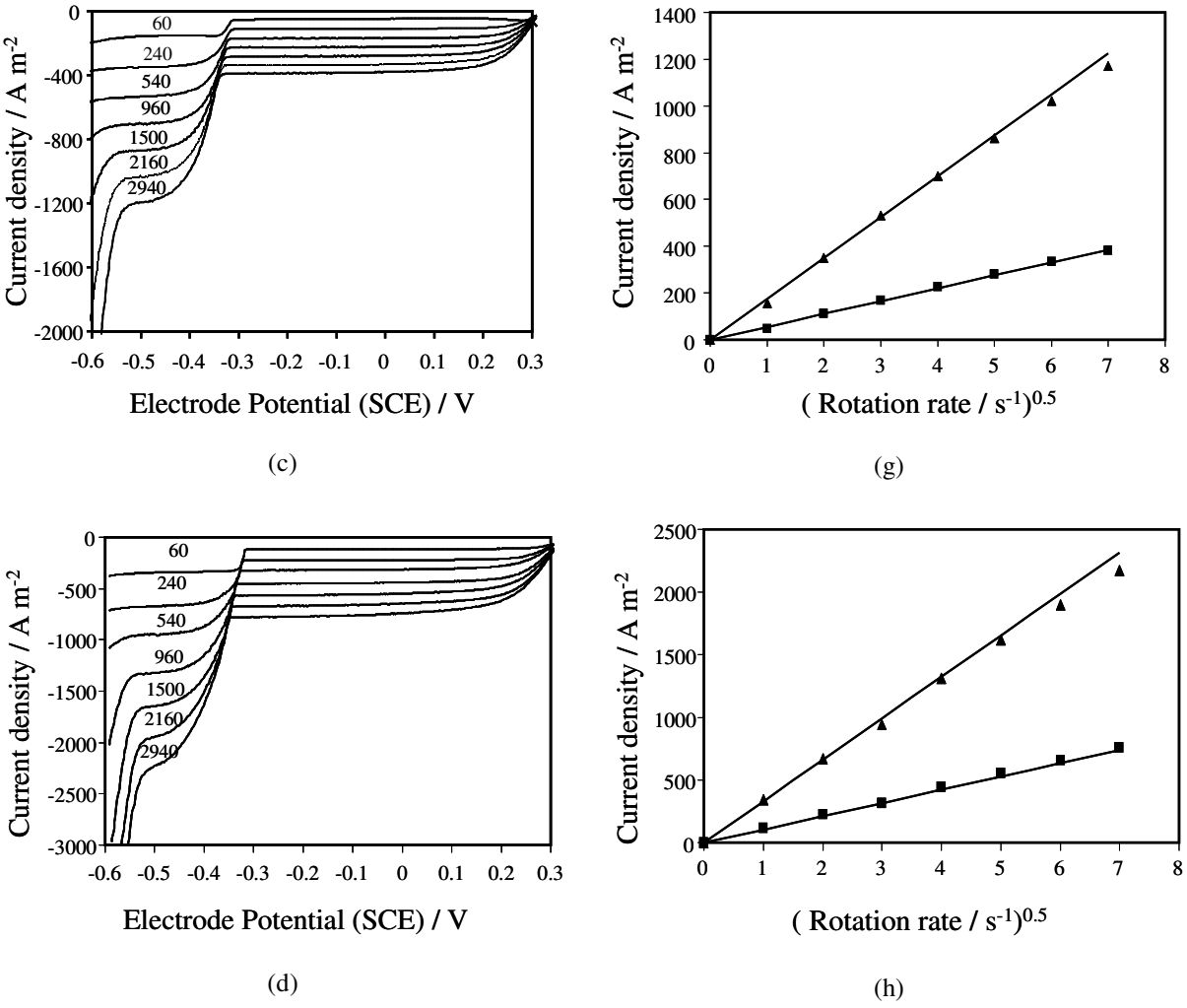

Figure 6-74. Reduction current and Experimental data (▲■) and Predictions (—) from Levich equation [6-16], for solutions of 4 kmol m^{-3} HCl + 1 kmol m^{-3} NaCl containing; (a,e)5 mol m^{-3} of $CuCl_2$(aq) + 5 mol m^{-3} $CuCl_2^-$, (b,f) 10 mol m^{-3} of $CuCl_2$ (aq) + 10 mol m^{-3} $CuCl_2^-$, (c,g) 50 mol m^{-3} of $CuCl_2$(aq) + 50 mol m^{-3} $CuCl_2^-$ and (d,h) 100 mol m^{-3} of $CuCl_2$(aq) + 100 mol m^{-3} $CuCl_2^-$, at a scan rate of 10 mV s^{-1}.

The linear sweep voltammetry was also used to determine the concentration of $CuCl_2$(aq) and $CuCl_2^-$ in the actual WEEE leachate as shown in Figure 6-75(a). The overall Cu^{II} concentration was ca. 470 - 475 mol m^{-3} (Figure 6-75(b)), similar to that determined by inductive coupled plasma optical emission spectrophotometry (ICP) as ca. 470 mol m^{-3}. However, the $CuCl_2^-$ concentration was calculated to be ca. 1 ppm due to the near total oxidation of $CuCl_2^-$ to $CuCl_2$(aq). This was a result of oxidation of the solution, as it has been exposed to O_2 (air).

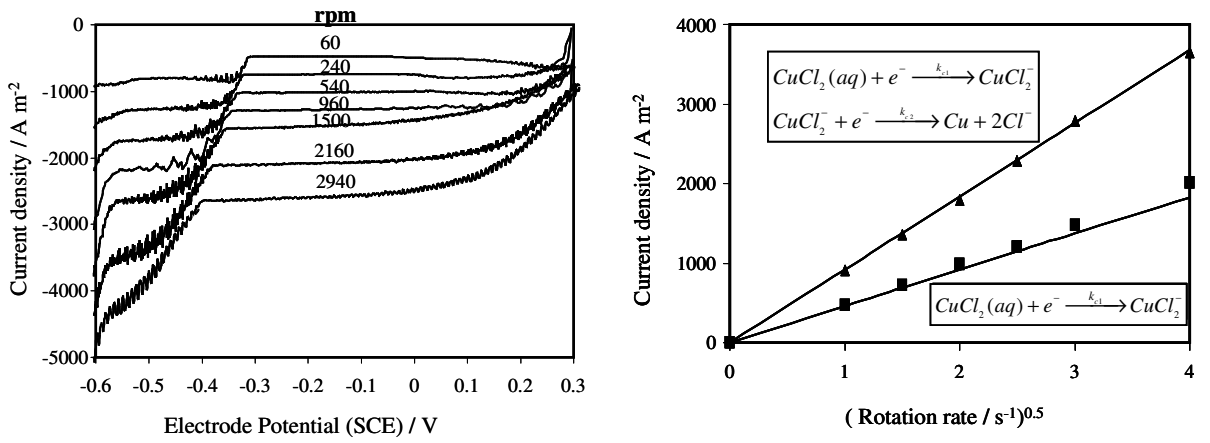

(a) (b)

Figure 6-75. (a) Reduction current and (b) Experimental data (▲■) correlated with Predictions (—) from Levich's equation [6-16] for the WEEE leachate (Chapter 4, section 4.2.2).

Mixed oxidation states species and its effect to the electrodeposition of Cu from $CuCl_2$(aq) or $CuCl_2^-$ was also investigated using cyclic voltammetry. Figure 6-76 shows the cyclic voltammogram and the negative-going scan alone for solutions containing (a) 5.5 mol m^{-3} of $CuCl_2$(aq), (b) 5.14 mol m^{-3} of $CuCl_2^-$ and (c) 2.75 mol m^{-3} of $CuCl_2$(aq) + 2.57 mol m^{-3} of $CuCl_2^-$ in 4 kmol m^{-3} HCl+ 1 kmol m^{-3} NaCl, at a scan rate of 10 mV s^{-1} and at rotation rates for 240, 540, 960, 1500 and 2160 rpm, with all scans starting at the open circuit potentials.

Figure 6-76(a) illustrates that for the solution with $CuCl_2$(aq) only, a reduction current was observed for potentials < + 0.40 V (SCE), corresponding to the reduction of $CuCl_2$(aq) to $CuCl_2^-$. As the disc electrode potential continued to sweep to more negative potentials, a significant increase in current was detected at ca. -0.35 V (SCE), caused by the reduction of $CuCl_2^-$ to Cu. This is confirmed by Figure 6-76(b), which showed little current; < -0.35 V (SCE) was observed for solutions containing $CuCl_2^-$ only. The onset of H_2 evolution was detected at potentials ≤ -0.50 V (SCE). During the positive-going potential scan, stripping peaks of Cu to $CuCl_2^-$ were observed for both cases. Figure 6-76 (c) depicts the same characteristics for solutions containing a mixture of $CuCl_2$(aq) and $CuCl_2^-$, the reduction of $CuCl_2$(aq) to $CuCl_2^-$, the reduction of $CuCl_2^-$ to Cu, the onset of H_2 evolution and the stripping of Cu to $CuCl_2^-$. No additional characteristics were detected by the cyclic voltammogram to suggest the presence of extra reduction or oxidation steps caused by the mixed oxidation states species.

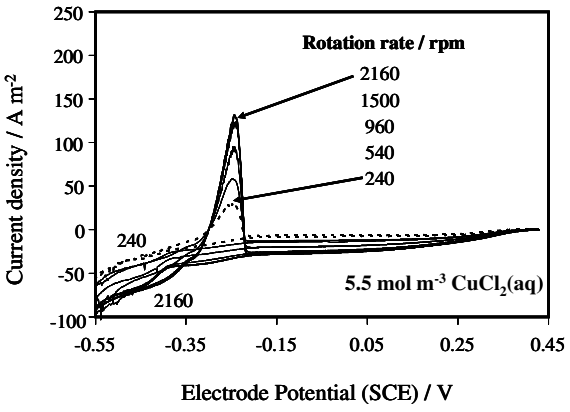

(a)

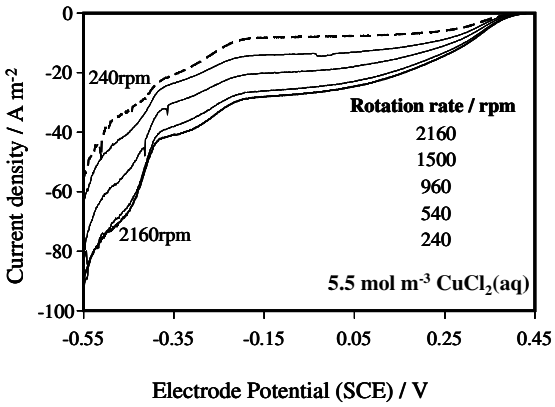

(a)

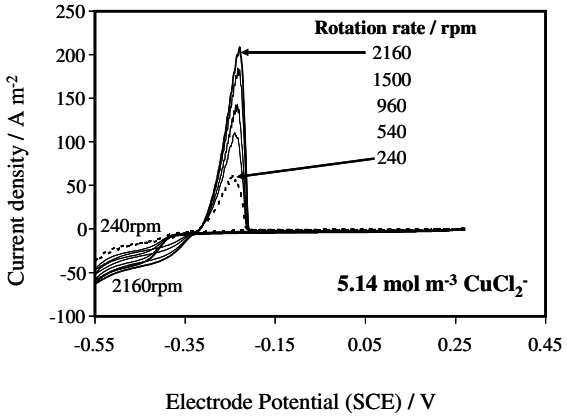

(b)

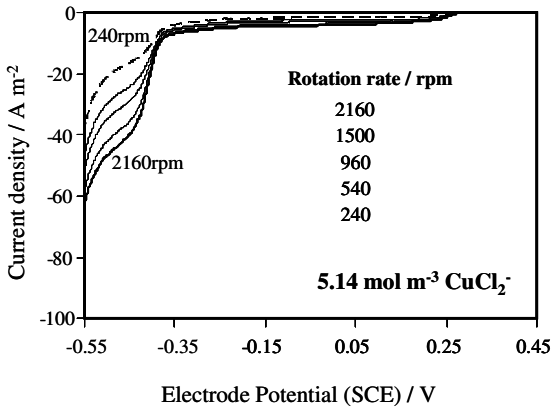

(b)

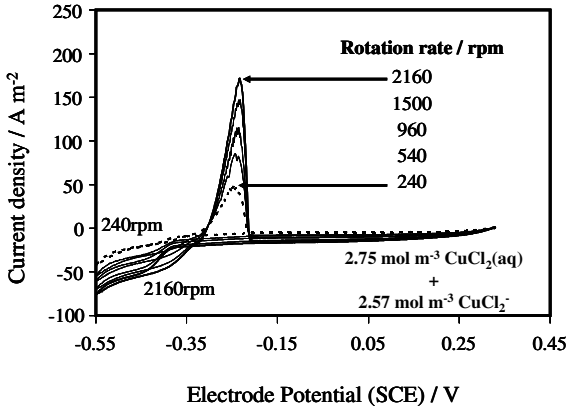

(c)

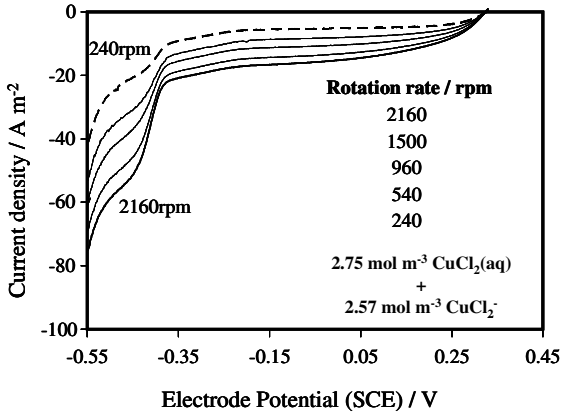

(c)

Figure 6-76. Cyclic voltammogram for negative scan alone for solutions of 4 kmol m^{-3} HCl + 1 kmol m^{-3} NaCl containing: (a) $CuCl_2(aq)$, (b) $CuCl_2^-$ and (c) a mixture of $CuCl_2(aq)$ and $CuCl_2^-$ at a scan rate of 10 mV s^{-1}.

This was supported by Figure 6-77(a) and (b), which showed good agreement between the cyclic voltammogram obtained experimentally for the solutions containing a mixture of $CuCl_2(aq)$ and $CuCl_2^-$ (50% of solution containing only $CuCl_2(aq)$ + 50% of solution containing only $CuCl_2^-$) , and the average current density calculated from the solutions containing only $CuCl_2(aq)$ or $CuCl_2^-$ when the electrode was rotated at 1500 and 2160 rpm.

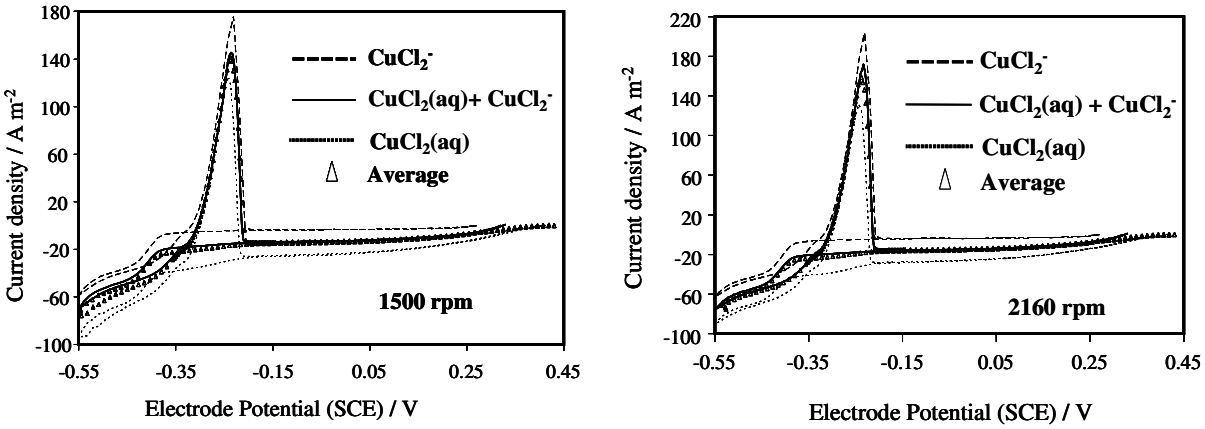

(a) (b)

Figure 6-77. Cyclic voltammogram for solutions 4 kmol m^{-3} HCl + 1kmol m^{-3} NaCl containing $CuCl_2(aq)$, $CuCl_2^-$ and a mixture of the two, obtained experimentally for rotation rate at; (a)1500 rpm and (b) 2160 rpm, scan rate 10 mV s^{-1}, compared against an averaged value calculated for the mixture.

6.6. Electrochemical Reactor Experiments

Two types of electrochemical reactors were used: a) mesh cathode in a fluidised bed of inert particles; and b) a circulating particulate bed cathode. The use of inert glass beads (590-840 μm) in fluidised bed electrochemical reactors has been reported to enhance mass transfer rates [18,19] and to improve copper deposit morphologies [22]. For low concentrations of copper in WEEE leachate ca. < 10 mol m^{-3}, a three dimensional cathode of circulating graphite particles was utilised. As explained in Chapter 5 (Gold Electrodeposition), the circulating graphite particulate bed electrode (CPBE) is a 3-dimensional electrode with a large specific surface area; the collisions of particles may improve the morphology of the metals deposits (as copper deposited from chloride solutions has been reported to be dendritic [9]) and continuous operation is possible by removing the particulates hydraulically. However, potential and current distributions across the thickness of the bed could be an issue [4]. Therefore, this study attempted to determine the effects of applied potential on the behaviour

of both reactors, whether adequate rates and charge yields of copper electrodeposition in the actual WEEE leachate could be achieved, and if coherent and adherent copper deposits could be produced by either reactor.

6.6.1. Electrodeposition of $CuCl_n^-$ with Mesh Electrode in a Fluidised Bed of Inert Particles

Figure 6-78 shows a voltammogram for the electrodeposition of Cu and H_2 evolution on a Cu-coated Ti mesh cathode in a fluidised bed of glass beads with a flow rate of 0.85 dm^3 min^{-1}. At -0.35 V (SCE), Cu was deposited under mixed kinetic and mass transport control, at a rate (current) that was c.a. 72 % of the mass transport limiting current. At -0.40 V (SCE), the deposition rate was c.a. 97 % of the mass transport limiting rate. Total mass transport control for Cu deposition was achieved at -0.45 V (SCE) and the rate of H_2 evolution began to increase rapidly for potentials < -0.55 V (SCE).

The mass transfer rate in this reactor depended on the momentum of the inert particulates as well as the frequency of which the particulates collide with the mesh cathode. Generally an increase in electrolyte flow rate would increase the momentum of the particulates and subsequently increased the expansion or voidage of the fluidised bed, thus reduced the collision frequency [14]. As a result, an optimal bed voidage existed for the maximum mass transport rate, as depicted in Figure 6-79, which showed the dependency of the mass transfer coefficient and bed voidage on liquid velocity for spherical particles for $0.4 < Re_p < 500$ with diameters ranged from 590 - 840 μm. For this system (Figure 6-78) the flow rate was 0.85 dm^3 min^{-1}, corresponding to a bed voidage of 0.5.

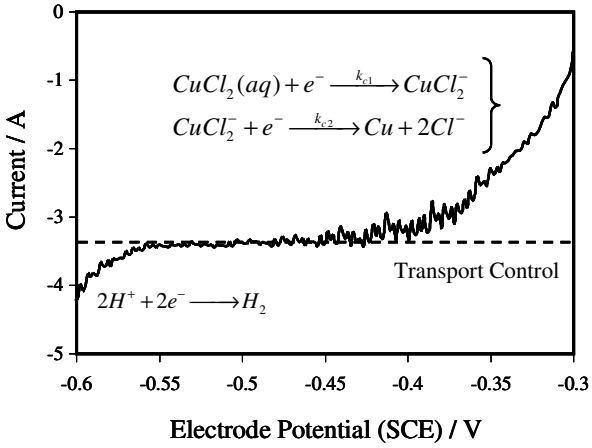

Figure 6-78. Voltammogram for the reduction of $CuCl_2$ (aq) and $CuCl_2^-$ and H_2 evolution on a Cu-coated Ti mesh cathode, in a fluidised bed of 590-840 µm glass beads, at a scan rate of 10 mV s^{-1}, at a flow rate of 0.85 dm^3 min^{-3}, bed expansion of 0.5 and initial copper concentration of 470 mol m^{-3}.

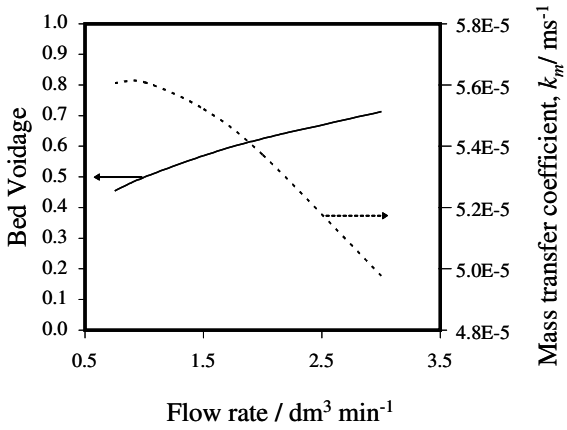

Figure 6-79. The optimal bed voidage for fluidised bed predicted by correlations in literature [16].

Figure 6-80 shows the effects of applied cathode potential on the time dependence of copper concentration, $ln(c/c_0)$ and, current density at a flow rate of 0.85 dm^3 min^{-1} and an initial Cu concentration of 470 mol m^{-3}. The mass transfer coefficient (k_m) was estimated from the gradient of the plot based on the equation for a plug flow cathode operating in the batch recycle system [19]:

$$c_{i,t} = c_{i,t=o} \exp\left\{-\frac{\dot{\mathrm{v}}\,t}{V}\left[1-\exp\left(-\frac{k_m A a L}{\dot{\mathrm{v}}}\right)\right]\right\} \qquad [6\text{-}31]$$

$$I_{L,t} = nF\,\dot{\mathrm{v}}\,c_{i,t=0}\left[1-\exp\left(-\frac{k_m A a L}{\dot{\mathrm{v}}}\right)\right]\exp\left\{-\frac{\dot{\mathrm{v}}\,t}{V}\left[1-\exp\left(-\frac{k_m A a L}{\dot{\mathrm{v}}}\right)\right]\right\} \qquad [6\text{-}32]$$

As the cathode potential was decreased from -0.35 to -0.45 V (SCE), the mass transport and Cu deposition rate doubled (Figure 6-80 and Figure 6-81). Lower decay rates of concentration and current density for -0.35 V (SCE) implies mixed transport and kinetic control, rather than total transport control at -0.45 V (SCE). Further decrease in cathode

potential would increase the rate of H_2 evolution (Figure 6-78). The deviations shown in Figure 6-81 from the exponential decay in concentration, and hence current density, with time predicted by equations [6-31] and [6-32] for -0.45 V (SCE), was ascribed to a time-dependent effective surface area of cathode. Current density-time data for -0.45 V (SCE) indicated there was a small contribution from H_2 evolution at $t > 10^4$ s, the rate of which increased rapidly at < -0.55 V vs. SCE. In addition, the kinetics of H_2 evolution on Cu is much faster than that on Ti as presented in Figure 3-9 (pp 65). An exchange current density, $j_{o,H_2/Ti}$ of 1.26×10^{-3} A m^{-2} and Tafel slope of 135 mV decade^{-1} for H_2 evolution on titanium metal and $j_{o,H_2/Cu}$ of 3.98×10^{-4} A m^{-2} and Tafel slope as 105 mV decade^{-1} for H_2 evolution on copper metal in 1 kmol m^{-3} H_2SO_4 solutions [25].

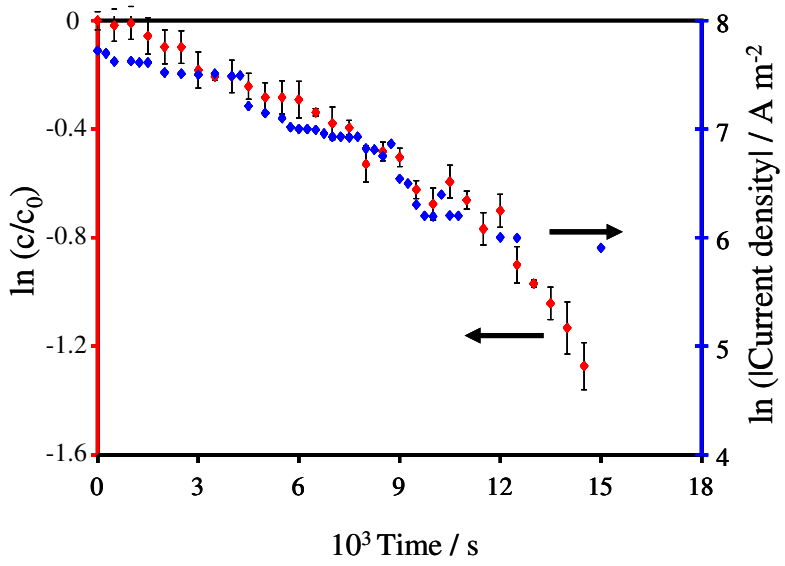

Figure 6-80. Time dependence of the ($CuCl_2$(aq) and $CuCl_2^-$); ($[Cu^{II}]_0$ = 470 mol m^{-3}) concentration (red ◊) and reduction current density (blue ◊) in fluidised bed electrolyte reactor with 590-840 µm glass beads, batch recycle model at - 0.35 V (SCE) ; flow rate = 0.85 dm^3 min^{-1} , k_m = 2.14×10^{-5} m s^{-1}.

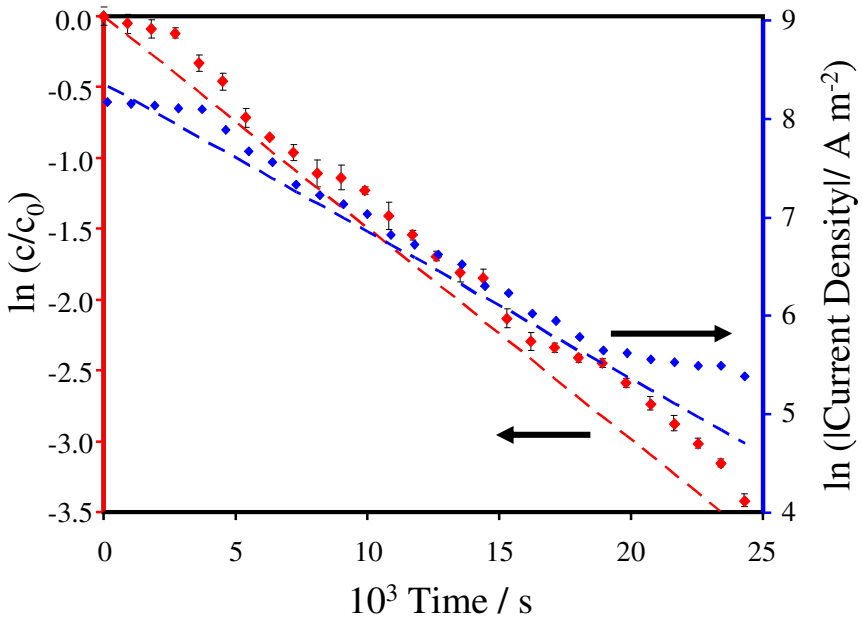

Figure 6-81. Time dependence of the ($CuCl_2$(aq) and $CuCl_2^-$); ($[Cu^{II}]_0$ = 470 mol m^{-3}) concentration (red ◊); model prediction (---) and reduction current density (blue ◊); model prediction (---) in fluidised bed electrolyte reactor with 590-840 µm glass beads, batch recycle model at -0.45 V (SCE); flow rate = 0.85 dm^3 min^{-1}, k_m = 4.6×10^{-5} m s^{-1}.

The charge yield was expected to decrease as the cathode potential decreased from -0.35 to -0.45 V (SCE), due to the increase in the rate of H_2 evolution. However, experimental results showed that as the cathode potential decreased from -0.35 to -0.45 V (SCE), the charge yield increased from 0.84 to 0.92 (Figure 6-83), contradicting the expectation. If the rate of the reduction of $CuCl_2$(aq) to $CuCl_2^-$ was much faster than that of the reduction of $CuCl_2^-$ to Cu at -0.35 V (SCE), then it was possible that some of the $CuCl_2$ (aq) ions were reduced to $CuCl_2^-$, which were dispersed from the cathode surface without being further reduced to form Cu. As ICP could not distinguish between $CuCl_2$(aq) and $CuCl_2^-$, the $CuCl_2^-$ would be treated as $CuCl_2$(aq) in the calculation for charge efficiency. Hence, the apparent charge yield at -0.35 V (SCE) was lower than its actual value.

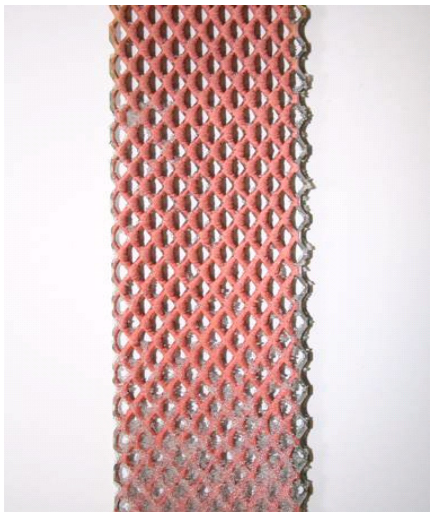

(a)

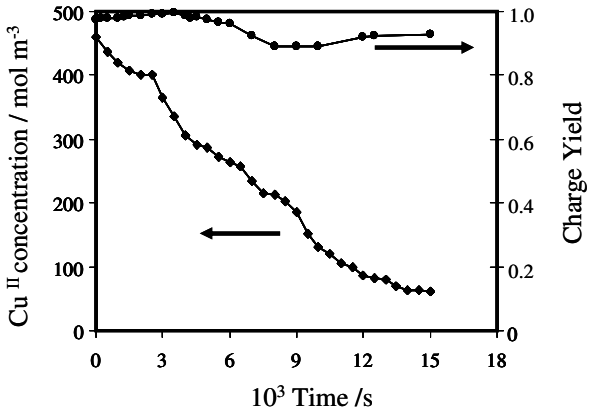

(b)

Figure 6-82. Image of copper deposits on a mesh electrode in the fluidised bed electrolyte reactor operating at a feeder cathode potential of -0.45 V (SCE).

Figure 6-83. Depletion of dissolved copper concentration with time during batch recycle reduction in fluidised bed electrolyte reactor with 590-840 μm glass beads; flow rate = 0.85 dm^3 min^{-3}; -0.45 V (SCE).

Copper purities of > 99.79 % was confirmed by ICP with a trace of Ag found in the sample, however this is not the case when it was analysed by XRF as shown in Table 6-13. From ICP measurement, it was found that Cu was contaminated with traces of silver due to reaction [6-14] with the reversible electrode potential calculated from equation [6-15] for $AgCl_3^{4-}$ activity of 0.001, was ca. -0.11 V (SCE). As explained in section 6.2.2 (thermodynamics of Ag-Cl-H_2O), it was found that the presence of $AgCl_4^{3-}$ can affect the purity of deposited copper metal. It was summarises that copper deposition were achieved with charge yield >0.90 and specific electrical energy consumptions (SEEC) of ca. 2 000 kW h $tonne^{-1}$, while depleting Cu^{2+} ions concentration from 470 to ca. 35 mol m^{-3} under mass transport control at potentials of -0.45 V (SCE) using the reactor containing a fluidised bed electrolyte.

Table 6-13. XRF analysis for copper deposition at -0.45 V (SCE).

Formula	Net intensity	Statistical error / %	LLD / ppm	Analyzed layer / μm	XRF concentration
Cu	123.30	0.36	1.8	460	0.677
Cl	16.01	1.01	5.5	43	0.309
Na	0.64	3.87	13.9	4.7	0.0098
Si	0.21	9.71	2.0	15	0.0022
Ti	0.46	7.83	2.1	97	0.0020

6.6.2. Electrodeposition of low concentration of $CuCl_n^-$ in circulating particulate bed electrode

Figure 6-84 illustrates images of Cu deposits in the circulating particulates bed reactor after the pre-plating with Cu (a) on the feeder Cu cathode and (b) on the graphite particles in the catholyte compartment. Even distribution of Cu deposition was observed on both the feeder cathode and in the packed bed of Cu particulates. On the feeder cathode, most Cu deposition occurred along the area corresponding to the descending packed bed and the draft tube. A smooth deposit of Cu was observed on the feeder cathode area due to electrodeposition from $CuSO_4$ solutions prior to the electrodeposition from the actual WEEE leachate. This even distribution of Cu deposition was also reflected in the catholyte compartment as shown in Figure 6-84(b).

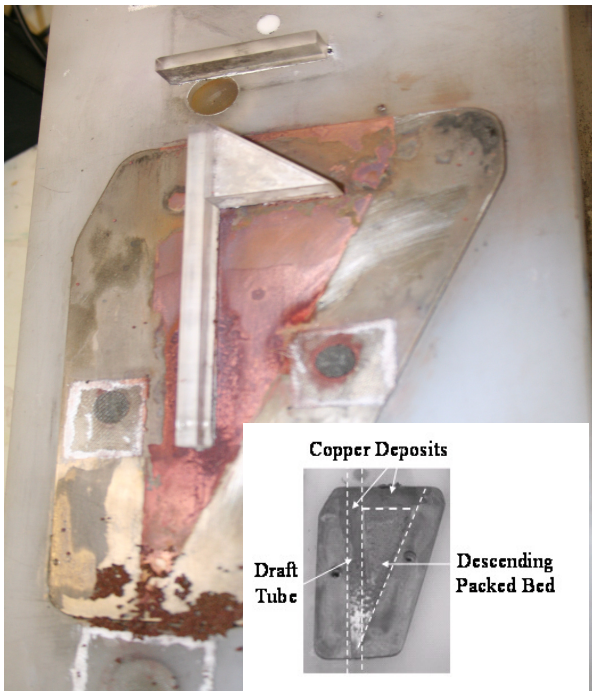

(a)



(b)

Figure 6-84. Images of copper pre-plating in the circulating particulate bed reactor: (a) on the feeder cathode electrode and (b) on the virgin graphite particles inside the catholyte compartment. Electrowinning from 1 kmol m^{-3} $CuSO_4$ acidified to pH 0.5 with H_2SO_4, operated for 1.5 hrs at 3 A.

Figure 6-85 illustrates the images of copper deposits after the deposition from the simulated WEEE leachate in the CPBE. Since the voidage in the draft tube and above the packed bed was higher with respect to that in the packed bed, the effective conductivity of electrolyte in those areas was also higher, and hence became the preferred paths for the current flow. In order to maximise the proportion of the current passing through the particulate bed and so fully utilise the large surface area provided by the Cu particles to ensure high Cu removal rates, the feeder cathode areas corresponding to the draft tube and above the packed bed were insulated (lacquered) with acrylic paint to block the current routes by-passing the packed bed. Pieces of Cu deposits were formed along the draft tube and the descending packed bed; bridging and interlock between of Cu particulates were observed due to significant amount of Cu deposits.

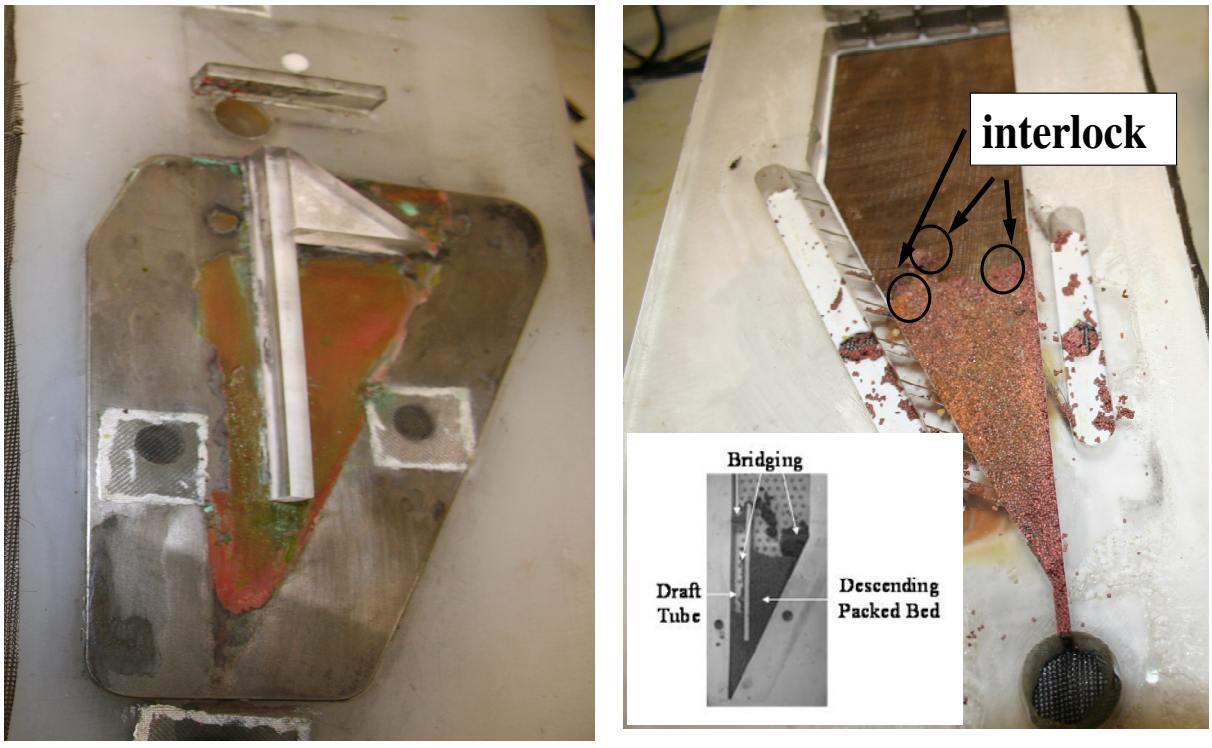

(a) (b)

Figure 6-85. Images of copper deposits after Cu deposition from the simulated WEEE leachate in the circulating particulates bed reactor: (a) on the feeder cathode electrode and (b) on the Cu pre-coated graphite particles inside the catholyte compartment.

For an electrolyte with average flow rate of 0.25 dm^3 min^{-1} and an initial Cu^{II} concentration of 15 mol m^{-3}, Figure 6-86(a) and (b) respectively show the time dependence of (ln) copper concentration and current at applied feeder cathode potentials of -0.36, -0.38 and -0.40 V (SCE).

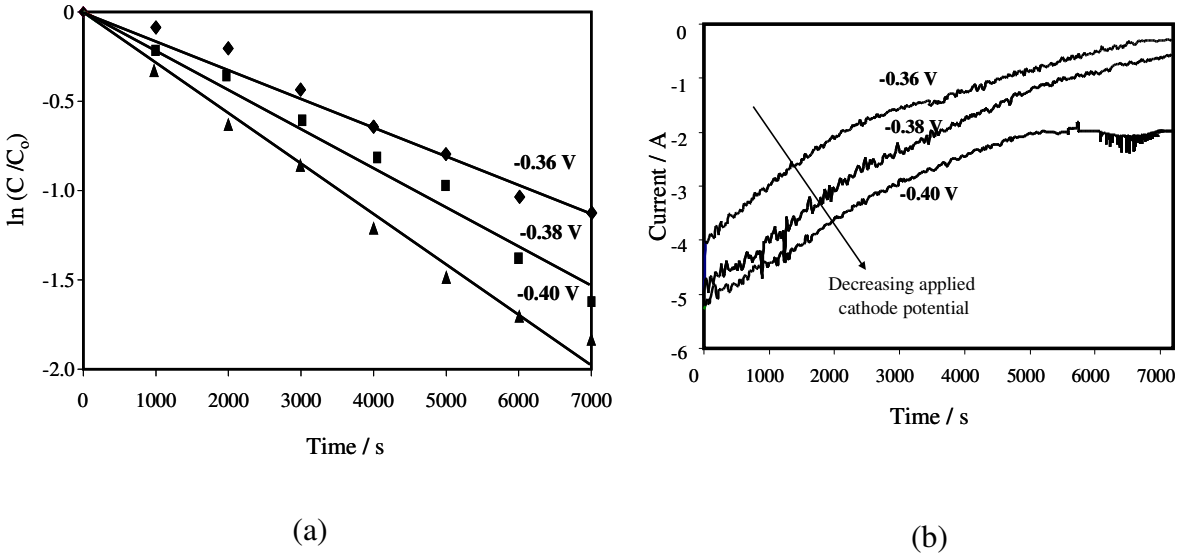

(a) (b)

Figure 6-86. Effects of cathode feeder potential on the time dependence of (a) copper concentration in the form of ln (c/c_0) and charge efficiency, and (b) current, for copper deposition in a circulating particulates bed reactor at a flow rate of 0.25 dm^3 min^{-1} and an initial copper concentration of 15 mol m^{-3}.

As the applied feeder cathode potential decreased from -0.36 to -0.40 V (SCE), the rate of Cu deposition increased. The reversible potential for the reduction of $CuCl_2$(aq) to $CuCl_2^-$ could be estimated by equation [6-6]. For $CuCl_2$(aq)/$CuCl_2^-$ ratio between 20 and 0.05, the reversible potential for the reduction of $CuCl_2$(aq) to $CuCl_2^-$ was estimated to be between 0.37 and 0.22 V (SCE). With applied cathode potentials between -0.36 and -0.40 V (SCE), the rate of the reduction of $CuCl_2$(aq) to $CuCl_2^-$ was likely to be under total mass transport control (refer Figure 6-78) and the decreasing applied cathode potential would have little effect on its rate. On the other hand, the reversible potential for the reduction of $CuCl_2^-$ to Cu could be estimated by equation [6-7]. For $CuCl_2^-$ concentrations between 10 and 1 mol m^{-3}, the reversible potential was estimated to be between -0.21 and -0.28 V (SCE). The increase in the removal rate of Cu as the applied cathode potential decreased from -0.38 to -0.40 V (SCE) indicated that the reduction of $CuCl_2^-$ to Cu was under mixed kinetic and mass transport control.

Assuming the reduction rate of $CuCl_2^-$ to Cu was fast and all $CuCl_2^-$ generated from the reduction of $CuCl_2$(aq) were reduced to Cu instantaneously, the concentration of $CuCl_2^-$ in the electrolyte was insignificant and Cu concentrations (c) measured by the ICP was contributed by $CuCl_2$(aq) only (knowing that ICP could not distinguish between $CuCl_2$ (aq) and $CuCl_2^-$ and it measured the total Cu ions concentration), the overall charge (Q_c) required to reduce

$CuCl_2$(aq) to Cu in the catholyte reservoir could be calculated from the concentration:

$$Q_c = 2 \cdot V_c \cdot F \cdot (c_0 - c) \quad [6\text{-}33]$$

Where V_c is the volume of the catholyte.

The charge supplied by the potentiostat (Q_I) could be calculated from the current:

$$Q_I = \int I \, dt \quad [6\text{-}34]$$

The overall charge yield (Q_{yield}) can be estimated by:

$$Q_{yield} = Q_c \Big/ Q_I \quad [6\text{-}35]$$

As the applied feeder cathode potential was decreased from -0.36 to -0.40 V (SCE), the overall copper removal rate increased, but the overall charge yield decreased from 0.70 to 0.58 as shown in Figure 6-87. The measured copper concentration was assumed to be in the form of Cu ions, but in reality, it would have been present as a mixture of $CuCl_2$(aq) and $CuCl_2^-$ ions, so the overall charge efficiency could be higher than presented in Figure 6-87.

H_2 bubbles were observed at the beginning of the experiments for applied feeder cathode potentials of -0.40 V (SCE), while no H_2 bubbles were observed at an applied feeder cathode potential of -0.36 V and 0.38 V (SCE). This is shown clearly at >5000 s for applied potential of -0.40 V (SCE) (Figure 6-86 (b)). Theoretically, the rate of H_2 evolution should not be significant for potentials > -0.5 V (SCE). However, due to the potential distribution across the circulating particulate bed cathode, overpotentials and current densities increased towards the membrane. As an increase in current densities would in turn increase potential drops across the bed cathode, the increase in current density across the packed bed cathode would be amplified. Since the rate of H_2 evolution was in the kinetically controlled region, a small increase in the overpotential led to a significant increase in its current density. This could explain the difference in the initial current (4 – 5.5A) for applied cathode potentials between -0.36 and -0.40 V (SCE) (refer Figure 6-86 (b)). As copper concentrations decreased with time, reaction rate and current density also decreased with time.

For applied cathode potential at -0.38 V (SCE), no H_2 bubbles were observed for times > 600 s as illustrated in Figure 6-86 (b). As the current decreased with decaying copper concentrations, the potential drop across the bed cathode decreased and the overpotential was

no longer large enough for H_2 evolution. H_2 evolution decreased cathode charge yields so its rate should be minimised.

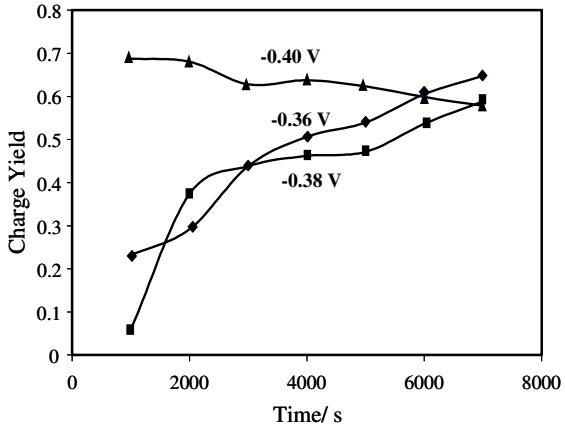

Figure 6-87. Effects of cathode feeder potential on time dependence of charge yield, for copper deposition in a CPBE reactor at a flow rate of 0.25 dm^3 min^{-1} and initial copper concentration of 15 mol m^{-3}.

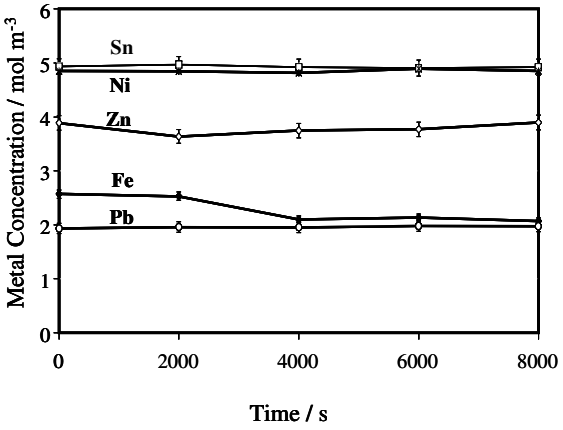

Figure 6-88. Time dependences of tin, nickel, zinc, iron and lead ion concentrations, for copper deposition in a CPBE reactor at a flow rate of 0.25 dm^3 min^{-1} and initial copper concentration of 15 mol m^{-3}; cathode potential = -0.38 V.

Figure 6-88 shows the time dependences of tin, nickel, zinc, iron and lead ion concentrations in the simulated WEEE leachate. There were no abrupt changes in the concentrations of any of those metals, except for iron which is acknowledged that Fe^{3+} can be reduced to Fe^{2+} (reaction [6-36]) as the reversible potential given by equation [6-37]. However, iron would not have been reduced to elemental form, thus remained in the solution. As reported by Dew and Phillips [26,27], copper electowinning in aqueous sulphate solutions from concentrations below 1 gL^{-1} containing equivalent of greater amounts of Fe^{II} or Fe^{III} using a 'Chemelec' cell, the reduction of of Fe^{III} and Fe^{II} at the cathode had a negative effects on the charge yield of copper electrowinning . Nonetheless, co-deposition was not reported and the copper purity achieved was >99.99% (confirmed by ICP).

$$Fe^{3+} + e^- \rightleftharpoons Fe^{2+} \qquad [6\text{-}36]$$

$$E_{Fe^{3+}/Fe^{2+}}\,(\mathbf{SHE})\ /\ \mathbf{V} = 0.775 + 0.059 \log\left\{\left(Fe^{3+}\right)/\left(Fe^{2+}\right)\right\} \qquad [6\text{-}37]$$

Noting that most of the iron will be removed via eddy current separation prior to the leaching

process, as explained in Chapter 4 (Materials and Experimental Methods), this should not be a barrier to achieve high charge efficiency for copper deposition.

The experiments had demonstrated the feasibility of using the circulating particulates bed cathode for the electrowinning of copper metal from the WEEE leachate. Cu^{II} ions can be depleted to concentrations that were analytically undetectable limits ca. 100 ppm (Figure 6-86 (a))at -0.38 V (SCE), recovered with reasonable charge yield ca. 0.7 at 7000 s (Figure 6-87) and very low specific electrical energy consumption (SEEC) of 800-1300 kW h (tonne Cu)$^{-1}$ for cell voltages (U_{cell}) of 2.0-3.0 V as measured using equation [2-35].

6.7. Deposit Morphologies

The morphology of the Cu deposits was one of the important factors determining if the mesh cathode in the fluidised bed of inert particles or the circulating particulates bed reactor was feasible for the recovery of Cu from the catholyte (WEEE leach solution). Cu deposits formed from chloride media tend to be dendritic [5,28], breaking easily from the cathode's surface, re-dissolving in the catholyte and so decreasing charge yields [9,11]. Coherent and adherent Cu deposits are essential for maintaining high charge efficiencies, achieving a reasonable Cu loading on the electrode and enabling the transfer of metal-coated cathodes to the electro-refining stage.

Figure 6-89 shows a SEM image of dendritic Cu deposited under total mass transport control at -0.50 V (SCE) on a mesh cathode, in the absence of glass beads at flow rate of 1.85 dm^3 min^{-1} [21] The Cu deposit clearly had a high voidage and was not adherent.

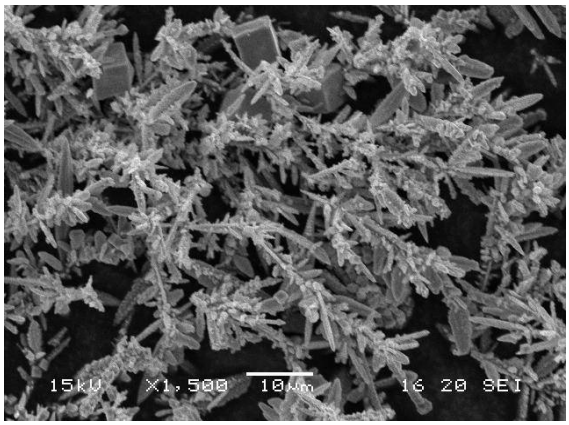

E_c = -0.50 V (SCE) (No fluidised bed cathode)

Figure 6-89. SEM images of copper deposits on titanium mesh cathode with no fluidised inert particles. Image courtesy of Cheng et al.[21].

Figure 6-90 (a) and (b) show SEM images of copper deposits on the Ti mesh cathode in a fluidised bed of glass beads, operating at cathode potentials of -0.35 and -0.45 V(SCE) respectively. The Cu morphology obtained for -0.35 V (SCE), at which deposition occurred under mixed kinetic and mass transport control, was a compact adherent cauliflower structure with little voidage, similar to that obtained in the circulating particulate bed reactor. When Cu was deposited under total mass transport control on a mesh cathode at -0.45 V (SCE), the shape of the deposits was more irregular and the voidage was higher than that for -0.35 V (SCE). However, the structures were still detached and adherent. The purity of copper deposits at -0.45 V (SCE) (as per reported in section 6.6.1) has been confirmed by ICP to achieve a purity of 99.79 %. In addition, the purity of copper deposits at -0.35 V and -0.45 V (SCE) was identified qualitatively via XRD, as shown in Figure 6-91. In contrast with the ICP results, the resulting diffraction patterns [29] shows the presence of solid $CuCl_2$ on the surface of elemental copper, as the existence of acidic chloride and oxygen would have caused corrosion of the electrodeposited copper once the potential was removed. Hence, to minimise the copper oxidation rates, the electrode surfaces were rinsed with aqueous sodium hydroxide (NaOH) as soon as it is removed from the reactor.

The potential at which the electrodeposition of Cu occurred is important, as better quality deposits are usually achieved when deposition occurs in the kinetic controlled region rather than under mass transport control [21]. If the Cu deposits have a porous structure and the potential is low enough for H_2 evolution to occur, the H_2 bubbles evolved from the Ti electrode may lift some of the Cu deposits (on top of the Ti mesh cathode) off the surface.

Overall, the presence of fluidised glass particles improved the Cu deposits morphology, but adherent deposits were only achieved when Cu was deposited under mixed kinetic and mass transport control.

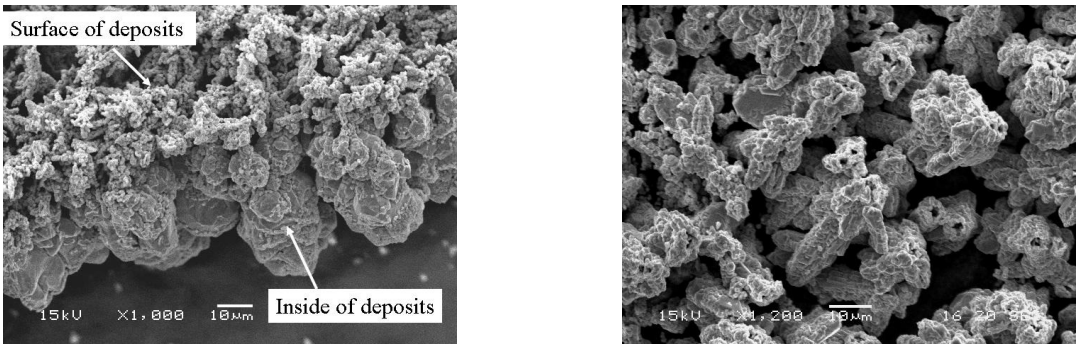

(a) Ec = -0.35 V (SCE) (b) Ec = -0.45 V (SCE)

Figure 6-90. SEM images of copper deposits on titanium mesh cathode in a fluidised bed of glass beads at cathode potentials of: (a) -0.35 V (SCE), (b) -0.45 V (SCE).

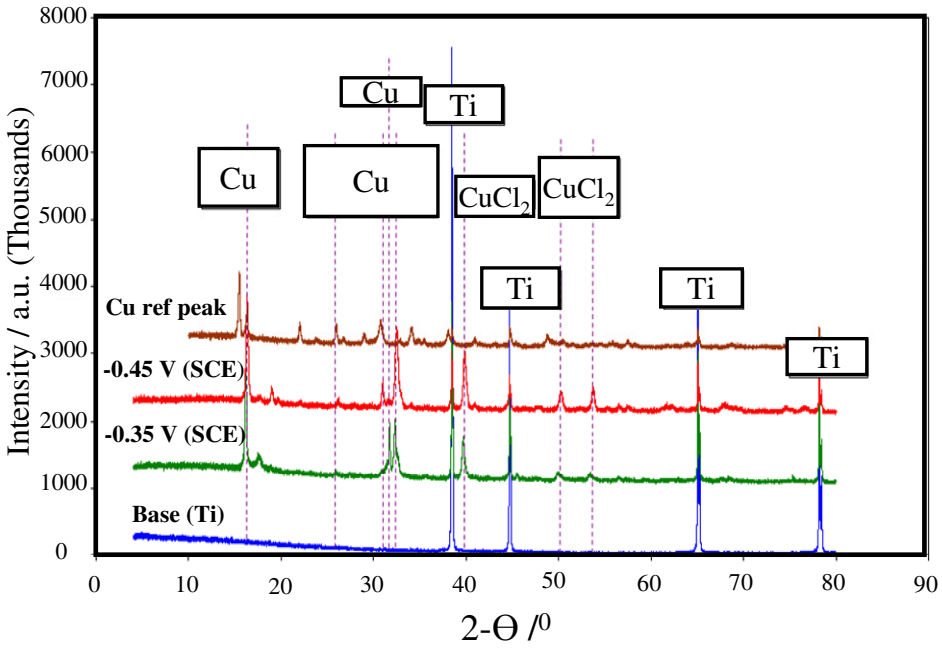

Figure 6-91. XRD spectrum of Cu deposit samples at -0.35 V and -0.45 V (SCE) on Ti mesh electrode.

Figure 6-92 shows a SEM image of copper deposits on a copper particle in the circulating particulate bed reactor, operating under mixed kinetic and mass transport control, at a feeder cathode potential of -0.38 V (SCE). The average diameter of Cu-coated graphite particles, measured under a microscope, was 485 and 510 μm, respectively, before and after Cu deposition. Therefore, the increase in thickness of the Cu deposits was ca. 25 μm. The Cu deposits were adherent to the particles and the SEM image showed a compact cauliflower structure with little voidage. Random samples of Cu particles were chosen from the packed bed cathode and they all showed similar structure to that of Figure 6-92, which proved that the constant collisions between the Cu particulates in the circulating particulates bed reactor was able to improve the deposits morphology.

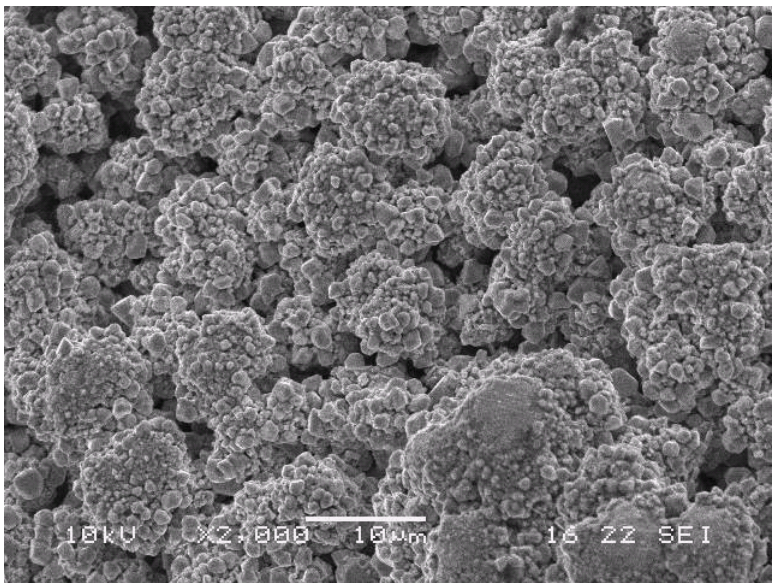

Figure 6-92. SEM image of copper deposits on a copper particle in the circulating particulate bed reactor operating at a feeder cathode potential of -0.38 V (SCE).

6.8. Chapter Summary

The presence of mixed oxidation state copper (II-I) species was confirmed by absorption spectra in the visible light region. However, cyclic voltammetry analysis showed that they had no significant effect on the electrodeposition of Cu.

The experimental results demonstrated the feasibility of using both the mesh cathode in a fluidised bed of inert particles and the circulating particulate bed reactor for the electrodeposition of copper from the chloride leach solution. Copper purities of > 99.79%

(confirmed by ICP) were achieved with charge yields of > 0.90 and specific electrical energy consumptions of ca. 2 000 kW h tonne^{-1}, while depleting copper ion concentrations from 470 to ca. 35 mol m^{-3} with reactor containing fluidised bed electrolyte operated under mass transport control at potentials of -0.45 V (SCE). Adequate Cu deposit morphologies, reaction rates and charge yields can be achieved, providing the electrode potential, flow rate and initial dissolved copper concentration were carefully controlled.

For the circulating particulate bed reactor, decreasing the cathode feeder potential from -0.36 to -0.40 V (SCE) increased the Cu deposition rate, but decreased charge yields from 0.70 to 0.58, due to H_2 evolution resulting from the potential distribution across the circulating particulate bed cathode. Concentrations of 15 mol m^{-3} of $CuCl_2$(aq) and $CuCl_2^-$ ions in 4 kmol m^{-3} HCl + 1 kmol m^{-3} NaCl in aqueous electrolyte were reduced successfully to elemental copper in a circulating bed of 0.5-1 mm graphite particles, in an electrochemical reactor incorporating a cation- permeable membrane and operated in bath recycle mode. Depletion to concentrations $< 5\times10^{-3}$ mol m^{-3} was kinetic and mass transport controlled at an applied potential of -0.38 V (SCE). Specific electrical energy consumptions of ca. 800-1300 kW h (tonne Cu)$^{-1}$ were achieved for cell voltages of 2.0-3.0 V and fractional current efficiencies of ca. 0.70.

SEM images confirmed that adherent and coherent Cu deposits were achieved with both circulating particulate bed reactor and the reactor with a mesh cathode in a fluidised bed of inert particulates, for Cu deposition under mixed kinetic and mass transport control.

6.9. References

[1] McConnell, H. and Davidson, N., 1950, Optical Interaction between the Chloro-complexes of Copper(I) and Copper(II) in Solutions of Unit Ionic Strength 1. *J. Am. Chem. Soc*, 72 (7): 3168-3173.

[2] Bard, A.J., Parsons, R. and Jordan, J., 1985, Standard potentials in aqueous solutions, Marcel Dekker, New York.

[3] Powell, K.J., Brown, P.L., Byrne, R.H., Gajda, T., Hefter, G., Sjoberg, S. and Wanner, H., 2007, Chemical speciation of environmentally significant metals with inorganic ligands. Part 2: The Cu^{2+}-OH^-,Cl^-, CO_3^{2-} , SO_4^{2-}, and PO_4^{3-} systems (IUPAC Technical Report). *Pure and App. Chem*., 79: 895-950.

[4] Wang, M., Zhang, Y. and Muhammed, M., 1997, Critical evaluation of thermodynamics of complex formation of metal ions in aqueous solutions. III. The system Cu(I,II)-Cl^--e at 298.15 K. *Hydromet*., 45 (1/2): 53-72.

[5] Kekesi, T. and Isshiki, M., 1997, Electrodeposition of copper from pure cupric chloride hydrochloric acid solutions. *Chim. & Mat. Sci. J. App. Electrochim*., 27 (8): 982-990.

[6] Fritz, J.J., 1985, Thermodynamic properties of chloro-complexes of silver chloride in aqueous solution. *J. Sol. Chem*., 14 (12): 865-879.

[7] Welham, N.J., Kelsall, G.H. and Diaz, M.A., 1993, Thermodynamics of Ag-Cl-H_2O, Ag-Br-H_2O and Ag-I-H_2O systems at 298 K. *J. Electroanal. Chem*., 361 (1/2): 39.

[8] Primer A., 1996, Fundamentals of modern UV-visible spectroscopy. Hewlett Packard.

[9] Winter, D.G., Covington, J.W. and Muir, D.M., 1982, Studies related to the electrowinning of copper from chloride solutions. In: P.D. Parker, Editor, Chloride Electrometallurgy, AIME, New York : 167–188.

[10] Lee, H.P.and Nobe, K., 1986, Kinetics and mechanisms of Cu dissolution in chloride media . *J. Electrochem. Soc*., 133(10):2035-2043.

[11] Albert, L., Winand, R., 1982, Copper electrowinning in chloride aqueous solutions, in: [Ed.] P.D. Parker, Chloride Electrometallurgy Proceedings Symposium, Warrendale: The Metallurgical Society of AIME.: 203-219.

[12] Muir, D.M., 1982, Electrowinning of copper from copper(I) electrolytes: III: Diffusion coefficients and rates of electron transfer in copper(I) electrolytes, Stevenage: Warren Spring Laboratory.

[13] Majima, H., Peters, E., Awakura, Y., Park, S.K. and Aoki, M., 1989, Electrical conductivity of acidic chloride solutions. *Metall. and Mat. Trans. B*, 20 (3): 337-343.

[14] Bertocci, U. and Turner, D.R., 1974, Chapter II-6: Copper, Encyclopedia of

electrochemistry of the element, Vol II, New York: Marcel Dekker.

[15] Puvvada, G. and Tran, T, 1995, The cementation of Ag(I) ions from sodium chloride solutions onto a rotating copper disc. *Hydromet*., 37: 193-206.

[16] Jovic, V.D., Stojanovic, M.V., Jovic, B.M. and Gajic-Krstajic, L.J., 1992, Electrochemical deposition of Ag, Pd and Ag-Pd alloy from chloride containing electrolyte. *J. Serbian Chem. Soc*., 57(12): 951-962.

[17] Meredith RW and Tobias CW, 1962, Conduction in heterogeneous systems. *Adv. Electrochim. and Electrochem. Eng*., 2 : 15-47.

[18] Cabin D.C. and Gabe D.R., 1974, Electrodeposition from a fluidised bed electrolyte- I. The mass transport correlation. *Electrochim. Acta*, 19: 645-652.

[19] Walker, A. T. S. and Wragg, A. A., 1980, Mass transfer in fluidised bed electrochemical reactors. *Electrochim. Acta*, 25 (3): 323-330.

[20] Cheng, C.Y., Kelsall, G.H. and Robson, A., 2008, Recovery of Metals from 4 M HCl and 1 M NaCl Solutions by Circulating Particulates Bed Reactor and Mesh Cathode in a Fluidised Bed of Inert Particles - Part 1. Modelling. Personal Communication.

[21] Cheng, C.Y. and Kelsall, G.H., 2008, Recovery of Metals from 4 M HCl and 1 M NaCl Solutions by Circulating Particulates Bed Reactor and Mesh Cathode in a Fluidised Bed of Inert Particles - Part II. Experimental. Personal Communication.

[22] Kelsall, G.H. and Gudyanga, F.P., 1991, Electrochechemical Reactor Design Consideration for Simultaneous Tin Electrowinning and Cr^{2+} Electrogeneration. *Dechema Monogr*, 123: 167.

[23] Cheng, C.-Y., Diaz, M. A., Kelsall, G. H. and Robson, A. C., 2006, Gold Electrowinning from Acidic Aqueous Chloride in a Packed Bed Electrode. *ECS Transactions*, 2 (3): 317-328.

[24] Kelsall, G., 2007, CE 408 - Electrochemical Engineering and Technology Lecture Notes, Imperial College London.

[25] Appleby, A.J., Chemla, M., Kita, H. and Bronoel, G. in Encyclopedia on Electrochemistry of the Elements, Ch.IX-A3, Vol.IX, A.J.Bard (Ed.) Marcel Dekker, New York, 1982: 383-597.

[26] Dew, D.W. and Phillips, C.W., 1985, The effect of Fe(II) and Fe(III) on the efficiency of copper electrowinning from dilute acid Cu(II) sulphate solutions with the Chemelec cell. Part I. Catholic and anodic polarisation studies. *Hydromet.,*14 (3): 331–349.

[27] Dew, D. W. and Phillip, C.V., 1985, The effect of Fe(II) and Fe(III) on the efficiency of copper electrowinning from dilute acid Cu(II) sulphate solutions with the chemelec cell.

Part II. The efficiency of copper electrowinning from dilute liquors. *Hydromet.*, 14 (3): 351-367.

[28] Mackinnon, D. J., Brannen, J. M. and McMillan, R. S., 1985, Factors affecting the structure of copper deposits electrowon from aqueous chloride electrolyte. *J. App. Electrochim.*, 15 (5): 649-658.

[29] Powder Diffraction File, Inorganic Phases, X-ray powder diffractometry (X'Pert PRO model).

7. SELECTIVE ELECTRODEPOSITION OF TIN FROM TIN (Sn^{IV})- LEAD (Pb^{II}) AQUEOUS CHLORIDE SOLUTIONS

7.1. Chapter Overview

Mixtures of different metal ions with similar electrode potentials, such as Sn^{IV}/Sn and Pb^{II}/Pb in chloride solutions, will be difficult to separate from each other by electrodeposition, affecting the purity of the recovered metals and hence their reuse value. A system that recovers the metal non-selectively as an alloy, requiring subsequent purification steps, is likely to cost more than a process of direct, selective metal recovery, unless there is a commercial outlet for the alloy. This is especially pertinent as the heavy metal ions are often dilute and the recovery costs must be significantly lower than the value of the metal recovered as well as the environmental well-being contribution. Thus, the experiments for which results are reported below attempted to establish the feasibility or otherwise, of selective recovery of tin from synthetic Sn^{IV}-Pb^{II} aqueous chloride solutions, simulating those produced by leaching WEEE.

This chapter is divided into five main sections. In the first, the thermodynamics of tin-chloride-water (Sn-Cl-H_2O), and lead-chloride-water (Pb-Cl-H_2O) systems are presented. In the second, the electrodeposition kinetic of $SnCl_n^{(4-n)+}$ which demonstrates typical voltammograms for different rotation rates (60 – 2940 rpm) were measured. The third section describes the usage of rotating (vitreous carbon) disc electrodes to determine reduction and electrodeposition kinetic data, such as current exchange density and Tafel slope, for Sn^{IV} solutions in 4 kmol m^{-3} HCl + 1 kmol m^{-3} NaCl. Experiments with a rotating vitreous carbon cathode confirmed model predictions from a kinetic model, discussed in the fourth section (section 7.3), for a small electrode potential window within which to achieve selective electrodeposition of tin from synthetic Sn^{IV}-Pb^{II} aqueous chloride solutions, from which Pb could be electrodeposited subsequently. This paves the way for the last section, the results of selective tin electrodeposition using an electrochemical reactor with a Ti/Ta_2O_5-IrO_2 anode, cation-permeable membrane and a Ti mesh cathode in a fluidised bed of 590-840 μm glass beads to enhance mass transfer rates and to improve deposit morphologies. The effects of cathode potential on electrodeposition rates, charge yields and specific electrical energy consumptions were also determined.

7.2. Thermodynamics

7.2.1. Tin

Tremendous efforts have been done in the late 60's and early 70's on tin electrochemical reactions of tin in aqueous electrolytic solutions [1,2,3] including chloride media [4,5,6,7]. Most of the researchers concluded that tin is present in the oxidation state Sn^{II} (stannous) and Sn^{IV} (stannic) in aqueous solution. However, Stirrup and Hampson [8] envisaged that the kinetics of Sn^{II}/Sn^{IV} reaction were not completely clear and emphasised that further work are needed to explain the phenomena. According to Kragten [4], House and Kelsall [12], Sn^{II} and Sn^{IV} ions have such a strong tendency to form chloride complexes that even at a concentration of 1 kmol m^{-3} the highest complexes: $SnCl_4^{2-}$ and $SnCl_6^{2-}$ complex are formed. Kragten [4] reported that relation for the solubility of tin in solutions with pH up to 1 as;

$$\log\left[Sn\right]_{\max} = -3.00 - 4.00 \cdot pH \qquad [7\text{-}1]$$

This entails a maximum solubility for tin of $[Sn]_{max} = 10^{-3}$ kmol m^{-3} at pH = 0, however it rapidly increases with a decline in the pH and results in a value of $[Sn]_{max} = 10^{-1}$ kmol m^{-3} for pH= -0.5. This solubility increases even further with an increase in free chloride concentration [12] as per shown in Figure 7-93. The solubility diagram shows that all Sn present in solution in the form of Sn^{IV} whereby the presence of lower oxidation state species i.e. Sn^{II} is negligible. However, a two reduction waves of the Sn^{IV}-chloro complexes is the most reported reduction route [6,8,12] and will be discussed in section 7.2.

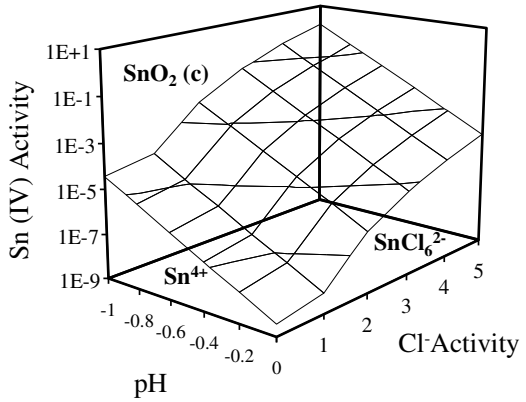

Figure 7-93. Solubility of Sn^{IV} species in aqueous chloride media at 298 K [12].

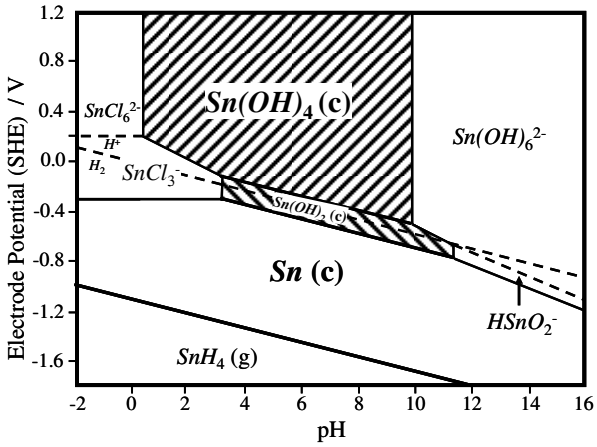

Figure 7-94. Potential pH diagram for tin-chloride-water. Activities: Dissolved tin and chloride activities = 10^{-3} and 5 respectively; 298 K, 1 atm [12].

Figure 7-94 shows the pH- potential diagram of Sn-Cl-H_2O with dissolved tin and chloride activities were 10^{-3} and 5 respectively. At pH 0, the relevant dissolution reactions are:

$$SnCl_6^{2-} + 2e^- \rightleftharpoons SnCl_4^{2-} + 2Cl^- \qquad [7\text{-}2]$$

$$E_{SnCl_6^{2-}/SnCl_4^{2-}}\textbf{(SHE) / V} = 0.1928 + 0.0296\log\left\{\left(SnCl_6^{2-}\right)/\left(SnCl_4^{2-}\right)\right\} - 0.059\log\left(Cl^-\right) \qquad [7\text{-}3]$$

$$SnCl_4^{2-} + 2e^- \rightleftharpoons Sn + 4Cl^- \qquad [7\text{-}4]$$

$$E_{SnCl_4^{2-}/Sn}\textbf{(SHE) / V} = -0.190 + 0.0296\log\left(SnCl_4^{2-}\right) - 0.118\log\left(Cl^-\right) \qquad [7\text{-}5]$$

The formation of Sn^{II} and Sn^{IV} chloride complexes reduces the predominance areas of elemental Sn from Sn-H_2O system [12]. Additionally, the inclusion of $Sn(OH)_4$ limits the predominance areas of stannite and stannate ions to the alkaline region as reported by Vetter [11].

7.2.2. Lead

Comprehensive reviewed thermodynamic data [13] were used to calculate potential-pH and solubility diagrams for Pb-H_2O and Pb-Cl-H_2O systems [14] for which the full set of data and equations are given in Appendix B(f) and C(f). The amphoteric nature of Pb^{II} and Pb^{IV} is reflected in the activity-pH diagrams, shown in Figure 7-95 and Figure 7-96, which shows the

effect of changing that activity on the pH dependent chemical reactions. As hypothesized, the higher oxidation state (Pb^{IV}) oxide is more stable and hence less soluble than the lower oxidation state (Pb^{II}) oxide. This is also reflected in Figure 7-97**,** the potential-pH diagram for the Pb-H_2O system at 298 K, which shows that the area of stability of PbO_2 extends over a wider pH range than that of PbO [14].

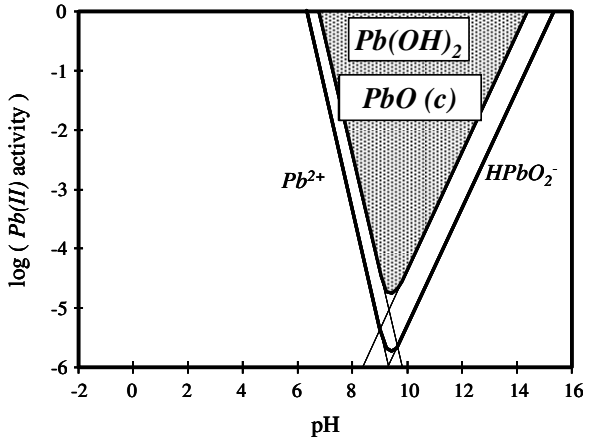

Figure 7-95. Activity-pH diagrams for Pb^{II} species in equilibrium with PbO (red) and $Pb(OH)_2$ (ppt.) at 298 K, 1 atm [14].

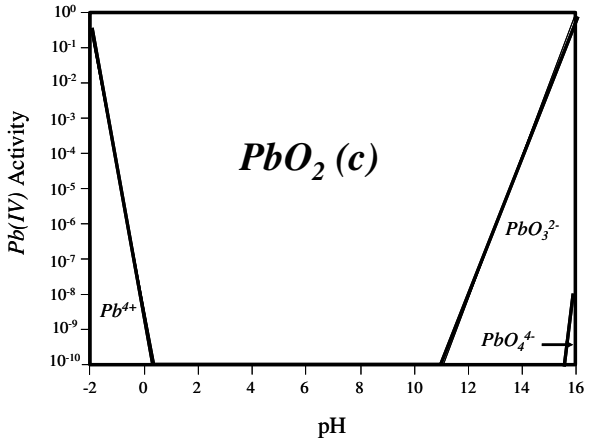

Figure 7-96. Activity-pH diagram for Pb^{IV} species in equilibrium with *PbO_2*, at 298 K, 1 atm [14].

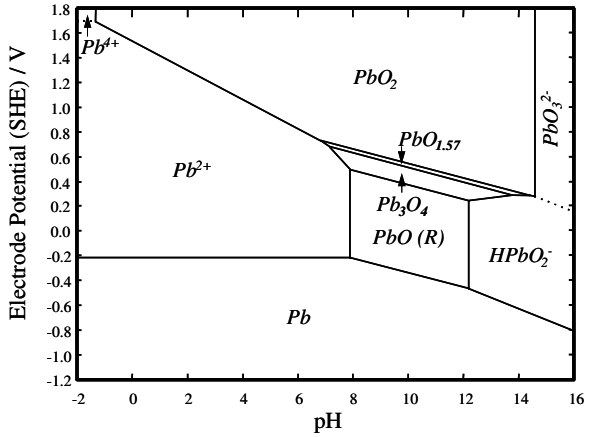

Figure 7-97. Potential-pH diagram for lead-water system. Dissolved lead and chloride activities = 10^{-3} and 5 respectively; 298 K, 1 atm [14].

In chloride media lead undergoes dissolution processes [14]

$$PbCl_n^{n-2} + 2e^- \rightleftharpoons Pb + nCl^- \quad [7\text{-}6]$$

$$Pb + 2H^+ + nCl^- \rightleftharpoons PbCl_n^{(2-n)} + H_2 \quad [7\text{-}7]$$

When $n = 2$, a dissolution/precipitation occurs:

$$PbCl_2 + 2e \rightleftharpoons Pb + 2Cl^- \quad [7\text{-}8]$$

$$E_{PbCl_2/Pb}\textbf{(SHE) / V} = -0.269 + 0.0591\log\left(Cl^-\right) \quad [7\text{-}9]$$

$$Pb + 2H^+ + 2Cl^- \rightleftharpoons PbCl_2(c) + H_2 \quad [7\text{-}10]$$

$$\log\left[Cl^-\right] = \mathbf{pH} - 4.54 \quad [7\text{-}11]$$

The precipitate lead chloride, $PbCl_2(c)$, is sparingly soluble in aqueous solutions:

$$PbCl_2(s) \rightleftharpoons Pb^{2+}(aq) + 2Cl^-(aq) \quad [7\text{-}12]$$

$$\log\left[Pb^{2+}\right] = -4.82 - 2\log\left[Cl^-\right] \quad [7\text{-}13]$$

$$K_{sp} = 1.17\times10^{-5}$$

but dissolves in high chloride concentrations [16][17] as chloro-complexes:

$$PbCl_2 + nCl^- \rightleftharpoons PbCl_{2+n}^{n-} \quad [7\text{-}14]$$

In general, Pb^{II} undergoes progressive ligand substitution with increasing chloride concentration:

$$Pb^{2+} + nCl^- \rightleftharpoons PbCl_n^{(2-n)} \quad [7\text{-}15]$$

The cumulative stability constant, β_n, is given by:

$$\beta_n = \frac{\left(PbCl_n^{(2-n)}\right)}{\left(Pb^{2+}\right)\left(Cl^-\right)^n} \quad [7\text{-}16]$$

where $\log \beta_1 = 1.60$, $\log \beta_2 = 1.78$, $\log \beta_3 = 1.68$ and $\log \beta_4 = 1.38$ [18].

The Pb^{II} activity-Cl^--pH diagram (Figure 7-98) for the Pb-Cl-H_2O system at 298 K and 1 atm. calculated from the above equilibrium equations and mass balances, shows the Pb^{II} species distribution as a function of chloride activity with total dissolved lead concentration of 10 mol Pb^{II} m^{-3}. At $(Cl^-) > 1.4$, $PbCl_4^{2-}$ species predominate. Figure 7-99 shows the potential-pH diagram for the Pb-Cl-H_2O system. The effect of the $PbCl_n^{(2-n)}$ complexes increased the region of stability of the Pb^{II} dissolved species, in comparison with those in the Pb-H_2O systems (Figure 7-97) and the effect is greater when there is higher activity of (Cl^-).

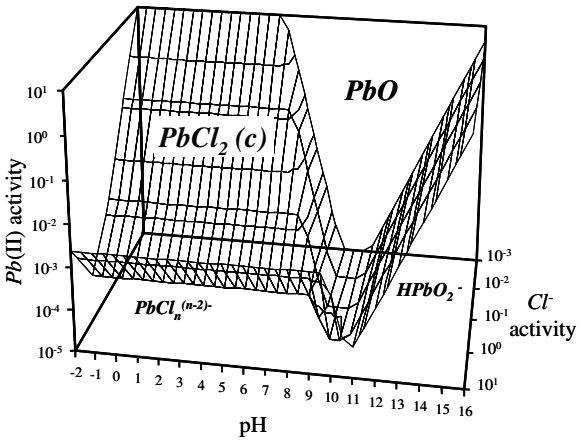

Figure 7-98. Solubility of Pb^{II} species in aqueous chloride media at 298 K, 1 atm.

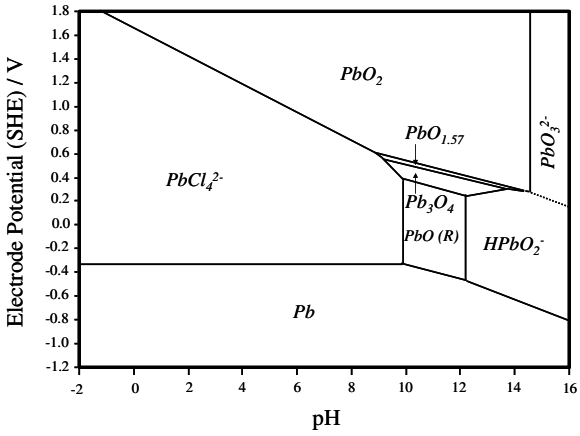

Figure 7-99. Potential pH diagram for lead-chloride-water. Activities: Dissolved tin and chloride activities = 10^{-3} and 5 respectively; 298 K, 1 atm [14].

Superimposing the Sn-Cl-H_2O and Pb-Cl-H_2O systems potential pH diagrams, revealed a small window of operation, where selective Sn^{II} reduction is thermodynamically more favourable ($E^{\circ}_{Sn^{2+}/Sn} = -0.30$ V(SHE), $E^{\circ}_{Pb^{2+}/Pb} = -0.40$ V(SHE); for concentration ratios $[Sn^{II}]$:$[Pb^{IV}]$ as 3:1). However, it must be remembered that these diagrams represent the thermodynamic feasibility of these species without taking into considerations the kinetics of these reactions. Experimentally determined kinetic parameters are presented in the following section.

7.3. Transport and Kinetic Analyses

7.3.1. Determining the reduction kinetics of Sn^{IV} chloro- complexes

Figure 7-100 shows the effect of rotation rate of a vitreous carbon (VC) disc electrode on

voltammograms, in which the potential was swept initially in a negative-going direction from -0.40 V to -1.10 V (SCE). Current densities due to reactions [7-2] and [7-4] in the potential range $E_{SnCl_6^{2-}/SnCl_4^{2-}}$ [7-3] to $E_{SnCl_4^{2-}/Sn}$ [7-4] shown in Figure 7-94 were extremely small, possibly due to the pH-dependent polymerisation of the ill-characterised Sn^{IV} species in solution and the properties of the VC electrode. Hence, it was not possible to determine the kinetic parameters for reduction of Sn^{IV} to Sn^{II}. The reduction always proceeds directly to tin metal depending on the electrode potential and the pH in the solution. The reduction of Sn^{IV} gave a single wave, which was not completely separated from the hydrogen evolution. Monien [5] reported the similar phenomena of Sn^{IV} reduction at a planar mercury electrode using chronopotentiometry, whereby the reduction was found to be irreversible and complicated by chemical complex formation which precedes the electrode reaction. In contrast to the investigation done by Monien [5], Stirrup and Hampson [8] reported that Sn^{IV} reduction mechanism was found to be two-electron transfer to form Sn metal in 0.1 -5 kmol m^{-3} HCl aqueous solutions.

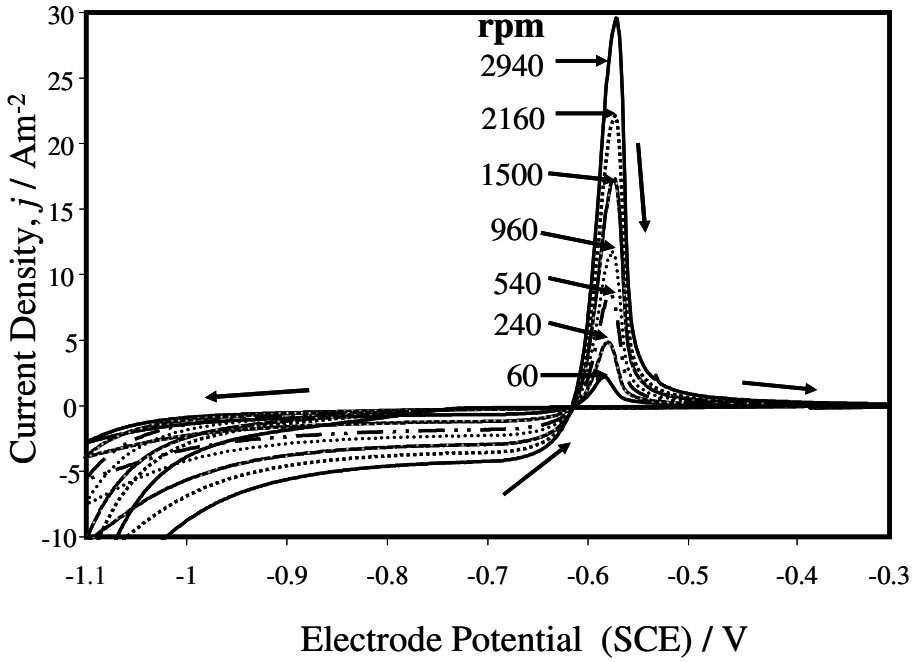

Figure 7-100. Cyclic voltammogram of a vitreous carbon rotating disc electrode rotating at 16 s^{-1} in 1 mol m^{-3} Sn^{IV} in 4 kmol m^{-3} HCl + 1 kmol m^{-3} NaCl at a scan rate of 5 mV s^{-1}.

The reactions predicted by Figure 7-100 to have occurred during negative-going potential scans are for the reduction of 1 mol m^{-3} Sn^{IV} in 4 kmol m^{-3} HCl + 1 kmol m^{-3} NaCl at a scan

rate of 5 mV s^{-1}:

At the negative-going potential scans the predicted reactions are:

$$E < E_{SnCl_6^{2-}/SnCl_4^{2-}} = -0.095 \text{ V(SCE)}; \; SnCl_6^{2-} + 2e^- \rightleftharpoons SnCl_4^{2-} + 2Cl^- \quad [7\text{-}17]$$

$$E < E_{SnCl_4^{2-}/Sn} = -0.525 \text{ V(SCE)}; \quad SnCl_4^{2-} + 2e^- \rightleftharpoons Sn + 4Cl^- \quad [7\text{-}18]$$

$$E < E_{H^+/H_2} = -0.750 \text{ V(SCE)}; \qquad 2H^+ + 2e^- \rightleftharpoons H_2 \quad [7\text{-}19]$$

and at the positive-going potential scans the predicted reactions are:

$$E > E_{SnCl_4^{2-}/Sn} = -0.525 \text{ V(SCE)}; \quad Sn + 2e \rightarrow SnCl_4{}^{2-} + 2Cl^- \quad [7\text{-}20]$$

$$E > E_{SnCl_6^{2-}/SnCl_4^{2-}} = -0.095 \text{ V(SCE)}; \; SnCl_6^{2-} + 2e \rightarrow SnCl_4{}^{2-} + 2Cl^- \quad [7\text{-}21]$$

Experimentally, at -0.60 V (SCE), Sn^{IV} began to reduce to form Sn on the electrode's surface. At potentials ca. < -0.85 V (SCE), H_2 evolution occurred. The current loop between the negative-going and positive-going potential sweeps was due to nucleation and growth of Sn on the carbon substrate, which increased the surface area. As the potential was swept from -0.65 V to -0.4 V (SCE), the Sn deposited was stripped from the electrode surface showing a well defined tin oxidation peaks, ca. -0.58 V (SCE). The anodic and cathodic charges, Q_A and Q_C at 25 s^{-1} were determined by integration of current-time data giving values of 1.04×10^{-6} C and 1.18×10^{-6} C, respectively, over the range of the potential used. Hence, the charge yield for tin deposition was estimated as ca. 0.87 and the balance being due to hydrogen evolution, for which the equilibrium potential was estimated at < ca. -0.85 V (SCE) in the solutions used. Figure 7-101 shows the effect of the RDE rotation rate on the limiting current density for reduction of 1 mol m^{-3} Sn^{IV} at Sn pre-plated VC rotating disc electrode in 4 kmol m^{-3} HCl + 1 kmol m^{-3} which shows a straight line that obeys the Levich equation [7-22].

$$j_L = 1.554nFD_i^{2/3}\nu^{-1/6}f^{1/2}c_i \quad [7\text{-}22]$$

The value of the diffusion coefficient for Sn^{IV}/Sn^{II} was measured as 1.25×10^{-10} m^2 s^{-1} was than compared with values reported by Monien [5] ca. 7.8×10^{-10} m^2 s^{-1} (Sn^{IV} reduction in 4 kmol m^{-3} NH_4Cl + 1 kmol m^{-3} HCl) which is close to the value deduced from this work. However, Monien [5] emphasised that the chloride concentration has to be ca. 10 kmol m^{-3} in order to avoid any preceding chemical reaction on the electrode reaction. In addition, the

conclusion made by Monien [5] was echoed by Kadish et al. [9] whom reported that both the oxidation of Sn^{II} and the reduction of Sn^{IV} are complex processes, which resulted from one or more chemical reactions are competitive with the electron transfer steps, and perhaps mixed Sn^{II}-Sn^{IV} complex may be formed. Futhermore, Vetter [11] reported that for the Sn^{IV} reduction onto mercury and platinum electrodes in 4 kmol m^{-3} showed that Sn^{IV} species de-polymerised in the aqueous chloride solutions.

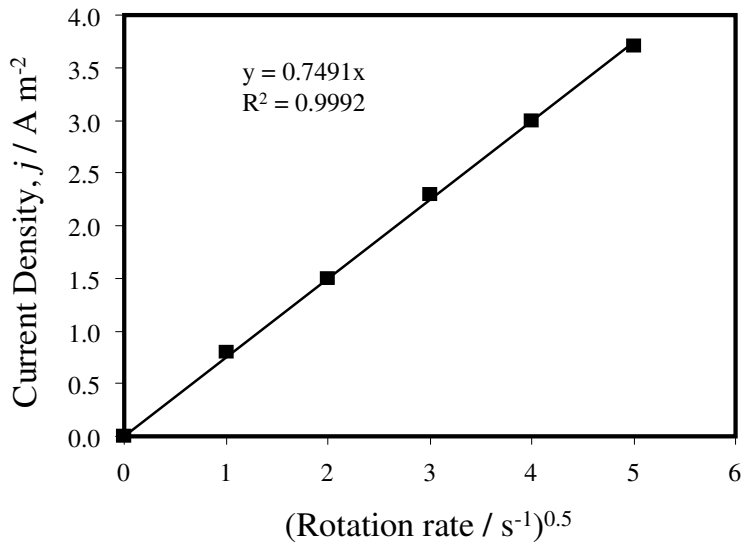

Figure 7-101. Effect of the RDE rotation rate on the limiting current density for reduction of 1 mol m^{-3} Sn^{IV} at vitreous carbon rotating disc electrode in 4 kmol m^{-3} HCl + 1 kmol m^{-3} NaCl.

7.3.2. Determining the reduction kinetics of Sn^{II} chloro- complexes

Figure 7-102 shows the effects of electrode potential and rotation rate of the VC disc electrode in 1 mol m^{-3} Sn^{II} in 4 kmol m^{-3} HCl and 1 kmol m^{-3} NaCl on which the reduction curves are shown in Figure 7-103. The VC rotating disc was pre-plated with Sn prior to Sn^{II} reduction process, which was calculated that 1×10^{-5} C of charge would need to be passed in order to coat the VC disc with a monolayer of tin. The data was used to arrive at values for the mass transfer coefficient, at different rotation rates. The mass transport limiting current densities, current density plateaus, are taken from this plot (Figure 7-102) for each rotation rate and plotted against the square root of the rotation rate, as illustrated in Figure 7-104. The straight line obtained, obeys the Levich equation [7-22]. The diffusion coefficient of Sn^{II} calculated from the slope is 9.0×10^{-10} m^2 s^{-1}. This value is similar to those obtained by Kiekens et al.[10] for a solution containing 7×10^{-3} kmol m^{-3} Sn^{II} and 4 kmol m^{-3} HCl, and

using glassy carbon as electrode material, which was 7.9×10^{-10} m^2 s^{-1} at room temperature.

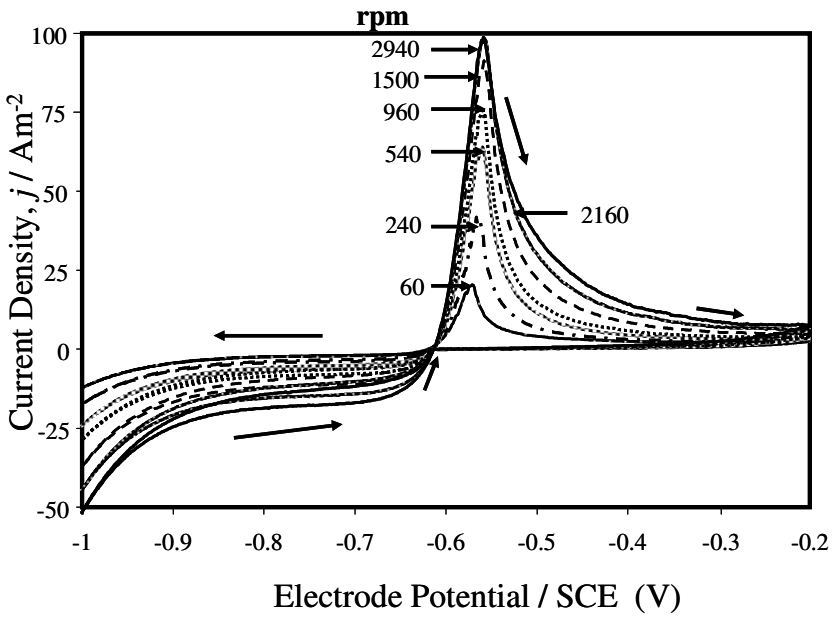

Figure 7-102. Cyclic voltammogram of a Sn-plated VC rotating disc electrode rotating at 16 s^{-1} in 1 mol m^{-3} Sn^{II} + 4 kmol m^{-3} HCl + 1 kmol m^{-3} NaCl at a scan rate of 5 mV s^{-1}.

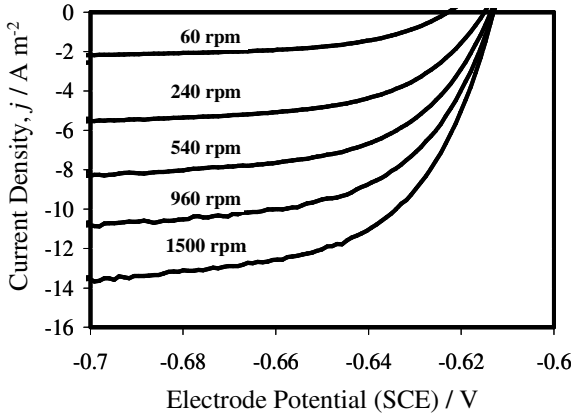

Figure 7-103. Reduction of 1 mol m^{-3} Sn^{II} at Sn pre-plated VC rotating disc electrode in 4 kmol m^{-3} HCl + 1 kmol m^{-3} NaCl.

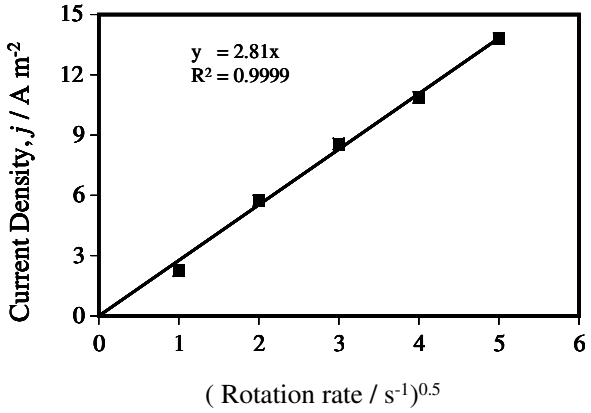

Figure 7-104. Effect of the RDE rotation rate on the limiting current density.

This diffusion coefficient value was then used to determine the Nernst diffusion layer, δ_N, and k_m values for each rotation rates which are tabulated in Table 7-14 below. It was found that

the faster the rotation rate, the more compressed the diffusion layer becomes and the greater the transport limited flux.

Table 7-14. Calculated δ_N and k_m values for different rotation rates.

Rotation rate / s^{-1}	Square root of rotation rate / $s^{-0.5}$	$\delta_N \times 10^{-5}$ / m	$k_m \times 10^{-5}$ / m s^{-1}
1	1	5.97	1.34
4	2	2.99	2.68
9	3	1.99	4.02
16	4	1.49	5.36
25	5	1.19	6.70

The Tafel line in Figure 7-105 yields the values of exchange current density and Tafel slope for the experimental data corresponding to the reduction scan in Figure 7-102.

$$j_{Sn} = -j_0 \exp\left(-\beta_{Sn}\eta_{Sn}\right) \qquad [7\text{-}23]$$

Values of j_0, and β were derived as 1.8 A m^{-2} and 32mV $decade^{-1}$ respectivly.

In order to investigate the reaction kinetics of the side reaction, H_2 evolution on Sn pre-plated electrode:

$$2H^+ + 2e^- \rightleftharpoons H_2 \qquad [7\text{-}24]$$

Voltammetry was carried out in 4 kmol m^{-3} HCl and 1 kmol m^{-3} NaCl electrolyte in the absence of Sn^{II} or Sn^{IV} to avoid Sn deposition. Figure 7-106 shows the analysis using Tafel slopes on hydrogen evolution at a tin pre-plated electrode which was measured using equation [7-25] The values were derived as $j_o = 7.07\times10^{-5}$ A m^{-2} and Tafel slope of 93 mV $decade^{-1}$ respectively.

$$j_{H_2} = -j_{0,H_2(Sn)} \exp\left(-\beta_{H_2}\eta_{H_2}\right) \qquad [7\text{-}25]$$

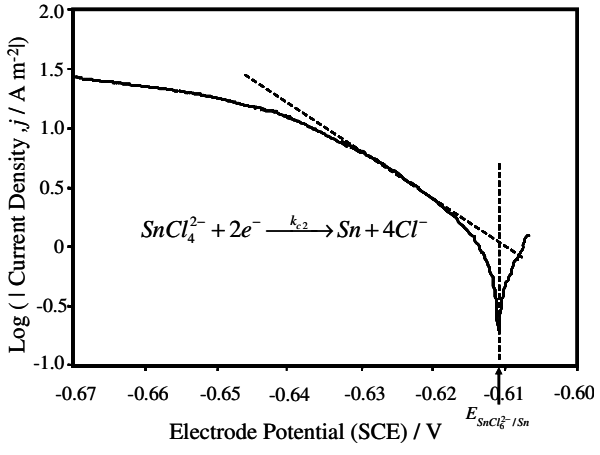

Figure 7-105. Tafel plot for reduction of 1 mol m^{-3} Sn^{II} at Sn pre-plated VC electrode in 4 kmol m^{-3} + 1 kmol m^{-3} NaCl, scan rate 10 mV s^{-1}, rotation rate of 36 s^{-1}.

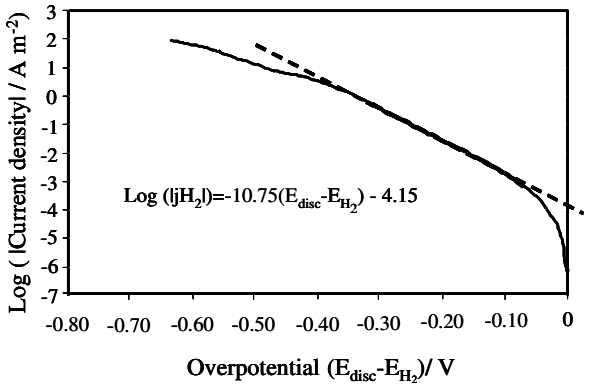

Figure 7-106. Analysis using Tafel plots on hydrogen evolution at a Sn pre-plated VC electrode in 4 kmol m^{-3} HCl + 1 kmol m^{-3} NaCl at a scan rate of 5 mV s^{-1} and a rotation rate of 16 s^{-1}.

Table 7-15 summarises the kinetic parameters obtained experimentally and from the literature [8].

Table 7-15. A summary of the kinetic parameters obtained from various sources

Reactions	Exchange current density and Tafel slope	Literature	Rotating disc
$SnCl_4^{2-}$ / Sn	$j_{o,\,Sn}$ / A m^{-2}	10^3	1.8
	Tafel slope Sn/ mV $decade^{-1}$	64	32
$SnCl_6^{2-}$ / Sn	$j_{o,\,Sn}$ / A m^{-2}	5×10^{-1}	-
	Tafel slope Sn/ mV $decade^{-1}$	36	-
H^+ / H_2	$j_{o,\,H2\,(Sn)}$ / A $.m^{-2}$	10^{-6}	7.07 x 10^{-5}
	Tafel slope H_2/ mV $decade^{-1}$	120	93

Due to the difficulty in reproducibility and discrepancies between the kinetic parameters reported here and those in literature, the kinetic parameters calculated here should be used

only for the similar conditions as per reported. The electrochemical kinetic parameters for deposition of Sn will be used to adjust model parameters in Maple™.

7.3.3. Determining the molar ratio of tin complexes in solution

Few reports have been published on the electrochemical kinetics of the oxidation and reduction of tin complexes with rotating disc electrodes made of vitreous carbon using HCl supporting electrolyte [19,20]. These studies reveal it is not possible to make a quantitative evaluation of the Sn^{IV}/Sn^{II} reduction because the reduction proceeds directly to tin metal. In addition, the reduction of Sn^{IV} gave a single wave, which was not completely separated from the hydrogen evolution as observed. However, an attempt was made to determine the Sn^{IV}/Sn^{II} molar ratio using a rotating ring disc electrode (RRDE), to detect Sn^{IV} species dissolved at the vitreous carbon disc electrode, by the oxidation of Sn^{II} species at the Pt ring electrode. The schematic diagram of the RRDE system and possible reactions is shown in Figure 7-107.

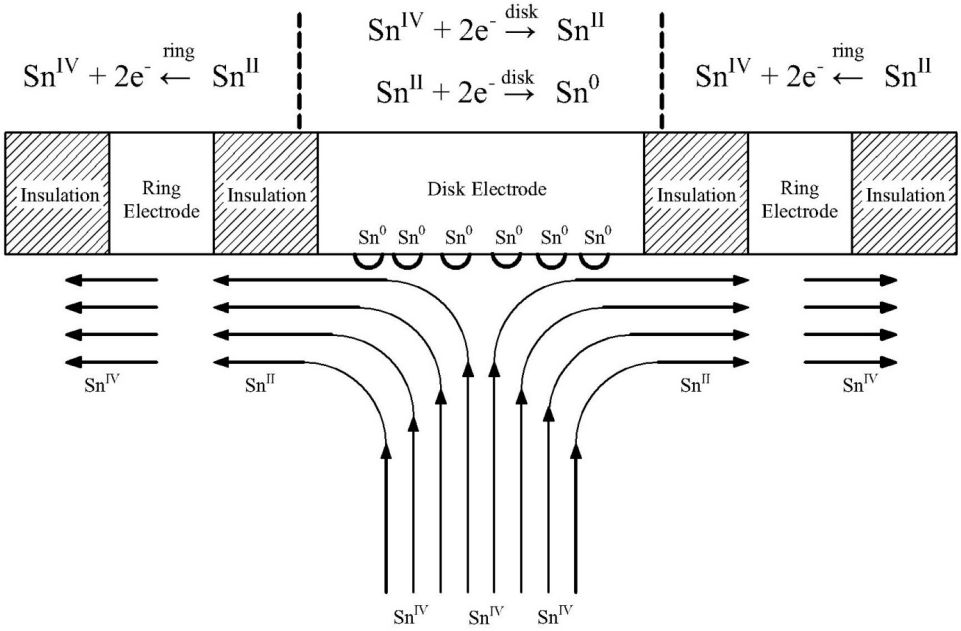

Figure 7-107. Schematic diagram of the rotating (Pt) ring- (vitreous carbon) disc electrode (RRDE) and possible electrode reactions.

Figure 7-108 shows the voltammogram of ring current correspond to disc current. The potential range varied between 0 V (SCE) to -0.70 V (SCE) and then was reversed to -0.20 V (SCE). The ring potential was held at a constant oxidation potential of +0.60 V (SCE) by

Autolab Bi-potentiostat module, well above the reversible potential of interest, $E_{SnCl_6^{2-}/SnCl_4^{2-}} = 0.151$ V (SCE), such that oxidation would be mass transport controlled.

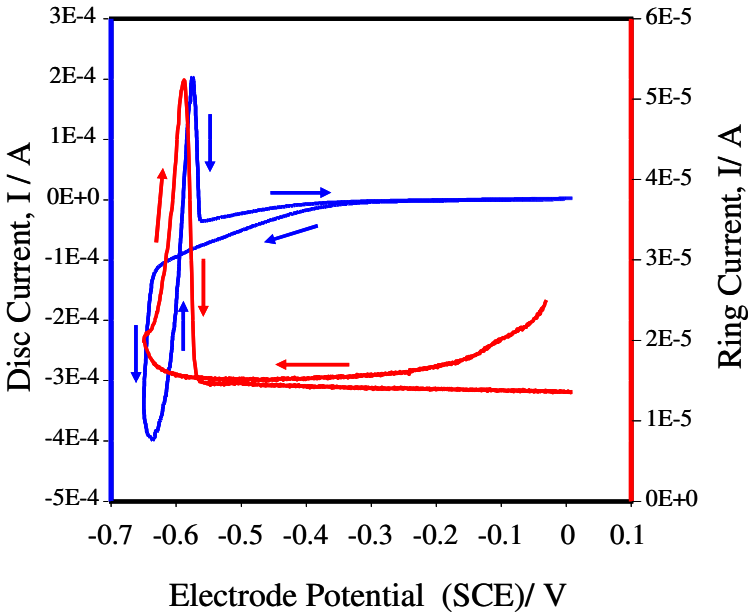

Figure 7-108. Cyclic voltammogram on glassy carbon in 1 mol m^{-3} Sn^{IV} + 4 kmol m^{-3} HCl and 1 kmol m^{-3} NaCl. Ring potential +0.6 V (SCE), pH 0, rotation rate 16 s^{-1}, scan rate 5 mV s^{-1}.

When the disc was off, the ring current is essentially zero, assuming no Sn^{II} in the bulk solution. However, the current depicted is an artefact of start-up which can be neglected. Reaction that may happen at the disc at the reverse scan is:

For the disc-ring system:

$I_{D,Sn^{IV}}$: $$SnCl_6^{2-} + 2e^- \xrightarrow{Disc} SnCl_4^{2-} + 2Cl^- \quad [7\text{-}26]$$

$I_{D,Sn^{II}}$ $$SnCl_4^{2-} + 2e^- \underset{Disc}{\overset{Disc}{\rightleftarrows}} Sn + 4Cl^- \quad [7\text{-}27]$$

While at the forward scan, reaction that may happen is:

$I_{R,Sn^{II}}$ $$SnCl_6^{2-} + 2e^- \xleftarrow{Ring} SnCl_4^{2-} + 2Cl^- \quad [7\text{-}28]$$

Thus, the apparent collection efficiency (N_{app}) is given as:

$$N_{apparent} = \frac{I_{Ring}}{|I_{Disc}|} = \frac{I_{R,Sn^{II}}}{|I_{D,Sn^{IV}}| + |I_{D,Sn^{II}}|} \quad [7\text{-}29]$$

A background ring current ca. 1 x 10^{-2} mA was observed, indicating that Sn^{2+} produced at the disc was being oxidised back to its initial form in the bulk solutions. N_{app} can also be determined experimentally and is illustrated in Figure 7-109.

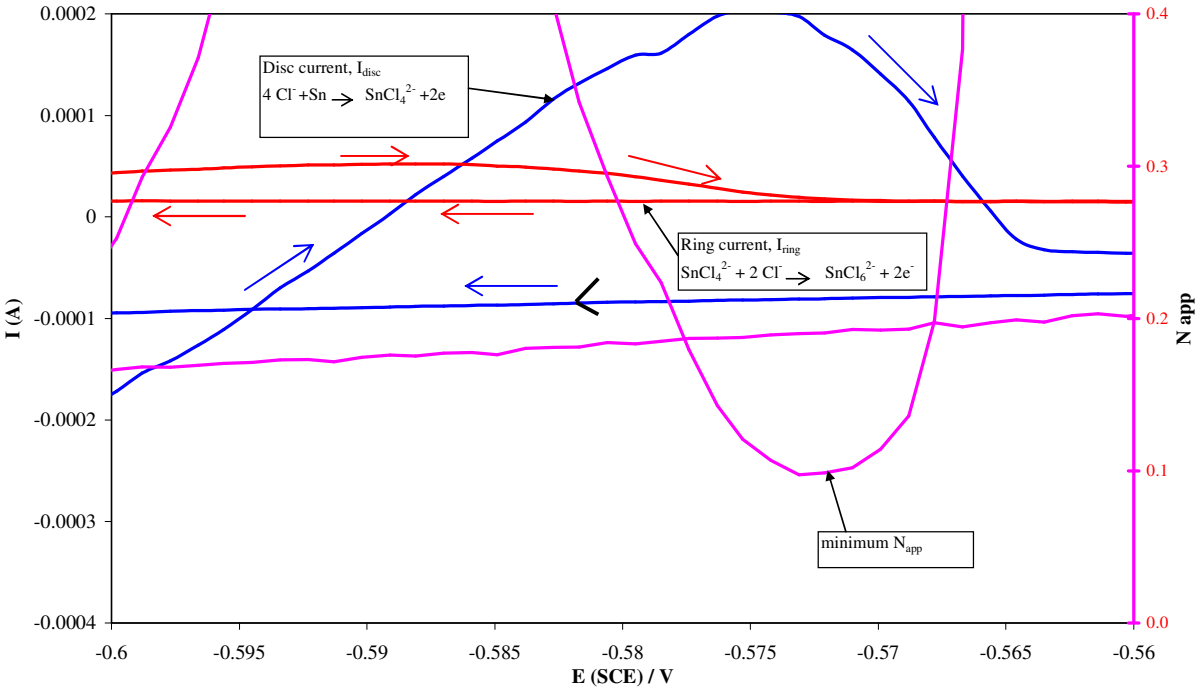

Figure 7-109. The apparent collection efficiency plots; $N_{app} = I_{ring}/ I_{disc}$.

From the figure, it is apparent that the collection efficiency did not follow the geometrical collection efficiency which is 21.8%. The apparent collection efficiency was measured as ca. 10% at the oxidation peak of the disc and subsequently inhibited at E > -0.578 V (SCE). Theoretically, if the species formed at the disc electrode are completely stable and totally soluble (Sn species solubility is best achieved reductively in [Cl-] > 5 kmol m^{-3} as discussed previously in section 7.2.1), only a fraction of the species formed at the disc electrode reach the surface of the ring. However, the apparent result shows a great contrast with the theoretical data. This might be due to the growth of oxide layers on the electrode, such as $[Sn(OH)_4]^{2-}$ (refer to potential –pH diagram, Figure 7-93) that is stable in acidic regions that would perhaps inhibit the oxidation of Sn^{2+} to Sn^{4+} at the ring. The reactions that might be occurring are:

$$SnCl_6^{2-} + nH_2O \rightarrow [Sn(OH)_x Cl_{6-x}]^{2-} + Cl^- + H^+ \qquad [7\text{-}30]$$

$$SnCl_6^{2-} + 5H_2O \rightarrow [Sn(OH)_4Cl_2]^{2-} + Cl^- + H^+ \quad [7\text{-}31]$$

It is suggested that the exact nature of the inhibiting surface species and layer thickness for Sn needs to be investigated. These experimentally obtained efficiencies, which deviate so greatly from the theoretical value and for which the reproducibility is so poor, render the ring-disc electrode technique unsuitable for evaluating the molar ratio of tin complexes in aqueous chloride solutions. Thus, the exact nature of the inhibiting surface species and layer thickness for Sn needs to be investigated further by other techniques that can be used to interrogate the electrode | electrolyte interface in situ; possibly by means of surface sensitive techniques such as XPS to examine the surface species and oxidation states [21]. Futhermore, it is probable that higher concentrations of HCl may obviate the problem, enabling the ring electrode to function as a reliable sensor.

7.4. Modelling of the Mechanisms Occurring in the System

Models have been developed in Maple^{TM} (Appendix E(c)) to predict current densities-potential relationships of the tin and lead complexes in solution. For multi-steps reductions (Sn), the current densities were predicted by steady state balance of surface concentrations, whilst for single step reductions (Pb), the current densities were predicted by the extended Butler-Volmer equation. Reduction of $PbCl_4^{2-}$ ions follows this reaction:

$$PbCl_4^{2-} + 2e \rightleftharpoons Pb + 4Cl^- \quad [7\text{-}32]$$

From experimental data obtained previously on lead(II) chloride kinetics by Robson [22], values of j_o and Tafel coefficient were derived as 4.47×10^{-1} A m^{-2} and 28.5 mV dec^{-1} respectively, for a concentration of 1 mol m^{-3}. Hydrogen evolution kinetics were also included in the model predictions. Model parameters, such as heterogeneous reaction rate constants, were adjusted according to the experimental data obtained from the rotating disc experiment.

7.4.1. Electrochemical Reduction of Sn^{IV} Ions from Aqueous Chloride Electrolytes

Reactions at the cathode:

$$SnCl_6^{2-} + 2e \rightleftharpoons SnCl_4^{2-} + 2Cl^- \quad [7\text{-}33]$$

$$E_{SnCl_6^{2-}/SnCl_4^{2-}}(SHE) = 0.1928 + 0.0295\log\left(SnCl_6^{2-}/SnCl_4^{2-}\right) - 0.059\log\left(Cl^-\right) \quad [7\text{-}34]$$

$$SnCl_4^{2-} + 2e \rightleftharpoons Sn^0 + 4Cl^- \quad [7\text{-}35]$$

$$E_{SnCl_6^{2-}/Sn^0}(SHE) = -0.1901 + 0.0295\log\left(SnCl_4^{2-}\right) - 0.118\log\left(Cl^-\right) \quad [7\text{-}36]$$

Reduction Mechanism:

$$SnCl_6^{2-} \underset{k_m}{\overset{k_m}{\rightleftarrows}} SnCl_6^{2-}(surface) \quad [7\text{-}37]$$

$$SnCl_6^{2-}(surface) + 2e^- \xrightarrow{k_{c1}} SnCl_4^{2-}(surface) + 2Cl^- \quad [7\text{-}38]$$

$$SnCl_4^{2-}(surface) \underset{k_m}{\overset{k_m}{\rightleftarrows}} SnCl_4^{2-} \quad [7\text{-}39]$$

$$SnCl_4^{2-}(surface) + 2e^- \xrightarrow{k_{c2}} Sn + 4Cl^- \quad [7\text{-}40]$$

For steady state mass balance on Sn^{IV} and Sn^{II} surface concentrations, i.e.

$$\left(\frac{d\left(SnCl_6^{2-}\right)_{surface}}{dt}\right) = 0 \text{ and } \left(\frac{d\left(SnCl_4^{2-}\right)_{surface}}{dt}\right) = 0:$$

$$k_m[SnCl_6^{2-}] - k_m[SnCl_6^{2-}]_{surface} - k_{c1}[SnCl_6^{2-}]_{surface} = 0 \quad [7\text{-}41]$$

$$k_{c1}\left[SnCl_6^{2-}\right]_{surface} - k_{c2}\left[SnCl_4^{2-}\right]_{surface} - k_m\left[SnCl_4^{2-}\right]_{surface} + k_m\left[SnCl_4^{2-}\right] = 0 \quad [7\text{-}42]$$

The current densities due to the reduction of Sn^{IV} to Sn^{II} and of Sn^{II} to tin metal are given respectively by:

$$j_{Sn(IV)} = -n_{e,Sn^{IV}}.F.k_{c1}.\left[SnCl_6^{2-}\right]_{surface} \quad [7\text{-}43]$$

$$j_{Sn(II)} = -n_{e,Sn^{II}}.F.k_{c2}.\left[SnCl_4^{2-}\right]_{surface} \quad [7\text{-}44]$$

where:
$$k_{ci} = k_{ci'}\exp\left\{\frac{-\alpha_i nF(E - E_i^0)}{RT}\right\} \quad [7\text{-}45]$$

A mass transfer coefficient of k_m= 5.4×10^{-5} m s^{-1} was used in the model, as determined by Levich's equation, for a disc electrode rotation rate of 16 s^{-1}. The rate coefficients (and $k_{c1'}$ = 1×10^{-10} s^{-1} and $k_{c2'}$= 5×10^{-6} s^{-1} were selected from data adjusted according to experimental data obtained from the Sn^{IV} rotating disc experiment as shown in Figure 7-110. Figure 7-111 combines all the reacting species, which indicates that there is a small window of potential ca. 80 mV of selective recovery of elemental tin. However, the reaction could not achieve transport control as hydrogen evolution and alloy formation might occur, with the rate of overall reduction of $SnCl_6^{2-}$ ions to elemental tin becoming totally mass transport controlled at

potentials <- 0.65 V (SHE). Increasing the overpotential of tin deposition results in hydrogen evolution partial current densities increased, so decreasing the current efficiencies for Sn^{IV} reduction. Figure 7-112 shows the model prediction of current efficiencies-electrode potential behaviour for Sn deposition. Predicted charge efficiencies (Φ^e) were 0.95 even at 1 mol Sn^{IV} m^{-3} (-0.36 V < E (SHE) < -0.25 V). The high current efficiencies reflected tin's well known high hydrogen overpotential (j_o < 10^{-6} A m^{-2}, Tafel slope= 120 mV $decade^{-1}$). The potential gap between a feasible potential for selective tin deposition and that of co-deposition of Sn-Pb is around 100 mV (i.e. -0.25 to -0.35 V), meaning that there is a room to manoeuvre.

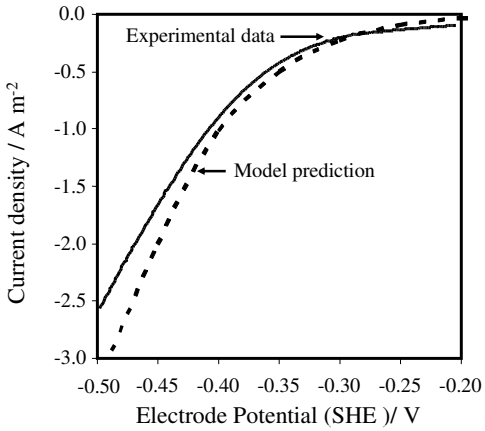

Figure 7-110. Prediction of potential-current relationship from the kinetic model solved with Maple™, compared to experimental data for the reduction of 1 mol m^{-3} Sn^{IV} in 4 kmol m^{-3} HCl +1 kmol m^{-3} NaCl.

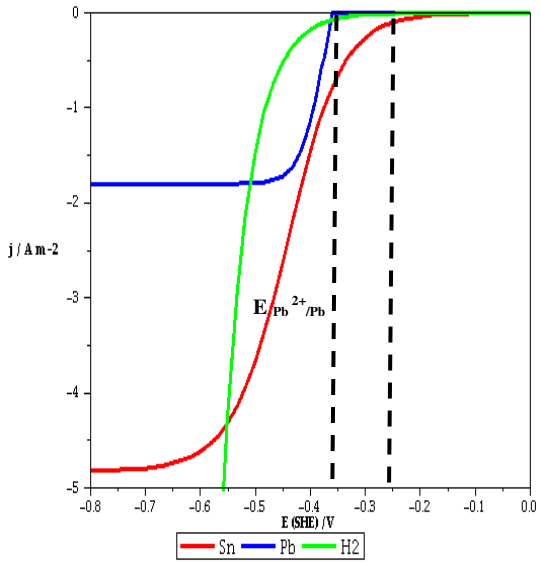

Figure 7-111. Model prediction of current density-electrode potential behaviour for reduction of $PbCl_4^{2-}$, $SnCl_6^{2-}$ and hydrogen evolution.

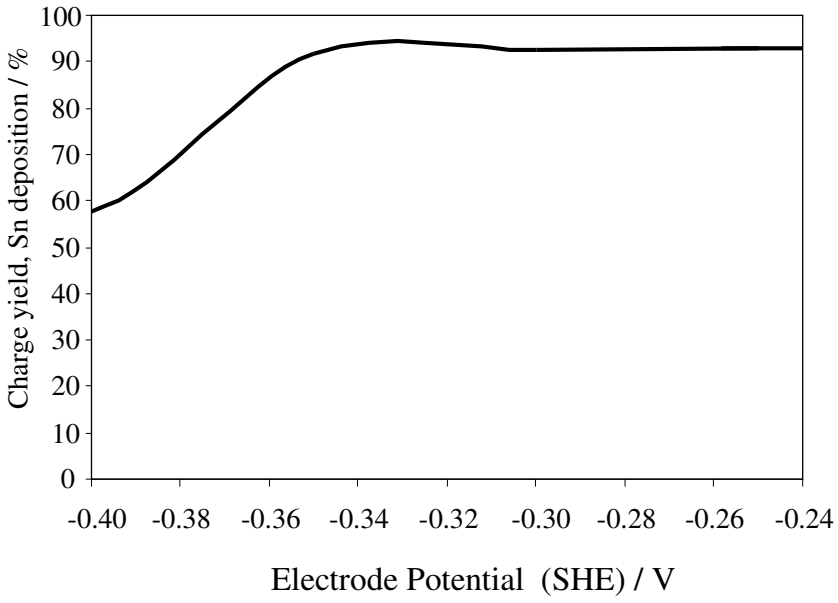

Figure 7-112. Model prediction of current efficiencies-electrode potential behaviour for Sn deposition ($\Phi^{e}_{Sn} = j_{Sn} / (j_{Sn} + j_{Pb} + j_{H2})$).

7.5. Electrochemical Reactor Experiments

For the purpose of determining the possibility of selective tin metal recovery potentiostatically, initial laboratory experiments were carried through using a titanium mesh cathode with a surface area of 135 cm^2 in fluidised bed electrolyte of glass beads, separated by a Nafion N-424 cation permeable membrane from anode. The reactor was operated for a total of three hours under potentiostatic control. Initially, the titanium mesh was pre-plated with elemental tin to eliminate the loss of efficiency due to the reduction of hydrogen. Figure 7-113 indicates the time dependences of the tin concentration and current of Sn pre-plating on titanium mesh in the fluidised bed electrolyte reactor. By determining dissolved tin concentrations in solution, samples taken from the reservoirs at various times using inductively coupled plasma emission specotroscopy (ICP), it was found that ca. 72 % of the tin was recovered from solution in about 2.5 hours as shown in Figure 7-113 which both the concentrations and current decayed with time, due to overall reaction:

$$SnCl_6^{2-} + 4e^- \rightarrow Sn + 4Cl^- \qquad [7\text{-}46]$$

It was observed that the peak in the magnitude of the (negative) reduction current after 1500 s was due to area increasing with time ca. 40 μm, while the concentration of disolved tin in

solution decreased approaching to approximately 2.85 mol m^{-3} from the initial concentration of 10 mol m^{-3} of $SnCl_6^{2-}$. Model prediction of fluidised bed reactor operating with continous recirculation of the electrolyte (equation [7-47]) was used to predict the final concentration of Sn^{IV} as it was operated under mass transport control.

$$I_{L,t} = nF\dot{v}c_{i,t=0}\left[1-\exp\left(-\frac{k_m AaL}{\dot{v}}\right)\right]\exp\left\{-\frac{\dot{v}t}{V}\left[1-\exp\left(-\frac{k_m AaL}{\dot{v}}\right)\right]\right\} \qquad [7\text{-}47]$$

The value of Sn^{IV} chloride final concentration deviated from the model prediction value ca. 64% as 1 mol m^{-3} $SnCl_6^{2-}$ was expected in the catholyte reservoir.

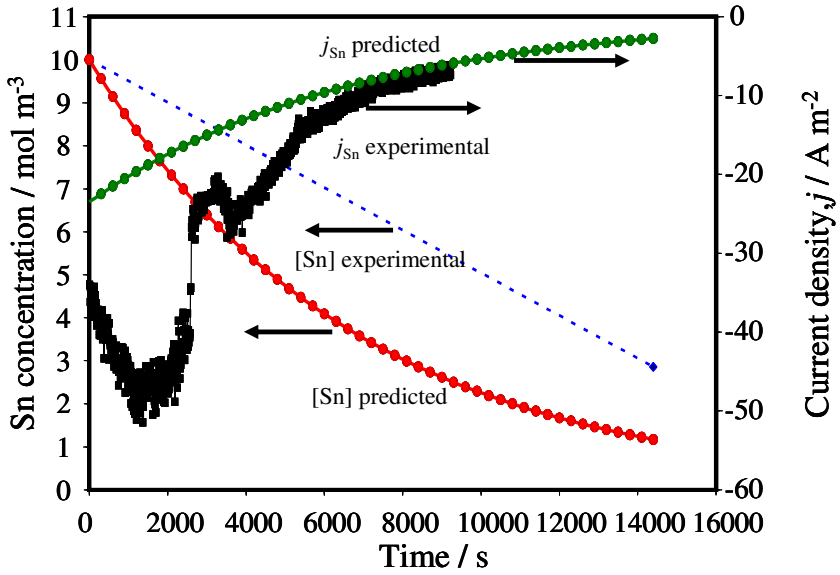

Figure 7-113. Sn pre-plating in fluidised bed electrolyte reactor with 590-840 µm glass beads, batch recycle model at - 0.70 V (SCE), flow rate = 0.85 dm^3 min^{-1}, k_m = 5.36 x 10^{-5} , $V_{catholyte}$ = 2 dm^{-3} , together with PFER-CSTR model predictions.

Following the tin pre-plating experiment, 0.3 mol m^{-3} of Pb^{II} chloride solution was added into the reservoir which contained 2.85 mol m^{-3} Sn^{IV} chloride to determine the possibility of tin metal to be selectively deposited under control electrode potential. With the aid of model predictions and experimental data, a value of < $E^0_{Pb^{2+}/Pb}$ = -0.61 V (SCE) i.e 0.60 V (SCE) was chosen to initiate the experiment to allow selective recovery of elemental tin.

It was observed that Sn^{IV} could be depeleted to analytically undetectable concentrations and recovered with relatively high charge yield of 0.85 at an applied cathode potential of -0.60 V

(SCE) and a flow rate of 0.85 dm^3 min^{-1}.

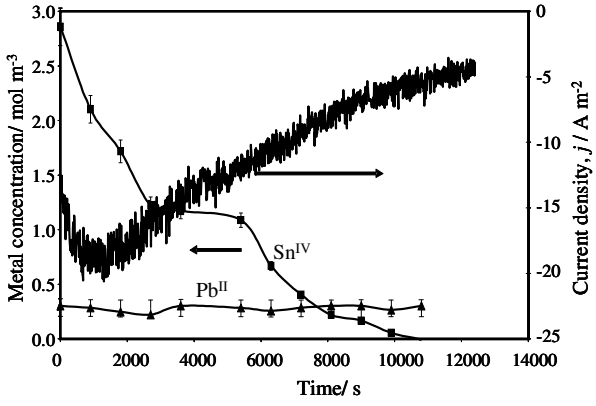

Figure 7-114. Sn deposition in fluidised bed electrolyte reactor with 590-840 μm glass beads, batch recycle model at - 0.60 V (SCE) reversible potential of Pb^{2+}/Pb, flow rate = 0.85 dm^3 min^{-1}.

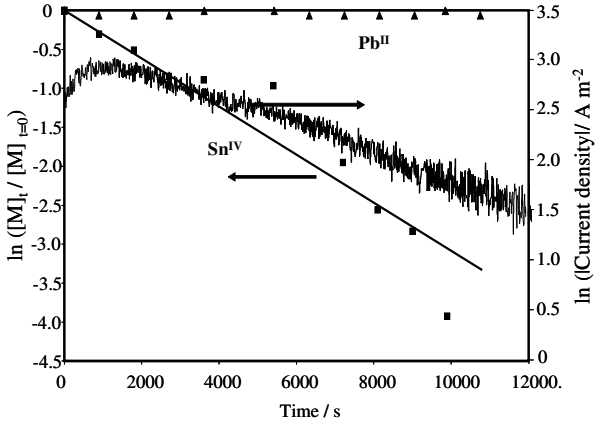

Figure 7-115. Time dependence of the Sn^{4+} ($[Sn^{4+}]_0$ = 2.85 mol m^{-3})and Pb^{2+} ($[Pb^{2+}]_0$ = 0.3 mol m^{-3}) concentration and reduction current density in fluidised bed electrolyte reactor with 590-840 μm glass beads, batch recycle model at - 0.60 V (SCE) reversible potential of Pb^{2+}/Pb, flow rate = 0.85 dm^3 min^{-1}.

The time- log current density plot in Figure 7-115 shows the time dependences of the metals concentration and current density. The current density decay was consistent with exponential concentration indicating that the contribution of hydrogen evolution current to the measured current was very small.

For cell voltages (U_{cell}) of 2-3 V and fractional charge yield (CE) of 0.85, the specific electrical energy consumption (SEEC) for tin electrowinning is between 1000 -1600 kWh (tonne Sn)$^{-1}$ with purity >99.99 % confirmed by XRF and ICP. The higher current densities and the presence of the dielectric fluidised phase in the mesh cathode of fluidised bed of inert particles electrochemical reactor resulted in higher cell voltages and therefore higher specific energy requirements [23].

7.6. Chapter Summary

Experiments with a rotating vitreous carbon cathode confirmed model predictions from a kinetic model for a small electrode potential window within which to achieve selective electrodeposition of tin from synthetic Sn^{IV}-Pb^{II} aqueous chloride solutions, from which Pb

could be electrodeposited subsequently. However, the rotating ring-disc experiment failed to assist in determining the molar ratio of tin chloro-complexes due to the growth of oxide layers [24], which suppressed further Sn^{II} oxidation to Sn^{IV} at the ring. It is probable that higher concentrations of HCl may obviate the problem, enabling the ring electrode to function as a reliable sensor. Futhermore, the experiments had demonstrated the feasibility of using the mesh cathode in a fluidised bed of inert particles to recover Sn selectively from synthetic Sn^{IV}-Pb^{II} aqueous chloride solutions. It was observed that Sn^{IV} could be depeleted to analytically undetectable concentrations and recovered with relatively high charge efficiency of 0.85 at an applied cathode potential of -0.60 V (SCE) and a flow rate of 0.85 dm^3 min^{-1}. However, the reaction could not achieve transport control as hydrogen evolution and alloy formation might occur, with the rate of overall reduction of $SnCl_6^{2-}$ ions to elemental tin becoming totally mass transport controlled at potentials <- 0.65 V (SHE). Increasing the overpotential of tin deposition results in hydrogen evolution partial current densities augmented, so decreasing the current efficiencies for Sn^{IV} reduction. In addition, the high current efficiencies reflected tin's well known high hydrogen overpotential ($j_o < 10^{-6}$ A m^{-2}, Tafel slope= 120 mV $decade^{-1}$).

7.7. References

[1] Lingane, J.L., 1966, Analytical Chemistry of Selected Metallic Elements. Reinhold, New York., 102-106.

[2] Charlot, V.G., Collumeau, A. and Marchon, M.J.C. 1971, Oxidation-Reduction Potentials of Inorganic Substances in Aqueous Solution. IUPAC – Selected Constants. Butterworths, London, 49.

[3] Vetter, K.J, 1967, Electrochemical Kinetics, Academic Press, New York, 481.

[4] Kragten, J., 1975, The complexometry of tin(IV). *Talanta,* 22 (6): 505-510.

[5] Monien, H., 1969, Electrochemical and reaction kinetics of the tin(IV) reduction in chloride medium at a planar mercury electrode. *Electroanal. Chem. & Interfacial Electrochem*., 20: 119-128.

[6] Lerner, H., Austin, L.G., 1965, The kinetics of the stannous/ stannic redox reaction at carbon electrodes. *J. Electrochem. Soc*., 112 (6): 636-638.

[7] Vicente, V.A. and Bruckenstein, S., 1972, Rotating gold ring-disk study of tin(II) in 4.0 molar hydrochloric acid. *Anal. Chem*., 44 (2): 297-300.

[8] Stirrup, B.N. and Hampson, N., 1976, The active dissolution of tin in acidic chloride electrolyte solutions: a rotating disc study. *J. Appl. Electrochem*, 6 353-360.

[9] Kadish, K.M., Stamp, J., Chemla, M. and Fatouros, N., 1973, Electron Transfer Studies of Sn(IV)/Sn(II) in Acid Media. *Anal. Letters*, 6, 909.

[10] Kiekens, H. Verplaetse, E. Temmerman, 1981. Electrochemical study of the oxidation of tin(II) at glassy carbon electrodes. *Talanta*, 28: 192-194.

[11] Vetter, K.J., 1967, Electrochemical Kinetics. Academic Press, New York (196,. 481.

[12] House, C.I. and Kelsall, G.H.,1984, Potential-pH diagrams for Sn-Cl-H_2O system. *Electrochim. Acta*, 29: 1459-1464.

[13] Bard, A.J., Parsons, R. and Jordan,J., 1985, Standard Potentials in Aqueous Solutions, Marcel Dekker, N.Y., 1985, (a) Lead data: Z.Galus, 220-233.

[14] Kelsall, G.H. and Gudyanga, F.P., 1990, Thermodynamics of Pb-S-Cl-H_2O Systems at 298 K. *J. Electroanal. Chim*., 280: 267-282.

[15] Senanayake, G. and Muir, D.M., 1988, Studies on liquid junction potentials in concentrated chloride solutions and determination of ionic activities and hydration numbers by the emf method. *Electrochim. Acta*,33(1): 3-9.

[16] Paramguru, R.K., Kuzeci, E. and Kammel, R., 1988, Direct Electrowinning Of Lead From Suspension Galena Concentrate Anode In Different Electrolytes. *Metall. Trans. B*

,19b(1): 59-65.

[17] Dandapani, B. and Ghali, E., 1982, Electrodissolution of lead sulfide in different acidic media. *J. Electrochem. Soc*., 129 : 271-276.

[18] Changa, J.C., Stability Product Constants, in CRC Handbook of Chemistry and Physics, 73rd (1992/3) Edition, D.R. Linde (Ed). 8-43.

[19] Garcia-Gabaldon, V., Perez-Herranz, V., Garcia-Anton, J. and Guinon, J.L., 2007, Electrochemical study of the activating solution for electroless plating of polymers. *J App. Electrochem.*, 37 1145-1152.

[20] Kiekens, P., Verplaetse, H., Donche, H. and Temmerman, E., 1982, Kinetic behaviour of the Sn(IV)- Sn(II) couple in acidified concentrated bromide solutions at a glassy carbon rotating ring-disk electrode. *Electrochim Acta*, 27 (5):623-627.

[21] Dawson, R. J., 2006, Electrochemical Recovery of Platinum and Palladium from Alumina-Supported Catalysts Ph.D., Imperial College London.

[22] Robson, A., 2005, Metal Recovery from End-of-Life Electrical and Electronic Systems. MPhil/PhD Transfer.

[23] Kelsall, G. H. and Gudyanga, F. P., 1991, Electrochechemical Reactor Design Consideration for Simultaneous Tin Electrowinning and Cr^{2+} Electrogeneration. *Dechema Monogr*, 123:167.

[24] Buckle, R. and Roy, S., 2008, The recovery of copper and tin from waste tin stripping solution: Part I. Thermodynamic analysis. *Sep. & Purif. Tech*., 62 (1): 86-96.

8. NICKEL-ZINC ELECTRO-CO-DEPOSITION

8.1. Chapter Overview

Al^{III}, Fe^{II}, Zn^{II} and Ni^{II} remained in solutions after recovery of Au, Cu, Sn and Pb from the WEEE leachate. Hence, this chapter is divided into three main sections. In the first, the thermodynamics of iron-chloride-water (Fe-Cl-H_2O), aluminium-chloride-water (Al-Cl-H_2O), Ni-chloride-water (Ni-Cl-H_2O) and zinc-chloride-water (Zn-Cl-H_2O) systems are presented. Although unlike for Al, it is possible to electrodeposit Fe from aqueous solution, it was decided to add NaOH (+ air) to increase the pH to ca. 3 to precipitate '$Fe(OH)_3$', which was recovered by filtration. This option also enabled subsequent electro-co-deposition of Ni and Zn with high charge yields, as the higher pH decreased the driving force for hydrogen evolution. Since another project in the Electrochemical Engineering research group at Imperial College London had developed an electrodeposition process for recovering nickel alone from industrial (sulfamate) effluents, the following section reports experimental results of the reduction kinetics of zinc(II) at a Pt rotating disc electrode in 4 kmol m^{-3} HCl and 1 kmol m^{-3} NaCl.

Ionic species generated in the dissolution process of Ni^{II} and Zn^{II} in aqueous chloride media; among others are Ni^{2+}, Zn^{2+}, Ni^{II} and Zn^{II} chloro-complexes, H^+. and OH^-. Available equipment were not capable to measure each species concentrations in-situ at the nanometre scale without disturbing the system. Hence, an alternative approach is required by simulation of the system theoretically. Therefore, in the third section, a one dimensional mathematical model was developed and solved in MAPLE^{TM} to predict the kinetics of Ni-Zn electrodeposition, which was validated experimentally. The model also considered the potential and concentration profiles in the cathode | electrolyte boundary layer for conditions in which migration and convective diffusion contribute to overall transport rates, to predict the depletion rates in the batch recycle reactor and hence enable comparison with the attained experimental data.

8.2. Precipitation of $Fe(OH)_3$ and $Fe(OH)_2$

A possibility for the recovery of nickel and zinc is to raise the pH with addition of NaOH (+air), and precipitate the metal hydroxide. As the overpotential for hydrogen evolution is dependent on pH, this also raises the possibility of electrowinning metals such as Ni and Zn at a much higher current efficiency by increasing the pH progressively, ultimately to that

required to precipitate $Fe(OH)_2$ and $Fe(OH)_3$. Hence, Figure 8-116 and Figure 8-117 present the activity of various Fe^{3+} and Fe^{2+} species in aqueous solution as a function of pH [1]. At pH of about 4, the overall solubility of Fe^{III} is at its lowest point. Therefore, the precipitation of ionic species is most likely at this pH. For the purpose of nickel-zinc electro-co-deposition, the formation of insoluble $Fe(OH)_3$ is preferred.

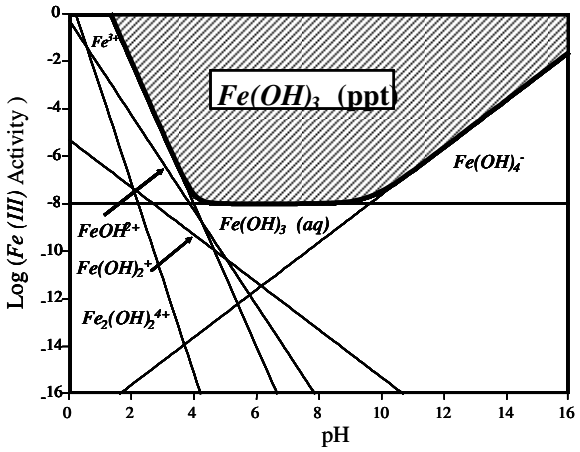

Figure 8-116. Solubility (activity-pH) diagram for $Fe(OH)_3$ (ppt) in equilibrium with aqueous Fe^{III} species at 298 K [1].

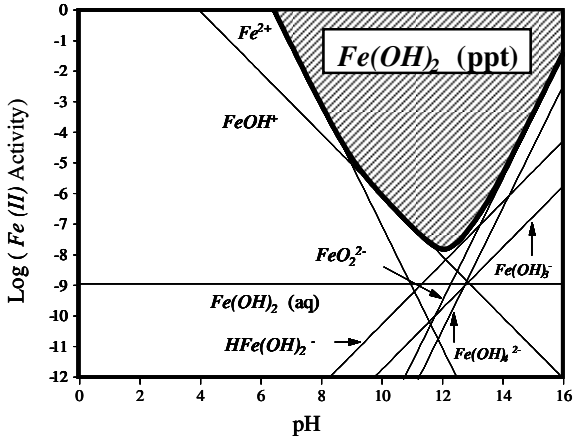

Figure 8-117. Solubility (activity-pH) diagram for $Fe(OH)_2$ (ppt) in equilibrium with aqueous Fe^{II} species at 298 K [1].

The potential-pH diagram for iron at an activity of 10^{-6} and a temperature of 298 K shown in Figure 8-118, predicts the formation of insoluble species, namely Fe_2O_3 , $Fe(OH)_3$ and $Fe(OH)_2$, at pH $\geq$ 3 and above ca. -0.60 V (SHE). In addition, Figure 8-119 confirms that aluminium would be recovered at a very negative potential above ca. -1.9 V (SHE) [2] and therefore, will not affect the efficiency of nickel-zinc electro-co-deposition.

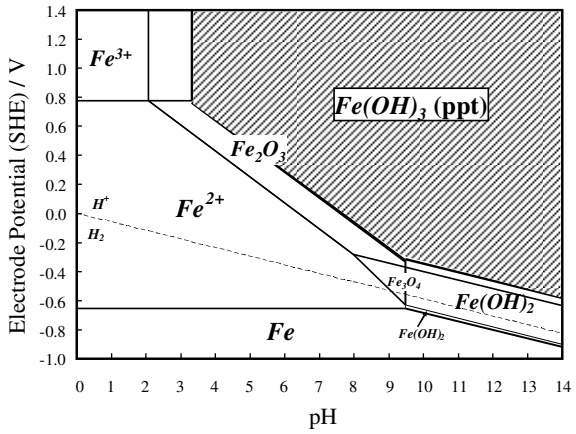

Figure 8-118. Potential pH diagram for iron-water system. Dissolved iron activity = 10^{-6}; 298 K, 1 atm [1].

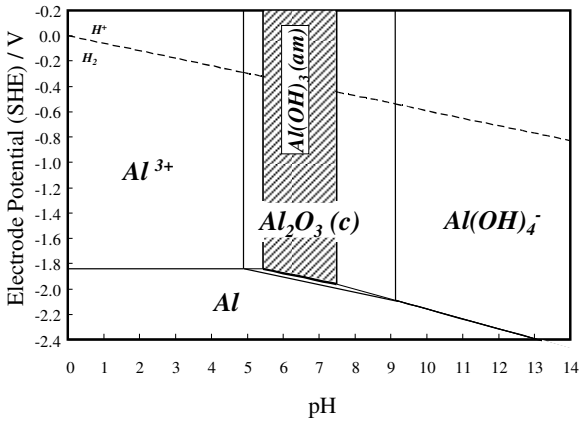

Figure 8-119. Potential pH diagram for aluminium- water. Activities: Al^{3+} = 10^{-6}; 298 K, 1 atm [2].

Precipitation experiments are carried out to determine the theoretical predictions from the potential-pH diagrams (Figure 8-118). The experiments were performed using a titration technique, where the dissolved salt of the metal of interest was titrated against an alkaline solution, NaOH which was explained in detail in Chapter 4 (Materials and Experimental Methods). The objective of these experiments was to measure the pH at which the dissolved metal precipitates in acidic conditions. All solutions contain 18 mol m^{-3} Ni^{II}, 30 mol m^{-3} Zn^{II} and 10 mol^{-3} Fe^{III} in 4 kmol m^{-3} HCl and 1 kmol m^{-3} NaCl.

Figure 8-120 shows the results on the precipitation experiments for the sample at pH 3.00, 3.25, 3.50 and 3.75. The pH of the samples remains constant at the end of the experiments. Fe^{II} starts to precipitate at pH 3.25. The sample of pH 3.25 was filtered and the EDX result of the filtrate is shown in Figure 8-121 which illustrates a high peak for Fe. Eventually, pH 3.25 is chosen for the nickel-zinc electro-co-deposition investigations.



Figure 8-120. Precipitation experiments in solutions contained 18 mol m^{-3} Ni^{II}, 30 mol m^{-3} Zn^{II} and 10 mol^{-3} Fe^{III} in 4 kmol m^{-3} HCl and 1 kmol m^{-3} NaCl.

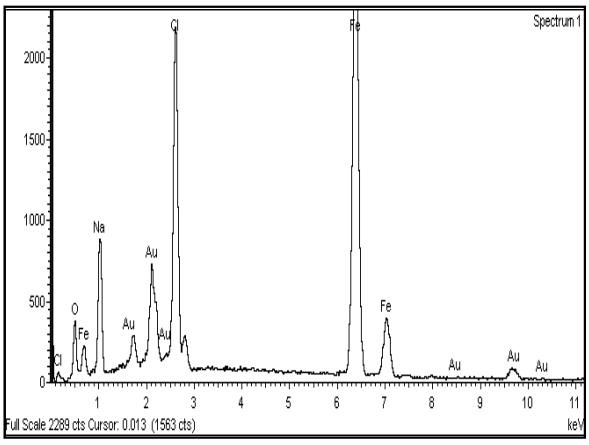

Figure 8-121. EDX reading for filtrate in sample pH 3.25. (Au being coated on the filtrate).

8.3. Speciation and Equilibrium Potentials

8.3.1. Nickel

Using thermodynamic data available in literature [3,4], the thermodynamic conditions necessary for depositing nickel from Ni-H_2O and Ni-Cl-H_2O have been evaluated to construct a potential-pH diagram as shown in Figure 8-122 and Figure 8-123. The full set of data used are given in Appendix B(h).

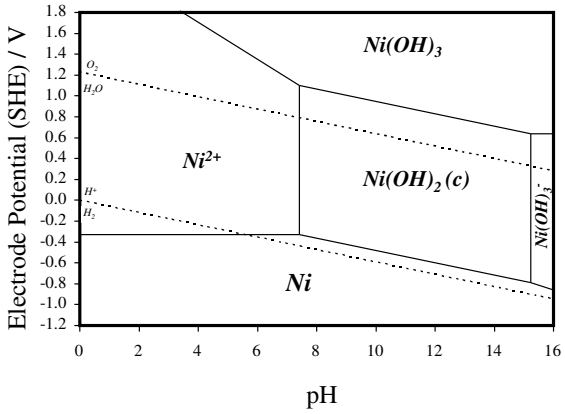

Figure 8-122. Potential pH diagram for nickel- water. Activities: Ni^{2+} = 10^{-3} kmol m^{-3}; 298 K, 1 atm.

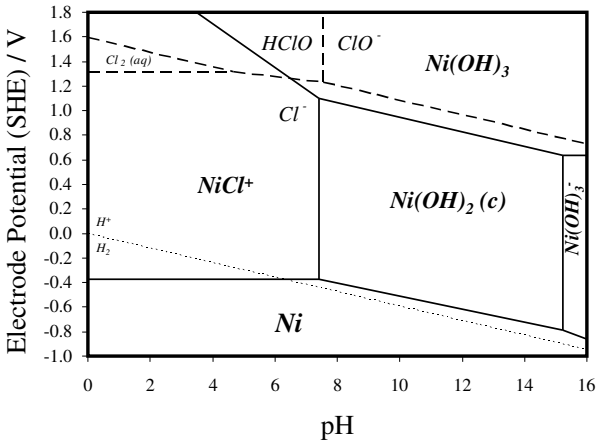

Figure 8-123. Potential pH diagram for nickel-chloride-water. Activities: Dissolved nickel and chloride activities = 10^{-3} and 5; 298 K, 1 atm.

According to Ji and Cooper [4] and Schlesinger and Paunovic [5], in the presence of chlorides, species like $NiCl_{adsorbed}$ and $NiCl^+$ interfere with the formation of nickel hydroxide and thickening the oxide formation. In contrast, research by Lee and Nam [6] reported that in the speciation diagram of nickel containing $NiCl_2$ and HCl, most nickel exist as Ni^{2+} up to 5 molality of HCl. Therefore, careful consideration of the predominant species is required, thus the data presented in Figure 8-123 was referenced to the most cited paper [4]. Ji and Cooper [4] reported that there was indefinite description of the electrode mechanism of nickel electrodeposition in acidic aqueous chloride media due to the fact that the intermediate species involved in the electron transfer have not been identified.

The equilibrium potential which $NiCl^+$ ions are reduced to elemental nickel, Ni, via reaction [8-1] is given in equation [8-2].

$$NiCl^+ + 2e^- \rightleftharpoons Ni + Cl^- \qquad [8\text{-}1]$$

At 298 K: $$E_{NiCl^+/Ni}(\text{SHE}) / \text{V} = -0.2354 + 0.0296 \log\left(NiCl^+\right) - 0.0592 \log\left(Cl^-\right) \qquad [8\text{-}2]$$

In solutions of pH > (5.925 –0.5 log (Ni^{2+})), Ni^{2+} ions become less soluble and passivate as crystalline nickel hydroxide $Ni(OH)_2$. Clearly shown in Figure 8-122, the equilibrium potential for water reduction to H_2 gas is very close to the pure Ni metal deposition potential. Hence, it is difficult to deposit nickel without simultaneous H^+ reduction taking place via

reaction [8-3]:

$$2H^+ + 2e^- \rightleftharpoons H_2 \qquad [8\text{-}3]$$

At 298 K: $$E_{H^+/H_2}(\text{SHE}) / \text{V} = -0.0592\,pH - 0.0296 \log P_{H_2} \qquad [8\text{-}4]$$

The competition between reactions [8-1] and [8-3] was found to be detrimental to nickel deposition especially in acidic solutions [7]. A plausible explanation for the pH effect is that the hydrogen discharge that occurs will disrupt the discharge of nickel due to the bubble formation and competition for reduction sites. Initially, H_2 evolution lowers the nickel deposition efficiency. Moreover, H_2 bubbles may adhere to the electrode and reduce the electroactive area available for deposition. In addition, bubble evolution may depreciate the morphology of the nickel deposit. The scale of these effects is influenced by the magnitude of the overpotential.

The addition of chloride ions did not change the structure of the pH-potential diagram as shown in Figure 8-123, given *log K* as -0.17 (specified for 0.937 kmol m^{-3} $NiCl_2$ + 2 kmol m^{-3} NaCl) [4]. It is believed that the addition of chloride promote the deposition of nickel due to a catalysis of electron transfer via so-called 'chloride ion bridge' between Ni^{2+} ions and the cathode surface [9]. Previous electrodeposition studies shows that the addition of 2 kmol m^{-3} NaCl increases the current efficiency of nickel deposition [7], whereby it promotes the deposition of nickel, or in other words, inhibits the hydrogen evolution. The addition of NaCl would also increase the activity coefficient of nickel to a lesser extent, and thus the precipitation pH will be lower than a given nickel concentration. The measured surface pH will be a combined outcome of these two opposite effects [4]. As far as the surface pH during the nickel electrodeposition is concerned, it is important to know the pH at which insoluble nickel hydroxide starts to form and this is shown in Figure 8-124. With chloride present in the solution, the following eight species (Ni^{2+}, $NiCl^+$, $Ni(OH)_2$, $Ni(OH)_3^-$, $Ni_2(OH)^{3+}$, $Ni(OH)_4^{2-}$, $Ni(OH)^+$, $Ni_4(OH)_4^{4+}$) must be taken into account over the whole range of pH (0-14), although only two of them (Ni^{2+} and $NiCl^+$) may exist in significant amount at the given pH. While there is a concentration polarization near the cathode surface during nickel electrodeposition, the precipitation pH estimated from the bulk nickel concentration will give a safer upper limit where the surface pH can ultimately go without the risk of the formation of insoluble nickel hydroxide. The solubility product, K_{sp}, of nickel hydroxide at 25°C is cited as 5.47×10^{-16} by CRC Handbook [10]. This value does not account for the effect of the ionic strength. It was found in the present calculations that this value was applicable for up to 1 kmol m^{-3} $NiCl_2$ [4].

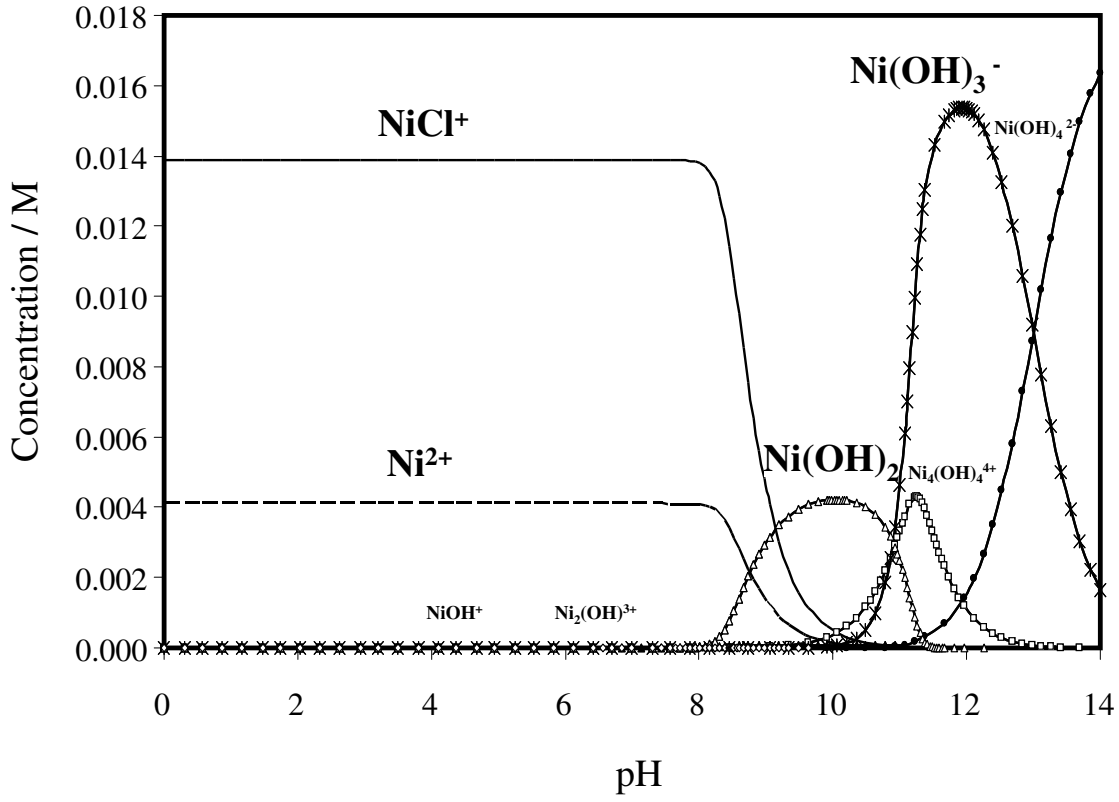

Figure 8-124. Distribution curves of nickel species in 18 mol m^{-3} Ni^{II} and 5 kmol m^{-3} Cl^-; 298 K. Stability constant (*K*) values extracted from Ji and Cooper, 1996 [4].

Accordingly, these distribution curves reflect the real situation in the solution as a function of pH, provided that the equilibrium quotients used in the calculations are reliable. It is obvious that at the pH range of 0-14, the predominant species are Ni^{2+} and $NiCl^+$ in the acidic region. The amounts of other species $Ni(OH)^+$, $Ni(OH)_2$ (aq) , $Ni(OH)_3^-$, $Ni(OH)_4^{2-}$, Ni_2OH^{3+} and $Ni_4(OH)_4^{4+}$ are negligible. Predicted concentrations do not appear to allow for NiO (c) limiting concentrations in neutral solutions. In addition, for dilute nickel recovery, it is important to ascertain the solution pH has an optimal range which is not too high to cause $Ni(OH)_2$ deposition, and not too low to cause excessive hydrogen evolution that retards Ni or Ni-H alloys deposition. Thermodynamic calculations and experimental evidence has revealed that 3.25 is the ideal operating condition.

8.3.2. Zinc

Using thermodynamic data available in literature [3], the thermodynamic conditions necessary (Appendix B(g)) for depositing zinc from a simple zinc-water and zinc–chloride-water systems have been evaluated to produce a potential-pH diagram, shown in Figure 8-125 and

Figure 8-126. The reversible potential reaction [8-5]:

$$ZnCl^{+} + 2e^{-} \rightleftharpoons Zn + Cl^{-} \qquad [8\text{-}5]$$

of $ZnCl^{+}$/ Zn is given in equation [8-6]:

$$\text{At 298 K: } E_{ZnCl^{+}/Zn}(\text{SHE}) / \text{V} = -0.7768 + 0.0296\log\left(ZnCl^{+}\right) - 0.0592\log\left(Cl^{-}\right) \qquad [8\text{-}6]$$

As shown in Figure 8-126,

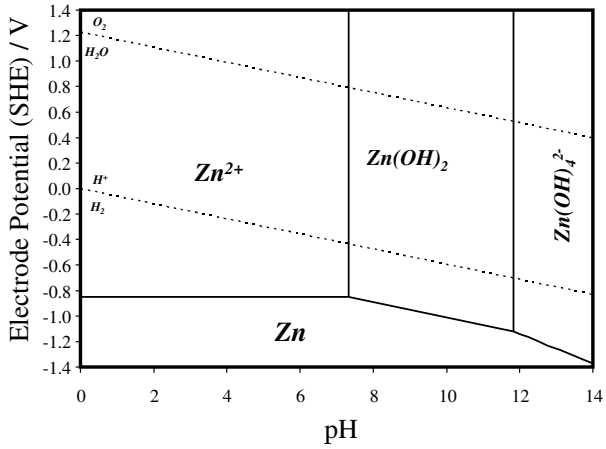

Figure 8-125. Potential pH diagram for nickel- water. Activities: Zn^{2+} = 10^{-3} kmol m^{-3}; 298 K, 1 atm [12].

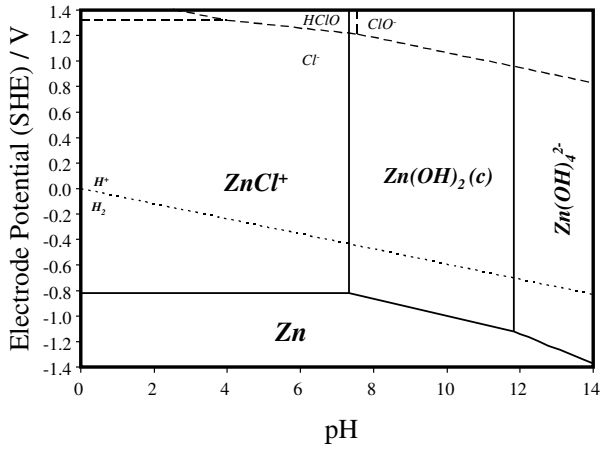

Figure 8-126. Potential pH diagram for nickel-chloride-water. Activities: Zn^{II} = 10^{-3}, Cl^{-} = 5; 298 K, 1 atm.

The significance of the zinc species distribution is realised in understanding what may happen in terms of the predominant zinc species in the solution at a particular pH and as the pH changes. The speciation in acidic zinc chloride electrolytes was estimated from equilibrium constant for Zn^{II} taken from Baes and Mesmer [14] and Mathias et al. [13]. Accordingly, these distribution curves reflect the real situation in solution as a function of pH, provided that the equilibrium quotients used in the calculations are reliable. It is obvious that over the pH range from 0-14 the predominant species are Zn^{2+} and $ZnCl^{+}$ in the acidic region. The amounts of other species $Zn(OH)_2$ (c), $Zn(OH)_3^{-}$, $Zn(OH)_4^{2-}$, $Zn(OH)^{+}$ and $Zn_2(OH)^{3+}$ are negligible. It was realised that predicted concentrations do not appear to allow for ZnO(c) limiting concentrations in neutral solutions as shown in Figure 8-127.

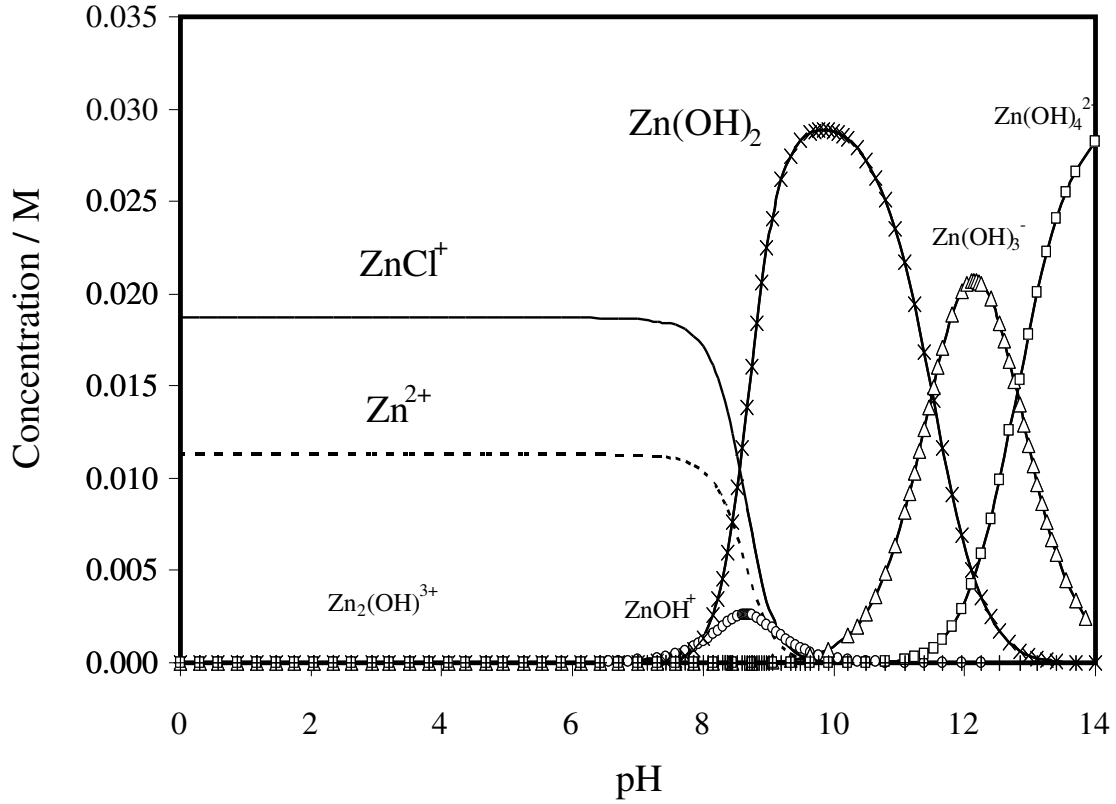

Figure 8-127. Distribution curves of zinc species in 20 mol m^{-3} Zn^{II} and 5 kmol m^{-3} Cl^-, 298 K. Stability constant (*K*) values extracted from Mathias et al., 1990 [13] and Baes and Mesmer, 1976 [14].

Zinc electrowinning, typically from ca. 1 kmol m^{-3} Cl^-+ 1 kmol m^{-3} $ZnCl^+$ at ca. 25 °C, involves a minimum of three cathodic reactions coupled to anodic oxygen evolution:

Ti / Zn cathode $$ZnCl^+ + 2e^- \longrightarrow Zn + Cl^- \quad [8\text{-}7]$$

$$2H^+ + 2e^- \longrightarrow H_2 \quad [8\text{-}8]$$

Ti/Ta_2O_5-IrO_2 anode $$2H_2O \longrightarrow O_2 + 4H^+ + 4e^- \quad [8\text{-}9]$$

As its standard potential is -0.7768 V vs. SHE, reaction [8-7] occurs in parallel with reaction [8-8]. It is only the low exchange current density for hydrogen evolution on zinc that enables high current efficiencies to be achieved for reaction [8-7], in the absence of any adventitious dissolved impurities [15] that could be co-reduced at the cathode and catalyse [8-8]. This makes establishing a mechanism for zinc deposition rather difficult, especially allowing for the additional effects of heavy metal impurity species e.g. nickel. Not surprisingly, much of the literature has focussed on determination of the 'intrinsic' current efficiency for zinc

deposition and the effects of impurities typical of industrial zinc electrolytes [16]. The effect of reaction [8-9] appears on the pH alteration of the catholyte compartment due to the transport of protons from the anolyte side.

8.4. Electrolyte composition and complexation for the Zinc- Nickel- Chloride System

We have used chloride salts of zinc and nickel in the plating solutions that are considered here. Table 8-16 shows the contents of the bath in 4 kmol m^{-3} HCl and 1 kmol m^{-3} NaCl that was under investigation, which illustrates the real concentration in the WEEE leachate under investigation.

Table 8-16. Composition of the nickel-zinc plating baths used in this study.

	Plating bath
Zn^{II}	30 mol m^{-3}
Ni^{II}	18 mol m^{-3}
Total metal	48 mol m^{-3}
Zn^{II}: Ni^{II}	0.375
Measured pH	3.25

Despite the $NiCl^{+}$ concentration being higher compared to Ni^{2+}, note that there are several debates [4,6,9] on the Ni^{II} speciation in aqueous chloride media as explained earlier in section 8.3.1. Thus, in this work, Ni^{2+} will be treated as the predominant species. Since the complex formation constants of $ZnCl^{+}$ which are extremely small ($Log\ K^{o}$ =-0.17 [4]); the complexing should have little effect on the equilibrium potential of Zn^{2+} in aqueous chloride solutions, therefore in the following section Zn^{2+} will be treated as the predominant species.

8.5. Determining the reduction kinetics of zinc(II) in 4 kmol m^{-3} HCl and 1 kmol m^{-3} NaCl:

8.5.1. An experimental study

Figure 8-128 shows the voltammogram of zinc deposition from 30 mol m^{-3} Zn^{II}+ 4 kmol m^{-3} HCl + 1 kmol m^{-3} NaCl solutions which had a bulk pH value of 3.25 on platinum (Pt) rotating disc surface rotates at 60 - 1500 rpm with a scan rate of 10 mV s^{-1}. The potential was swept

initially in a negative-going direction from -0.40 V to -1.10 V (SCE). In the case of the zinc chloride containing solutions, the negative current densities in each cycle were the sum of H^+ and Zn^{2+} reduction current densities, meanwhile the presence of positive current densities were due to Zn metal oxidation to Zn^{2+}. In pH = 3.25 systems, the start of a small peak in the cathodic polarization curves ca. -0.95 V (SCE) corresponded to the zinc bulk deposition as can be seen in Figure 8-128, where the reduction of Zn^{2+} gave a single wave not completely separated from the hydrogen evolution. At -0.95 V (SCE), Zn^{2+} began to reduce to form Zn on the electrode's surface. At potentials ca -1.10 V (SCE), H_2 evolution occurred. The current loop between the negative-going and positive-going potential sweeps was due to nucleation and growth of Zn on the platinum substrate, which increased the surface area. In the reduction curve, the onset of strong current densities was observed at an applied potential of -1.0 V (SCE) but in subsequent rotation was seen at ca. -0.80 V (SCE). This trend was expected due to more energy that was required to nucleate zinc on a foreign substrate than on a zinc substrate. Once the Pt disc was coated with a monolayer of zinc atoms, the rate of zinc deposition increased. It was calculated that 2×10^{-5} C of charge would need to be passed in order to coat the Pt disc with a monolayer of zinc. However, due to the proportion of charge that contributed to hydrogen evolution and zinc deposition was rather difficult to distinguish, the potential at which a zinc monolayer forms can not be known with certainty. Although the finite area under the anodic peaks suggests that all of the nickel that was deposited on the Pt fully dissolves, it is evident from the fact that the onset of high current densities begins at more positive overpotentials in each subsequent rotation, which the zinc deposits do not dissolve completely.

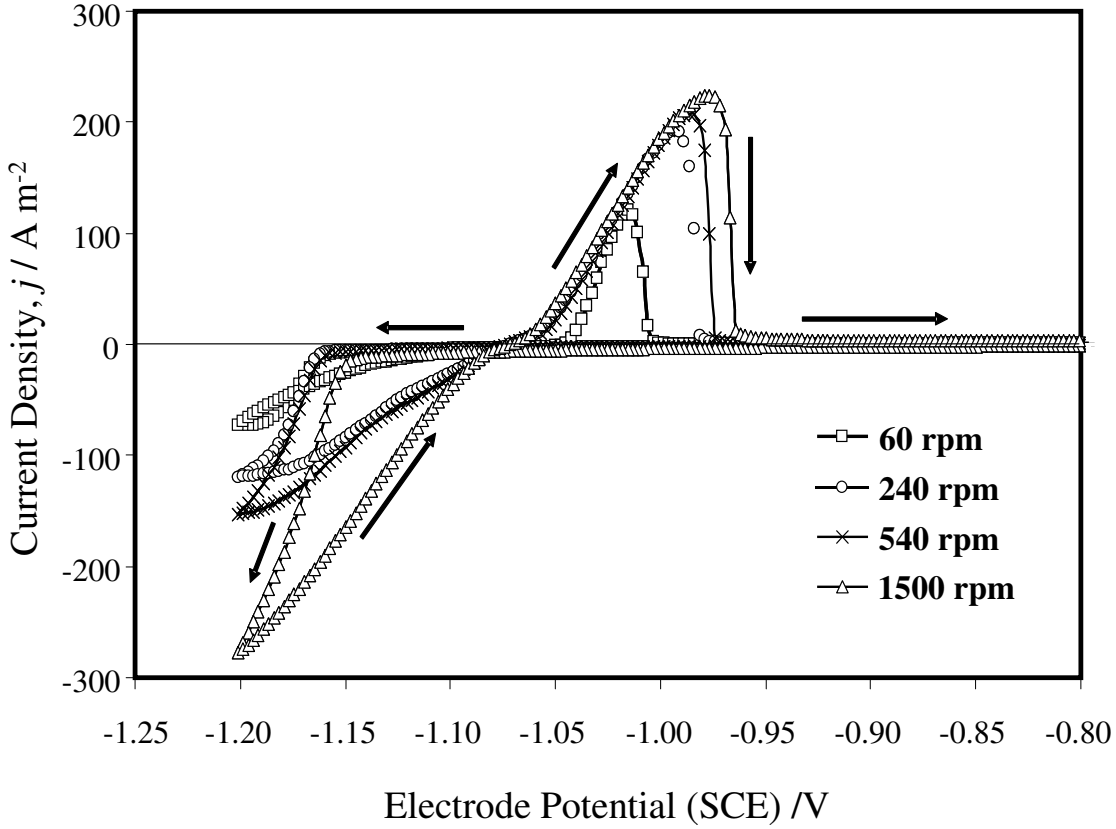

Figure 8-128. Cyclic voltammogram of Pt in 30 mol m^{-3} Zn^{II} + 4 kmol m^{-3} HCl + 1 kmol m^{-3} NaCl solutions at pH 3.25; scan rate, 10 mV s^{-1}; rotating rate, 60- 1500 rpm; sweep reversal at -1.20 V (SCE).

As the potential was swept from -1.20 V to -0.80 V (SCE), the Zn deposited was stripped from the electrode surface showing a well defined tin oxidation peaks, ca. -1.00 V (SCE). For dilute systems, the stripping peak potential was in the vicinity of -1.05 to -1.10 V, which is very close to the reversible potential of zinc E^0 Zn^{2+}/ Zn = - 1.008 V (SCE). Other authors have found similar results [17,18,19]. The anodic and cathodic charge, Q_A and Q_C at 25 s^{-1} were measured as 4.41×10^{-5} C and 3.60×10^{-5} C over the range of the potential used, respectively. Hence, the charge yield for zinc deposition may be estimated as ca. 0.82. This value indicates that hydrogen evolution occurred at more negative potentials, thus decreasing charge yields.

When the potential was stepped from a value where no electrochemical reactions occurred, to a region where the reduction or oxidation reaction is mass transfer controlled, the concentration of reactant was depleted, the diffusion layer thickness increased and the current decreased with time. For a stationary electrode and quiescent solutions, the only transport

effect was diffusion at short time scales. The diffusion coefficient can then be calculated from the current time response as described by the Cottrell equation [8-10].

$$i_d(t) = \frac{nFAD_i^{1/2}C_i}{\pi^{1/2}t^{1/2}} \qquad [8\text{-}10]$$

As can be seen in Figure 8-129, the current resulting from a potential step decays to zero which inversely proportional to the square root of time. The diffusion coefficient of Zn^{2+} calculated from the slope is 4.54×10^{-10} m^2 s^{-1}. This value was close to to those obtained by Newman et al. [28] for ions at infinite dilution in water at 25°C i.e. 7.10×10^{-10} m^2 s^{-1} for Zn^{2+}. In addition, this value was also used by Mathias et al. [13] in their modelling work on zinc-nickel electro-co-deposition. It must also be pointed out that experimental values for kinetic parameters may be retrieved from the literature but are usually produced at very specific conditions depending on the electrode potential and the pH in the solution which produces a range of different ionic species. This diffusion coefficient value, D_i was then used to determine the Nernst diffusion layer thickness, δ_N, , for each rotation rate and subsequently k_m values was calculated by knowing that $k_m = \frac{D_{Zn^{2+}}}{\delta_N}$ and are tabulated in Table 8-17 below.

Table 8-17. Calculated δ_N and k_m values for different rotation rates.

Rotation rate / s^{-1}	Square root of rotation rate / $s^{-0.5}$	$\delta_N \times 10^{-5}$ / m	$k_m \times 10^{-5}$ / m s^{-1}
1	1	4.96	0.92
4	2	2.47	1.84
9	3	1.65	2.75
16	4	1.24	3.67
25	5	0.99	4.58

Further experiments were carried out with the rotating Pt disc electrode, pre-coated with Zn, concentrating on the potential regions relevant to those in the cathode of the reactor to be able to determine the current exchange density and the Tafel slope of zinc deposition.

The Pt electrode, rotating at 1500 rpm, was pre-coated with Zn at -1.10 V (SCE) for 1000s in

4 kmol m^{-3} HCl + 1 kmol m^{-3} NaCl solutions containing 10 mol m^{-3} Zn. The total charge passed was ca. 0.4 C (22 500 C m^{-2}), corresponding to > 2000 monolayers of Zn. Figure 8-130 shows the resulting voltammogram as the potential of the Zn-coated disc electrode was swept from -0.95 to -1.20 V (SCE) at 5 mV s^{-1}. The kinetics of Zn deposition on Zn was very fast and the mass-transport limiting current was reached with overpotentials ≥ 0.05 V.

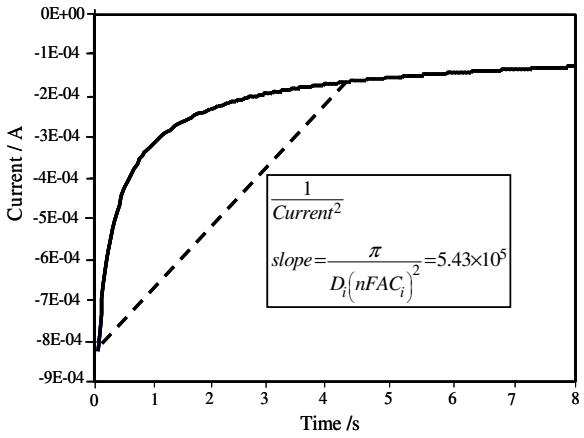

Figure 8-129: Current time response for the reduction of 30 mol m^{-3} zinc chloride ions on a Pt stationary electrode in 4 kmol m^{-3} HCl + 1 kmol m^{-3} NaCl, at -1.10 V (SCE); 298 K, 1 atm. Diffusion coefficient value for Zn derived from the slope based on Cottrell equation [8-10].

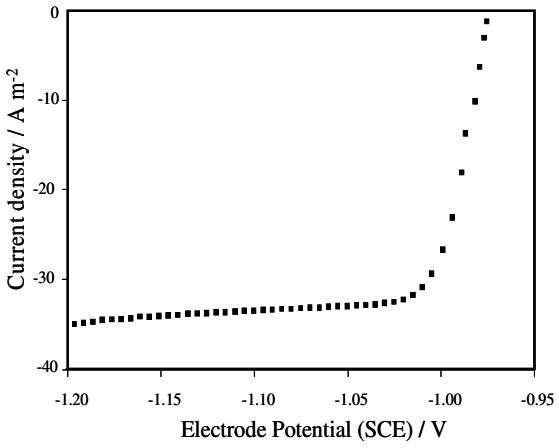

Figure 8-130: Disc voltammogram for Zn deposition and H_2 evolution on Zn-coated disc electrode in 30 mol m^{-3} Zn^{II} + 4 kmol m^{-3} HCl + 1 kmol m^{-3} NaCl at a scan rate of 2.5 mV s^{-1} and a rotation rate of 25 s^{-1}.

Due to the low Zn^{2+} concentrations involved and the competing reaction (H_2 evolution), the accessible range of current was restricted to less than an order of magnitude below the limiting current as shown in Figure 8-130, therefore restricting the accuracy of the Tafel slope and the exchange current density derived. The Koutecký-Levich equation [8-11] relates current and rotation rate for a rotating disc electrode, for the case when the current is controlled both by kinetics (first term on the right hand side) and diffusion (second term on the right hand side).

$$\left|-\frac{1}{j}\right| = \frac{1}{\nu_e F k_i C_i} + \frac{1.61 \upsilon^{1/6}}{\nu_e F C_i D_i^{2/3}} \cdot \frac{1}{f^{1/2}} \qquad [8\text{-}11]$$

From a set of Koutecký-Levich plots of j^{-1} vs. $f^{1/2}$, at various potentials, the kinetic rate coefficients k and the kinetic current densities can be derived by extrapolation of the experimental data to infinite transport rate ($f^{1/2} \rightarrow 0$). Thus, eliminating the diffusion limitations; the exchange current density and Tafel slope can then be derived from the potential dependence of the kinetic current density shows the Koutecký-Levich plot of the current density for Zn deposition at various disc potentials. The kinetic current densities, in the absence of diffusion limitations, were determined at different disc potentials from Levich-Koutecký plot, and log (kinetic current density) was plotted against electrode potential in Figure 8-132 for Zn deposition. The kinetic rate constant, k_i for Zn^{II}/Zn was calculated as 1.03×10^{-4} m^2 s^{-1}. From Figure 8-132, the exchange current density and Tafel slope for Zn deposition were estimated as 12.59 A m^{-2} and 85 mV $decade^{-1}$.

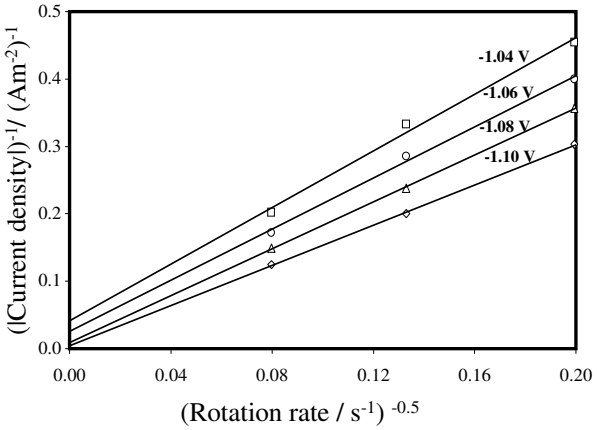

Figure 8-131. Koutecký- Levich plot of current density Zn deposition on Zn pre-plated Pt disc electrode in 30 mol m^{-3} Zn^{II} + 4 kmol m^{-3} HCl + 1 kmol m^{-3} NaCl at different disc potentials (E (SCE) / V).

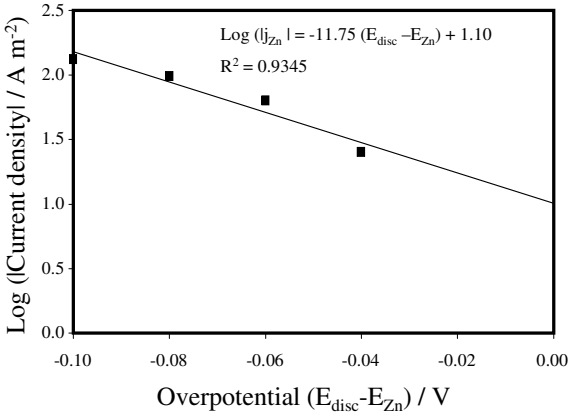

Figure 8-132. Log kinetic current density of Zn deposition determined from Koutecký- Levich plot against overpotential ($E_{disc} - E_{Zn}$) for Zn deposition on Zn pre-plated Pt electrode in 30 mol m^{-3} Zn^{II} in 4 kmol m^{-3} HCl and 1 kmol m^{-3} NaCl.

Voltammetry analysis was carried out in 4 kmol m^{-3} HCl and 1 kmol m^{-3} NaCl solutions in the absence of Zn^{II} to avoid Zn deposition in order to investigate the reaction kinetics of the side reaction, H_2 evolution [8-13] on Ni stationary electrode,

$$2H^+ + 2e^- \rightleftharpoons H_2 \qquad [8\text{-}12]$$

Figure 8-133 shows the analysis using Tafel slopes on hydrogen evolution at nickel stationary electrode which mimics the real process that will be carried out later with the parallel mesh nickel cathode reactor. The value were derived as $j_0 = 6.61\times10^{-5}$ A m^{-2} and Tafel slope of 111 mV decade^{-1}, respectively.

$$j_{H_2} = -j_{0,H_2(Zn)} \exp\left(-\beta_{H_2}\eta_{H_2}\right) \qquad [8\text{-}13]$$

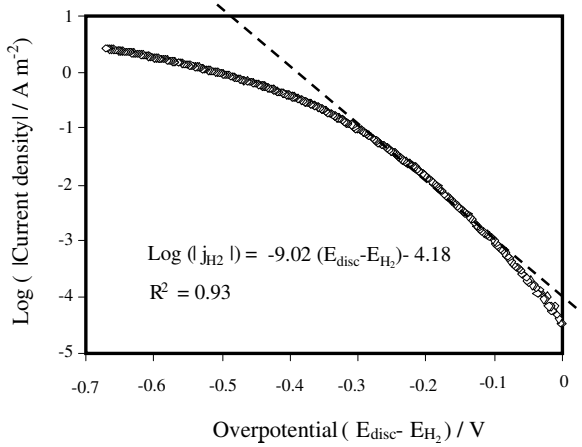

Figure 8-133. Analysis using Tafel plots on hydrogen evolution current density on Ni wire working electrode (A = 1.5×10^{-4} A m^{-2}) in 4 kmol m^{-3} HCl and 1 kmol m^{-3} NaCl at pH 3.25; scan rate of 2.5 mV s^{-1} ,rotating rate 1500 rpm.

Evidence of uncompensated ohmic potential losses at higher current densities, causing curvature at *j* well below transport limited values. Correct by estimating distance (d) between electrode and Luggin probe tip and knowing conductivity (κ_{eff}) of electrolyte solution: $\Delta\phi_s = j \cdot d / \kappa$, then subtract from *E* at any *j*. Bubbles may cause decreased conductivities due to void fraction of electrolyte solution occupied by bubbles.

Table 8-18 summarises the kinetic parameters obtained from various sources [9,20,25].

Table 8-18: A summary of the kinetic parameters obtained from various sources.

Reactions	Exchange current density and Tafel slope	Literature	Rotating disc
Zn^{2+} / Zn	$j_{0,\,Zn}$ / A m^{-2}	304	12.59
	Tafel slope Zn/ mV decade^{-1}	76.1	85
		Barton and Scott [20]	
Ni^{2+} / Ni	$j_{0,\,Ni}$ / A m^{-2}	2×10^{-3}	-
	Tafel slope Ni / mV decade^{-1}	128	-
		Mathias and Chapman [25]	
H^{+} / H_2	$j_{0,\,H2\,(Ni)}$ / A .m^{-2}	10^{-3}	6.61×10^{-5}
	Tafel slope H_2 / mV decade^{-1}	120	111
		Piatti et al.[9]	

The electrochemical kinetic parameters for dissolution and deposition of Zn that have been determined will be used to adjust model parameters in Maple™.

8.6. Interactions of Electrodeposition Potentials between Nickel and Zinc

As explained in literature survey on electro-co-deposition, nickel-zinc was the most challenging combination in this work compared to others e.g. chromium-nickel or chromium-zinc combinations; where both cations could discharge in a very close potential range when alone. There is evidence that they interact with each other's deposition. The presence of zinc will shift the deposition potential of nickel to a more cathodic value, and both metals tend to discharge together [22] with zinc being more abundant than the solution Zn: Ni ratio would suggest [23]. Where two cations could discharge, one would expect to see two nucleation related current rise at the corresponding potentials for each of the metals. In this case, that of nickel should come before zinc. Unfortunately, this was not the case here, even in uncomplexed mixtures. The case is presented in Figure 8-134, where the mixed system

nucleation fell in between that of pure nickel and zinc. To investigate further the nature of the electrodeposition interactions, cyclic voltammograms were obtained as shown in Figure 8-134. Three different cycles are superimposed within the same figure in order to understand the interaction between nickel and zinc deposition as well as the H_2 evolution which was the competing reaction that will decrease the current efficiencies of Zn-Ni electro-co-deposition.

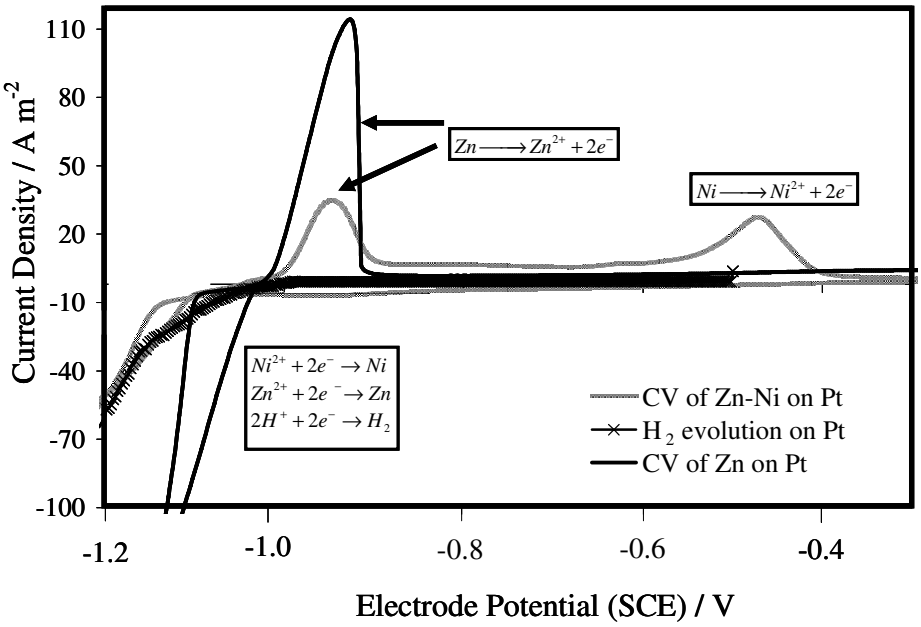

Figure 8-134. CV of (a) Zn-Ni deposition (b) Zn deposition on a Pt rotating disc electrode from 30 mol m^{-3} Zn^{II}, 18 mol m^{-3} Ni^{II} , 4 kmol m^{-3} HCl + 1 kmol m^{-3} NaCl solutions at pH 3.25 , scan rate, 10 mV s^{-1}; rotating rate, 1500 rpm and (c) H_2 evolution on Pt RDE 4 kmol m^{-3} HCl + 1 kmol m^{-3} NaCl solutions at pH 3.25.

The cathodic scan did not change much from the blank profile until beyond -0.80 V (SCE) where a sharp current rise suggested some nucleation. Nickel deposition could have occurred alone earlier (e.g. around -1.0 V (SCE)) only that it was masked by the proton reduction currents between -1.0 and -1.2 V (SCE). The nucleation jump beyond -1.2 V could be due to zinc alone, with zinc depositing onto the Pt disc as well as the nickel or nickel-hydride lattice already formed. At such cathodic potentials, nickel continued to discharge naturally, and this enabled Ni-Zn alloy formation. In comparison with electrodeposition of pure zinc and nickel, Ni-Zn alloy deposition exhibits a zinc deposition potential shifted approximately 50 mV toward more positive potentials.

On the anodic scan, as the dissolution potential of zinc near -1.0 V (SCE) was approached,

zinc dissolves which stripping peak were observed as shown in Figure 8-134, thus exposing more nickel-based surfaces. This is in agreement with earlier observations for Zn^{II} micro-kinetics studies. The dissolution of zinc from the Ni-Zn alloy leaves a porous nickel layer which starts to dissolve at -0.59 V (SCE). This porous nickel layer was reported earlier in Swathirajan's work [29]. In the range of -0.40 to +0.04 V (SCE), the cathodic current level during the anodic-direction scan was less than during the cathodic-direction sweep (Figure 8-134). This was due to the dissolution of nickel.

It is commonly agreed that the reduced nickel content was mainly due to the slow kinetics of nickel deposition relative to that of zinc [24,27]. Hence, even though it has a more noble electrode potential and should have acquired much larger driving force by the potential zinc can deposit, the nickel deposition rate fails to catch up. In addition, this voltammetric study of zinc-nickel alloy deposition showed that there was a competition between Ni-Zn and H_2 evolution. It seems promising to try to control these processes by using an appropriate deposition current pattern providing the micro-kinetics data of each metal. To recapitulate, the incipient electrodeposition potentials of nickel-zinc mixtures, as found on cathodic polarization curves, usually fell in between those of single cations.

8.7. Model Development

The following subsection summarizes the main electrochemical reactions that have been used in MAPLE ™.

8.7.1. Electrochemical Reactions

The main reactions at the cathode are the electrodeposition of metals, such as the multi-step reduction of Ni and Zn: the reduction of Ni^{2+} to Ni and the reduction of Zn^{2+} to Zn.

$$Ni^{2+} + 2e^- \rightleftharpoons Ni \qquad [8\text{-}14]$$

$$Zn^{2+} + 2e^- \rightleftharpoons Zn \qquad [8\text{-}15]$$

Its reversible potential ($E_{Ni^{2+}/Ni}$ and $E_{Zn^{2+}/Zn}$) can be calculated by the Nernst equation for 298 K:

$$E_{Ni^{2+}/Ni}(SHE)/V = -0.2405 + 0.0296 \log\left(Ni^{2+}\right) \qquad [8\text{-}16]$$

$$E_{Zn^{2+}/Zn}(SHE)/V = -0.7626 + 0.0296\log\left(Zn^{2+}\right) \quad [8\text{-}17]$$

where bracket represents concentration in mol dm^{-3} . The current density (j_{Ni} and j_{Zn}) can then be estimated by the Butler-Volmer equation, allowing for transport controlled system:

$$j_i = -\frac{j_{0,k}\exp\left[\beta_k\eta_k\right]}{\left\{1+\left(\frac{j_{0,k}}{j_{L,k}}\right)\exp\left[\beta_k\eta_k\right]\right\}} \quad [8\text{-}18]$$

The Tafel coefficient (β) of reaction *k* are defined as:

$$\beta_{k,c} = -\frac{\alpha_k n_k F}{RT} \quad ; \quad \beta_{k,a} = \frac{\left(1-\alpha_k\right)n_k F}{RT} \quad [8\text{-}19]$$

a and c denote anodic and cathode reactions, respectively. A sufficient overpotential ($\eta_{Ni} = E - E_{Ni^{2+}/Ni}$) and ($\eta_{Zn} = E - E_{Zn^{2+}/Zn}$) is applied to drive reaction into mixed kinetic and mass-transport control to ensure high conversion of Ni^{2+} and Zn^{2+};

The limiting current density for reaction k ($j_{L,k}$) can be estimated by:

$$j_{L,k} = n_k F k_{m,k} c_k \quad [8\text{-}20]$$

There is one possible side reaction at the cathode: the H_2 evolution:

$$2H^+ + 2e^- \rightleftharpoons H_2 \quad [8\text{-}21]$$

$$E_{H^+/H_2}(\text{SHE})/\text{V} = -0.0592\,pH - 0.0296\log P_{H_2} \quad [8\text{-}22]$$

$$j_{H_2} = -j_{0,H_2}\exp\left(-\beta_{H_2}\eta_{H_2}\right) \quad [8\text{-}23]$$

The kinetic parameters for individual reactions used in the model has been summarised in Table 8-18. The anode loss reaction is mainly oxygen evolution from water:

$$2H_2O \rightleftharpoons O_{2(g)} + 4H^+ + 4e^- \quad [8\text{-}24]$$

$$E_{O_2/H_2O}(\text{SHE})/\text{V} = 1.229 - 0.0592\,pH + 0.0148\log\left(P_{O_2}\right) \quad [8\text{-}25]$$

$$j_{O_2} = j_{0,O_2}\exp\left(-\beta_{O_2}\eta_{O_2}\right) \quad [8\text{-}26]$$

The current density of O_2 evolution (j_{O_2}) (reaction[8-24]) is kinetically controlled, with an exchange current density ($j_{O_2,0}$) of 10^{-6} A m^{-2} and transfer coefficient (α_{O_2}) of 0.5 ($\beta_{O_2} = \frac{\alpha_{O_2} n_{O_2} F}{RT}$).

8.7.2. Electrode Kinetics and Charge Efficiencies

Experimental and literature values of the kinetic parameters for each reaction were substituted in the extended Butler-Volmer equation [8-18], allowing for mass transport limitations, to predict the partial and total current density - electrode potential behaviour and hence the potential dependence of the charge efficiency (Φ_e) for reaction. In the first instance, the partial current densities due to the three cathodic reactions ([8-14],[8-15],[8-21]) were assumed to be simply additive, involving no chemical interactions, e.g. in terms of the surface coverage of intermediates. Hence, models have been developed in Maple™ (www.maplesoft.com) to predict current densities- potential relationships of the zinc (II) and nickel (II) in aqueous chloride solution.

From experimental data obtained previously on zinc (II) chloride kinetic values of j_0 and Tafel coefficient were derived as 12.59 A m^{-2} and 85 mV $decade^{-1}$ respectively, for a concentration of 30 mol m^{-3}. Hydrogen evolution kinetics was also included in the model predictions. A mass transfer coefficient of $k_m = 2.17\times10^{-5}$ m s^{-1} was used in the model, as determined by Levich's equation, for a disc electrode rotation rate of 16 s^{-1}. The corresponding parameters for nickel deposition were retrieved from the literature and measured as $j_0 = 2\times10^{-3}$ A m^{-2} and 128 mV $decade^{-1}$. For the hydrogen evolution reaction [8-21] on nickel electrode, values of $j_0 = 6.61\times10^{-5}$ A m^{-2} and a Tafel slope of 111 mV $decade^{-1}$ at 298 K were used. The kinetics parameters used in the model were summarised in Table 8-18. Figure 8-135 illustrates the predicted partial and total current density - potential behaviour for reactions [8-15], [8-16] and [8-23], together with the potential dependence of the charge yield for reaction [8-15] and [8-16]. The losses in zinc and nickel charge yields at < -1.0 V (SCE) were due to hydrogen evolution. In addition, the reaction could not proceed to mass transport controlled region due to hydrogen evolution as well.

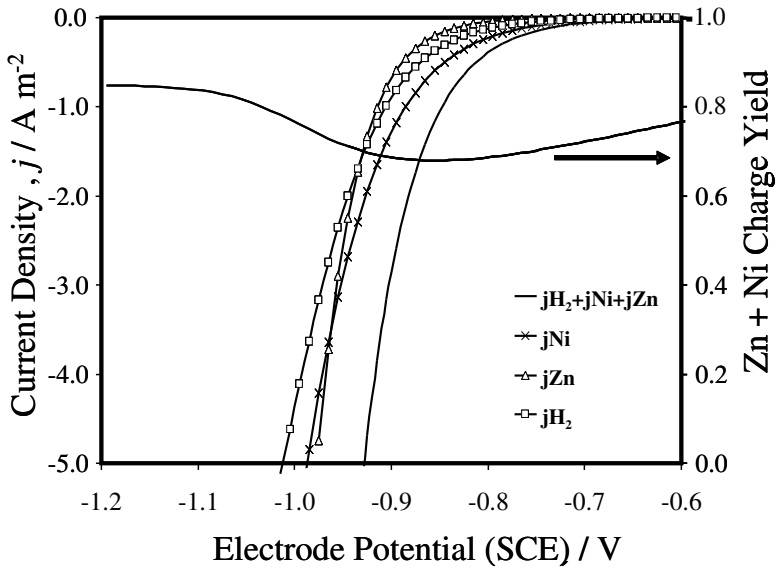

Figure 8-135. Model prediction of current density and charge efficiencies ($\Phi^{e}_{Zn+Ni} = j_{Zn+Ni} / (j_{Zn} + j_{Ni} + j_{H2})$ - electrode potential behaviour for reduction of Zn^{II}, Ni^{II} and hydrogen evolution.

8.7.3. Modelling of dissolved nickel (II) and zinc (II) concentration and potential profiles in the cathode | electrolyte boundary layer

The model developed by Mathias and Chapman [25,27] was used as a starting point for the model of the diffusion boundary layer of a divided-membrane reactor that is being developed in this work, which will aid the presentation of experimental results. The approach was to use partial current density distribution data from a parallel plate membrane-divided reactor for the zinc-nickel system and a one-dimensional transport model, which includes the significant effect of migration. However, complexation was neglected due to the dilute concentration of nickel and zinc in the bath at pH 3 and cluttered kinetic mechanisms of Ni species in aqueous chloride solutions. A one-dimensional model along the direction of the current flow had been developed for the reactor with parallel plate electrodes. The species considered in the reaction system were: Ni^{2+}, Zn^{2+}, Na^{+}, Cl^{-}, H^{+}, SO_4^{2-}, O_2, and H_2. Their concentrations are governed by the material balance:

$$\frac{\partial C_i}{\partial t} = -\nabla \bullet N_i + R_i \qquad [8\text{-}27]$$

Steady-state operation is assumed:

$$\frac{dC_i}{dt} = 0 \qquad [8\text{-}28]$$

The flux (N_i) is described by the Nernst-Planck equation in dilute solution:

$$N_i = -D_i \nabla C_i - z_i F u_i C_i \nabla \phi + v C_i \quad [8\text{-}29]$$

The ionic mobility, u_i, is given by the Nernst-Einstein equation:

$$u_i = \frac{D_i}{RT} \quad [8\text{-}30]$$

The initial metal ions concentrations and diffusion coefficients used in the models are summarised in Table 8-19 and Table 8-20 respectively.

Table 8-19. A summary of initial metal ions concentration at pH 0 used in the models.

Species	Initial concentration / mol m^{-3}
Ni^{2+}	18
Zn^{2+}	30
Na^{+}	1000
H^{+}	0.01
Cl^{-}	5000
HCl	5000
NaCl	1000

Table 8-20. A summary of diffusion coefficients of metal ions.

Species	Diffusion Coefficient×10^{-9} / m^2 s^{-1}	Reference
Ni^{2+}	1.334	Newman [28]
Zn^{2+}	0.454	This work
Cl^{-}	2.032	Newman [28]

H^+	9.312	Newman [28]
OH^-	5.260	Newman [28]
Na^+	1.334	Newman [28]
SO_4^{2-}	1.065	Newman [28]

Note that NaOH (+ air) was added to the actual solutions (catholyte) to increase the pH to ca. 3.25 and subsequently precipitate '$Fe(OH)_3$', which was recovered by filtration;. Therefore, the increment of Na^+ ions will be taken into account in the model.

All properties were assumed to be uniform across the entire length of the reactor. Plug flow was assumed and there was no mixing of electrolyte in the vertical direction. In order to account for the mixing of electrolyte in the x-direction, the model geometry was divided into five subdomains which are: the cathode diffusion layer, the bulk catholyte, the membrane as the separator of both anolyte and catholyte, the bulk anolyte and the cathode diffusion boundary layer Figure 8-136. The bulk electrolyte was assumed to be well-mixed in the x-direction, as bubbles evolved from the electrodes contributed to the mixing of the electrolyte.

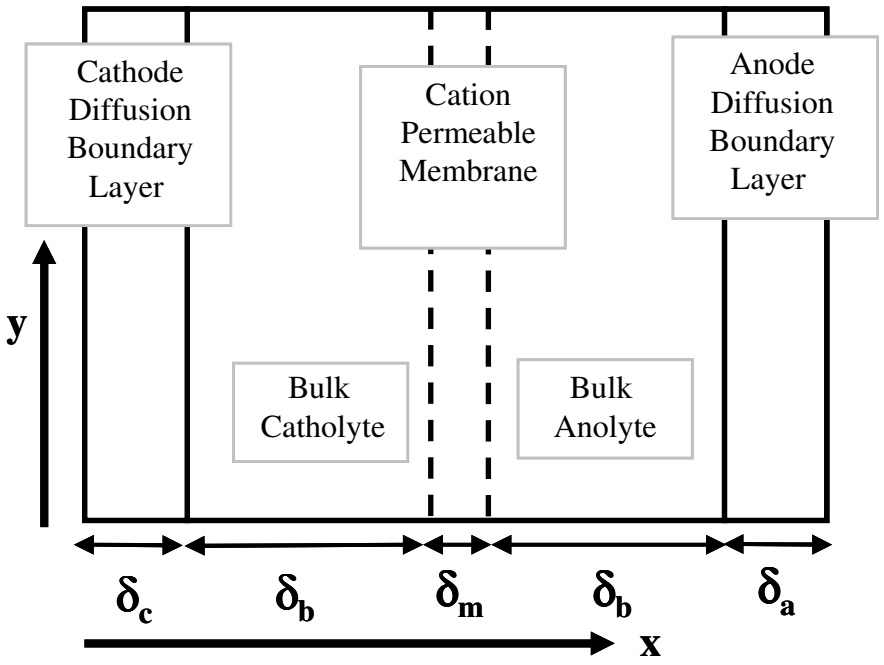

Figure 8-136. Schematic diagram of the model geometry for the reactor with parallel plate electrodes.

The thickness of cathode diffusion boundary layer (δ_c) can be estimated by:

$$\delta_c = \frac{D_{Zn^{2+}}}{k_{m,c}} \quad [8\text{-}31]$$

The mass transport was assumed to be controlled by convective diffusion and the mass transfer coefficient at the hydrogen-evolving cathode ($k_{m,c}$) can be estimated by:

$$k_{m,c} = a_{\text{constant}} \cdot \left(1.3 + 1.7 \cdot \text{v}^{0.71}\right) \cdot 10^{\left[-5+0.24\left(\frac{0.5\, j_{H_2}}{1000}\right)^{0.38}\right]} \quad [8\text{-}32]$$

where $a_{constant}$ is a factor depending on the nature of surface of the electrode, with a value of 1 for aged electrode and a value of 1.5 for new electrode [26].

Similarly, the thickness of the anode diffusion boundary layer (δ_a) can be estimated by:

$$\delta_a = \frac{D}{k_{m,a}} \quad [8\text{-}33]$$

It was assumed that the empirical formula of equation [8-33] can also be used to estimate the mass transfer coefficient at the oxygen-evolving anode ($k_{m,a}$), allowing for the O_2 bubble evolution rate being half that of the corresponding hydrogen-evolving cathode:

$$k_{m,a} = a_{\text{constant}} \cdot \left(1.3 + 1.7 \cdot \text{v}^{0.71}\right) \cdot 10^{\left[-5+0.24\left(\frac{0.5\, j_{O_2}}{1000}\right)^{0.38}\right]} \quad [8\text{-}34]$$

As an estimate, the average current density was assumed to be 1000 A m^{-2}. The cathode efficiency was assumed to be 1 and the (mean) cathode diffusion boundary layer estimated by equations [8-31] and [8-32] was 50 μm. The anode diffusion boundary layer estimated by equations [8-33] and [8-34] was 125 μm. As an initial estimate, the thickness of both the anode and cathode diffusion boundary layer was assumed to be 100 μm in this model.

The electrolyte velocity was assumed to be uniform within the bulk electrolyte (v_{ave}). The no-slip condition was applicable at the surface of electrodes, i.e. v = 0.

The mass transport in the horizontal direction (x) was assumed to be dominated by diffusion and migration, equation [8-35] is then simplified to:

$$N_i = -D_i \frac{dC_i}{dx} - z_i F u_i C_i \frac{d\phi}{dx} \quad [8\text{-}35]$$

The material balance, equation [8-35] becomes:

$$\frac{d}{dx}\left(-D_i \frac{dC_i}{dx} - z_i F u_i C_i \frac{d\phi}{dx}\right) = \sum_k \upsilon_{ik} r_k \quad [8\text{-}36]$$

The boundary condition at the surface of anode and cathode, for equation [8-36] is given by:

$$N_i = \sum_k \frac{\upsilon_{ik} j_k}{n_k F} \quad [8\text{-}37]$$

Subscript '*i*' and '*k*' represents reacting species and reaction, respectively. N_i is the flux of species i normal to the surface of the electrode, υ_{ik} is the stoichiometric factor species i in reaction k and j_k is the current density of reaction *k*.

At the inlet of the reactor, the concentration was specified:

$$C_i = C_{i,in} \quad [8\text{-}38]$$

Equation [8-38] is applied to (i–1) species, (all species except Na^+, as it is not involved in any reactions), together with the electroneutrality condition:

$$\sum_i z_i C_i = 0 \quad [8\text{-}39]$$

For systems where concentration gradients in electrolyte solutions can be ignored, the potential (ϕ) can be described by the Laplace's equation (Newman 1991c):

$$\nabla^2 \phi = 0 \quad [8\text{-}40]$$

and the current density (j) by:

$$j = -\kappa \nabla \phi \quad [8\text{-}41]$$

where κ is the conductivity.

$$\kappa = F^2 \sum_i z_i^2 u_i c_i \quad [8\text{-}42]$$

The potential drop within the catholyte, the membrane and the anolyte was assumed to be

ohmic.

Potential drop in membrane: $$\Delta\phi_{l,m} = \frac{j_{ave} d_m}{\kappa_m} \quad [8\text{-}43]$$

Potential drop in catholyte: $$\Delta\phi_{l,c} = \frac{j_{ave} d_c}{\kappa_{l,0}}$$

Potential drop in anolyte: $$\Delta\phi_{l,a} = \frac{j_{ave} d_a}{\kappa_{l,0}} \quad [8\text{-}44]$$

The cell voltage was calculated by:

$$U_{cell} = -\left(E_A + \eta_A - E_C - \eta_C + IR\right) \quad [8\text{-}45]$$

and,

$$IR = \Delta\phi_{l,c} + \Delta\phi_{l,m} + \Delta\phi_{l,a} \quad [8\text{-}46]$$

The equations were solved using the *'dsolve'* solver in MAPLE™ software. The full algorithm and the codes are given in Appendix E(d).

8.7.4. Mathematical Model of a cation permeable membrane containing Na^+ and H^+

One of the goals of this work is to develop an isothermal, steady-state, one dimensional mathematical model of the ion- exchange membrane with two cations (H^+ and Na^+). Protons (H^+) are released at the anode side as the oxygen evolution reactions (reaction [8-24]) proceeds and flow across the Nafion toward the aqueous solution. Moreover, the presence of Na^+ ions can have the added benefit of limiting the flux of H^+ ions through the membrane to the cathode. In this work, we are interested to develop a mathematical model of the present membrane so as to know the flux of H^+ that being transported to the catholyte side (Figure 8-137) that alters the pH of the solution which is very important in Ni-Zn electro-co-deposition process as well as determining the extend of the ohmic drop across the membrane.

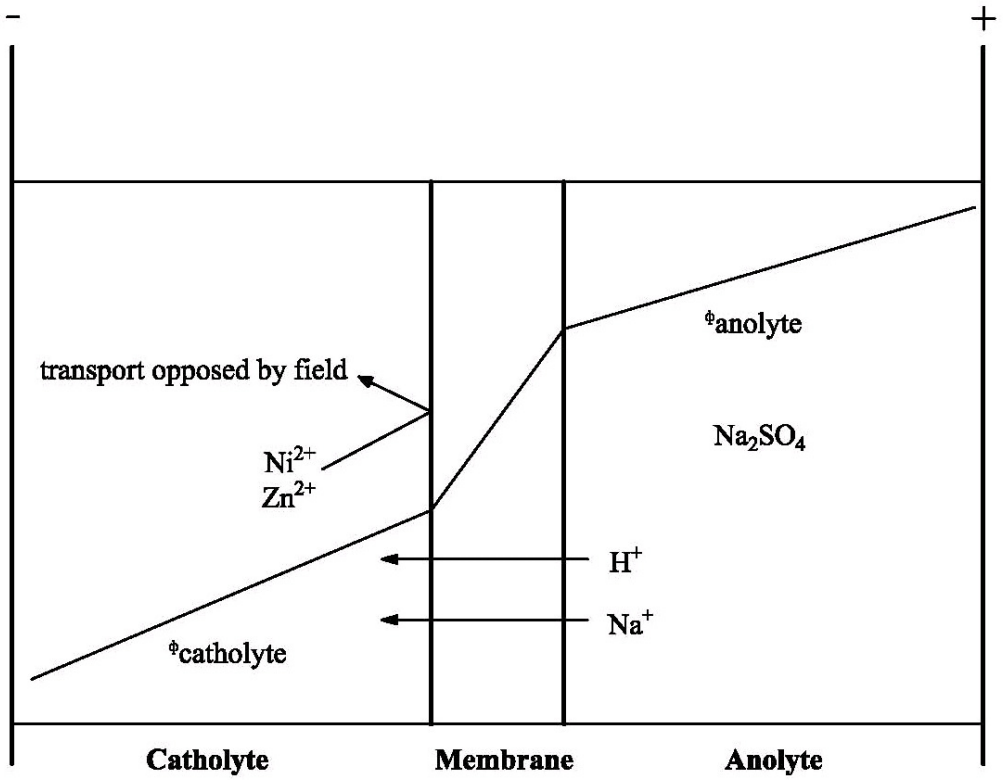

Figure 8-137. Schematic of cation membrane transport process.

Assuming migration is only due to potential drop across membrane, the individual fluxes of H^+ and Na^+ ions can be found as follows:

$$N_{M,H^+} = \frac{j_{M,H^+} \cdot A_m}{F} \quad [8\text{-}47]$$

$$N_{M,Na^+} = \frac{j_{M,Na^+} \cdot A_m}{F} \quad [8\text{-}48]$$

The ratio of j_{M,Na^+} to j_{M,H^+} will change with time, as their relative concentrations in the anolyte change. The H^+ and Na^+ fluxes through the membrane were assumed to be related by:

$$j_{M,Na^+} \cdot \left[H^+\right]_A = 0.144 \cdot j_{M,H^+} \cdot \left[Na^+\right]_A \quad [8\text{-}49]$$

Where 0.144 is the ratio between the diffusion coefficients of Na^+ and H^+ ions. Mass balances for fluxes of H^+ and Na^+ ions in the anolyte with the reactor system shown schematically in Figure 8-136 and operated in batch recycle mode can be written as:

$$V_A \frac{d\left[H^+\right]_A}{dt} = \frac{j_{A,H^+} \cdot A_A}{F} - \frac{j_{M,H^+} \cdot A_M}{F} \quad [8\text{-}50]$$

$$V_A \frac{d\left[Na^+\right]_A}{dt} = -\frac{j_{M,Na^+} \cdot A_M}{F} \quad [8\text{-}51]$$

Where V and A denote volume (m^3) and area (m^2), respectively; subscripts / superscripts C, A and M denote cathode / catholyte, anode / anolyte and membrane, respectively.
Given the initial concentrations in the anolyte were:

$\left[Na^+\right]_{A,t=0}$ = 1000 mol m^{-3}

$\left[H^+\right]_{A,t=0}$ = 1×10^{-4} mol m^{-3}

Initially, the majority of the current will be carried by the Na^+, because their concentration is so much larger compared to the proton concentration. However, as soon as oxygen begins to evolve the proton concentration in the anolyte will rapidly increase and at some point protons will begin to migrate preferentially to the sodium ions. Thus, the time evolution of the ratio of the two currents will depend on the time evolution of the proton concentration in the anolyte.

The mass balance of H^+ in the catholyte operated in batch recycle mode can be written as:

$$V_C \frac{d\left[H^+\right]_C}{dt} = -\frac{j_{C,H^+} \cdot A_C}{F} + \frac{j_{M,H^+} \cdot A_M}{F} \quad [8\text{-}52]$$

The equations were solved using the *'solve'* solver in MAPLE™ software. The full algorithm and the codes are given in Appendix E(d).

A more complicated mathematical modelling of a cation-exchange membrane containing two cations, H^+ and K^+ described using a multi-component diffusion (extended Stefan-Maxwell diffusion) which was used in modelling a CO_2-H_2O electrolyser [34]. However, in the work for which results are reported here, a simpler approach was taken which sufficiently provides some insights on macroscopic quantities such as the evaluation on catholyte pH changes due to H^+ produced by anodic oxygen evolution and transported through the membrane which subsequently increase the catholyte pH with time.

8.8. Results and Discussion on the one-dimensional model of Ni^{II}-Zn^{II} electro-co-deposition

As reported in the previous Chapter (Chapter 6 and 7) on the same setup of reactor system which is operated in batch recycle mode, the fluidised bed of glass bead will increase the electrolyte velocity, which in turn increases the mean mass transport rate due to convection enhanced by the mesh cathode, and more importantly due to the effect of glass particle collision frequency with the electrode thinning at the boundary layer. Therefore, those results will not be reported here. Batch recycle electrolyses at -1.10 V (SCE) with fluidised bed flowing at 6×10^{-5} m^3 s^{-1}, produced the expected exponential decay of Zn^{II}-Ni^{II} electro-co-deposition with time with cell voltages (U_{cell}) varied around 2.8- 3.0 V, as shown in Figure 8-138. The reactor was operated for a total of three hours under potentiostatic control. The dissolved Ni^{II} concentrations in solution was determined by taking samples from reservoir at various time online via fibre optics by measuring the Ni^{II} concentration with UV-Visible spectrophotometry (λ_{max} = 393 nm [33]) as shown in Figure 8-139. However, the concentration of Zn^{II} was verified using inductively coupled plasma emission specotroscopy (ICP) due to the colourless nature of Zn^{II} in chloride. It was observed that Zn^{II} and Ni^{II} could be depeleted to analytically undetectable concentrations and the linear sweep voltammetry (before and after) electro-co-deposition of Zn^{II}- Ni^{II} in fluidised bed electrolyte reactor illustrates in Figure 8-140 shows current decrements.

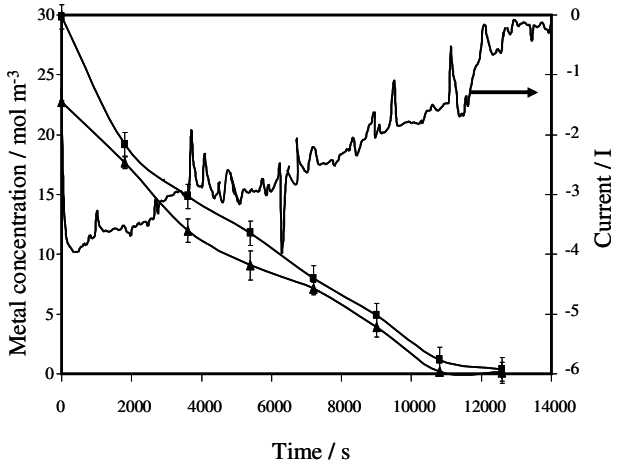

Figure 8-138. Time dependence of the Zn^{2+} ($[Zn^{2+}]_{t=0}$ = 30 mol m^{-3} ; ■)and Ni^{2+} ($[Ni^{2+}]_{t=0}$ = 18 mol m^{-3}; ▲) concentration and reduction current in fluidised bed electrolyte reactor with 590-840 μm glass beads, batch recycle model at – 1.10 V (SCE), flow rate = 6 x 10^{-5} m^3 s^{-1}.

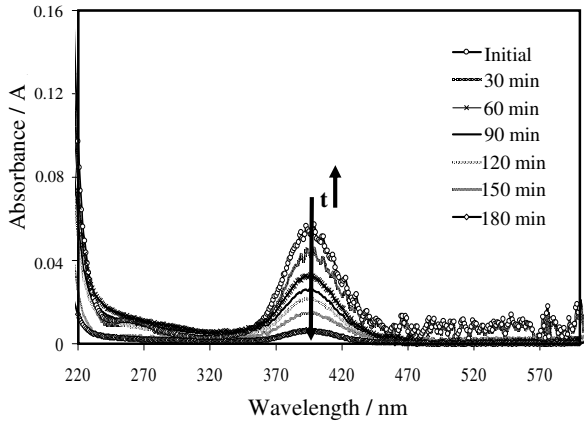

Figure 8-139. Absorbance of solution during Zn^{II}-Ni^{II} electro-co-deposition in fluidised bed electrolyte reactor at -1.10 V (SCE); path length 1 mm measured via fibre optics.

The overall charge required to reduce Zn^{2+} to Zn and Ni^{2+} to Ni (Q_c) in the catholyte reservoir could be calculated from the concentration:

$$Q_c = 2 \cdot V_c \cdot F \cdot (c_0 - c) \qquad [8\text{-}53]$$

V_c is the volume of the catholyte.

The charge supplied by the potentiostat (Q_I) could be calculated from the current:

$$Q_I = \int I \, dt \qquad [8\text{-}54]$$

The overall charge yields (Q_{eff}) could be estimated by:

$$Q_{eff} = Q_c / Q_I \qquad [8\text{-}55]$$

Charge yields for zinc-nickel electro-co-deposition decreased from ca. 0.85±0.01 with time (Figure 8-141) due to the small increases in the time-dependent catholyte pH to values above ca. 3.25, caused by protons produced by anodic oxygen evolution, resulting in the increase of ratio of proton to sodium ion transport through the membrane with time. This produced an

increase in the partial current densities for hydrogen evolution at the cathode. However, a bigger spike of pH increment would be possible provided longer time taken to recover a more concentrated Zn^{II}-Ni^{II} solution. In this case, the NaOH additions to the anolyte or the addition of buffer such as boric acid (HBO_3) should be considered as alternatives to control the catholyte pH. It was envisaged that a more complicated model involving the cathode surface pH changes are required as being investigated experimentally by Deligianni and Romankiw [36] and Ji et al. [11] for Ni-Fe electro-co-deposition and Ni electrodeposition respectively.

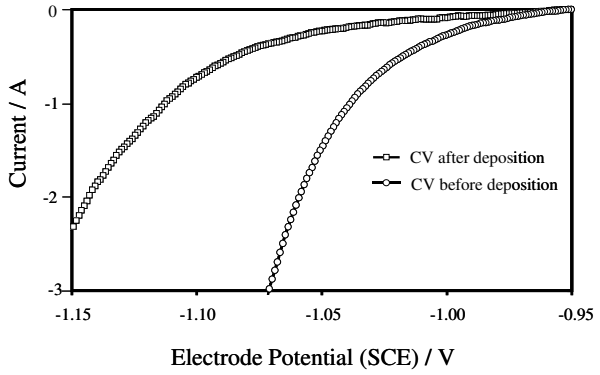

Figure 8-140. Linear sweep voltammetry for Zn^{II}-Ni^{II} electro-co-deposition in fluidised bed electrolyte reactor; (○) and (□) represent linear sweep voltammetry before and after electro-co-deposition.

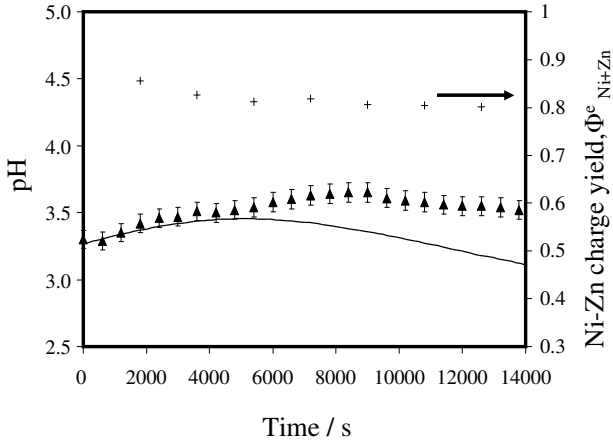

Figure 8-141. Time dependences of catholyte pH (▲) with 2% errors for each reading; (---) is the predicted catholyte pH; Ni-Zn charge yield, Φ^{e}_{Zn+Ni} (+).

Predicted boundary layer profiles for each species are presented in Figure 8-142. The most noteworthy feature of the plot is the concentration decrement of Zn^{2+} and Ni^{2+} in the solution at the diffusion layer. In addition, the figures illustrate the pH changes and Na^{+} concentration as a function of boundary layer thickness. The pH of the surface of the electrode increases steadily with the depleting thinkness of the boundry layers.

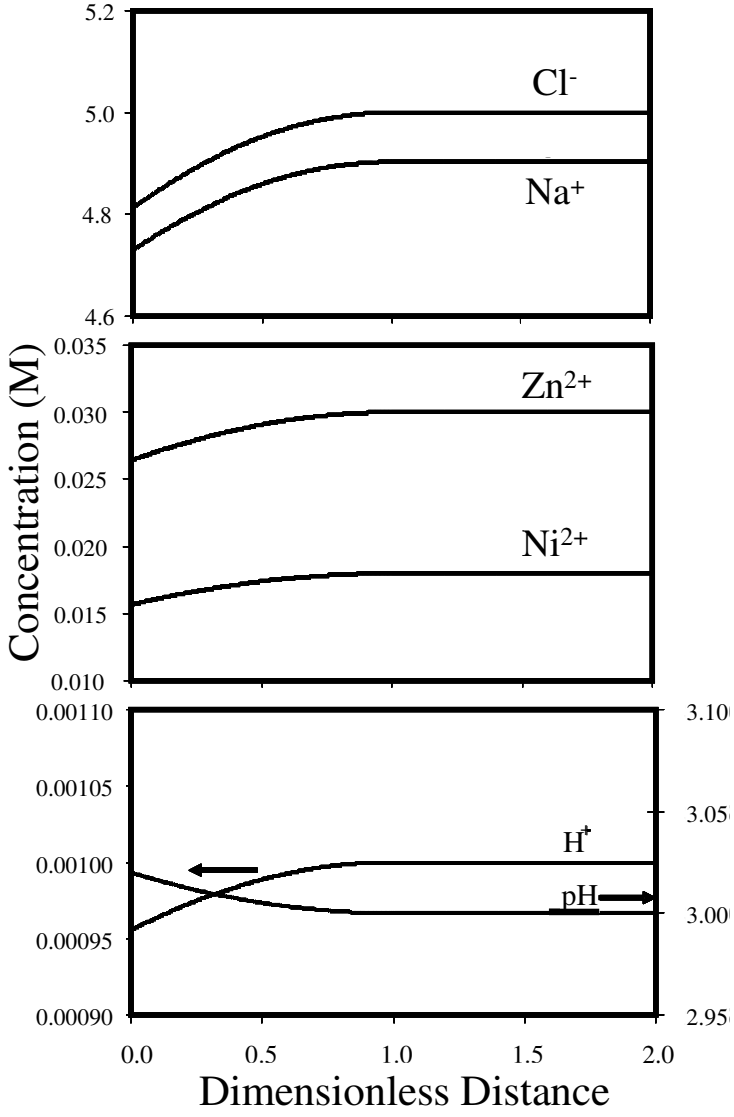

Figure 8-142. Boundary layer concentration profiles for Zn^{2+}, Ni^{2+}, Cl^-, Na^+, H^+ as predicted by the mass transfer model.

Assumed the conversion per pass was small ca. 0.3, the predicted flux from the concentration gradients at the electrode (Figure 8-142), integrated over the area enable comparison with experimental results for Zn^{2+} and Ni^{2+} depletion rates in the batch recycle reactor (Figure 8-143).

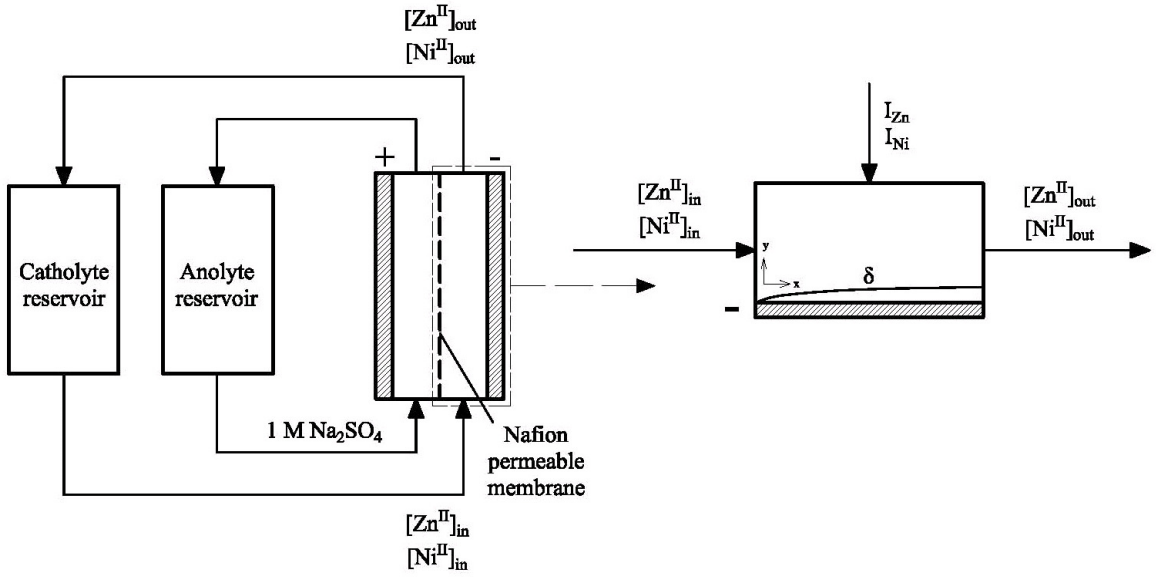

Figure 8-143. Magnification of the cathode boundary layer of the fluidised bed electrolyte reactor.

The predicted partial current density for Zn (j_{Zn}) was 55.28 A m^{-2} which was greater than that for Ni (j_{Ni} = 46.32 A m^{-2}), as reflected in the experimental data for Zn^{II}- Ni^{II} concentrations depleted in a fluidised bed electrolyte with a nickel mesh cathode (Figure 8-138). At electrode potential of -1.10 V (SCE), the total current density was ca. 120 A m^{-2} for which (j_{Zn} = 52 A m^{-2}, j_{Ni}= 45 A m^{-2} and j_{H2} = 24.28 A m^{-2}). A good approximation was achieved between the experimental and predicted partial current density of each species with a small deviation of 0.07±0.01 recorded. In addition, the predicted potential drop across the anolyte, membrane and catholyte was very small (Appendix E(d)) resulted in cell voltage, U_{cell} of 3.0 V and was successfuly validated experimentally (as reported in section 8.8).

8.9. Chapter Summary

The ultimate challenge of achieving efficient zinc-nickel electro-co-deposition was due to the competing process of hydrogen evolution. In addition to the bulk proton concentration in solution, H^+ ions were the product of anodic oxygen evolution and will diffuse from the anolyte to the catholyte and subsequently be reduced to hydrogen, thereby decreasing zinc-nickel reduction charge yields. Despite the thermodynamic predictions from Zn-Cl-H_2O and Ni-Cl-H_2O potential-pH diagram of the hydrogen overpotential being much larger than that of zinc and nickel reversible, zinc-nickel can still be electrodeposited in aqueous HCl with high charge efficiencies ca. 0.85 due to careful potentiostatic control (-1.10 V (SCE)) operated in a membrane separated fluidised bed electrolyte electrochemical reactor incorporating nickel mesh cathode, Ti/Ta_2O_5-IrO_2 anode and cation permeable membrane which basically allowed the migration of protons (H^+) and Na^+. Concentrations <50 mol m^{-3} of Zn^{2+} and Ni^{2+} ions in 4 kmol m^{-3} HCl + 1 kmol m^{-3} NaCl diluted to pH 3.25 which allowed precipitation of '$Fe(OH)_3$' were successfully reduced to a Ni-Zn alloy. The small decrease in the charge yield from 0.85 as a function of time resulted from the time-dependent decrease in catholyte pH, due to anodic oxygen evolution causing the partial proton current density through the membrane to increase with time. As a result, model incorporating anolyte and catholyte material balances were developed to evaluate on catholyte pH changes which shows insignificant pH increment for the reactor operated for ca. 3 hours that successfully recovered the alloy to analytically undetectable concentrations. In addition, the one dimensional mathematical model which considered the potential and concentration profiles in the cathode | electrolyte boundary layer for conditions in which migration and convective diffusion all contribute to overall transport rates, showed concentration decays of Zn^{2+} and Ni^{2+} in the solution at the diffusion layer in agreement with the larger process in an electrochemical reactor.

8.10. References

[1] Kelsall, G.H. and Williams, R.A., 1991, Electrochemical Behavior of Ferrosilicides (Fe_xSi) in Neutral and Alkaline Aqueous Electrolytes. I. Thermodynamics of Fe-Si-H_2O Systems at 298 K. *J. Electrochem. Soc*., 138 (4): 951-957.

[2] Mechelhoff, M., 2008, Electrochemical Investigation of Electrocoagulation Reactors for Water Purification. Ph.D. Thesis, Chemical Engineering, Imperial College London.

[3] Bard, A.J., Parsons, R. and Jordan, J., 1985, Standard potentials in aqueous solutions, Marcel Dekker, New York.

[4] Ji, J. and Cooper, W.C., 1996, Nickel speciation in aqueous chloride solutions. *Electrochim. Acta*, 41 (9): 1549-1560.

[5] Schlesinger, M. and Paunovic, M., 2010, Modern Electroplating, 5th ed., John Wiley & Sons, New York, 176-179.

[6] Lee, M.S. and Nam, S.H., 2009, Chemical Equilibria of Nickel Chloride in HCl Solution at 25°C. *Bull. Korean Chem. Soc*., 30(10): 2203-2207.

[7] Fleischmann, M. and Saraby-Reintjes, A., 1984, The Simultaneous Deposition of Nickel and Hydrogen on Vitreous Carbon. *Electrochim. Acta*, 29 (69): 69-75.

[8] Sillen, L.G. and Martell, A.E., 1971, Stability Constants of Metal-Ion Complexes, Supplement No. 1, Special Publication No. 25, p. 173. The Chemical Society, London.

[9] Piatti, R.C.V., Arvía, A.J. and Podestá, J.J., 1969, The electrochemical kinetic behaviour of nickel in acid aqueous solutions containing chloride and perchlorate ions. *Electrochim. Acta*, 14 (7): 541-560.

[10] Lide, D.R., 2004, CRC Handbook of Chemistry and Physics, 85th Ed.. CRC Press.

[11] Ji, J., Cooper, W.C., Dreisinger, D.B. and Peters, E., 1995, Surface pH measurements during nickel electrodeposition. *J. App. Electrochem*., 25 (7): 642.

[12] Kelsall, G.H., Guerra, E., Li, G. and Bestetti, M., 2000, Model of Local Current Efficiencies and Specific Electrical Energy Consumptions in Zinc Electrowinning Cells. *ECS Trans.,* 326-337.

[13] Mathias, M.F., Villa, C.M. and Chapman, T.W., 1990, A model of zinc-nickel alloy electrodeposition in an industrial-scale cell. *J. App. Electrochem*., 20:1-10.

[14] Baes, C.F. and Mesmer, R.E., 1976, The Hydrolysis of Cations, John Wiley & Sons, New York.

[15] Beshore, A.C., Flori, B. J., Schade, G. and O'Keefe, T.J., 1987, Nucleation and growth of zinc electrodeposited from acidic zinc solutions. *J. App. Electrochem.*, 17 (4): 765-772.

[16] Frazer, E.J. and Lwin, T., 1987, Identification of optimum conditions for zinc electrowinning in high-purity synthetic electrolytes. *J. App. Electrochem.*, 17 (3): 453-462.

[17] Karahan, I.H. and Guder, H.S., 2009, Electrodeposition and properties of Zn, Zn-Ni, Zn-Fe and Zn-Fe-Ni alloys from acidic chloride-sulphate electrolytes. *Trans.- Ins. of Metal Finish.*, 87: 155-158.

[18] Lin, Y.P. and Selman, J.R., 1999, Electrodeposition of Corrosion-Resistant Ni-Zn Alloy. I. Cyclic Voltammetric Study. *J. Electrochem. Soc.*, 140 (5): 1299.

[19] Wu, Z., Fedrizzi, L. and Bonora, P.L., 1996, Electrochemical studies of zinc-nickel codeposition in chloride baths. *Surf.& Coatings Tech.*, 85 (3): 170-174.

[20] Barton, G.W. and Scott, A.C., 1994, Industrial applications of a mathematical model for the zinc electrowinning process. *J. App. Electrochem.*, 24 (5): 377.

[21] Cornell, A., 2002, Electrode Reactions in the Chlorate Process. Ph.D. Thesis, Royal Institute of Technology, Stockholm.

[22] Pushpavanam, M. and Balakrishnan, T.D., 1996, Zinc-nickel alloy deposition in the presence of citrate ions. *App. Electrochem.*, 26 (10): 1065-1070.

[23] Kharlamov, V.V., Vakka, A.B., Azarchenko, T.L. and Vagramyan, T.A., 1991, Anomalous deposition of a zinc-nickel alloy from sulfate-chloride baths. *Soviet Electrochem.*, 27 (8): 938.

[24] Lin, Y.P. and Selman, J.R., 1999, Electrodeposition of Corrosion-Resistant Ni-Zn Alloy. I. Cyclic Voltammetric Study. *J. Electrochem. Soc.*, 140 (5): 1299.

[25] Mathias, M.F. and Chapman, T.W., 1990, A Zinc-Nickel alloy electrodeposition kinetics model from thickness and composition measurements on the rotating disc electrode. *J. Electrochem. Soc.*, 137 (1): 102-110.

[26] Gijsbers, H.F.M. and Janssen, L.J.J., 1989, Distribution of mass transfer over a 0.5-m-tall hydrogen-evolving electrode. *J. App. Electrochem.*, 19 (5): 637-648.

[27] Mathias, M.F. and Chapman, T.W., 1990, A Zinc-Nickel alloy electrodeposition kinetics model from thickness and composition measurements on the rotating disc electrode. *J. Electrochem. Soc.*, 137 (1): 102-110.

[28] Newman, J.S., 1991, Electrochemical Systems. Prentice Hall, 2nd ed.: 255.

[29] Swathirajan, S.S., 1987, Electrodeposition of zinc + nickel alloy phases and electrochemical stripping studies of the anomalous codeposition of zinc. *J. Electroanal. Chim. & Interfacial Electrochem.*, 221 (1): 211.

[30] Bockris, J.O.M. and Potter, E.C., 1952, The mechanism of hydrogen evolution at nickel cathodes in aqueous solutions. *J. Electrochem. Soc.*, 99 (4): 169-186.

[31] Gijsbers, H.F.M. and Janssen, L.J.J., 1989, Distribution of mass transfer over a 0.5-m-tall hydrogen-evolving electrode. *J. App. Electrochem.*, 19 (5): 637-648.

[32] Santana, A.I.C., Diaz, S.L., Barcia, O.E. and Mattos, O.R., 2009, A Kinetic Study on Nickel Electrodeposition from Sulfate Acid Solutions. *J. Electrochem. Soc.*, 156 (8): 326-330.

[33] Kelsall, G.H. and Kovaleva, A., 2010, Electrodeposition of Nickel from Sulfamate Effluents. *ECS Trans.*, 28 (6): 317-327.

[34] Delacourt, C. and Newman, J., 2008, Mathematical Modeling of a Cation-Exchange Membrane Containing Two Cations. *J. Electrochem. Soc.*, 155 (11): B1210-B1217.

[35] Mathias, M.F. and Chapman, T.W., 1990, A Zinc-Nickel alloy electrodeposition kinetics model from thickness and composition measurements on the rotating disc electrode. *J. Electrochem. Soc.*, 137 (1): 102-110.

[36] Deligianni, H. and Romankiw, L.T., 1993, In situ surface pH measurement during electrolysis using a rotating pH electrode. *IBM J. Res. and Dev.*, 37 (2): 85.

9. CONCLUSIONS

9.1. General Conclusions

This chapter provides a summary of the results of a novel process to recover metals selectively by electrodeposition by pumping aqueous acidic chloride solutions produced by leaching of shredded WEEE through the potentiostatically controlled cathode of an electrochemical reactor. The WEEE solutions containing various metals in 4 kmol m^{-3} HCl + 1 kmol m^{-3} NaCl prepared from the previous project at Imperial College London contained low concentrations of precious metals, including Ag, Au and base metals such as Cu, Sn, Ni, Zn, Al and Fe which Cu predominates. Mathematical models to predict the micro- and reactor-scale kinetics for the electrochemical reduction of Au, Cu, Sn and Zn were developed and successfully validated experimentally.

9.2. Gold Electrodeposition

Electrodeposition from low concentrations of dissolved gold requires electrodes with high mass transport rate coefficients and specific surface areas to increase cross-sectional current densities and optimise capital and operating costs. Experimental results demonstrated that the CPBE was suitable for the recovery of Au from the leach solution produced by leaching metals from WEEE. Concentrations < 0.5 mol m^{-3} (< 10^2 g m^{-3}) of $AuCl_4^-$ and $AuCl_2^-$ ions in 4 kmol m^{-3} HCl + 1 kmol m^{-3} NaCl in aqueous electrolyte were successfully reduced to elemental gold in CPBE of 0.5-1.0 mm graphite particles, in an electrochemical reactor incorporating a cation-permeable membrane and operated in bath recycle mode. The temporal decay of the solution absorbance of $AuCl_4^-$ ions at 312 nm was recorded successfully on-line by quartz flow cell connected to a UV-visible spectrophotometer using fibre optics, enabling its time dependent concentration to be determined in real time. Total dissolved gold concentrations were effectively determined by inductively-coupled plasma optical emission spectrophotometry (ICP-OES) which complemented the results obtain from the UV spectrophotometer.

Depletion to concentrations < 5×10^{-3} mol m^{-3} (< 1 g m^{-3}) was under mass transport controlled at an applied potential of +0.20 V (SCE) and specific electrical energy consumption (SEEC) of ca. 800-1300 kW h (tonne Au)$^{-1}$ for cell voltages (U_{cell}) of 2.0-3.0 V and fractional charge yield of ca. 0.95. Assuming 5p per kWh, the electrical energy cost was around £65 $tonne^{-1}$ of Au removed, which was a very small fraction of the price of Au (about £33.3×10^6 $tonne^{-1}$), so

that Au recovery was both technically and economically viable.

The reduction of $AuCl_4^-$ at a Pt rotating disc electrode (RDE) was successfully modelled using the multi-step mechanism for reduction of $AuCl_4^-$ ions which was proposed by Cheng et al. [60]. In addition, the results from the reactor experiments were modelled in terms of a mass transport controlled reaction in a plug flow electrochemical reactor operated in batch recycle with a continuous stirred tank reservoir. SEM images confirmed that adherent and coherent Au deposits were achieved with CPBE for Au deposition under mass transport control at +0.20 V (SCE), whereas Au deposition from aqueous chloride aqueous solutions has been reported in the literature as producing dendrites.

9.3. Copper Electrodeposition

The presence of mixed oxidation state copper(II-I) species was confirmed by absorption spectra in the visible light region . However, cyclic voltammetry analysis revealed that they had no significant effect on the electrodeposition of Cu.

The kinetic model for multi-step reduction of $AuCl_4^-$ ions was modified successfully to describe the reduction of $CuCl_2^-$ (aq) at a Pt rotating disc electrode (RDE) and validated experimentally. As copper is the dominant element in WEEE and hence in the leach solution, its electrodeposition was investigated using an electrochemical reactor with a Ti/Ta_2O_5-IrO_2 anode, cation-permeable membrane and a Ti mesh cathode in a fluidised bed of 590-840 μm glass beads to enhance mass transfer rates and to improve copper deposit morphologies. The experimental results demonstrated the feasibility of using both the mesh cathode in a fluidised bed of inert particles and at lower Cu^{II} concentrations (<10 mol m^{-3}) utilising the circulating particulate bed reactor for the electrodeposition of copper from the chloride leach solution. Copper purities of > 99.79 % (0.21 % Ag) determined by ICP analysis were achieved with charge yields of > 0.90 and specific electrical energy consumptions of ca. 2000 kW h $tonne^{-1}$, while depleting copper ion concentrations from 470 to ca. 35 mol m^{-3} with the reactor containing fluidised bed electrolyte operated under mass transport control at -0.45 V (SCE). The possibility of recovering even a fraction of this investment represents a saving for the company involved. For example, the price of copper (purity of > 99.99%) which is predominant in shredded electronic scrap is currently around ca. £5.5k $tonne^{-1}$. A comparison with the specific electrical energy consumption (SEEC) of electrodeposition, which is ca. 2×10^3 kW h $tonne^{-1}$ of copper, corresponding to £100 $tonne^{-1}$ (assuming 5p per kWh), shows that recovery of copper from WEEE leaching solutions is likely to be economically viable,

depending on the capital investment requirements. In addition, adequate Cu deposit morphologies, reaction rates and charge yields can be achieved, providing the electrode potential, flow rate and initial dissolved copper concentration were carefully controlled.

Concentrations of 15 mol m^{-3} of $CuCl_2(aq)$ and $CuCl_2^-$ ions in aqueous 4 kmol m^{-3} HCl + 1 kmol m^{-3} NaCl were reduced successfully to elemental copper (purities >99.99%) in a circulating bed of 0.5-1 mm graphite particles, in an electrochemical reactor incorporating a cation- permeable membrane and operated in bath recycle mode. Decreasing the cathode feeder potential from -0.36 to -0.40 V (SCE) increased the Cu deposition rate, but decreased charge yields from 0.70 to 0.58, due to H_2 evolution resulting from the potential distribution across the circulating particulate bed cathode. Depletion to concentrations $< 5\times10^{-3}$ mol m^{-3} was kinetic and mass transport controlled at an applied potential of -0.38 V (SCE). Specific electrical energy consumptions of ca. 800-1300 kW h (tonne Cu)$^{-1}$ were achieved for cell voltages of 2.0-3.0 V and fractional charge yields of ca. 0.7. Furthermore, SEM images confirmed that adherent and coherent Cu deposits showing 'cauliflower' structure were achieved with circulating particulate bed reactor for Cu deposition under mixed kinetic and mass transport control.

9.4. Selective Electrodeposition of Tin from Aqueous Sn^{IV}-Pb^{II} Chloride Solutions

Attempts to determine the molar ratio of tin chloro-complexes ($Sn^{IV}Cl_6^{4-}$: $Sn^{II}Cl_4^{2-}$) using a rotating ring-disc (RRDE) electrode failed due to the growth of oxide layers on the ring electrode that suppressed the oxidation of Sn^{II} to Sn^{IV}. Results of experiments with a rotating vitreous carbon cathode confirmed predictions of a kinetic model that a small (100 mV) electrode potential window existed within which to achieve selective electrodeposition of tin from synthetic Sn^{IV}-Pb^{II} aqueous chloride solutions at a molar ratio of 3:1, leaving a solution from which Pb could be electrodeposited subsequently.

The experiments demonstrated the feasibility of using the mesh cathode in a fluidised bed of inert particles to recover Sn selectively from synthetic Sn^{IV}-Pb^{II} aqueous chloride solutions. It was observed that Sn^{IV} could be depeleted to analytically undetectable concentrations (Sn purity > 99.99%) and recovered with relatively high charge yield of 0.85 at an applied cathode potential of -0.60 V (SCE) and a flow rate of 0.85 dm^3 min^{-1} with for spherical particles for $0.4 < Re_p < 500$ with diameters ranged from 590 - 840 μm. However, selective deposition of tin could not be achieved under transport control as hydrogen evolution and alloy formation might occur, with the rate of overall reduction of $SnCl_6^{2-}$ ions to elemental tin

becoming totally mass transport controlled at potentials <- 0.65 V (SHE). Increasing the overpotential of tin deposition resulted in increasing hydrogen evolution partial current densities, so decreasing the charge yields for Sn^{IV} reduction. In addition, the high charge yields reflected tin's well known high hydrogen overpotential ($j_0 < 10^{-6}$ A m^{-2}, Tafel slope = 120 mV $decade^{-1}$).

9.5. Nickel—Zinc Electro-co-deposition

Al^{III}, Fe^{II}, Zn^{II} and Ni^{II} remained in solutions after recovery of Au, Cu, Sn and Pb from the WEEE leachate. Although unlike for Al, it is possible to electrodeposit Fe from aqueous solutions, it was decided to add NaOH (+ air) increase the pH to ca. 3.25 to precipitate '$Fe(OH)_3$', which was recovered by filtration. This option also enabled subsequent electro-co-deposition of Ni and Zn with high charge yields, as the higher pH decreased the driving force for hydrogen evolution.

Results of potentiodynamic experiments with a rotating vitreous carbon disc electrode in 30 mol m^{-3} aqueous zinc(II) chloride solutions of pH 3.25, implied that nickel could be deposited with a charge yield of ca. 0.46 at -1.1 V (SCE). At more negative potentials, deposition kinetics decreased, probably due to passivation by $Ni(OH)_2$ as a result of an increase in local pH caused by hydrogen evolution. The ultimate challenge of achieving efficient zinc-nickel electro-co-deposition is limited by the competing process of hydrogen evolution. In addition to the bulk proton concentration in solution, H^+ ions are the product of anodic oxygen evolution and will diffuse from the anolyte to the catholyte and subsequently be reduced to hydrogen, thereby decreasing zinc-nickel charge yields. Despite the thermodynamic predictions from Zn-Cl-H_2O and Ni-Cl-H_2O potential-pH diagrams, zinc-nickel alloys could still be electrodeposited in aqueous HCl with charge efficiencies ca. 0.85, due to the hydrogen overpotential being much larger than that of zinc and nickel reversible electrode potential. This was achieved by potentiostatic control of a nickel mesh cathode at -1.10 V (SCE) operated in a fluidised bed electrolyte electrochemical reactor incorporating a Ti/Ta_2O_5-IrO_2 anode and cation-permeable membrane which allows the migration of H^+ and Na^+ ions.

Concentrations <50 mol m^{-3} of Zn^{2+} and Ni^{2+} ions in 4 kmol m^{-3} HCl + 1 kmol m^{-3} NaCl, diluted to pH 3.25 to enable precipitation of '$Fe(OH)_3$', were successfully reduced to a Ni-Zn alloy. The small decrease in the charge yield from 0.85 as a function of time resulted from the time-dependent decrease in catholyte pH, due to anodic oxygen evolution causing the partial proton current density through the membrane to increase with time. As a result, a model

incorporating anolyte and catholyte material balances were developed to evaluate catholyte pH changes which predicted insignificant pH increment when the reactor was operated for ca. 3 hours. Hence, the alloy was deposited successfully and the solutions depleted to analytically undetectable concentrations.

In addition, a one dimensional mathematical model was developed to predict the potential and concentration profiles in the cathode | electrolyte boundary layer for conditions in which migration and convective diffusion contribute to overall transport rates. This enabled predictions of the concentration decays of Zn^{2+} and Ni^{2+} in the solution at the diffusion layer, which was successfully validated experimentally.

9.6. Chapter Summary

Having summarised the conclusions of each chapter, Figure 10-144 outlines the proposed protocol for sequential selective metal recovery from WEEE leach solutions. Electrodeposition from low concentrations of dissolved metals requires electrodes with high mass transport rate coefficients and specific surface areas to increase cross-sectional current densities and optimise capital and operating costs (Detailed costing given in Appendix G). Therefore, to recover gold from solutions with concentrations < 10 mol m^{-3} in the WEEE leachate, a three-dimensional cathode was used consisting of a circulating particulate bed of 0.5-1.0 mm diameter graphite particles, on which ($Au^{III}Cl_4^-$ + $Au^{I}Cl_2^-$) ions were reduced at mass transport controlled. As copper is the dominant element in WEEE and hence in the leach solution, its electrodeposition was investigated using a two-dimensional electrode electrochemical reactor with a Ti/Ta_2O_5-IrO_2 anode, cation-permeable membrane and a Ti mesh cathode in a fluidised bed of 590-840 μm glass beads to enhance mass transfer rates and to improve copper deposit morphologies. While depleting Cu^{II} concentrations from 470 to 35 mol m^{-3}, copper purities of > 99.79 % were achieved with a charge yield of 0.90 and specific electrical energy consumptions of ca. 2000 kW h $tonne^{-1}$. In addition, the circulating particulate bed cathode depleted solutions rapidly from 15 mol m^{-3} Cu^{II} to ca. 100 ppm under mixed kinetic and mass transport control. Experiments with a rotating vitreous carbon cathode confirmed predictions from a kinetic model for a small electrode potential window within which to achieve selective electrodeposition of tin from synthetic Sn^{IV}-Pb^{II} aqueous chloride solutions, from which Pb could be electrodeposited subsequently. However, the rate of tin deposition could not be controlled by transport control, as H_2 evolution and alloy formation then occurred, with the rate of overall reduction of $SnCl_6^{2-}$ ions to elemental tin becoming

totally mass transport controlled at potentials < -0.65 V (SHE). Finally, residual dissolved metals, such as Al^{III}, Fe^{II}, Zn^{II} and Ni^{II} in the WEEE leachate, which cannot be electrodeposited in aqueous chloride media at pH 0 were treated separately. NaOH (+ air) was added to the solutions to increase the pH to ca. 3.25 in order to precipitate '$Fe(OH)_3$', which was recovered subsequently by filtration. This option also enabled subsequent electro-co-deposition of Ni and Zn with high charge yields, as the higher pH decreased the driving force for H_2 evolution. Other species such as Al can be precipitate as $Al(OH)_3$ at a higher pH ; Ba and Mg which were present as trace metals in the WEE leachate will be recycled in the electrolyte back into the leaching process.

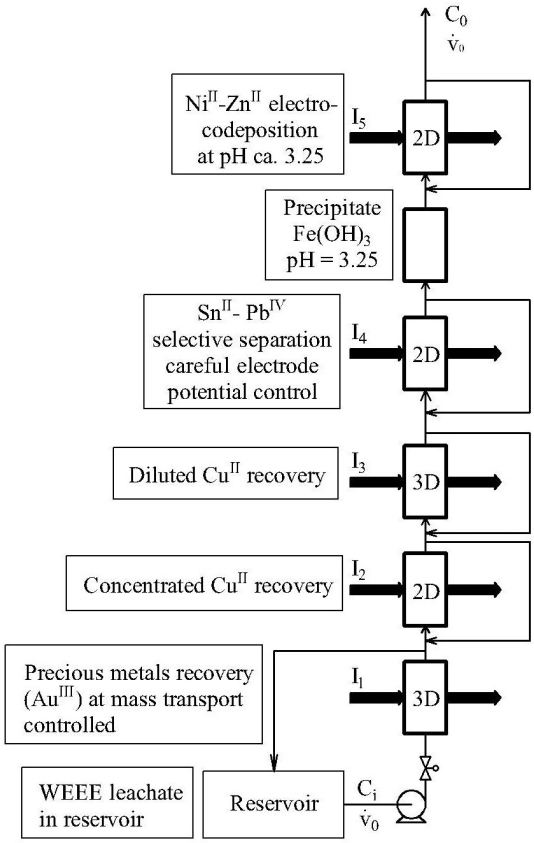

Figure 10-144. Schematic of electrochemical process for sequential selective metal recovery from multi-metal containing WEEE leachate.

10. FUTURE WORK

Before technology transfer could be considered, the following developments are needed:

10.1. Experimental Work

(a) In the light of the present study, the WEEE leachate originated from printed circuit boards (PCBs) containing Sn-Pb solders. The current PCB fabrication mainly uses Cu-Ag solders; therefore, electro-refining is needed to purify the Cu and produce a valuable Ag product. The search of appropriate solvent and anion are required e.g. the whole lattice could be dissolved in H_2SO_4 and Cu can be electro-refined. During the process, copper dissolves into the solution ($E^{\ominus}_{Cu^{2+}/Cu}(\text{SHE}) = 0.341$ V) from the anodes leaving the impurities i.e. Ag as an anode slime, which normally sinks to the bottom of the cell ($E^{\ominus}_{Ag^{+}/Ag}(\text{SHE}) = 0.800$ V).

(b) The rotating ring-disc experiment failed to assist in determining the molar ratio of tin chloro-complexes due to the growth of oxide layers, which suppressed further Sn^{II} oxidation to Sn^{IV} at the ring. It is probable that higher concentrations of HCl may obviate the problem, enabling the ring electrode to function as a reliable sensor.

(c) The nature of the electrodeposit morphology could be studied in detail as a function of electrode potential, concentration, pH and inclusion / exclusion of hydrogen.

(d) Nickel-zinc interactions: Mechanistic studies would be useful to highlight the intricate details of these processes, enabling their control. The effects of total cation concentration, pH as well as complexation effects will require detailed studies.

(e) Other species which are not recovered from the WEEE leachate, such as Al can be precipitate as $Al(OH)_3$ at a higher pH ; Ba and Mg which were present as trace metals in the WEE leachate will be recycled in the electrolyte back into the leaching process.

(f) The design of the circulating particulate bed electrochemical reactor (CPBE) could be improved by the following modifications:

- The angle to the horizontal of the inclined edge of the descending bed should be increased, thus, lowering the possibility of stationary particles, which resulted in dead areas.

- Pressure taps could be incorporated to measure the pressure drop across the bed.
- A weir with a removable separator should be added at the top of the reactor to allow the particles to be removed and replaced continuously.

(g) Detailed investigations of the performance of the anode and the ion-permeable membrane lifetime experiments should be undertaken.

10.2. Modelling Work

(a) Due to the complexity and significant interactions between the model variables, parameter estimation and optimisation by Global Sensitivity Analysis could be used to improve the model predictions.

(b) The (micro-) kinetics models developed for Cu reduction, Sn^{IV}-Pb^{II} selective deposition and Ni-Zn electro-co-deposition although giving reasonable results could be extended to allow a more full description of the processes such that one model would describe adequately the deposition process from various concentrations of solution.

(c) To improve the one-dimensional Zn-Ni interactions model, the effects of bubble evolution on mass transfer rates could be included and the effects of varying the diffusion boundary layer thickness could be investigated.

APPENDICES

Appendix A: Nernst Equations for all metals, used in the calculation for Figure 3.13 (pp 68)

Cu^{II} to Cu^{I}: $$CuCl_2(aq) + e^- \rightleftharpoons CuCl_2^- \quad [11\text{-}1]$$

$$E_{CuCl_2(aq)/CuCl_2^-}\textbf{(SHE) / V} = 0.4917 + 0.0591\log\left\{\left(CuCl_2(aq)\right)/\left(CuCl_2^-\right)\right\}$$

Cu^{I} to Cu(s): $$CuCl_2^- + e^- \rightleftharpoons Cu + 2Cl^- \quad [11\text{-}2]$$

$$E_{CuCl_2^-/Cu}\textbf{(SHE) / V} = 0.2240 + 0.0591\log\left(CuCl_2^-\right) - 0.118\log\left(Cl^-\right)$$

Sn^{IV} to Sn^{II}: $$SnCl_6^{2-} + 2e^- \rightleftharpoons SnCl_4^{2-} + 2Cl^- \quad [11\text{-}3]$$

$$E_{SnCl_6^{2-}/SnCl_4^{2-}}\textbf{(SHE) / V} = 0.1928 + 0.0296\log\left\{\left(SnCl_6^{2-}\right)/\left(SnCl_4^{2-}\right)\right\} - 0.059\log\left(Cl^-\right)$$

Sn^{II} to Sn(s): $$SnCl_4^{2-} + 2e^- \rightleftharpoons Sn + 4Cl^- \quad [11\text{-}4]$$

$$E_{SnCl_4^{2-}/Sn}\textbf{(SHE) / V} = -0.141 + 0.0296\log\left(SnCl_4^{2-}\right) - 0.118\log\left(Cl^-\right)$$

Au^{III} to Au^{I}: $$AuCl_4^- + 2e^- \rightleftharpoons AuCl_2^- + 2Cl^- \quad [11\text{-}5]$$

$$E_{AuCl_4^-/AuCl_2^-}\textbf{(SHE) / V} = 0.9251 + 0.0296\log\left\{\left(AuCl_4^-\right)/\left(AuCl_2^-\right)\right\} - 0.059\log\left(Cl^-\right)$$

Au^{I} to Au(s) $$AuCl_2^- + e^- \rightleftharpoons Au + 2Cl^- \quad [11\text{-}6]$$

$$E_{AuCl_2^-/Au}\textbf{(SHE) / V} = 1.152 + 0.059\log\left(AuCl_2^-\right) - 0.118\log\left(Cl^-\right)$$

Pd^{IV} to Pd^{II}: $$PdCl_6^{2-} + 2e^- \rightleftharpoons PdCl_4^{2-} + 2Cl^- \quad [11\text{-}7]$$

$$E_{PdCl_6^{2-}/PdCl_4^{2-}}\textbf{(SHE) / V} = 1.2915 + 0.0296\log\left\{\left(PdCl_6^{2-}\right)/\left(PdCl_4^{2-}\right)\right\} - 0.059\log\left(Cl^-\right)$$

Pd^{II} to Pd(s): $$PdCl_4^{2-} + 2e^- \rightleftharpoons Pd + 4Cl^- \quad [11\text{-}8]$$

$$E_{PdCl_4^{2-}/Pd}\textbf{(SHE) / V} = 0.5551 + 0.0296\log\left(PdCl_4^{2-}\right) - 0.118\log\left(Cl^-\right)$$

Pb^{II} to Pb(s): $$PbCl_4^{2-} + 2e^- \rightleftharpoons Pb + 4Cl^- \quad [11\text{-}9]$$

$$E_{PbCl_4^{2-}/Pb}\textbf{(SHE) / V} = -0.1735 + 0.0296\log\left(PbCl_4^{2-}\right) - 0.118\log\left(Cl^-\right)$$

Ag^I to Ag(s): $$AgCl_4^{3-} + e^- \rightleftharpoons Ag + 4Cl^- \quad [11\text{-}10]$$

$$E_{AgCl_4^{3-}/Ag}\textbf{(SHE) / V} = 0.4743 + 0.059\log\left(AgCl_4^{3-}\right) - 0.237\log\left(Cl^-\right)$$

H_2 evolution: $$2H^+ + 2e^- \rightleftharpoons H_2 \quad [11\text{-}11]$$

$$E_{H^+/H_2}(\text{SHE}) / \text{V} = 0 - 0.059\,pH + 0.0296\log\left(P_{H_2}\right)$$

Cl_2 evolution:

$$2Cl^- \rightleftharpoons Cl_{2(aq)} + 2e^- \quad [11\text{-}12]$$

$$E_{Cl_2/Cl^-}(\text{SHE}) / \text{V} = 1.396 + 0.0296\log\left(Cl_2(aq)\right) - 0.059\log\left(Cl^-\right)$$

Pt^{IV} to Pt^{II}: $$PtCl_6^{2-} + 2e^- \rightleftharpoons PtCl_4^{2-} + 2Cl^- \quad [11\text{-}13]$$

$$E_{PtCl_6^{2-}/PtCl_4^{2-}}\textbf{(SHE) / V} = 0.7297 + 0.0296\log\left\{\left(PtCl_6^{2-}\right)/\left(PtCl_4^{2-}\right)\right\} - 0.059\log\left(Cl^-\right)$$

Pt^{II} to Pt(s): $$PtCl_4^{2-} + 2e^- \rightleftharpoons Pt + 4Cl^- \quad [11\text{-}14]$$

$$E_{PtCl_4^{2-}/Pt}\textbf{(SHE) / V} = 0.8438 + 0.0296\log\left(PtCl_4^{2-}\right) - 0.118\log\left(Cl^-\right)$$

Mg^{II} to Mg(s): $$Mg^{2+} + 2e^- \rightleftharpoons Mg \quad [11\text{-}15]$$

$$E_{Mg^{2+}/Mg}\textbf{(SHE) / V} = -2.3558 + 0.0296\log\left(Mg^{2+}\right)$$

Al^{III} to Al(s): $$Al^{3+} + 3e^- \rightleftharpoons Al \quad [11\text{-}16]$$

$$E_{Al^{3+}/Al}\textbf{(SHE) / V} = -1.794 + 0.019\log\left(Al^{3+}\right)$$

Zn^{II} to Zn(s): $$Zn^{2+} + 2e^- \rightleftharpoons Zn \quad [11\text{-}17]$$

$$E_{Zn^{2+}/Zn}\textbf{(SHE) / V} = -0.7626 + 0.0296\log\left(Zn^{2+}\right)$$

Ni^{II} to Ni(s): $$Ni^{2+} + 2e^- \rightleftharpoons Ni \quad [11\text{-}18]$$

$$E_{Ni^{2+}/Ni}\textbf{(SHE) / V} = -0.2405 + 0.0296\log\left(Ni^{2+}\right)$$

Cr^{III} to Cr^{II}: $$Cr^{3+} + e^- \rightleftharpoons Cr^{2+} \quad [11\text{-}19]$$

$$E_{Cr^{3+}/Cr^{2+}}\textbf{(SHE) / V} = -0.424 + 0.059\log\left(Cr^{3+}/Cr^{2+}\right)$$

Cr^{II} to Cr(s): $$Cr^{2+} + 2e^- \rightleftharpoons Cr \qquad [11\text{-}20]$$

$$E_{Cr^{2+}/Cr}\textbf{(SHE) / V} = -0.90 + 0.0296\log\left(Cr^{2+}\right)$$

Ba^{II} to Ba(s): $$Ba^{2+} + 2e^- \rightleftharpoons Ba \qquad [11\text{-}21]$$

$$E_{Ba^{2+}/Ba}\textbf{(SHE) / V} = -2.92 + 0.0296\log\left(Ba^{2+}\right)$$

Fe^{III} to Fe^{II}: $$Fe^{3+} + e^- \rightleftharpoons Fe^{2+} \qquad [11\text{-}22]$$

$$E_{Fe^{3+}/Fe^{2+}}\textbf{(SHE) / V} = 0.775 + 0.059\log\left(Fe^{3+}/Fe^{2+}\right)$$

Fe^{II} to Fe(s): $$Fe^{2+} + 2e^- \rightleftharpoons Fe \qquad [11\text{-}23]$$

$$E_{Fe^{2+}/Fe}\textbf{(SHE) / V} = -0.474 + 0.0296\log\left(Fe^{2+}\right)$$

Metal Ion	**Concentration assumed in Nernst equation / mol m^{-3}**
Cu	50
Sn, Pb, Al, Zn, Fe	10
Pd, Au, Ag, Pt, Mg, Cr, Co, Ni, Ba	0.1

Appendix B: Thermodynamic data

The following thermodynamic values are extracted from Bard et.al. [1]. At some points NBS [2], data is added, this is indicated with a '*'. Note that not all of the data is used in calculations, however useful for future references.

(a) Thermodynamic values for the Cl-H_2O system

Species	ΔH_f^0 / J mol^{-1}	S^0 / J mol^{-1} K^{-1}	ΔG_f^0 / J mol^{-1}
Cl^-	-166853.3	56.701	-131056
$Cl_{2\,(g)}$	0	222.957	0
$Cl_{2\,(aq)}$	-21090	127.6	7200
Cl_3^-	-197740	138.9	-120080
ClO^-	-107100	42	-36800
$ClO_{2\,(aq)}$	74900	173.2	117600
ClO_2^-	-66500	101.3	17200
ClO_3^-	-99200	162.3	-3300
ClO_4^-	-129330	182	-8620
HCl	-166853	56.701	-131056
HClO	-120.9	142	-79900
$HClO_2$	-51900	188.3	5900
$HClO_3$	-99200	162.3	-3300
$HClO_4$	-129330	182	-8620
$HClO_4 \cdot H_2O$ (c)	-382210	-	-
OH^-	-229994	-10.75	-157293
H_2O	-285830	69.91	-237178
H_2	0	130.684	0
H^+	0	0	0
O_2	0	205.028	0

O_2 (aq)	-11700	110.9	16300

(b) Thermodynamic values for the Au-Cl-H_2O system

Species	**ΔH_f^0 / J mol^{-1}**	**S^0 / J mol^{-1} K^{-1}**	**ΔG_f^0 / J mol^{-1}**
Au(c)	0	47.40	0
Au^+	-	-	176000
Au^{3+}	-	-	440000
AuO_3^{3-}	-	-	-51900
H AuO_3^{2-}	-	-	-142000
H_2 AuO_3^-	-	-	-218000
$Au(OH)_3$(c)	-424700	190	-317000
$Au(OH)_3$	-	-	-283500
AuCl(c)	-35000	-	-
$AuCl_2^-$	-	-	-151000
$AuCl_3$(c)	-118000	-	-
$AuCl_3.2H_2O$(c)	-715000	-	-
$AuCl_4^-$	-322000	267	-234600

(c) Thermodynamic values for the Cu-Cl-H_2O system

Species	**ΔH_f^0 / J mol^{-1}**	**S^0 / J mol^{-1} K^{-1}**	**ΔG_f^0 / J mol^{-1}**
Cu_2O	-171000	92.52	-148100
CuO (c)	-161.7	42.7	-134000
$Cu(OH)_2$ (ppt)	-443700	87.2	-359500
$HCuO_2^-$	-	-	-258900
CuO_2^{2-}	-	-	-183900
Cu (c)	0	33.2	0
Cu^+ (aq)	72100	41	50300

$Cu^{2+}(aq)$	65780	-97.2	65700
CuCl(c)	-137000	87.6	-119800
$CuCl_2(c)$	-218300	108.2	-173900
$CuCl_2 \cdot 2H_2O$	-1158500	151	-993900
$CuCl_2^-(aq)^*$	-	-	-240100
$CuCl_3^{2-}(aq)^*$	-	-	-376000
$CuCl^{+*}$	-	-	-68200

Extra:

$CuCl_2^-(aq)^{**}$	-277820	214.5	-245880
$CuCl_3^{2-}(aq)^{**}$	-457880	214.9	-373330
$CuCl_4^{3-}(aq)^{**}$	-	-	-506900
$CuCl^{+**}$	-93480	-0.2	-69770

** Experimental data provided by Wang et al. [3].

Stability constants for species critical to the speciation of Cu^{II} in aqueous chloride solutions at 25°C.

Reaction	**Log_{10} *K***
$Cu^{2+} + Cl^- \rightleftharpoons CuCl^{+***}$	0.83± 0.09
$Cu^{2+} + 2Cl^- \rightleftharpoons CuCl_2(aq)^{***}$	0.60± 0.30

*** Experimental data provided by Powell et al.[4].

(d) Thermodynamic values for the Ag-Cl-H_2O system

Species	**ΔH_f^0 / J mol^{-1}**	**S^0 / J mol^{-1} K^{-1}**	**ΔG_f^0 / J mol^{-1}**
Ag(c)	0	42.57	0
Ag	0	0	37260
Ag^+	105630	72.71	77160
Ag^{2+}	268740	-87.91	269160
AgO^+	0	0	225630

AgO^-	0	0	22980
$Ag_2O(c)$	-31060	121.39	-11220
$Ag_2O_2(c)$	-24280	27630	117.21
$Ag(OH)_2^-$	0	0	260370
AgOH	-124.470	61.95	-80210
AgO(c)	-12140	57.35	14650
$Ag_2O_3(c)$	33910	100.46	121390
$AgO_2(c)$	-30060	184.02	-10990
AgCl(c)	-127130	96.28	-109860
AgCl	-61610	129.35	-54160
$AgCl_2^-$	-245300	231.49	-215580
$AgCl_3^{2-}$	0	0	-345970
$AgCl_4^{3-}$	0	0	-478460
$AgClO_2(c)$	8790	134.62	75770
$AgClO_2$	38930	174.14	94180
$AgClO_3(c)$	-25530	149.86	71200
$AgClO_3$	6280	235.25	73760
$AgClO_4(c)$	-31140	163.25	88320
$AgClO_4$	-23780	254.93	68520

(e) Thermodynamic values for the Sn-Cl-H_2O system

Species	**ΔH_f^0 / J mol^{-1}**	**S^0 / J mol^{-1} K^{-1}**	**ΔG_f^0 / J mol^{-1}**
Sn(gray)	2500	44.8	4600
Sn(white)	0	51.5	0
Sn^{2+}	-	-22.7	-27240

Sn^{4+}	-	-	2720
SnO(c)	-286000	56.6	-257000
SnO_2(c)	-580700	52.3	-519900
SnO_2(Hydr.white)	-	-	-477500
$Sn(OH)^+$	-	-	255600
$HSnO_2^-$	-	-	-410000
SnO_3^{2-}	-	-	-574965
$Sn(OH)_6^{2-}$	-	-	-1299000
H_2 $Sn(OH)_6$(c)	-	-	-1433300
$SnCl_2$	-349800	(122.6)	-302100
$SnCl^+$	-	106.7	-167900
$SnCl_3$-*	-	-	-431500
$SnCl_4^{2-}$*	-	-	-560900
$SnCl_6^{2-}$*	-	-	-785800

(f) Thermodynamic values for the Pb-Cl-H_2O system

Species	**ΔH_f^0 / J mol^{-1}**	**S^0 / J mol^{-1} K^{-1}**	**ΔG_f^0 / J mol^{-1}**
Pb(c)	0	64.89	0
Pb^{2+}	1630	21.3	-24310
Pb^{4+}	-	-	302500
PbO(yellow)	-217900	69.4	-188500
PbO(red)	-219200	67.8	-189300
PbO(hydrate,.white)	-	-	-183720

$Pb_2O_3(c)$	-	-	-411.780
$Pb_3O_4(c)$		211	-616200
$PbO_2(c)$	-276650	76.6	-218990
$PbO_{1.57}(c)$	-	-	-211210
$H\ PbO_2^-$	-	-	-339000
$Pb(OH)_2(c)$	-514600	88	-420900
PbO_4^{4-}	-	-	-282100
$PbCl^+$	-	-	-164810
$PbCl_2(c)$	-359200	136.4	-313970
$PbCl_3^{-*}$	-	-	-426300

Stability constants for species critical to the speciation of Pb^{IV} in aqueous chloride solutions at 25°C.

Reaction	**$Log_{10}\ K^o$**
$Pb^{2+} + 4Cl^- \rightleftharpoons PbCl_4^{2-*}$	1.46

(g) Thermodynamic values for the Zn-Cl-H_2O system

Species	**ΔH_f^0 / J mol^{-1}**	**S^0 / J mol^{-1} K^{-1}**	**ΔG_f^0 / J mol^{-1}**
Zn	0	41.6	0
Zn^{2+}	-152804	-107.53	-147160
$ZnOH^+$	-	-	-342000
$Zn(OH)_2(aq)$	-613880	-133	-461620
$Zn(OH)_2$ (undiss)	-	-	-521000
$Zn(OH)_2$ (β)	-641910	81.2	-553590
$Zn(OH)_2$ (s)	-643250	81.6	-555130

ZnO(c)	-348280	43.64	-318320
$Zn(OH)_4^{2-}$	-	-	-877400
$ZN(NH3)_4^{2+}$	577000	301	-307000

Stability constants for species critical to the speciation of Zn^{II} in aqueous chloride solutions at 25°C.

Reaction	**$Log_{10}\ K^{\circ}$**
$Zn^{2+} + Cl^- \rightleftarrows ZnCl^{+}$ ***	0.48

*** Data provided by Mathias et al. [8].

(h) Thermodynamic values for the Ni-Cl-H_2O system

Species	**ΔH_f^0 / J mol^{-1}**	**S^0 / J mol^{-1} K^{-1}**	**ΔG_f^0 / J mol^{-1}**
Ni	0	30.1	0
$Ni(OH)_3$ (c)	-667300	81.6	-541800
Ni^{2+}	-64000	-159	-46400
$Ni(OH)_2$(c)	-538100	79	-453100
NiO(c)	-244000	38.6	-216000
$Ni(OH)_3^-$	-	-	-586269

Stability constants for species critical to the speciation of Zn^{II} in aqueous chloride solutions at 25°C.

Reaction	**$Log_{10}\ K^{\circ}$**
$Ni^{2+} + Cl^- \rightleftarrows NiCl^{+}$ ***	-0.17

***Data provided by Ji and Cooper [9].

Appendix C: Reactions and E values

Here for every metal-chloride system a set of descriptive chemical and electrochemical reactions; the equation for the potential (vs. SHE) and the standard potential is given:

(a) Cl-H_2O system

Chemical reactions

$$Cl_2 + H_2O \rightleftharpoons H^+ + Cl^- + HClO(aq) \quad [11\text{-}24]$$

$$\log\left\{\left(\frac{HClO}{Cl_2(aq)}\right)\right\} = \log K + pH - \log\left(Cl^-\right)$$

$$HClO(aq) \rightleftharpoons H^+ + ClO^- \quad [11\text{-}25]$$

$$\log\left\{\left(\frac{ClO^-}{HClO}\right)\right\} = \log K + pH$$

Electrochemical reactions

$$Cl_2(aq) + 2e^- \rightleftharpoons 2Cl^- \quad [11\text{-}26]$$

$$E_{Cl_2/Cl^-}(\text{SHE}) / \text{V} = 1.396 + 0.0296\log\left(Cl_2(aq)\right) - 0.059\log\left(Cl^-\right)$$

$$Cl_2(g) + 2e^- \rightleftharpoons 2Cl^- \quad [11\text{-}27]$$

$$E_{Cl_2/Cl^-}(\text{SHE}) / \text{V} = 1.358 + 0.0296\log P\left(Cl_2\right) - 0.059\log\left(Cl^-\right)$$

$$HClO + H^+ + 2e^- \rightleftharpoons Cl^- + H_2O \quad [11\text{-}28]$$

$$E_{Cl^-/HClO}(\text{SHE}) / \text{V} = 1.494 - 0.0296\,pH + 0.0296\log\left(HClO\right) - 0.0296\log\left(Cl^-\right)$$

$$2HClO + 2H^+ + 2e^- \rightleftharpoons Cl_2(g) + 2H_2O \quad [11\text{-}29]$$

$$E_{Cl_2(g)/HClO}(\text{SHE}) / \text{V} = 1.630 - 0.0592\,pH + 0.0592\log\left(HClO\right) - 0.0296\log P\left(Cl_2\right)$$

$$ClO^- + 2H^+ + 2e^- \rightleftharpoons Cl^- + H_2O \quad [11\text{-}30]$$

$$E_{Cl^-/ClO^-}(\text{SHE}) / \text{V} = 1.718 - 0.0592\,pH + 0.0296\log\left(ClO^-\right) - 0.0296\log\left(Cl^-\right)$$

(b) Au-Cl-H_2O system

Chemical reactions

$$Au^{+} + 2Cl^{-} \rightleftharpoons AuCl_2^{-} \quad [11\text{-}31]$$

$$Au^{3+} + 4Cl^{-} \rightleftharpoons AuCl_4^{-} \quad [11\text{-}32]$$

Electrochemical reactions

$$AuCl_4^{-} + 2e^{-} \rightleftharpoons AuCl_2^{-} + 2Cl^{-} \quad [11\text{-}33]$$

$$E_{AuCl_4^{-}/AuCl_2^{-}}\textbf{(SHE) / V} = 0.9251 + 0.0296\log\left\{\left(AuCl_4^{-}\right)/\left(AuCl_2^{-}\right)\right\} - 0.059\log\left(Cl^{-}\right)$$

$$AuCl_2^{-} + e^{-} \rightleftharpoons Au + 2Cl^{-} \quad [11\text{-}34]$$

$$E_{AuCl_2^{-}/Au}\textbf{(SHE) / V} = 1.152 + 0.059\log\left(AuCl_2^{-}\right) - 0.118\log\left(Cl^{-}\right)$$

$$Au(OH)_3(c) + 3H^{+} + 2Cl^{-} + 2e^{-} \rightleftharpoons AuCl_2^{-} + 3H_2O \quad [11\text{-}35]$$

$$E_{AuCl_2^{-}/Au(OH)_3(c)}\textbf{(SHE) / V} = 1.469 - 0.0887\,pH + 0.0592\log\left(Cl^{-}\right) - 0.0296\log\left(AuCl_2^{-}\right)$$

(c) Cu-Cl-H_2O system

Chemical reactions

General: $$Cu^{+} + xCl^{-} \rightleftharpoons \left(CuCl_x\right)^{1-x}$$

$$Cu^{+} + Cl^{-} \rightleftharpoons CuCl(s) \quad [11\text{-}36]$$

$$Cu^{+} + 2Cl^{-} \rightleftharpoons CuCl_2^{-} \quad [11\text{-}37]$$

General: $$Cu^{2+} + xCl^{-} \rightleftharpoons \left(CuCl_x\right)^{2-x}$$

$$Cu^{2+} + Cl^{-} \rightleftharpoons CuCl^{+} \quad [11\text{-}38]$$

$$Cu^{2+} + 2Cl^{-} \rightleftharpoons CuCl_2(s) \quad [11\text{-}39]$$

Electrochemical reactions

$$CuCl_2(aq) + e^{-} \rightleftharpoons CuCl_2^{-} \quad [11\text{-}40]$$

$$E_{CuCl_2(aq)/CuCl_2^-}\textbf{(SHE) / V} = 0.4917 + 0.0591\log\left\{\left(CuCl_2(aq)\right)/\left(CuCl_2^-\right)\right\}$$

$$CuCl_2^- + e^- \rightleftharpoons Cu + 2Cl^- \qquad [11\text{-}41]$$

$$E_{CuCl_2^-/Cu}\textbf{(SHE) / V} = 0.2240 + 0.0591\log\left(CuCl_2^-\right) - 0.118\log\left(Cl^-\right)$$

(d) Ag-Cl-H_2O system

Chemical reactions

General: $$Ag^+ + xCl^- \rightleftharpoons \left(AgCl_x\right)^{1-x}$$

$$Ag^+ + Cl^- \rightleftharpoons AgCl(s) \qquad [11\text{-}42]$$

$$Ag^+ + Cl^- \rightleftharpoons AgCl(aq) \qquad [11\text{-}43]$$

$$Ag^+ + 2Cl^- \rightleftharpoons AgCl_2^- \qquad [11\text{-}44]$$

$$Ag^+ + 3Cl^- \rightleftharpoons AgCl_3^{2-} \qquad [11\text{-}45]$$

$$Ag^+ + 4Cl^- \rightleftharpoons AgCl_4^{3-} \qquad [11\text{-}46]$$

Electrochemical reactions

$$AgCl_2^- + e^- \rightleftharpoons Ag(s) + 2Cl^- \qquad [11\text{-}47]$$

$$E_{AgCl_4^{3-}/Ag}\textbf{(SHE) / V} = 0.4823 + 0.059\log\left(AgCl_2^-\right) - 0.1183\log\left(Cl^-\right)$$

$$AgCl_3^{2-} + e^- \rightleftharpoons Ag(s) + 3Cl^- \qquad [11\text{-}48]$$

$$E_{AgCl_4^{3-}/Ag}\textbf{(SHE) / V} = 0.4892 + 0.059\log\left(AgCl_3^{2-}\right) - 0.1775\log\left(Cl^-\right)$$

$$AgCl_4^{3-} + e^- \rightleftharpoons Ag + 4Cl^- \qquad [11\text{-}49]$$

$$E_{AgCl_4^{3-}/Ag}\textbf{(SHE) / V} = 0.4743 + 0.059\log\left(AgCl_4^{3-}\right) - 0.237\log\left(Cl^-\right)$$

(e) Sn-Cl-H_2O system

Chemical reactions

General: $$Sn^{2+} + xCl^- \rightleftharpoons \left(SnCl_x\right)^{2-x}$$

$$Sn^{2+} + Cl^- \rightleftharpoons SnCl^+ \quad [11\text{-}50]$$

$$Sn^{2+} + 2Cl^- \rightleftharpoons SnCl(s) \quad [11\text{-}51]$$

$$Sn^{2+} + 3Cl^- \rightleftharpoons SnCl_3^- \quad [11\text{-}52]$$

$$Sn^{2+} + 4Cl^- \rightleftharpoons SnCl_4^{2-} \quad [11\text{-}53]$$

General: $Sn^{2+} + xCl^- \rightleftharpoons \left(SnCl_x\right)^{4-x}$

$$Sn^{4+} + 4Cl^- \rightleftharpoons SnCl_4(s) \quad [11\text{-}54]$$

$$Sn^{4+} + 6Cl^- \rightleftharpoons SnCl_6^{2-} \quad [11\text{-}55]$$

Electrochemical reactions

$$SnCl_6^{2-} + 2e^- \rightleftharpoons SnCl_4^{2-} + 2Cl^- \quad [11\text{-}56]$$

$$E_{SnCl_6^{2-}/SnCl_4^{2-}}\textbf{(SHE) / V} = 0.1928 + 0.0296\log\left\{\left(SnCl_6^{2-}\right)/\left(SnCl_4^{2-}\right)\right\} - 0.059\log\left(Cl^-\right)$$

$$SnCl_4^{2-} + 2e^- \rightleftharpoons Sn + 4Cl^- \quad [11\text{-}57]$$

$$E_{SnCl_4^{2-}/Sn}\textbf{(SHE) / V} = -0.141 + 0.0296\log\left(SnCl_4^{2-}\right) - 0.118\log\left(Cl^-\right)$$

(f) Pb-Cl-H_2O system

Chemical reactions

General: $Pb^{2+} + xCl^- \rightleftharpoons \left(PbCl_x\right)^{2-x}$

$$Pb^{2+} + Cl^- \rightleftharpoons PbCl^+ \quad [11\text{-}58]$$

$$Pb^{2+} + 2Cl^- \rightleftharpoons PbCl_2(s) \quad [11\text{-}59]$$

$$Pb^{2+} + 2Cl^- \rightleftharpoons PbCl_2(aq) \quad [11\text{-}60]$$

$$Pb^{2+} + 3Cl^- \rightleftharpoons PbCl_3^- \quad [11\text{-}61]$$

$$Pb^{2+} + 4Cl^- \rightleftharpoons PbCl_4^{2-} \quad [11\text{-}62]$$

Electrochemical reactions

$$Pb^{2+} + 2e^- \rightleftharpoons Pb(s) \quad [11\text{-}63]$$

$$E_{Pb^{2+}/Pb}\textbf{(SHE)}\ /\ \textbf{V} = 1.2323 + 0.0296\log\left(Pb^{2+}\right)$$

$$PbCl^{+} + 2e^{-} \rightleftharpoons Pb(s) + Cl^{-} \qquad [11\text{-}64]$$

$$E_{PbCl^{+}/Pb}\textbf{(SHE)}\ /\ \textbf{V} = 0.5042 + 0.0296\log\left(PbCl^{+}\right) + 0.0296\log\left(Cl^{-}\right)$$

$$PbCl_2(aq) + 2e^{-} \rightleftharpoons Pb(s) + 2Cl^{-} \qquad [11\text{-}65]$$

$$E_{PbCl_2(aq)/Pb}\textbf{(SHE)}\ /\ \textbf{V} = -0.1282 + 0.0296\log\left(PbCl_2(aq)\right) + 0.0592\log\left(Cl^{-}\right)$$

$$PbCl_3^{-} + 2e^{-} \rightleftharpoons Pb(s) + 3Cl^{-} \qquad [11\text{-}66]$$

$$E_{PbCl_3^{-}/Pb}\textbf{(SHE)}\ /\ \textbf{V} = -0.1717 + 0.0296\log\left(PbCl_3^{-}\right) - 0.0887\log\left(Cl^{-}\right)$$

$$PbCl_4^{2-} + 2e^{-} \rightleftharpoons Pb + 4Cl^{-} \qquad [11\text{-}67]$$

$$E_{PbCl_4^{2-}/Pb}\textbf{(SHE)}\ /\ \textbf{V} = -0.1735 + 0.0296\log\left(PbCl_4^{2-}\right) - 0.118\log\left(Cl^{-}\right)$$

Appendix D: Mechanistic studies

Below are for the gold and copper electrode reactions a detailed reaction mechanism is developed. This leads to an equation for the current density vs. potential distribution specific for the postulated reaction mechanism [5].

(a) Electrochemical Reduction of $AuCl_n^-$ Ions from Aqueous Electrolytes

$$AuCl_4^- + 2e^- \rightleftharpoons AuCl_2^- + 2Cl^- \quad [11\text{-}68]$$

$$E_{AuCl_4^-/AuCl_2^-}(\text{SHE}) \ / \text{V} = 0.9251 + 0.0296\log\{(AuCl_4^-)/(AuCl_2^-)\} - 0.059\log(Cl^-) \quad [11\text{-}69]$$

$$AuCl_2^- + e^- \rightleftharpoons Au + 2Cl^- \quad [11\text{-}70]$$

$$E_{AuCl_2^-/Au}(\text{SHE}) \ / \text{V} = 1.152 + 0.0296\log(AuCl_2^-) - 0.118\log(Cl^-) \quad [11\text{-}71]$$

The overall reaction: $$AuCl_4^- + 3e^- \rightleftharpoons Au + 4Cl^- \quad [11\text{-}72]$$

$$E_{AuCl_4^-/Au}(\text{SHE}) \ / \text{V} = 1.0006 + 0.0197\log(AuCl_4^-) - 0.0789\log(Cl^-) \quad [11\text{-}73]$$

$$3AuCl_2^- \rightleftharpoons AuCl_4^- + Au + 2Cl^- \quad [11\text{-}74]$$

$$3\log(AuCl_2^-) = -7.66 + \log(AuCl_4^-) + 2\log(Cl^-) \quad [11\text{-}75]$$

Proposed Reduction Mechanism:

$$Au^{III}Cl_4^- \underset{k_m}{\overset{k_m}{\rightleftharpoons}} Au^{III}Cl_4^-(surface) \quad [11\text{-}76]$$

As the potential of zero charge is 1.002 V (SHE), at potentials positive of that value, the electrode is likely to adsorb negatively charged species, so for fractional coverage of the electrode with species of oxidation state +2 (θ_{II}) and +1 (θ_I), one possible sequence of elementary steps in the overall reaction is:

$$Au^{III}Cl_4^-(surface) + e^- \underset{k_{a1}}{\overset{k_{c1}}{\rightleftharpoons}} \overset{\theta_{II}}{Au^{II}Cl_3^-(ads)} + Cl^-(surface) \quad [11\text{-}77]$$

$$\overset{\theta_{II}}{Au^{II}Cl_3^-(ads)} + e^- \underset{k_{a2}}{\overset{k_{c2}}{\rightleftharpoons}} \overset{\theta_I}{Au^{I}Cl_2^-(ads)} + Cl^-(surface) \quad [11\text{-}78]$$

$$\overset{\theta_I}{Au^{I}Cl_2^-(ads)} \underset{k_{ads}}{\overset{k_{des}}{\rightleftharpoons}} AuCl_2^-(surface) \quad [11\text{-}79]$$

$$AuCl_2^-(surface) \underset{k_m}{\overset{k_m}{\rightleftarrows}} AuCl_2^- \quad [11\text{-}80]$$

$$Au^{I}Cl_2^-(ads) + e^- \underset{k_{a3}}{\overset{k_{c3}}{\rightleftarrows}} Au^{\theta_I} + 2Cl^-(surface)^{(1-\theta_I-\theta_{II})} \quad [11\text{-}81]$$

From a (steady state) mass balance on $AuCl_4^-$ (surf), $AuCl_2^-$ (surf), Au(II) and Au(I) adsorbed intermediates:

$$\frac{d[Au^{III}Cl_4^-]_{x=0}}{dt} = k_m[Au^{III}Cl_4^-] - k_m[Au^{III}Cl_4^-]_{x=0} + k_{a1}\Gamma\theta_{II}[Cl^-] - k_{c1}[Au^{III}Cl_4^-]_{x=0} = 0 \quad [11\text{-}82]$$

$$\frac{d\theta_{II}}{dt} = k_{c1}[Au^{III}Cl_4^-]_{x=0} - k_{a1}\Gamma\theta_{II}[Cl^-] - k_{c2}\Gamma\theta_{II} + k_{a2}\Gamma\theta_I[Cl^-] = 0 \quad [11\text{-}83]$$

$$\frac{d[Au^{I}Cl_2^-]_{x=0}}{dt} = k_{des}\Gamma\theta_I[Cl^-] - k_{ads}(1-\theta_I-\theta_{II})[Au^{I}Cl_2^-]_{x=0} - k_m[Au^{I}Cl_2^-]_{x=0} + k_m[Au^{I}Cl_2^-] = 0 \quad [11\text{-}84]$$

$$\begin{aligned}\frac{d\theta_I}{dt} &= k_{c2}\Gamma\theta_{II} - k_{a2}\Gamma\theta_I[Cl^-] - k_{c3}\Gamma\theta_I + k_{a3}\Gamma(1-\theta_I-\theta_{II})[Cl^-] \\ &\quad - k_{des}\Gamma\theta_I[Cl^-] + k_{ads}(1-\theta_I-\theta_{II})\left[AuCl_2^-\right]_{x=0} = 0\end{aligned} \quad [11\text{-}85]$$

The total current density is given by:

$$j = -F\left(k_{c1}[AuCl_4^-]_{x=0} + k_{c2}\Gamma\theta_{II} + k_{c3}\Gamma\theta_I - k_{a1}\Gamma\theta_{II} - k_{a2}\Gamma\theta_I - k_{a3}(1-\theta_I-\theta_{II})[Cl^-]^2\right) \quad [11\text{-}86]$$

$$j = -F\left(k_{c1}[AuCl_4^-]_{x=0} + (k_{c2}-k_{a1})\Gamma\theta_{II} + (k_{c3}-k_{a2})\Gamma\theta_I - k_{a3}(1-\theta_I-\theta_{II})\Gamma[Cl^-]^2\right) \quad [11\text{-}87]$$

where:
$$k_{ci} = k_{i,0}\exp\left\{\frac{-\alpha_i F(E-E_i^0)}{RT}\right\} \quad [11\text{-}88]$$

and:
$$k_{ai} = k_{i,0}\exp\left\{\frac{\alpha_i F(E-E_i^0)}{RT}\right\} \quad [11\text{-}89]$$

Appendix E: Maple™ code

(a) Mechanism of electrochemical reduction of $AuCl_n^-$

The code in Maple TM was developed from the proposed reduction mechanisms of $AuCl_n^-$ [5]

Maple™ Codes

```
Restart:
with(geometry):
with(plots):
PDEtools[declare](prime=x):
```

(i) Declare Constants

(ii) Declare Concentrations

```
cl := 5000:          chloride concentration (mol m-3)
au3 := 10:           gold(III) bulk concentration (mol m-3)
au1 := 0.01:         gold(I) bulk concentration (mol m-3)
Gamma:= 10:          number of adsorbed surface sites (mol m-3)
```

(iii) Calculate Equilibrium Electrode Potentials (SHE/V) at 298 K

```
e1 := simplify(0.9251+0.0296*log10((au3/1000)/(au1/1000))-0.0591*log10(cl/1000)):
e2 := simplify(1.152+0.0296*log10(au1/1000)-0.1183*log10(cl/1000)):
```

(iv) Calculate rate coefficients

```
k30b := 2e-9:  k20b := 2e-8:  k10b := 2e-8:  k30f := 4e-7:  k20f := 4e-7:  k10f := 6e-7:  kads:=
1e-8:  kdes := 1e-7:  km := 1e-5:

ka1 := k10b*exp((1-alpha1)*F*(E-e1)/(R*T)):
ka2 := k20b*exp((1-alpha2)*F*(E-e1)/(R*T)):
ka3 := k30b*exp((1-alpha3)*F*(E-e2)/(R*T)):
kc1 := k10f*exp(-alpha1*F*(E-e1)/(R*T)):
kc2 := k20f*exp(-alpha2*F*(E-e1)/(R*T)):
kc3 := k30f*exp(-alpha3*F*(E-e2)/(R*T)):
```

(v) Mass balance on $AuCl_4^-$ (surf), $AuCl_2^-$ (surf), Au(II) and Au(I) adsorbed intermediates:

```
eqn[1] := km*au3 - km*au3s + ka1*theta2*Gamma*(cl^2) - kc1*au3s*(1-theta1-theta2):

eqn[2] := kc1*au3s*(1-theta1-theta2) - ka1*theta2*Gamma*(cl^2) - kc2*theta2*Gamma +
ka2*theta1*Gamma*cl:

eqn[3] := kdes*theta1*Gamma*cl - kads*au1s - km*au1s + km*au1 :
```

```
eqn[4] := kc2*theta2*Gamma - ka2*theta1*Gamma*cl - kc3*theta1*Gamma + ka3*(1-theta1-theta2)*Gamma*cl - kdes*theta1*Gamma*cl + kads*au1s :
```

(vi) Solve numerical solution of the differential equation system using Maple's dsolve routine:

```
sol1:=solve({eqn[1], eqn[2], eqn[3], eqn[4]}, {au3s, au1s, theta1, theta2}):
```

(vii) Total current density

```
j := -F*(kc1*au3s*(1-theta1-theta2) + kc2*theta2*Gamma + kc3*theta1*Gamma - ka1*theta2*Gamma*(cl^2) - ka2*theta1*Gamma*cl - ka3*(1-theta1-theta2)*Gamma*cl):

jau3au2 := -F*(kc1*au3s*(1-theta1-theta2) - ka1*theta2*Gamma*(cl^2)):
jau2au1 := -F*(kc2*theta2*Gamma - ka2*theta1*Gamma*cl):
jau1au := -F*(kc3*theta1*Gamma- ka3*(1-theta1-theta2)*Gamma*cl):

j1:=subs(sol1,j):
j1au3au2:=subs(sol1,jau3au2):
j1au2au1:=subs(sol1,jau2au1):
j1au1au:=subs(sol1,jau1au):
authrees:=subs(sol1,au3s):auones:=subs(sol1,au1s):
thetaone:=subs(sol1,theta1):thetatwo:=subs(sol1,theta2):
```

(viii) Plot predicted electrode potential dependence of surface concentrations of $AuCl_4^-$ and $AuCl_2^-$ and fractional coverages of $Au^I(\theta_I)$ and $Au^{II}(\theta_{II})$ adsorbed species:

```
autwoads:= thetatwo*Gamma: auoneads:= thetaone*Gamma:

plot( [ authrees, autwoads, auoneads,auones], E=0..0.8, axesfont=[TIMES,9], labels=["E / V(SHE)","Au conc (mol/m3)"], labelfont=[TIMES,BOLD,9],title=("Potential-Au Distribution"),font=[TIMES,8],titlefont=[TIMES,BOLD,9],symbolsize=[7,10,10,7],color=[red,blue,green,black] , thickness=1, labeldirections=[horizontal, vertical] );
```

(b) Mechanism of electrochemical reduction of Cu^{II} in aqueous chloride solutions

The code in Maple™ was developed from the proposed reduction mechanisms of Cu^{II} in aqueous chloride solutions as presented in Chapter 6.

Maple™ Codes

```
Restart:
with(geometry):
with(plots):
```

```
PDEtools[declare](prime=x):
```

(i) Declare Constants

(ii) Declare Concentrations

```
cl:=5000:                chloride concentration (mol m-3)
cu2 := 5:                copper(II) bulk concentration (mol m-3)
cu1 := 0.001:            copper(I) bulk concentration (mol m-3)
```

(iii) Calculate Equilibrium Electrode Potentials (SHE/V) at 298 K

```
ee1 := evalf(0.4917+0.0591*log10((cu2)/(cu1))):
ee2 := evalf(0.224+0.0591*log10(cu1/1000)-0.1183*log10(cl/1000)):
```

(ix) Calculate rate coefficients

```
k10 := 1e-8: k20:=1e-8: kmcu:=1.98e-5:
ka1 := k10*exp((1-alpha1)*F*(e-ee1)/(R*T)):
ka2 := k20*exp((1-alpha2)*F*(e-ee2)/(R*T)):
kc1 := k10*exp(-alpha1*F*(e-ee1)/(R*T)):
kc2 := k20*exp(-alpha2*F*(e-ee2)/(R*T)):
```

(x) Mass balance on Cu^{II} surface concentration and Cu^{I} surface coverage

```
eqn[1] := (kmcu*cu2-kmcu*cu2s-kc1*cu2s):
eqn[2] :=kc1*cu2s-kc2*cu1s-kmcu*cu1s+kmcu*cu1:
```

(xi) Solve numerical solution of the differential equation system using Maple's dsolve routine:

```
sol1:=solve ({eqn[1], eqn[2]}, {cu2s, cu1s} ):
```

(xii) Total current density

```
j := -F*(kc1*cu2s+kc2*cu1s):j1:=subs(sol1,j):
```

(xiii) Plot model predictions of electrode potential dependence of Cu^{II} surface concentrations of Cu^{I} surface coverage

```
CuIIs:=cu2s:    coppertwo:=subs(sol1,CuIIs):
CuIs:=cu1s:     copperone:=subs(sol1,CuIs):
plot({copperone,coppertwo},e=-1..0.7,labels=["E","Cu(II)s"]);
```

(c) Mechanism of electrochemical reduction of Sn^{IV} Ions from Aqueous Chloride Electrolytes

The algorithm and mathematical codes presented here were used to model the Sn^{IV} ions from chlorides electrolytes for Sn^{IV}-Pb^{II} selective recovery as investigated in Chapter 7.

Maple™ Codes

```
Restart:
with(geometry):
with(plots):
PDEtools[declare](prime=x):
```

(iv) Declare Constants

(v) Declare Concentrations

```
cl:=5000:          chloride concentration (mol m-3)
sncl6 := 10:       tin(IV) bulk concentration (mol m-3)
sncl4 := 0.05:     tin(II) bulk concentration (mol m-3)
```

(vi) Calculate Equilibrium Electrode Potentials (SHE/V) at 298 K

```
ee1:=evalf(0.1928+(0.059/2)*log10(sncl6/sncl4)-0.059*log10(cl/1000));
ee2:=evalf(-0.1901+0.0296*log10(sncl4/1000)-2*0.059*log10(cl/1000));
```

(xiv) Calculate rate coefficients

```
k10 := 1e-10: k20:=5e-6: kmcu:=5.40e-5:
ka1 := k10*exp((1-alpha1)*F*(e-ee1)/(R*T)):
ka2 := k20*exp((1-alpha2)*F*(e-ee2)/(R*T)):
kc1 := k10*exp(-alpha1*F*(e-ee1)/(R*T)):
kc2 := k20*exp(-alpha2*F*(e-ee2)/(R*T)):
```

(xv) Mass balance on Sn^{IV} surface concentration and Sn^{II} surface coverage

```
eqn[1] := (kmcu*sncl6-kmcu*sncl6s-kc1*sncl6s):
eqn[2] :=kc1*sncl6s-kc2*sncl4s-kmcu*sncl4s+kmcu*sncl4:
```

(xvi) Solve numerical solution of the differential equation system using Maple's dsolve routine:

```
sol1:=solve ({eqn[1], eqn[2]}, {sncl6s, sncl41s} ):
```

(xvii) Total current density

```
j := -F*(kc1*sncl6s+kc2*sncl4s):j1:=subs(sol1,j):
```

(xviii) Plot model predictions of electrode potential dependence of Cu^{II} surface concentrations of Cu^{I} surface coverage

```
SnIVs:=sncl6s:    tinfour:=subs(sol1,SnIVs):
SnIIs:=sncl4s     tintwo:=subs(sol1,SnIIs):
plot({tinone,tintwo},e=-1..0.7,labels=["E","Sn(IV)s", "Sn(II)s"]):
```

(d) Modelling of dissolved nickel (II) and zinc (II) concentration and potential profiles in the cathode | electrolyte boundary layer.

The algorithm and the example of coding of MAPLE™ as per described in Chapter 8 are presented as below:

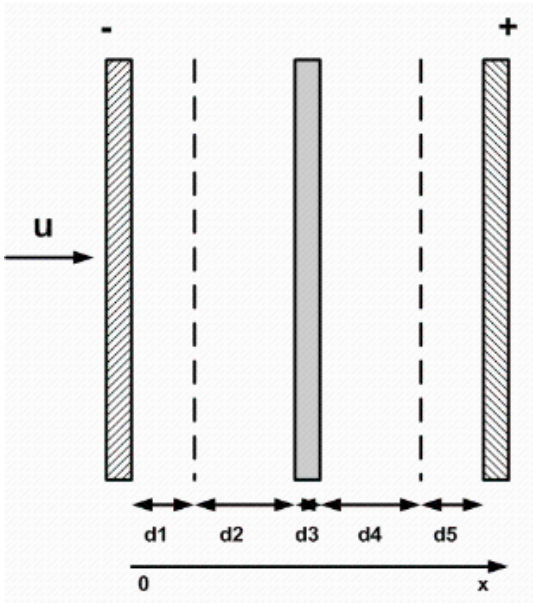

Parameters used in the Models

Symbols and their units are defined in the notation listing on pages 22-24.

Parameters	Values	Parameters	Values
F	96485	D_{Na^+}	1.33E-09
pH	3.25	D_{OH^-}	5.26E-09
T	298	$D_{Ni^{2+}}$	1.33E-9

R	8.314	D_{H^+}	9.31E-9
n_{Zn}	2	$D_{SO4^{2-}}$	1.07E-9
n_{Ni}	2	D_{Cl^-}	2.03E-9
n_{H2}	2	$D_{Na^+,m}$	1.33E-10
n_{O2}	4	$D_{H^+,m}$	9.31E-10
n_{H2}	2	κ_s	7.41E+5
n_{Cl2}	2	j_{0O2}	1.00E-8
d_1	0.0001	j_{0OH}	0.87
d_2	0.0018	j_{0Ni}	1.00E-4
d_3	0.00018	j_{0Zn}	3.20E-2
d_4	0.0018	$\beta_{Ni,c}$	50
d_5	0.0001	$\beta_{Ni,a}$	50
A_c	0.0135	$\beta_{Zn,c}$	30
A_a	0.0135	$\beta_{Zn,a}$	30
A_M	0.0169	$\beta_{Cl2,c}$	38
V_c	0.002	$\beta_{Cl2,a}$	77
V_a	0.002	$\beta_{H2,c}$	19
E_{Zn}^0	-0.763	$\beta_{H2,a}$	19
E_{Ni}^0	-0.241	$\beta_{O2,c}$	19
E_{H2}^0	0	$\beta_{O2,a}$	38
E_{O2}^0	1.229	$C_{Ni(II),in,c}$	18
$z_{Zn^{2+}}$	+2	$C_{Zi(II),in,c}$	30
$z_{Ni^{2+}}$	+2	$C_{Na,in,c}$	1000
z_{Cl^-}	-1	$C_{H,in,c}$	1
$z_{SO4^{2-}}$	-2	$C_{Cl,in\ c}$	5000
z_{H^+}	+1	$C_{SO4,in,\ a}$	1000

z_{Na^+}	+1	$C_{H,in,a}$	1.00E-4
$D_{Zn^{2+}}$	4.54E-10	$C_{Na,in,a}$	1000

Maple™ Codes

```
Restart:
with(geometry):
with(plots):
PDEtools[declare](prime=x):
```

(i) Declare Constants

(ii) Declare Concentrations

Catholyte

C1 is Ni^{2+} concentration, C2 is Zn^{2+} concentration, C3 is the H^+ concentration, C4 is Cl^- concentration, C5 is concentration of Na^+, C6 is concentration of SO_4^{2-}. Below is the bulk concentration of each species in solution in mol m^{-3}

Anolyte

C3a is the H^+ concentration, C5a is concentration of Na^+, C6a is concentration of SO_4^{2-}. Below is the bulk concentration of each species in solution in mol m^{-3}

(iii) Calculate Equilibrium Electrode Potentials (SHE/V) at 298 K

Example:

```
eNi2  := evalf(-0.245+R*T/(2*F)*ln(10)*log10(C1(x)/1000)):
```

(iv) Calculate the ionic mobility (u) with given Diffusion Coefficient [28]

Example:

```
u[Ni2]:= dNi2/ (R*T):
```

(v) Calculate the diffusion limiting current density

Example:

jL is the diffusion limiting current (A m^{-2})

jLNi := 1.554*2*F*(dNi2)^(2/3)*(nu)^(-1/6)*f^(1/2)*C1(x):

(vi) Establish the charge balance at the catholyte and anolyte according to electroneutrality equations [28]

Catholyte.charge balance:

2 ×[Ni 2+] + 2× [Zn 2+] + [H+]+[Na+] = [Cl-]

eq1a := 2*C1(x)+2*C2(x)+C3(x)+C5(x)-C4(x) = 0;

Anolyte.charge balance:

[H+] + [Na+] = 2 × [SO42-] + [OH-]

eq1b := C3a(x) + C5a(x) – 2*+C6a(x) = 0;

(vii) Calculate the distribution of electrode and electrolyte phase potential, depending on j(x)

Phi[e] is the electrode phase potential (V), Phi[s] is the electrolyte phase potential (V), x is the distance in the direction of current flow normalised with respect to L

Catholyte:

eq1c:=diff(phi[s](x),x,x)=(j(x))/(F^2*d1*((abs(2^2)*u[Ni2]*C1(x))+(abs(2^2)*u[Zn2]*C2(x))+(abs(1^2)*u[H2]*C3(x))+(abs(1^2)*u[Na]*C5(x))-(abs(-1^2)*u[Cl]*C4(x)))):

Anolyte:

eq1d:=diff(phi[an](x),x,x)=(jO2)/(F^2*d5*((abs(1^2)*u[H2]*C3a(x))+(abs(1^2)*u[Na]*C5a(x))-(abs(-2^2)*u[SO4]*C6a(x)))):

(viii) Establish the relationship between the concentration c and the local current density at the catholyte and anolyte. (Nernst-Plank equation)

Eq2 is the H^+ material balance, Eq3 is the Ni^{2+} material balance, Eq4 is the Zn^{2+} material balance, Eq5 is the Cl^- material balance, Eq 6 is the Na^+ material balance.

Example:

Eq2:=n1*F*v*((dh*diff(C3(x),x,x))+(z1*u[H2]*F*C3(x)*diff(phi[s](x),x,x))+(z1*u[H2]*F*diff(C3(x),x)*diff(phi[s](x),x)))=Ac*j2(x):

(ix) Define boundary conditions at the start of experiment (transient condition), when overpotential and time are zero

(x) Develop a Butler-Volmer Relationship between reaction current density and overpotential

j2(x) is the current due to hydrogen evolution, j3(x) is the current due to Ni(II) reduction, j4(x) is the current due to Zn(II) reduction, j5(x) is the current due to Cl_2 reduction

Example:

```
j2(x):=-j0H*(exp(-19.1882*(Eapplied-phi[s](x)-eH))):
j3(x):=-j0Ni*(exp(-bcNi*(Eapplied-phi[s](x)-eNi2))-exp(baNi*(Eapplied-phi[s](x)-
eNi2)))/(1+j0Ni/jLNi*exp(baNi*(Eapplied-phi[s](x)-eNi2))+j0Ni/jLNi*exp(-bcNi*(Eapplied-
phi[s](x)-eNi2))) :
```

(xi) Solve numerical solution of the differential equation system using Maple's dsolve routine

```
dsys:={eq1c,eq2,eq3,eq4,eq5,2*C1(x)+2*C2(x)+C3(x)+C5(x)-C4(x) = 0, C1(d1) = 18,
C2(d1) = 30, C3(d1) = 0.54, C4(d1) =5000 , D(C1)(d1) = 0, D(C2)(d1) = 0, D(C3)(d1) = 0,
D(C4)(d1)=0,phi[s](d1)=0,D(phi[s])(d1) = 0}:

sol1:=dsolve(dsys, numeric):

ya2:=u->subs(sol1(u),phi[s](x)):
ya3Ni2:=u->subs(sol1(u),C1(x)):
ya3Zn2:=u->subs(sol1(u),C2(x)):
ya3Cl2:=u->subs(sol1(u),C4(x)):
ya3H:=u->subs(sol1(u),C3(x)):
ya3pH:=u->subs(sol1(u),pH(x)):
ya3Na:=u->subs(sol1(u),C5(x)):
ya5:=u->subs(sol1(u),j2(x)):
ya7:=u->subs(sol1(u),j3(x)):
ya8:=u->subs(sol1(u),j4(x)):
ya9:=u->subs(sol1(u),j5(x)):
```

(xii) Calculate the potential drop across the catholyte, membrane and the anolyte

kappa[s] is the electrolyte phase's conductivity (S m^{-1})

```
kappa[catholyte] := 60; kappa[membrane] := 8.3; kappa[anolyte] := 21.08

solution1 := ya2(d1);
solutiond1d2 := solution1+abs(Totalj)*(x-d1)/kappa[catholyte];
```

```
solution2 := eval(solutiond1d2, x = d1+d2);
solutiond2d3 := solution2+abs(Totalj)*(x-d1-d2)/kappa[membrane];
solution3 := eval(solutiond2d3, x = d1+d2+d3);
solutiond3d4 := solution3+abs(Totalj)*(x-d1-d2-d3)/kappa[anolyte];
solution4 := eval(solutiond3d4, x = d1+d2+d3+d4);
solutiond4d5 := solution4+ya4(d1+d2+d3+d4);
solution5 := eval(solutiond4d5, x = d1+d2+d3+d4+d5);


drop1 := plot(solutiond1d2, x = d1 .. d1+d2, axes = boxed, titlefont = [TIMES, BOLD, 10],
labelfont = [TIMES, BOLD, 10], axes = boxed, title = "Potential distribution", labels = ["x",
"Potential(V)"], color = red, thickness = 2, labeldirections = [horizontal, vertical]);

drop2 := plot(solutiond2d3, x = d1+d2 .. d1+d2+d3, axes = boxed, titlefont = [TIMES,
BOLD, 10], labelfont = [TIMES, BOLD, 10], axes = boxed, title = "Potential distribution",
labels = ["x", "Potential(V)"], color = green, thickness = 2, labeldirections = [horizontal,
vertical]);

drop3 := plot(solutiond3d4, x = d1+d2+d3 .. d1+d2+d3+d4, axes = boxed, titlefont = [TIMES,
BOLD, 10], labelfont = [TIMES, BOLD, 10], axes = boxed, title = "Potential distribution",
labels = ["x", "Potential(V)"], color = blue, thickness = 2, labeldirections = [horizontal,
vertical]); display(drop1, drop2, drop3, title = "Solution Potential Distribution");
```

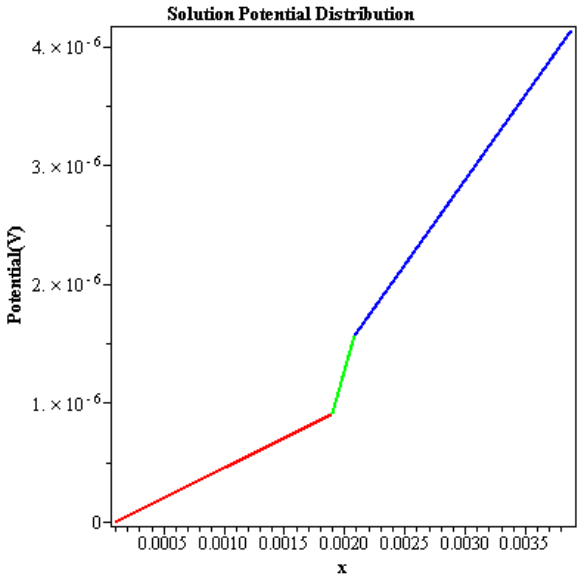

Figure 11-145. Predicted potential drop in the reactor

(xiii) Calculate the cell voltages, U

```
CellVoltage := evalf(AnPotential-Eapplied+solution5+0);
```

(xiv) Calculate the H^+ and Na^+ fluxes across the membrane

```
jm := -Totalj/(1+dNa*cb(t)/(dh*ca(t)));
```

eq[1] := diff(ca(t), t) = -Aa*Totalj/(F*Vc)+jm/(F*Vc);

eq[2] := diff(cb(t), t) = -Am*jm*dNa*cb(t)/(dh*ca(t)*F*Vc);

ICS := ca(0) = 0.1e-3, cb(0) = 1000;

(ICS: Initial Conditions)

sol := dsolve({ICS, eq[1], eq[2]}, numeric);

(xv) Predicting the catholyte pH

eq[3]:=diff(cc(t),t)=-(-curr1*Ac)/(Vc*F)+(jm*Am)/(Vc*F):

solve := dsolve({ICS, eq[1], eq[2], eq[3], cc(0) = 0.54}, numeric);

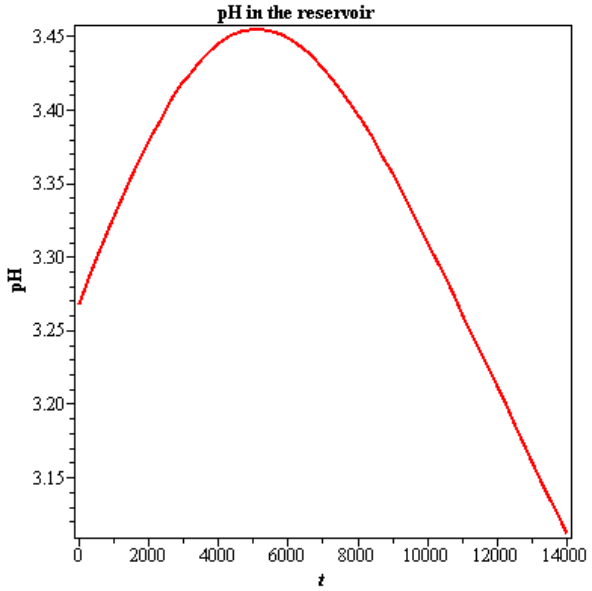

Figure 11-146. Predicted pH profiles in the catholyte.

Appendix F: Flow meter calibration

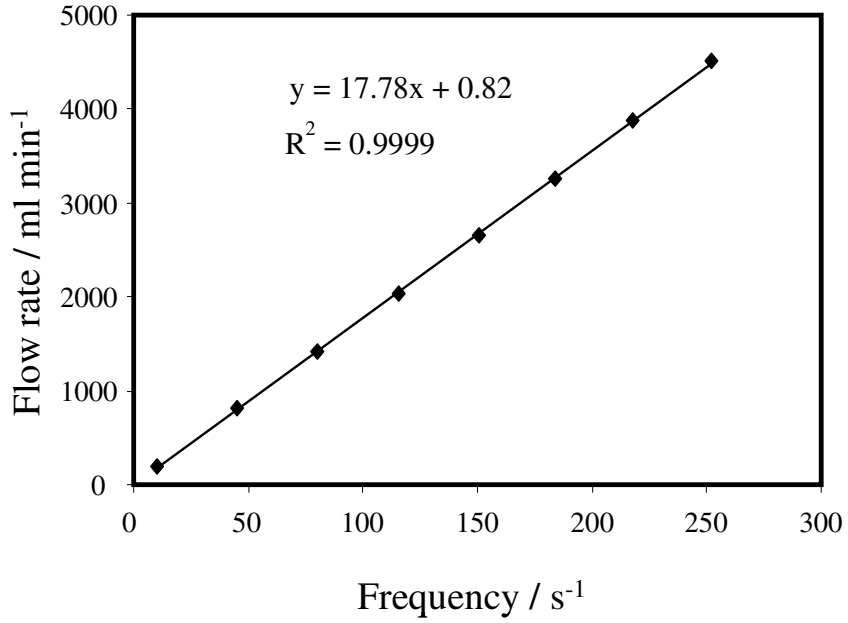

Figure 11-147. Flow meter calibration.

Appendix G: Costing

From the value of the recoverable metals present, the value of typical printed circuit boards scrap is ca. £5000 tonne^{-1} [6]. Average charge yield for electrowinning of Ag, Au, Cu, Sn, Pb, are estimated to be >0.8, corresponding to electrical energy costs of ca. £100 tonne^{-1} of boards processed (assuming 5 p per kWh), although a compromise in efficiency must be made to recover the Pb, Zn, Ni and Fe, the cost are still feasible <250 tonne^{-1} of shredded WEEE. Cheng et al. estimated that ten 100 kg day^{-1} leach column reactors, 1.6 m in height and 0.3 m in diameter, would be needed to dissolve the metals from the WEEE. Meanwhile, recovery of those metals from solution would require ca. fifteen 1.0 m × 0.3 m× 0.1 m electrochemical reactors, each with a circulating particulate bed cathode and mesh cathode of fluidised bed of inert particles; cathode area of ca. 5 m^2 together with electrical power supply by a 15 V, 3200 A transformer-rectifier. Detailed costs for the process equipment, instruments, and running costs have also been estimated for a plant capable of processing 1 tonne per day of shredded WEEE. A rough capital costing which includes cost of equipments, buildings and services per year within the process is given in Table 11-21.

Table 11-21. Capital cost of recovery plant processing 1 tonne per day of shredded WEEE.

Item	Cost / £	Lifetime/years
Electrochemical Reactor	7000	5
Transformer Rectifier	25000	5
Pumps (2)	1000	5
Fittings	800	5
Flowmeters	2000	5
Pipework	1200	5
Sensors	1000	5
Gas alarms	1000	5
Gas alarm sensors	200	1
Reservoirs	1500	5
Frame/ Support	3000	5
Frame support (tubing only)	3000	5
10 dm^3 of 4 kmol m^{-3} HCl + 1 kmol m^{-3} NaCl electrolyte	300	0.5
PVDF costs (1.5 m × 1 m × 20 mm)	22500	5
Manufacture costs	30000	5
Anode costs	5250	2
Cathode costs	1500	3
Mambrane costs	6000	1

Total Cost (including VAT) **111,150**

The equipment costs (including reactors, power supply, pumps, fittings, valves, instruments, pipe work, sensors, alarms, support frames and reservoirs) for a 1 tonne per day plant are ca. £120k. The assumption that the equipment costs constitute approximately one quarter of the costs for the plant, buildings and services, gives a total capital expenditure to construct and install such a plant of < £450k. Taking into account the expected lifetime for the different items of equipment, the total annual capital, operating and refining costs are < £120k, compared with an annual processed metal value of £500k shows that recovery of copper from WEEE leaching solutions is economically feasible.

References

[1] A.J. Bard, R. Parsons, J.Jordan, Standard potentials in aqueous solution, New York: Marcel Dekker, 1985.

[2] D.D. Wagman, W.H. Evans, V.B. Parker, R.H. Schumm, I. Halow, S.M. Bailey, K.L. Churney, R.L. Nuttall, The NBS Tables of Chemical Thermodynamic Properties. *J. Phys. Chem. Ref. Data*, 11(Supplement 2), 1982.

[3] M. Wang, Y. Zhang, M. Muhammed, Critical evaluation of thermodynamics of complex formation of metal ions in aqueous solutions III: The system Cu(I,II)-Cl-e at 298.15 K, *Hydromet*., 45, 1997, pp. 53-72.

[4] Powell, K. J., Brown, P. L., Byrne, R. H., Gajda, T., Hefter, G., Sjoberg, S. and Wanner, H., 2007, Chemical speciation of environmentally significant metals with inorganic ligands. Part 2: The Cu^{2+}-OH^-,Cl^-, CO_3^{2-} , SO_4^{2-}, and PO_4^{3-} systems (IUPAC Technical Report). *Pure and App. Chem*., 79 895-950.

[5] Cheng, C.-Y., Diaz, M. A., Kelsall, G. H. and Robson, A. C., 2006, Gold Electrowinning from Acidic Aqueous Chloride in a Packed Bed Electrode. *ECS Trans*., 2 (3): 317-328.

[6] Goosey, M. and Kellner, R., 2003, Recycling technologies for the treatment of end of life printed circuit boards (PCBs) *Circuit World*, 29 (3): 33-37.

[7] Cheng, C-Y., Kelsall, G. H., 2008, Recovery of Metals from Waste Electical and Electronic Equipment by Leaching and Electrowinning, The Resource Efficiency KTN, Personal communications.

[8] Mathias, M. F., Villa, C. M. and Chapman, T. W., 1990, A model of zinc-nickel alloy electrodeposition in an industrial-scale cell. *J. App. Electrochem*., 20 1-10.

[9] Ji, J., Cooper, W. C., Dreisinger, D. B. and Peters, E., 1995, Surface pH measurements during nickel electrodeposition. *J. App. Electrochem*., 25 (7): 642.

[10] Cheng, C.-Y., Diaz, M. A., Kelsall, G. H. and Robson, A. C., 2006, Gold Electrowinning from Acidic Aqueous Chloride in a Packed Bed Electrode. *ECS Trans.*, 2 (3): 317-328.

[11] Gamsjäger, H., Bugajski, J, Gajda, T., Lemire, R. and Preis, W., 2005, Chemical Thermodynamics of Nickel. Chem. Thermo. Vol. 6 (ed.) Elsevier Science.

[12] Newman, J. S., 1991, Electrochemical Systems. Prentice Hall, Second Edition 255.